

**Material Transport and Reaction Effects in Surface Topography
Evolution During Plasma Etching**

by

John Christopher Arnold

B.S. Chemical Engineering
Rensselaer Polytechnic Institute, 1985

M.S. Electrical Engineering
University of Arizona, 1989

**Submitted to the Department of Chemical Engineering
in Partial Fulfillment of the Requirements for the Degree of**

**Doctor of Philosophy
in
Chemical Engineering**

at the
MASSACHUSETTS INSTITUTE OF TECHNOLOGY
February, 1995

© Massachusetts Institute of Technology, 1995. All Rights Reserved.

Signature of Author _____
Department of Chemical Engineering

Certified by _____
Professor Herbert H. Sawin, Thesis Advisor
Departments of Chemical Engineering and
Electrical Engineering and Computer Science

Accepted by _____
Professor Robert E. Cohen
Chairman, Committee for Graduate Students

Science
1 FEB 17 1995

**Material Transport and Reaction Effects in Surface Topography
Evolution During Plasma Etching**

by

John Christopher Arnold

Submitted to the Department of Chemical Engineering on
September 16, 1994 in Partial Fulfillment of the Requirements for
the Degree of Doctor of Philosophy in Chemical Engineering

Abstract

The evolution of surfaces during plasma etching was investigated, using a combination of theoretical, numerical, and experimental techniques. The evolution and final shape of etched surface features were found to depend primarily upon the transport of energetic ions and neutral reactants into features and the kinetics of the etching reaction.

Transport of ions into features was analyzed by constructing theoretical and numerical models for the most important influences on the ion trajectory and comparing those models to industrial observations. The single most important factor affecting ion transport in features was found to be the reflection of those ions which strike the sidewalls at or near glancing incidence. Through comparison of numerical modeling and experimental analysis of etched features, ion reflection was isolated as the dominant cause of "microtrench" formation, wherein the depth of an etched feature is greater near the feature sidewalls. Microtrenching is a very serious problem in the fabrication of high-performance MOS transistors, because microtrenches impact the integrity of the gate oxide. Quantitative agreement between the numerical model and observations under conditions of varying sidewall geometry conclusively identified ion reflection as the cause of microtrenches. A related project showed that ion energy loss during reflection also plays an important role in feature etching for some systems.

Localized charging of insulator surfaces was also examined as a possible factor influencing ion transport and flux uniformity. Surface charging of this type arises from local (within the etched feature) imbalances in the electron and ion current densities. Direct experimental observation was not possible, so a numerical model for the "worst-case" scenario was constructed. This model suggested that surface charging could have a strong effect on the ion flux distribution within the feature, if the sidewall materials are sufficiently good insulators.

The transport of neutral reactants into features was studied as a possible cause for reduced etching rate in deep surface features. A numerical model for molecular

diffusion within features was constructed and combined with previously published kinetic data for the fluorine etching of silicon. In surface features with high aspect ratio (depth much greater than width), reactant transport limitations had a strong influence on the etching rate at the bottom. The effect of reactant (fluorine radical) transport was greater under process conditions which increased the fluorine reaction probability on the feature walls or bottom.

Application of the ion and reactant transport models to evolving features required development of a new algorithm for surface "advancement." Advancement refers to the process of predicting the surface evolution from the local topography and etching rates. The available methods were found to be lacking in accuracy and stability, so a new and improved method was developed.

The numerical modeling effort identified the surface reaction as the most important and least understood step in feature etching. The surface reaction ties the transport and advancement models together, converting ion and reactant flux data into local etching rates. A comprehensive description of the relationship between flux and etching rate is essential for simulation of topography evolution, yet very few systems have been studied in sufficient detail. Therefore, the second phase of this project focused on experimental measurement of the kinetics for polysilicon etching in chlorine discharges.

The experimental effort comprised two parts: the first, and more extensive, involved construction of equipment for laboratory simulation of industrial discharge processes. The technique chosen used discrete ion and radical beams to approximate the conditions present in a plasma etcher, while allowing independent control of the individual flux conditions. Sources for chlorine ion and radical beams were constructed and characterized. The final experimental work was a preliminary investigation of the etching kinetics. One important and novel result was the observation of an angular dependence in the ion etching yield: the etching rate was found to depend not just upon the ion flux and energy but also upon the ion arrival angle at the surface. This was the first known measurement of arrival angle effects under reactive ion etching conditions. Completion of this kinetic study by others will provide information very useful for future efforts in topography simulation.

Thesis supervisor: Professor Herbert H. Sawin
MIT Professor of Chemical Engineering and Electrical
Engineering and Computer Science

Dedication

To Sara,

who has lived her entire life with the
misery and shame of her father's membership
in that most listless and unproductive
class of parasites:

graduate students.

(At least there's hope for my redemption:
I wasn't in law school.)

Acknowledgements

This page is traditionally one of the easiest sections of the thesis to write. After all, what could be simpler than making a list of the people who have helped you? But there have been so many people who have helped me in so many different ways that it would be too easy to overlook someone. The only way to be sure that I don't leave anyone out is to not leave anyone in.

So: no list of names. Thanks to all who helped. On with the show!

Table of Contents

Abstract	3
Dedication	5
Acknowledgements	7
List of Figures	12
1. Introduction	19
1.1 Purpose	19
1.2 Plasma Etching Basics	20
1.3 Plasma Etching Research	23
Part I: Numerical Modeling of Topography Evolution	
2. Ion Transport: Dispersion and Reflection	29
2.1 Introduction and Mechanisms	29
2.2 Ion Flux Model	35
2.3 Visibility	45
2.4 Numerical Methods and Convergence	50
2.4.1 Two-dimensional Approximation	56
2.5 Applications	59
2.5.1 Microtrenching During Polysilicon Etching	59
2.5.2 High-density Oxide Etching	68
3. Ion Transport: Surface Charging	87
3.1 Introduction and Mechanism	87
3.2 Numerical Methods	90
3.3 Results and Conclusions	100
4. Reactant Transport	111
4.1 Introduction and Mechanisms	111
4.2 Transport Model and Numerical Methods	113
4.3 Application: Fluorine Etching of Deep Trenches in Silicon	118
4.3.1 Surface Reaction	119
4.3.2 Ion Flux	124
4.3.3 Reactant flux	133
4.3.4 Results	137
4.4 Combined Model for Reaction and Reactant Transport	148
5. Surface Advancement	152
5.1 History and Requirements	152
5.2 Equations for Surface Advancement	160
5.3 Treatment of Sharp Corners in the Initial Profile	163
5.4 Numerical Implementation	179
5.5 Application to Ion Milling	180

5.6 Convergence	195
5.7 Conclusions	199
6. Model Integration	202
6.1 Ion Flux to Sharp Corners	202
6.2 Etching Rate vs. Slope	206
6.3 Surface Reaction Kinetics	210
6.3.1 History	211
6.3.2 Fluorine-based etching of Si and SiO ₂	215
6.3.3 Chlorine-based etching of Si	224
6.3.4 Proposal for Additional Measurements	225
 Part II: Etching Experiments	
7. Equipment for Etching Polysilicon with Chlorine	227
7.1 Reactor Vessel and Vacuum System	227
7.1.1 Overview	227
7.1.2 Modifications for Off-normal Ion Incidence	229
7.2 Ion Flux and Energy Analysis	232
7.2.1 Measurement Technique	233
7.2.2 Gibson's Gridded Analyzer	237
7.2.3 High Isolation Analyzer	241
7.3 Ion Beam Source	246
7.3.1 ASTeX CECR	247
7.3.2 Modifications for Beam Energy Control	247
7.3.3 Ion Extraction Grids	255
7.3.4 Differential Pumping	261
7.4 Chlorine Atom Source	262
7.4.1 Principles of Operation	264
7.4.2 Beam Characterization	266
7.4.3 Modifications for Plasma Containment	267
 8. Polysilicon Etching Experiments	 273
8.1 Kinetic study	273
8.1.1 Plans	273
8.1.2 Etching with Chlorine Atoms and Argon Ions:	276
Effect of Flux Ratio	
8.1.3 Etching with Chlorine Atoms and Argon Ions:	281
Effect of Ion Incidence Angle	
8.1.4 Problems and Suggestions for Future Work	283
8.2 Etching of Patterned Surfaces	296
8.2.1 Sample Preparation	297
8.2.2 Etching and Results	302
8.2.3 Suggestions for Future Work	316
 References	 318

Appendices	325
A. Ion Reflection Model for Circular Via	325
A.1 Description of Via	325
A.2 Geometry for Ion Reflection in Via	325
B. Equivalence of 2- and 3-Dimensional	336
Visibility Calculations	
B.1 Rectangular Trenches	336
B.2 Circular Via	339
C. Interchange Factors for Neutral Transport	345
C.1 Introduction	345
C.2 Segments on Intersecting Lines	346
C.3 Segments on Parallel Lines	350
D. Development of Characteristic Equations for	353
Surface Advancement	
E. Comparison of Delooping to Entropy and Jump Conditions	365
E.1 Entropy Condition	365
E.2 Jump Condition	373
F. Shock Trajectories for Segment Advancement	378

List of Figures

Figure 1.1	Simplified Reactive Ion Etching system.	21
Figure 1.2	Elements of plasma etching process.	24
Figure 1.3	Elements of Surface Chemistry and Topography Evolution.	27
Figure 2.1	Effect of ion dispersion on flux to bottoms of different features.	32
Figure 2.2	Characteristic angles and trajectories for reflected ions.	38
Figure 2.3	Coordinate system used for flux calculations in long rectangular trenches.	41
Figure 2.4	Definitions of and relationships between in-plane angles for ion reflection in long rectangular trenches.	43
Figure 2.5	Identification of a point which may interfere with view between others.	49
Figure 2.6	Breakdown of Simpson's integration when resolution is low and calculations are noisy.	53
Figure 2.7	Ion Angular Distribution, Fractional Population per degree from macroscopic wafer normal.	62
Figure 2.8	Ion flux profile to bottom of surface feature.	64
Figure 2.9	Response surface for maximum nonuniformity with varying photoresist thickness and angle.	66
Figure 2.10	Offset (distance from foot of sidewall to microtrench) vs. photoresist and polysilicon angles.	67
Figure 2.11	Effect of line spacing (open feature width) on bottom ion flux profile.	69
Figure 2.12	Estimated evolution of isolated step etched at 400 W.	73
Figure 2.13	Total ion flux to feature bottom vs. distance from final sidewall foot and etching time, for 400 W sample.	74

Figure 2.14	Ion flux vs. distance from sidewall foot for isolated step	75
	etched at 800 W.	
Figure 2.15	SEM photo of isolated step etched at 800 W.	77
Figure 2.16	Microtrench depth and flux enhancement due to ion	78
	reflection vs. wafer bias power.	
Figure 2.17	Relative yield of reflected ions (vs. direct ions), as	80
	estimated from observed microtrench depths, vs. wafer bias power.	
Figure 2.18	Etching rate vs. ion energy for CF_4 of SiO_2 in an ECR,	82
	from the published work of Oehrlein, <i>et al.</i> [1994].	
Figure 2.19	Procedure for estimating energy of reflected ions.	84
Figure 2.20	Estimated ion energies before and after reflection, and	85
	energy loss coefficient, vs. wafer bias power.	
Figure 3.1	Mechanism for ion deflection by charging of feature surfaces. . .	89
Figure 3.2	Computational domain and boundary conditions for charging . . .	93
	of feature surfaces.	
Figure 3.3	Final surface potential for trench with aspect ratio 2.	101
Figure 3.4	Variation of extreme surface potentials with feature	103
	aspect ratio.	
Figure 3.5	Ion flux to the feature surface for different aspect ratios.	105
Figure 3.6	Effect of feature aspect ratio (depth/width) on loss of	106
	ions to the feature sidewalls.	
Figure 3.7	Maximum potential difference along surface for simplified	109
	conductance model.	
Figure 4.1	Ion angular distributions from Liu, <i>et al.</i> [1990].	126
Figure 4.2	Illustration of multiple ion reflection in rectangular	128
	trenches of varying aspect ratio (depth/width).	
Figure 4.3	Profile of ion flux to the bottom of a trench with aspect	129
	ratio 5.	

Figure 4.4	Profile of ion flux to the bottom of a trench with aspect ratio 20.	130
Figure 4.5	Comparison of error in computed ion flux to the number of reflections considered for different IAD's and aspect ratios.	132
Figure 4.6	Fluorine reaction probability predicted by the model of Gray [1992].	136
Figure 4.7	Effect of neutral transport to the bottom of a rectangular trench at reaction probabilities in the range reported by Gray [1992].	138
Figure 4.8	Effect of aspect ratio on fluorine flux, ion flux, and etching rate at the bottom of a rectangular trench.	139
Figure 4.9	Effect of substrate temperature on bottom surface etching rates for trenches of varying aspect ratios.	144
Figure 4.10	Effect of substrate temperature and IAD on the relative importance of reactant transport.	146
Figure 4.11	Effect of fluorine/ion flux ratio and ion energy on the relative importance of reactant transport.	147
Figure 5.1	The Angle Bisector algorithm.	154
Figure 5.2	Instability of the Angle Bisector algorithm due to excessive time step and strong slope dependence of etching rate.	155
Figure 5.3	Segment advancement algorithm.	156
Figure 5.4	Instability of segment advancement algorithm on flat surface with non-uniform etching rate.	158
Figure 5.5	Computation of ER_i	162
Figure 5.6	Comparison of Method of Characteristics with Angle Bisector method for etching rate which varies with surface slope.	164
Figure 5.7	Behavior of Angle Bisector algorithm in sharp corner with different etching rates on adjacent walls.	166
Figure 5.8	Examples of unstable shocks.	167

Figure 5.9	Flux function and stable profile for the intersection of two surfaces at 75° and -75° for the typical sputtering yield shown in Equation (5.5).	170
Figure 5.10	Evolution of various initial surfaces joining two inclined planes.	171
Figure 5.11	Delooping process.	175
Figure 5.12	Modeling of shocks in initial profile.	176
Figure 5.13	Treatment of shocks with segment advancement algorithm.	178
Figure 5.14	Example ion sputtering yield and etching rate curves for ion milling, from Equation (5.5).	181
Figure 5.15	Facet formation at convex shock under ion milling with typical sputtering yield.	182
Figure 5.16	Simulated evolution of initial profile described by Ducommun, <i>et al.</i> [1975].	184
Figure 5.17	Comparison of simulation shown in Figure 5.16 to dimensions reported by Ducommun, <i>et al.</i> [1975].	185
Figure 5.18	Evolution of 0° to 90° concave shock under ion milling with sputtering yield from Equation (5.5).	187
Figure 5.19	Effect of shock expansion on deep trench etching for two sputtering yield functions.	189
Figure 5.20	Expansion of 0° to 45° concave shock under ion milling with typical sputtering yield.	190
Figure 5.21	Evolution of a sharp step joining two horizontal planes.	192
Figure 5.22	Evolution of various steps joining two horizontal planes.	194
Figure 5.23	Convergence of predicted shock location with angular resolution.	197
Figure 5.24	Convergence of curved trajectories with time resolution.	200
Figure 6.1	Replacing shocks with smooth curves to avoid ion flux and etching rate discontinuities.	205

Figure 6.2	Effect of reactant availability on ion etching yield.	214
Figure 6.3	Ion-enhanced etching behavior for Silicon and Fluorine, according to Gray, <i>et al.</i> [1993].	221
Figure 6.4	Ion-enhanced etching behavior for Silicon Dioxide and Fluorine, according to Gray, <i>et al.</i> [1993].	222
Figure 7.1	Schematic view of multi-beam etching apparatus.	228
Figure 7.2	Measurement of etching rate at ion incidence angles other than normal.	231
Figure 7.3	Example of current to ion collector and Ion Energy Distribution.	234
Figure 7.4	Schematic diagram of typical gridded ion energy analyzer.	236
Figure 7.5	Gridded ion energy analyzer adapted from design by Gibson [1992].	238
Figure 7.6	Typical ion collector current vs. voltage for original energy analyzer.	239
Figure 7.7	Schematic diagram of new ion energy analyzer design.	244
Figure 7.8	Typical ion collector current vs. voltage for revised energy analyzer.	245
Figure 7.9	Schematic diagram of Compact ECR plasma source.	248
Figure 7.10	Effect of neutralizing filament current on ion beam flux at sample position.	251
Figure 7.11	Biasing liner, extraction grid, and neutralizing filament.	252
Figure 7.12	Effect of applied plasma bias on ion beam energy and current.	254
Figure 7.13	Effect of prolonged use on grid shape and ion beam intensity.	256
Figure 7.14	Effect of grid hole size on ion beam intensity.	258

Figure 7.15	Simplified schematic diagram of new radical (or atom) source	265
Figure 7.16	Effect of microwave power and feed gas flow rate on dissociation of chlorine in the new atom source.	268
Figure 7.17	Polysilicon etching rate with atom source alone, using original ampule and nozzle design.	270
Figure 7.18	Comparison of original and revised nozzle designs.	271
Figure 8.1	Variation of ion etching yield with chlorine atom/ion flux ratio.	280
Figure 8.2	Variation of ion etching yield with chlorine atom/ion flux ratio and ion incidence angle.	282
Figure 8.3	Current design for atom source vacuum seal.	285
Figure 8.4	Effect of feed gas flow rate and nozzle diameter on pressure, mean free path, and dimensionless parameter η at tip of nozzle.	289
Figure 8.5	Effect of feed gas flow rate and nozzle diameter on pressure inside ampule.	291
Figure 8.6	Effect of feed gas flow rate on ampule pressure and dimensionless parameter η for different nozzle arrays.	293
Figure 8.7	Beam intensity profiles for various values of dimensionless parameter η .	294
Figure 8.8	Concept for beam etching of initial surface feature.	298
Figure 8.9	Typical initial profiles for rectangular trenches of three nominal widths.	301
Figure 8.10	Typical surface profiles after beam etching for normal ion incidence.	303
Figure 8.11	Typical surface profiles after beam etching for 20° off-normal ion incidence.	305
Figure 8.12	Typical surface profiles after beam etching for 40° off-normal ion incidence.	307

Figure 8.13	Typical surface profiles after beam etching for 60° off-normal ion incidence.	309
Figure 8.14	Comparison of expected atom beam direction to observed "shelf" remaining on bottom of features etched at normal ion incidence.	312
Figure 8.15	Comparison of simulated and observed profiles for samples etched at 20° off-normal ion incidence.	313
Figure 8.16	Comparison of simulated and observed profiles for samples etched at 40° off-normal ion incidence.	314
Figure 8.17	Comparison of simulated and observed profiles for samples etched at 60° off-normal ion incidence.	315
Figure A.1	Circular via and coordinate system.	327
Figure A.2	Characteristic rays for ion reflection into circular via.	329
Figure A.3	Relationship between azimuthal angles about target point and central axis of feature.	333
Figure A.4	Location of origin point for reflected ray.	334
Figure B.1	Relationship between rotational angle and distance to sidewall for circular via.	340
Figure C.1	Geometry and nomenclature for calculation of interchange factor for two segments on intersecting lines.	347
Figure C.2	Geometry and nomenclature for calculation of interchange factor for two segments on parallel lines.	351
Figure E.1	Convex and concave envelopes over an arbitrary $f(p)$	368
Figure E.2	Evolution of example convex shock.	370
Figure E.3	Evolution of convex shock with non-tangential approach of envelope to $f(p)$	374

Chapter 1

Introduction

1.1 Purpose

The purpose of this project was to improve understanding of the factors affecting the control of plasma etching processes. The fundamental effect of any etching process is to selectively remove a portion of the surface material, leaving some pattern of open areas in the top surface. The "output" of the etching process is surface topography, and control of the process refers to the conformance of the final topographic profile to the desired shape.

Several parameters are used to characterize the performance of microelectronic etching processes. Principal among these are *uniformity*, describing variations from point to point on the wafer; *selectivity*, comparing the rates at which different materials are removed; *anisotropy*, referring to the relative etching rates parallel and perpendicular to the wafer surface, and *process stability* or *sensitivity*, considering the effect of changes in the process upon the etching performance. However, it is clear that these terms all refer to specific facets of one fundamental issue: surface topography evolution. The basic operation in etching is the incremental evolution of the surface topography in response to local process conditions, and uniformity, selectivity, anisotropy, and process stability are all used to describe

different aspects of that evolution.

This project sought a fundamental understanding of plasma etching processes and their performance. Surface topography evolution was thus the natural point of focus. A combination of theoretical and experimental techniques was used to analyze different contributions to topography evolution.

The division between theoretical and experimental methods is reflected in the organization of this document. The first major section, consisting of Chapters 2 through 6, is concerned with theoretical work supporting numerical simulation of topography evolution. The second major portion comprises Chapters 7 and 8 and focuses on experimental measurement of reaction kinetics for a specific surface material and etching process. The remainder of this Chapter provides an introduction to the topics of plasma etching and topography evolution.

1.2 Plasma Etching Basics

The plasmas used in microelectronic fabrication are typically generated by the ionization of a reactive gas at low pressure. The feed gas is introduced into a vacuum chamber at pressures of a few to several hundred milliTorr (mTorr), and a high electric field is applied to the gas. Figure 1.1 shows a typical "parallel-plate" system, which utilizes a pair of planar electrodes inside the chamber to transmit the electric field from a high-frequency (typically 13.56 Mhz) generator to the feed gas.

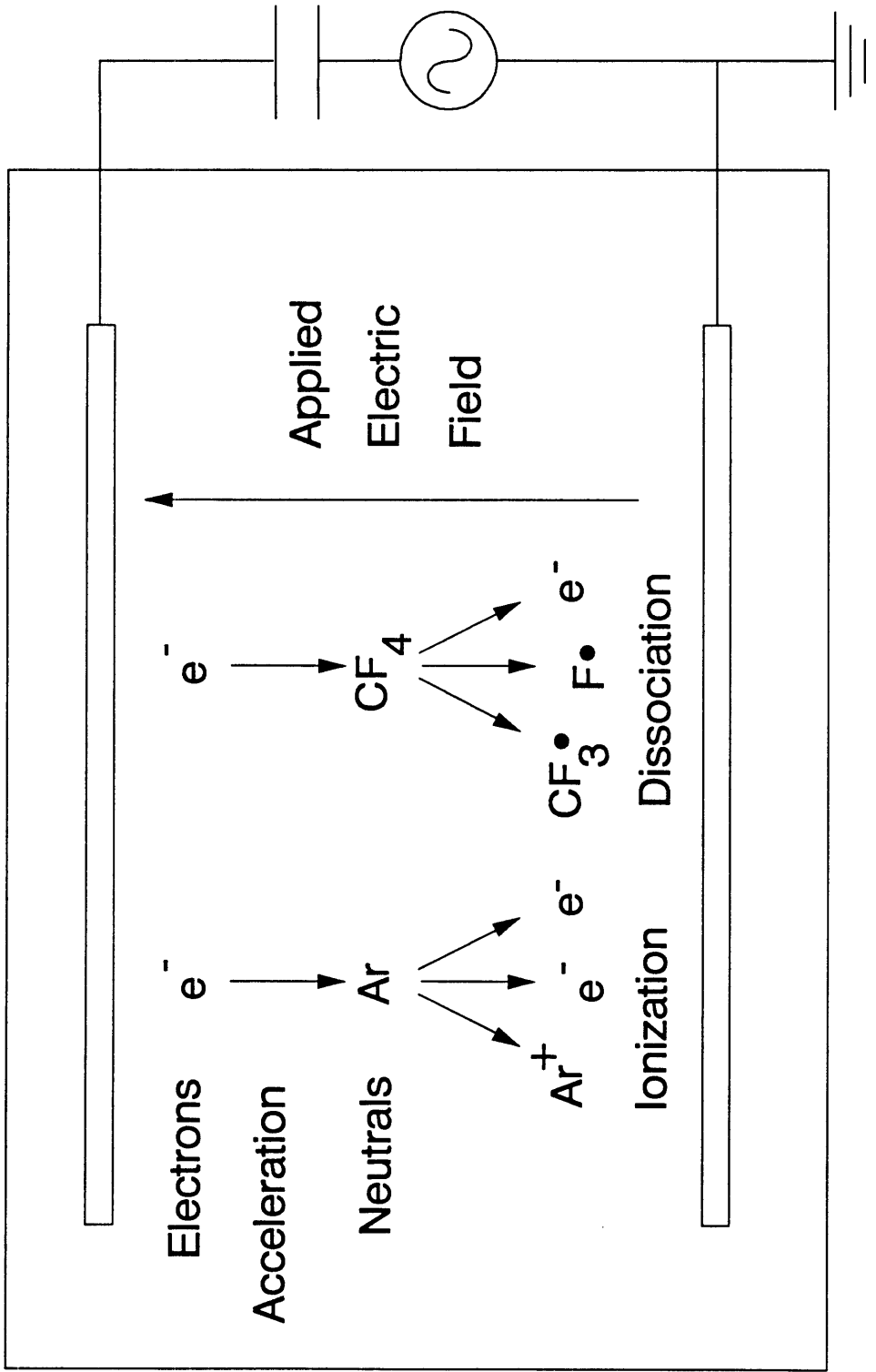


Figure 1.1: Simplified Reactive Ion Etching System

Free electrons in the gas are accelerated to high energies (several eV) by the imposed electric field. These energetic electrons collide with neutral gas molecules, inducing ionization and dissociation (and some reversible excitation, which produces a visible glow in the discharge region). Ionization occurs when the impact energy is sufficient to liberate an additional electron from the neutral species, producing a positively charged ion and an additional electron. Dissociation occurs when the collisional energy is transferred to one of the molecular bonds, breaking it and producing free radicals (Figure 1.1).

The ions and radicals generated in the plasma may be used in several ways, such as moving material from a bulk source to the wafer surface (sputter deposition), modifying the wafer surface without changing its topography (e. g. plasma hardening of photoresist), or removing material from the wafer surface (plasma or reactive ion etching). In plasma etching, the free radicals strike the wafer surface and react with it to produce volatile products which desorb and are pumped away. Selecting the feed gas, and hence the composition and excitation of the radicals produced, can allow selective etching (removal of one material without damaging another). The ions enhance etching by transferring energy to a localized region about the point of impact. The placement and orientation of the wafer determine the direction and energy of ion bombardment, and can promote directional or anisotropic etching. This is essential in the fabrication of modern VLSI products, which have microscopic features with similar lateral (parallel to the wafer surface) and vertical dimensions.

Plasma processes have several advantages over "wet" chemical etching, such as reduced cost and waste production, but it is their selectivity and anisotropy that make them indispensable. No advanced product, be it a high density memory chip, a silicon microprocessor, or a GaAs opto-electronic device, could be produced without plasma processes. The current trends in device design will inevitably increase the importance of plasmas in microelectronic manufacturing.

1.3 Plasma Etching Research

The plasma environment is very complex. The electric field, electrons, ions, neutrals, and radicals interact with each other in the bulk of the plasma, on the wafer surface and vacuum chamber walls, and in the "sheath" regions that form to isolate the plasma bulk from the wafer and walls. Direct observation of these interactions is frequently impossible, so the traditional approach to process development has been largely empirical. Process conditions such as gas feed rate, chamber pressure, and electric field strength were varied until the desired surface topography was achieved.

This crude technique has been adequate for a surprising range of needs, but clearly can not be expected to suffice indefinitely. A more fundamental understanding of the etching process will be needed, and research in this area is underway. The most common approach has been to divide the total etching process into individual (but interacting) topics which are sufficiently compact to be studied in detail. Figure 1.2 shows a conceptual diagram of a plasma etching process, beginning with the

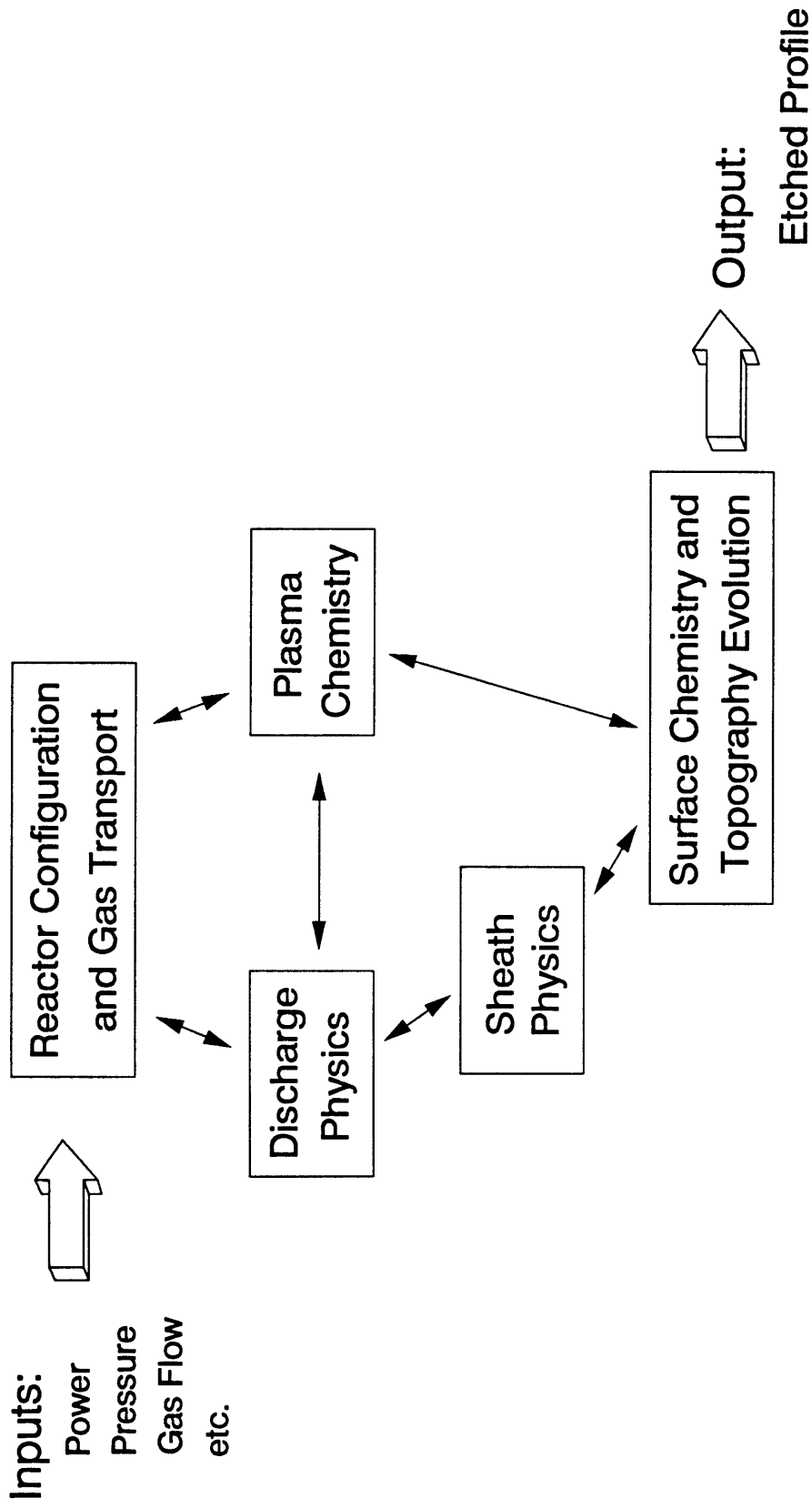


Figure 1.2: Elements of Plasma Etching Process

elements that are under direct control of the user (the "knobs"), and ending with the final surface topography (the process output). Major elements include:

Discharge Physics - the interactions of electrons and ions with the applied fields, each other, and the gaseous feedstocks to produce ionization and dissociation

Plasma Chemistry - the reactions of plasma products in the gas phase and with the chamber walls to produce reactive species

Sheath Physics - transport of ions and reactive species from the plasma bulk to the wafer surface

Surface Chemistry and Topography Evolution - the mechanisms and kinetics by which ions and reactive neutrals react with the wafer surface, and the effect of those reactions on surface topography

There are interactions between these elements, but complete analysis of those interactions is impossibly complex and they are commonly neglected. This work concentrates on the topics of Surface Chemistry and Topography Evolution, which are closely tied to Sheath Physics and Plasma Chemistry. The "feedback" from the surface to the sheath and plasma is relatively weak and the fluxes of ions and reactants arriving at the surface from the plasma are assumed to be independent of

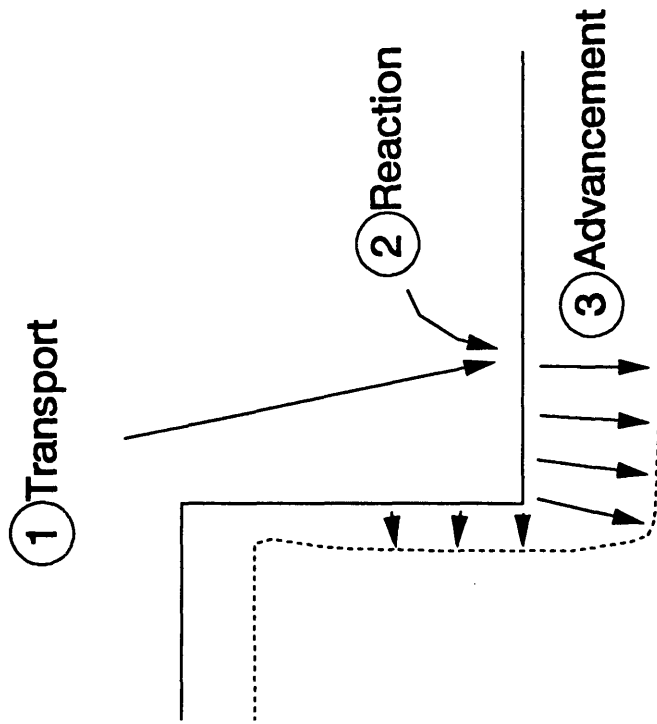
surface conditions.

The individual topics in Figure 1.2 can be further subdivided. Figure 1.3 shows a conceptual model and flowchart for etching within a surface feature (Surface Chemistry and Topography Evolution from Figure 1.2). The flowchart begins with plasma conditions, which determine the fluxes of ions and reactants approaching the wafer surface. After these species arrive at the surface, they must be transported into the feature. The local fluxes inside the feature are usually quite different from the values at the top surface. The next step in the process is the actual etching reaction on the surface. The reaction rate can vary from point to point along the surface, and the final step converts the local reaction rates to incremental changes in the surface topography or "profile."

The flowchart in Figure 1.3b also contains provisions for a set of side reactions leading to the frequently observed deposition of polymeric films on the wafer surface. The topics of deposition and redeposition, contained within the dashed box on the figure, are both interesting and pertinent to current industrial practice. However, they are also exceedingly complex and poorly understood, and were judged to be beyond the scope of this thesis.

Figure 1.3 describes both the actual etching process and the framework for a theoretical/numerical etching model. The flowchart may also be used as a guide for the layout of this document, which is divided into the same set of topics. Chapters

a) Process



b) Flowchart

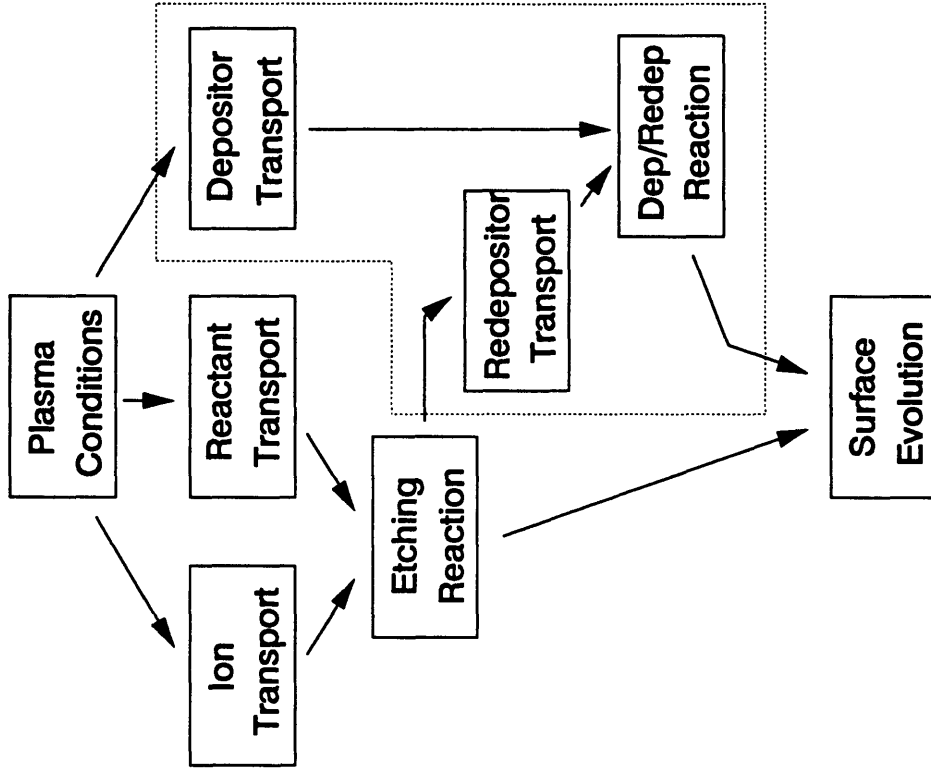


Figure 1.3: Elements of Surface Chemistry and Topography Evolution

2 and 3 consider two major factors influencing Ion Transport into surface features. Chapter 4 is concerned with Reactant Transport, while Chapter 5 analyzes Surface Advancement. The Etching Reaction is the subject of Part II (Chapters 7 and 8).

Chapter 2

Ion Transport: Dispersion and Reflection

2.1 Introduction and Mechanisms

Plasma etching owes the bulk of its utility to the ability of energetic, directed ions from the plasma to enhance the etching reaction rate. The energy borne by the ions striking the wafer surface allows useful etching rates at reasonable temperatures and radical concentrations. The directional approach of the ions to the surface allows etching to proceed anisotropically, thus enabling the fabrication of surface features with small lateral dimensions.

The simplest view of ion transport from the plasma to the surface arises from consideration of the electric field strengths in the plasma bulk and in the sheath. The plasma bulk is quasi-neutral and relatively free of electric fields. Therefore, ions move within the bulk with low energy and nearly isotropic direction. When an ion drifts from the bulk into the sheath above the wafer, it encounters electric fields that are both much stronger and directed toward the wafer surface. This field accelerates the ion toward the wafer. The absolute field strength in the sheath depends upon many factors, but the total sheath potential drop is typically between 20 and 500 Volts. These values are far higher than the nearly thermal energy possessed by the ion when it crossed into the sheath from the bulk, so the ion might be expected to

arrive at the wafer surface with an angle very near the surface normal and with an energy approximately equal to the sheath potential. This simplified view has led many people to think of the flux from the plasma as essentially an ion beam directed perpendicular to the wafer surface. The flux of ions to a given portion of a surface feature depends upon its angle: horizontal surfaces (those parallel to the macroscopic wafer surface) receive a high ion flux, while vertical surfaces are expected to receive no ion flux at all. The high ion flux causes horizontal surfaces to etch faster than vertical ones, and features with vertical sidewalls are formed.

However, this picture is not complete. Maintaining the radical and ion fluxes necessary for the desired etching rate requires a relatively high pressure. As a result, the ion's mean free path is on the order of the sheath width and collisions with the background gas are likely. Not only does the ion lose some energy during these collisions, but it is also deflected from its initial (perpendicular to the wafer) direction. The ions reach the wafer surface not with a single direction and energy, but with a distribution of angles and energies. The shape of this Ion Angle and Energy Distribution (IAED) depends strongly upon the discharge conditions, with lower pressure systems generally having tighter (more nearly monodirectional and monoenergetic) distributions.

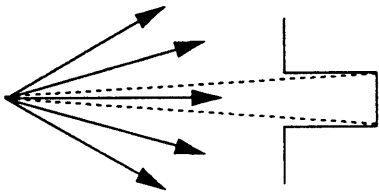
The principal effect of the IAED is geometric: because a substantial number of ions arrive at angles other than along the surface normal, the ion flux is not confined to horizontal surfaces. Not only does this increase the etching rate of

feature sidewalls, but it also reduces the ion flux and etching rate at the bottom of etched holes. This is illustrated in Figure 2.1, which shows the division of ion flux among the sidewalls and bottom of a pair of features with different aspect ratios. The total ion flux to a flat surface is (roughly) uniform; therefore, the number of ions entering the mouth of a masked feature is determined by the area at the top surface. If the ions are not perfectly directed, then a fraction of them land upon the sidewalls and the etching rate at the bottom decreases accordingly.

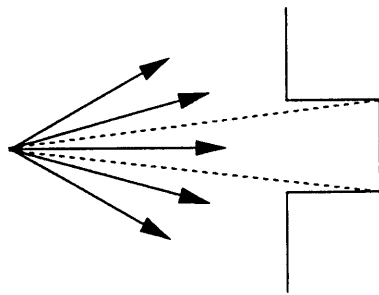
Figure 2.1 indicates that the fraction of ions lost to the sidewall increases with the depth of the feature. In fact, the division of ion flux between the sidewalls and bottom depends only upon the feature aspect ratio (defined as the depth divided by the width) for a given IAED. Features with higher aspect ratios (greater depth, smaller width, or some combination) have lower ion flux and etching rate at the bottom. This is commonly observed through the "RIE lag" effect, wherein the etched depth varies from feature to feature on a wafer depending upon the initial width of the mask opening.

The extent of RIE lag is determined by the shape of the IAED. If the arriving ion flux is distributed over a broader range of angles, then the fraction of ions landing on the sidewall will be greater and RIE lag will be more significant. Conversely, a tighter angular distribution causes the ion flux to more closely resemble the ideal beam discussed above and diminishes the effect of feature aspect ratio on bottom etching rate.

Ions dispersed
by collisions



Surface
features



Ion Angular
Distribution

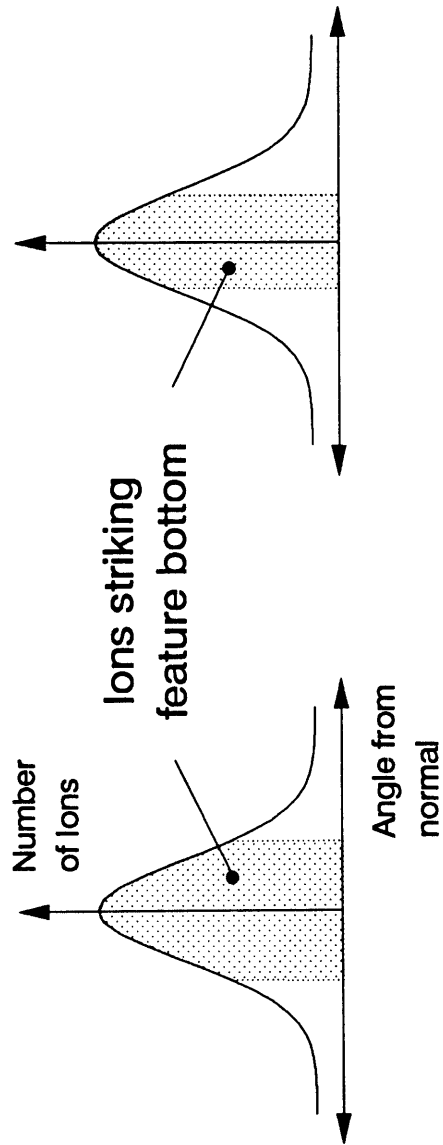


Figure 2.1: Effect of ion dispersion on flux to bottoms of different features. Shaded area represents portion of IAD striking feature bottom. Bottom of feature with higher aspect ratio (depth/width) receives lower ion flux.

The ions striking the sidewall can also affect the etching process on the feature bottom through reflection. When an ion strikes a surface, its energy must be conserved. For impingement angles near normal, the energy is distributed through a collision-cascade process among the molecules of the surface. The bonds among surface atoms become elongated, leading in some cases to bond breaking and liberation of surface material (etching). On the other hand, an ion striking the surface at an incident angle near glancing (nearly parallel to the surface) can not couple its energy efficiently into the surface bonds. The energy is retained by the ion, which "glances off" (or is reflected from) the surface and continues forward¹. The efficiency of energy transfer to the surface, and thus the probability of ion reflection and the amount of energy retained by the reflected ions, depends upon the ion mass and type, the surface composition and condition, and the ion arrival angle. Reflection probabilities and energy loss coefficients are well known only for light, inert ions scattering from clean and well-defined surfaces. However, it is reasonable to expect any ion-surface combination to exhibit some level of reflection if the arrival angle is sufficiently close to glancing.

Plasma etching processes are usually chosen to provide a reasonably directed ion flux and nearly vertical sidewalls. As a result, most of the ions striking sidewalls

¹ In the interest of completeness, it should be mentioned that very nearly all ions are neutralized via an electron tunnelling process just before they strike the surface. Therefore, the reflected particles should be referred to as "fast" or "high-energy" neutrals. However, the electronic state of the arriving particle is not thought to be nearly as important to the etching reaction as the energy, so the distinction between "ions" and "high-energy neutrals" is not essential for this discussion and has been omitted.

do so within a few degrees of glancing incidence, and the population of reflected ions may be substantial. After reflection, these ions proceed down into the feature and eventually land on the bottom. The reflected ions add to the "direct" (from the plasma) flux and can have a significant influence on the rate and uniformity of etching on the feature bottom.

The issue of reflected angle and energy loss bears further discussion. It was suggested above that reflected ions retain most of their energy, which in turn implies specular reflection. Because it is clearly impossible for the collision to occur without some loss of energy, the present work has been restricted to a "single-bounce" model. Reflected ions are tracked until they strike a subsequent surface. If the second collision is near normal incidence (as is usually the case), then the ion is simply added to the total ion flux. If, however, the second collision occurs at glancing incidence (as may occur in a feature with concave sidewalls), the ion is assumed to have lost all of its energy and is subsequently ignored. This approximation has been retained because it is simple (and thus computationally tractable), it appears to provide a reasonable reflection of reality in some important cases, and it presents a tremendous improvement over the previously available alternative (ignoring reflection altogether). Potential improvements include inclusion of reflected angle distributions and consideration of energy loss. Energy loss will be discussed in the context of an industrial oxide etching process later in this chapter.

The remainder of this chapter comprises four major components. The first of

these will describe the computation of the ion flux to a point on the surface from an analytical and geometric point of view. The second section will address the requirements and methods for computation of the visibility from a point on the surface to the plasma and to other surface regions. The third part will present the numerical methods used for the present work, and the final sections will detail the application of the ion dispersion and reflection model to industrial etching processes.

2.2 Ion Flux Model

Determining the ion-enhanced etching rate involves more than simply totalling up the number of ions striking the surface. This is because the relative influence of the ions varies according to such factors as the individual ion's energy, its arrival angle, and the condition of the surface. The influence of an ion on the etching rate is conventionally expressed in terms of a "yield," or number of surface atoms liberated (etched) per incoming ion. The yield depends not only upon the ion's trajectory and energy, but also upon the concentration of reactants on the surface in the vicinity of the ion landing site. For an incremental flux of ions to a particular surface location, the incremental change in etching rate may be expressed as

$$dER = dI(E,\theta) Y(E,\theta,C) , \quad (2.1)$$

where I is used throughout this thesis to represent ion flux, E is the ion energy, θ refers to the ion arrival angle with respect to the local surface normal, Y is used in

accordance with popular convention to express the etching yield per ion, and C may be viewed as the surface "Concentration" (of reactants), "Coverage" (by reactants), or "Condition." C takes into account the reactive nature of plasma etching, and incorporates the effect of such factors as reaction pathway, relative fluxes of ions and reactants, branching ratios between possible reaction products, surface temperature, composition, and morphology. In fact, C and Y may depend upon the ion flux for certain kinetic systems, making Equation (2.1) implicit. It should be clear that C is used in this context not as a single numerical parameter, but rather as a reminder that the functional dependence of Y on E and θ will vary from system to system and from point to point along the feature surface. The influence of reaction kinetics and reactant transport will be discussed in detail in subsequent chapters.

Equation (2.1) bears some resemblance to the "Ion-neutral synergism" model put forth previously by Gottscho, *et al.* [1992]. However, inspection of their work shows that they have assumed the etching yield to be linearly proportional the ion energy, while Gray, *et al.* [1993], have clearly demonstrated that this is not always the case. Equation (2.1) is thus a more general expression of the ion-enhanced etching rate.

Equation (2.1) describes the impact of a small portion of the total ion population with energies near E and arrival angles near θ . In order to compute the total etching rate, one must integrate dER over the entire range of energies and

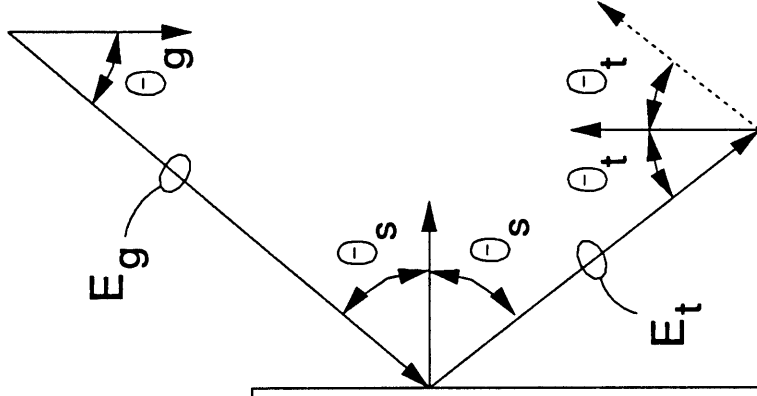
arrival angles

$$ER = \int \int_{E, \theta} Y(E, \theta, C) dI(E, \theta) , \quad (2.2)$$

bearing in mind that the population of arriving ions may be vanishingly small for some ranges of E and θ , and that the integration over arrival angle involves two spatial dimensions. The ion population is conventionally expressed through the Ion Angular and Energy Distribution (IAED) mentioned earlier, with the angle defined with respect to the macroscopic wafer surface normal. The etching yield, on the other hand, is always defined with respect to the local surface normal. Furthermore, the possibility that the ions may have experienced sidewall reflection before reaching the final target introduces a need for both geometric and energetic translation. Figure 2.2 qualitatively identifies the relationships between the ion angles and energies upon approach from the plasma, during and after reflection from the sidewall, and upon arrival at the target location. When these effects are incorporated, along with the finite reflection probability at the sidewall and the possibility of reflection beyond the target, Equation 2.2 becomes:

$$ER = \int \int \int_{E, A} Y(E_i, \theta_i, C) IAED(E_s, \theta_s) P(E_s, \theta_s) \times (1 - P(E_r, \theta_r)) \cos \theta_i dA dE. \quad (2.3)$$

1. Ions approach surface from plasma
with energy E_g and angle θ_g



2. Ions strike sidewall:
some are reflected
with energy E_t

3. Ions reach target with energy E_t
and angle θ_t

Figure 2.2: Characteristic angles and energies for reflected ions.

P is the reflection probability as a function of arrival angle and energy, and the subscripts g , s , and t refer to parameters in the gas (leaving the plasma sheath), at the sidewall, and at the target, respectively. The integration parameter A is used to emphasize the point that the arrival angle varies in two dimensions. The specific form of dA depends upon the choice of coordinate system.

Equation (2.3) provides a general expression for computation of the ion-enhanced etching rate. The etching physics and chemistry are coupled in through the input parameters $IAED$, P (and the associated energy loss upon reflection), and Y , which depend upon the plasma conditions, material set, and etching kinetics. The feature geometry and the location of the target point within the feature are expressed through the relationships between θ_g , θ_s , and θ_t . This project primarily focused on analysis of long rectangular trenches with two-dimensional symmetry about the midplane. The application of Equation (2.3) to this structure is discussed below.

For the long trench geometry, a convenient choice of coordinates is a spherical system oriented so that the axis of rotation is aligned with the longitudinal axis of the trench. The azimuthal angle rotates within a cross-sectional plane of the trench, with its reference chosen along the outward surface normal. To avoid confusion with previously published models, the azimuthal angle (commonly referred to as ϕ) is designated α , and the angle from the rotational axis (usually termed θ) is replaced by ψ , the angle from the cross-sectional plane. Both α and ψ are equal to

zero along the local surface normal. ψ increases (or decreases) to $\pm\pi/2$ for vectors parallel to the trench's longitudinal axis. α is determined by the projection of the position vector into the cross-sectional plane, with α positive for projections which lie counterclockwise from the local surface normal. These coordinates are similar to those used by Blech [1970], and are illustrated in Figure 2.3. In the (α, ψ) system, $dA = \cos\psi \, d\psi \, d\alpha$, and

$$ER = \int_E \int_{\alpha} \int_{\psi} Y(E, \theta, C) IAED(E_g, \theta_g) P(E_g, \theta_g) \times (1 - P(E, \theta)) \cos\theta_t \cos\psi \, d\psi \, d\alpha \, dE. \quad (2.4)$$

Because α lies within the same cross-sectional plane used to track the evolving surface profile, it is referred to as the "in-plane" angle. Similarly, ψ is called the "out-of-plane" angle. Each of the 3-Dimensional angles θ_g , θ_s , and θ_t can be decomposed into a combination of in-plane and out-of-plane components following the simple relationship

$$\cos\theta = \cos\alpha \cos\psi. \quad (2.5)$$

Specular reflection of an ion from a planar sidewall does not affect the

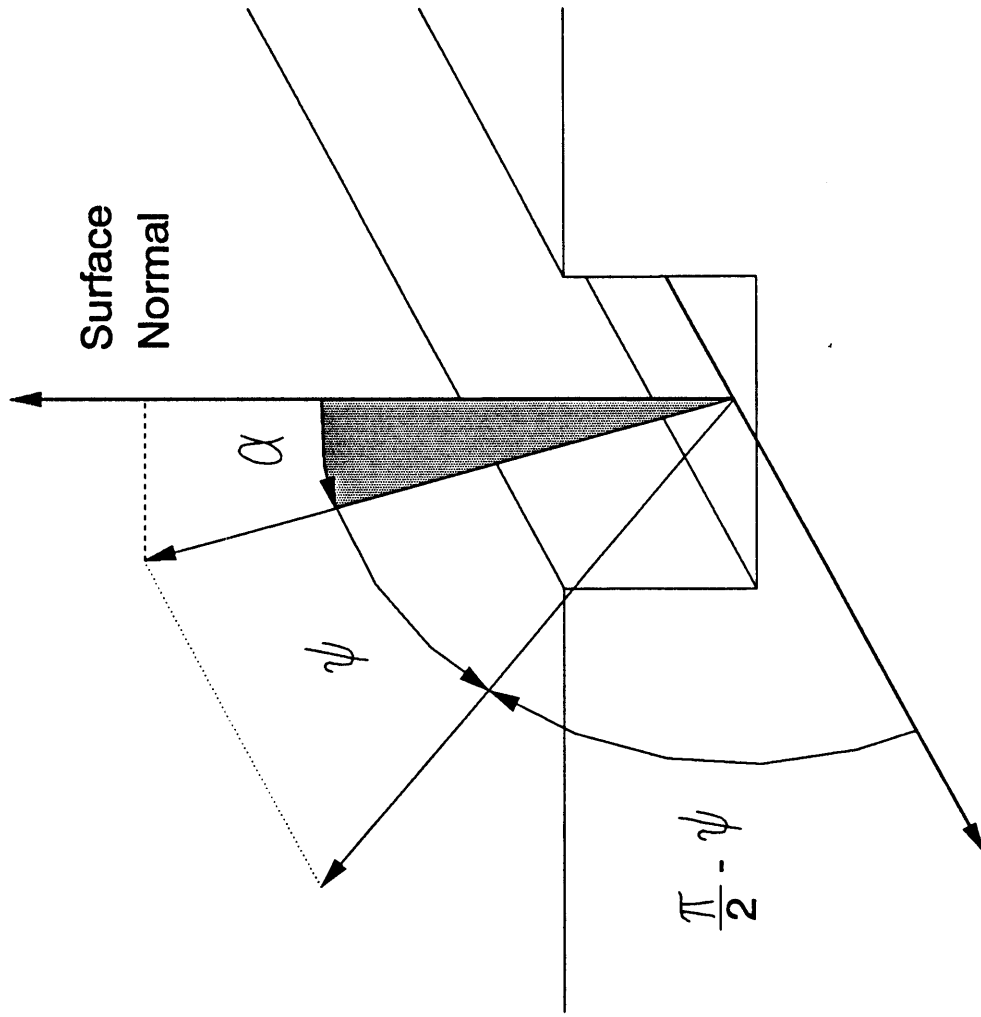


Figure 2.3: Coordinate system used for flux calculations in long rectangular trenches.

longitudinal velocity. Therefore, the out-of-plane angle is unchanged, and

$$\psi_t = \psi_s = \psi_g . \quad (2.6)$$

This considerable simplification is only valid for the long rectangular trench structure and specular reflection. The relationships between the in-plane components α_g , α_s , and α_t are illustrated in Figure 2.4. Figure 2.4 introduces some new terminology which requires explanation. First, the inclination angles of the surface at the target and reflection (sidewall) points are shown as θ_{Targ} and θ_{Side} , respectively. Note that these angles are defined with respect to a horizontal line in the cross-sectional plane, while the convention throughout this Chapter has been to reserve θ for 3-Dimensional angles defined with respect to the surface normal. This conflict is admittedly confusing; however, the use of θ for inclination angle is so thoroughly entrenched in profile evolution that it would be impractical to change it for this application. The second new term in Figure 2.4 is the angle χ , also defined with respect to a horizontal line passing through the target point, which describes the relative positions of the target and reflection point. The benefit of χ is that it is independent of θ_{Targ} and θ_{Side} . Once these three angles are known, the in-plane

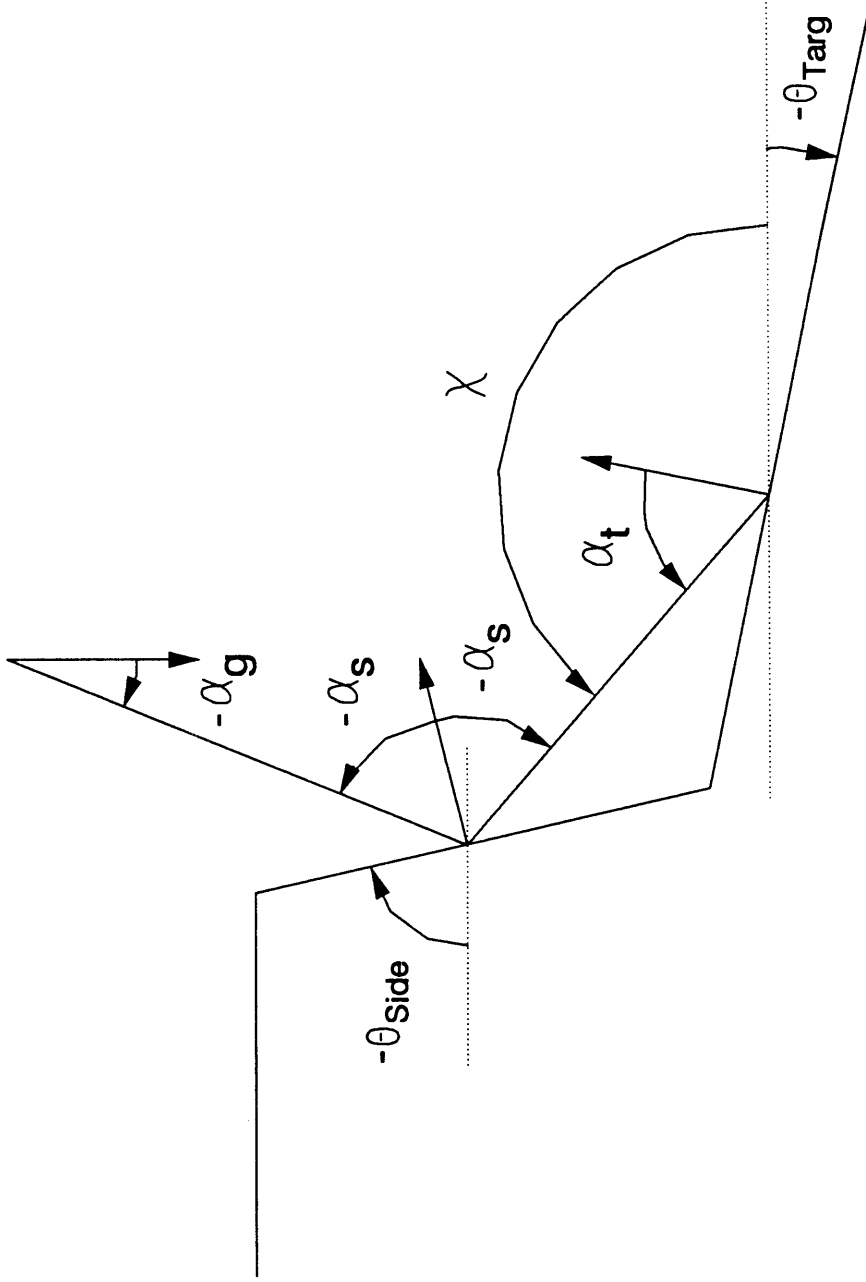


Figure 2.4: Definitions of and relationships between in-plane angles for ion reflection in long rectangular trenches.

incident and arrival angles may be found by

$$\alpha_t = \chi - \theta_{\text{Targ}} - \frac{\pi}{2}, \quad (2.7)$$

$$\alpha_s = \chi - \theta_{\text{Side}} - \frac{3\pi}{2}, \quad (2.8)$$

and

$$\alpha_g = \theta_{\text{Side}} - \alpha_s. \quad (2.9)$$

Note that the angles obtained from these Equations may require addition or subtraction of 2π to produce values in the conventional range.

Another industrially important feature type is the circular contact hole or "via." Vias were generally excluded from this project, because they would have required greater effort to model while not providing significant additional insight into etching physics. However, Appendix A provides an introduction to the topic of ion reflection in circular vias if consideration of these features becomes necessary in the future.

2.3 Visibility

The preceding sections have outlined a model for the computation of ion flux and the associated etching rate in surface features. Numerical implementation of this model for application to practical systems requires additional effort. One of the most critical issues is that of "visibility". The visibility calculation may be defined, for this case, as the process of determining, for each point on the feature surface:

- 1) whether or not the point has a direct view to the plasma (so that ions may travel directly from the plasma to the point), and what range of angles are contained in that direct view, and

- 2) which portions of the feature surface are positioned such that reflected ions leaving those regions could reach the target point. In order for this to be possible, the reflecting region must be "facing" the target with no other parts of the surface between them. In other words, a straight line from the reflection point to the target point must fall entirely within the vacuum region.

The origin of the term "visibility" is clear: the process is analogous to determining which portions of the plasma and feature walls would be visible to an observer at the target point. Accurate determination of the visibility for each target point is important for two reasons. First, accurate flux computation clearly requires that other regions of the feature be properly classified as "visible" or "invisible"

(blocked from view). Second, the computational efficiency is greatly increased if regions of space (α and ψ from the preceding section) where the flux is zero are eliminated from the numerical integration. For example, it is not necessary to compute the reflected flux from a certain region if it is already known that region does not have a direct view to the plasma. Therefore, the visibility data for each surface point (collectively referred to as the "visibility graph") should be computed and stored in a manner that permits rapid checking of plasma visibility for portions of the sidewall.

Visibility is an important issue in the field of computer graphics, and algorithms for computation of the visibility graph have been published elsewhere [Chazelle and Guibas, 1985]. Moreover, there are commercially available codes for the related problem of computing the exchange factors for radiative heat transfer between surfaces [Shapiro, 1983] (this topic will be discussed in more detail under the heading of Reactant Transport). However, the original constraints of this project motivated the development of a new computational algorithm and storage structure for the visibility graph. Specifically, this project was originally sponsored by DuPont Electronics in support of their ASEPEN topography simulation code. One element of that charter was to produce and use only codes that could be scaled to ASEPEN's target platform: a high-end personal computer of 1990. Therefore, memory constraints were given precedence over almost all other factors. As the published algorithms and codes typically required storage space that scaled with N^2 (N being the number of surface points or line segments), they were deemed unsuitable for

inclusion in ASEPEN. DuPont sponsorship ended before the project was completed, thus eliminating the initial motivation for algorithm development, but the advantages of conversion at that point would have been small.

The algorithm utilized throughout this project operates in the following manner: first, the surface is discretized to a set of points joined by straight line segments. This structure is called a "string" in the manner followed by others [Jewett, 1979]. The use of straight lines for interpolation between points is not required by the surface advancement scheme introduced in Chapter 5, but it does simplify the computation of reflected flux from the interpolated region by allowing the use of a single relationship between θ_g , θ_s , and θ_t . With the surface represented in this fashion, the visibility problem consists of three tasks: 1) determining the limiting angles of direct plasma visibility for each target point, 2) determining the list of wall segments visible from each target point, and 3) determining the limits of direct plasma visibility for each wall segment. For the sake of simplicity, the third task was recast as a special case of the first, with the visibility angles for each segment taken from its midpoint.

Once the surface has been discretized, computation of the visibility graph for each target point involves two passes through the list of point coordinates. Each pass consists of two parts, each starting at a point immediately adjacent to the target point and proceeding away from the target. For example, the first part of each pass begins at the point immediately to the left of the target point and proceeds leftward along

the string until the end is reached.

The first pass through the two ends of the string is used to identify those wall points which might restrict the view of other points or the plasma. Such points are characterized by an extremum in the polar angle of the line of sight drawn from the target point to the wall. Figure 2.5 shows an example: as the index of the test point is swept from $t - 1$ to 1, the line of sight initially rotates clockwise. The rotation reverses at point $t - 5$, identifying point $t - 5$ as one which at least has the capability of blocking the view to other parts of the surface or to the plasma. Such points are referred to as "blocking" points, and a list of their indices, coordinates, and polar angles from the target point is maintained.

The second pass determines which portions of the surface or plasma are actually blocked by the previously identified points. This is accomplished by tracking the visibility status of the test point with respect to each of the potential blocking points. The sweep begins with a point adjacent to the target; these points clearly cannot be blocked by any others. As the sweep proceeds along the string, the line of sight from the target to the test point will occasionally cross the line of sight to one of the blocking points, possibly changing the visibility status of the string with respect to that blocking point. If the test point is obscured by any of the blocking points, then it is invisible. If it is clear of all blocking points, then it is visible. The visibility data is stored as a list of beginning and ending indices for visible sections. The limiting view angles to the plasma are found by comparing the polar angles to the blocking

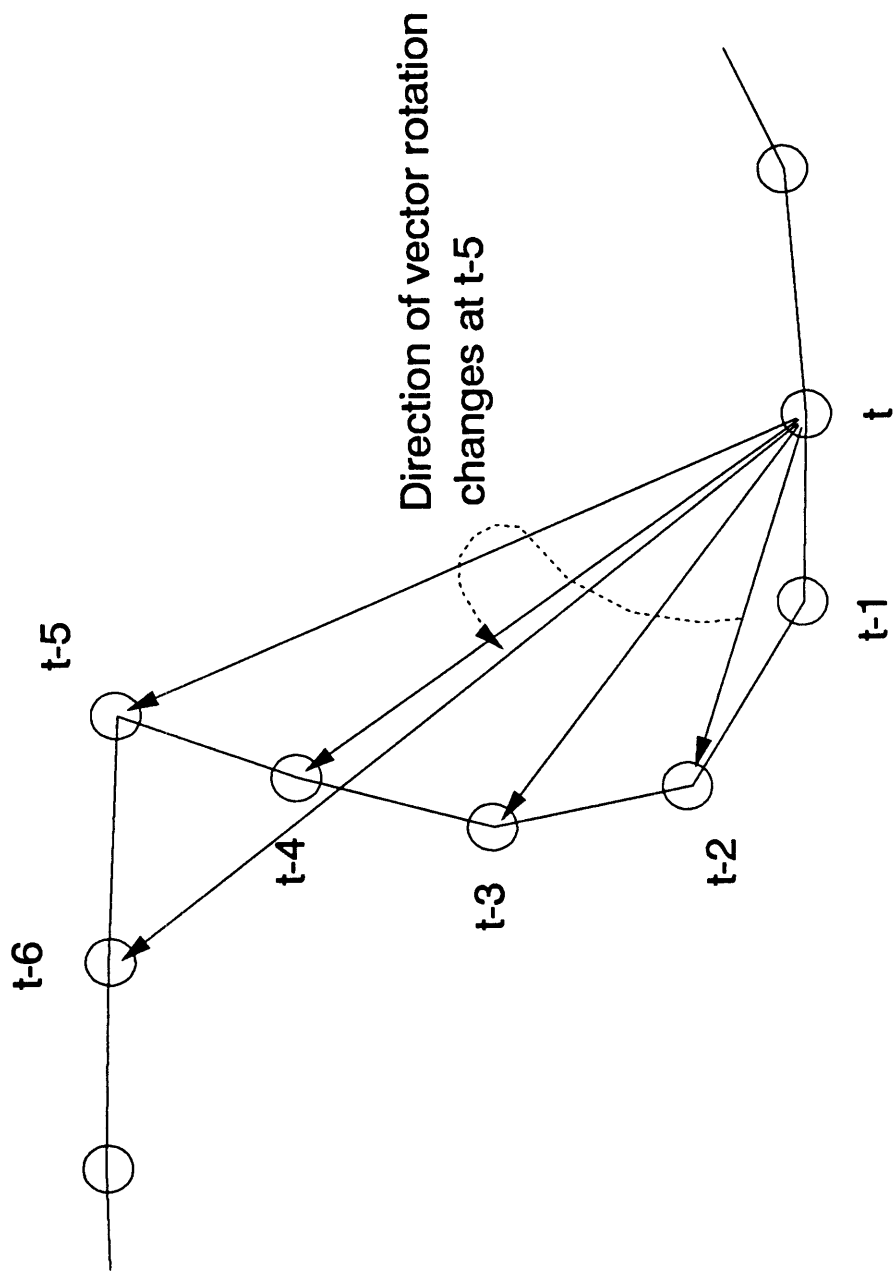


Figure 2.5: Identification of point $t-5$ as one which may interfere with the view between point t and other points.

points, and are also stored for later use.

The actual code used in this project is somewhat more complicated than the description presented above. For example, not all extrema in the polar angle vs. index graph are blocking points - the orientation of the surface must be taken into account to determine which are and which are not. Similarly, robust numerical implementation required additional constraints on the definition of "crossing" the line of sight. The explanation above was presented primarily as an introduction to an approach which may be useful in situations where memory is a critical constraint.

The visibility algorithm discussed above operates entirely in the cross-sectional plane of the trench. While this may seem like an obvious simplification for structures with two-dimensional symmetry, it should be noted that this is only valid for the long trench. Appendix B contains proof that the visibility of line segments in the cross-sectional plane is equivalent to visibility of plane segments in three dimensions for the long trench, and demonstration that a two-dimensional calculation is not valid for the circular via geometry.

2.4 Numerical Methods and Convergence

Once the required trigonometry is defined and the visibility graph is computed, calculation of the ion flux consists of nothing more than a series of

numerical integrations. The number of discrete integrations can be fairly large; each target point requires one double integration for the direct view to the plasma plus one for each visible sidewall segment. This process has proven to require more computer time than any other portion of the simulation, so the need for efficiency in the integration is clear.

The typical response to an efficiency requirement is to employ a high-order integration technique, such as Gaussian quadrature or the Romberg or Simpson enhancements to the trapezoidal method. These have certainly been established as efficient methods for obtaining a highly accurate solution. However, the requirements in this situation are somewhat different. Ion flux computation involves a large number of integrations, but the accuracy requirements are mild: the underlying physics and chemistry are so poorly understood that numerical errors up to a few percent would not greatly reduce the overall accuracy of the simulation.

The required accuracy was readily achievable with simple trapezoidal integration, with the number of integration points successively doubled until the relative change in solution dropped below about 0.001. Alternate methods were evaluated not on the basis of their ultimate convergence characteristics but on the computational cost required to achieve similar stability.

The Simpson and Romberg enhancements were tried and rejected because they were found to be unreliable under the conditions of this study. The rapid

convergence of these methods is achieved by measuring the rate of change in the computed solution as the number of integration points is increased and extrapolating to predict the true result. These methods thus depend upon an assumption that the approach to the correct solution is smooth - that the relative change in the error with increasing resolution either decreases or remains constant as the solution is approached. This is certainly a fair assumption when the error is very small, but it may not be reasonable when the resolution is low. This study uncovered several cases where the Romberg and Simpson methods would declare convergence prematurely - finding small changes in their predicted solutions and terminating while the actual error was still excessive. Figure 2.6 illustrates the effect of noise on the Simpson method. The relative change between resolution steps is zero at steps 4, 6, 10, and 13, even though the predicted solutions are incorrect by between 2% and 22% at those steps.

The Gaussian method was rejected primarily because of difficulties in choosing the required resolution in advance. The trapezoidal method is constructive: doubling the number of integration points requires evaluation of the integrand only at the new points. Thus, a 33-point trapezoidal integration requires only 33 evaluations, whether the integration begins with all 33 points or is built up in a sequence of 2, 3, 5, 9, 17, and then 33 point integrations. With the termination procedure defined above (repeatedly doubling the resolution until the relative change in the solution dropped below a preset tolerance), taking an additional step in resolution is relatively inexpensive. Gaussian quadrature, on the other hand, is not

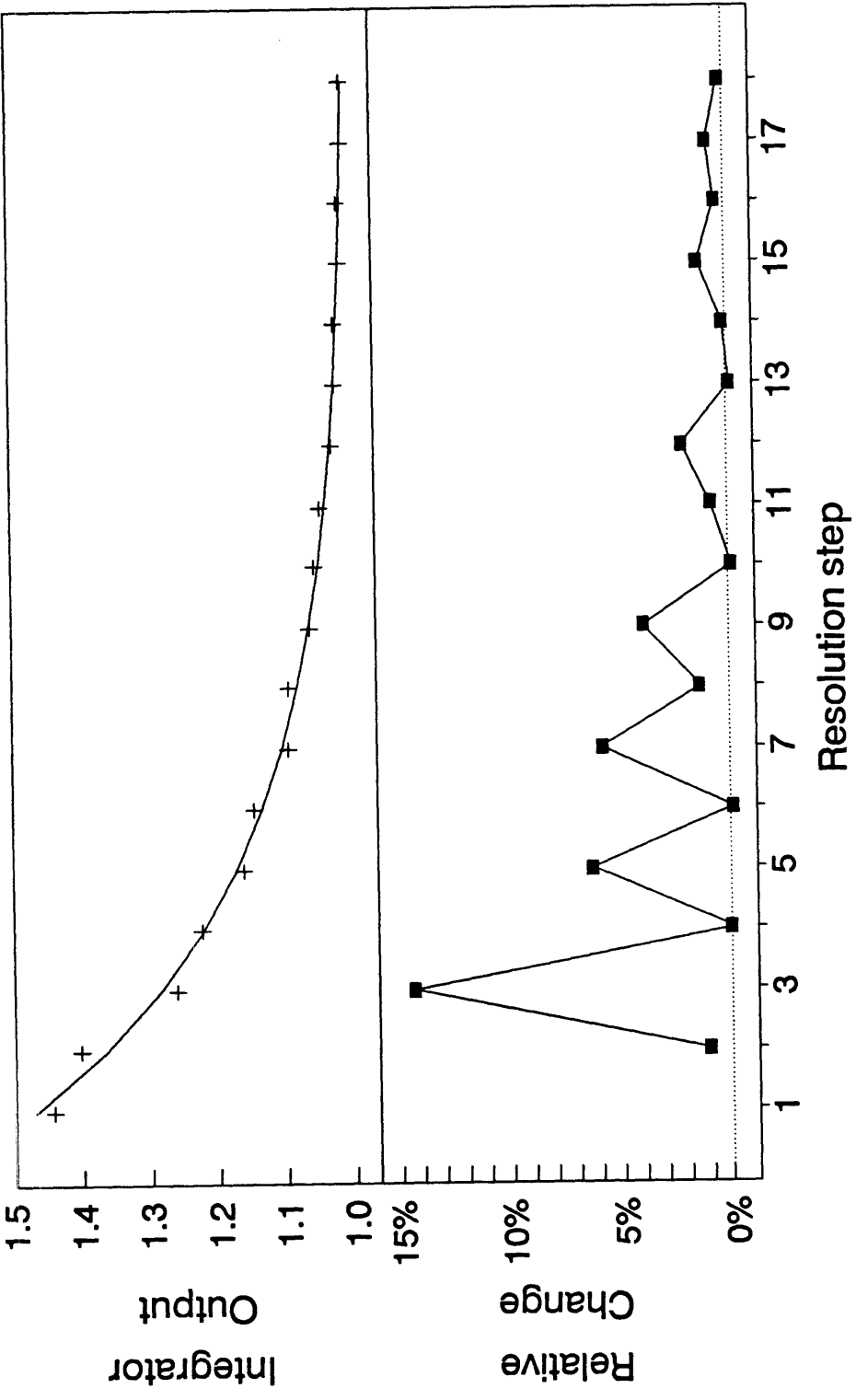


Figure 2.6: Breakdown of Simpson's integration when resolution is low and calculations are noisy. a) Output from trapezoidal integrator. b) Relative change estimated by Simpson's rule.

constructive. The integration points ("Gauss" points) do not repeat between resolution levels. Reaching an ultimate resolution of 33 (or so) points would require a sequence of 2, 4, 8, 16, and 32 point integrations, all independent and requiring a total of 62 evaluations. While the final solution would almost certainly have been more accurate than that obtained with the trapezoidal technique, this improvement would not offset the increased cost.

The competitive disadvantage of Gaussian quadrature could be reduced by standardizing the number of integration points at a particular level, but the nature of the integrand in this case makes it impossible to choose the optimum number of points in advance. The natural variables for integrating the ion flux in the rectangular trench are, as shown previously, energy and in-plane and out-of-plane arrival angles at the target. The reflection probability is highest near grazing incidence upon the sidewall. For any given sidewall slope, the reflection probability increases as the out-of-plane angle is increased. Yet the ion flux from the plasma is generally peaked near the macroscopic surface normal, which favors higher flux near the cross-sectional plane. Furthermore, shadowing of the sidewall truncates the reflected flux abruptly at certain angles. The resultant net flux may be peaked in-plane, peaked out-of-plane, or even zero across the entire angular range.

The latter observation did suggest an efficiency improvement which proved to be quite worthwhile. The integration limits on in-plane and out-of-plane angle were initially allowed to retain their natural values: the in-plane angle spanned the

range defined by the end points of the particular reflecting sidewall segment, and the out-of-plane angle ranged from 0 to $\pi/2$ (with the effect of angles from $-\pi/2$ to 0 found by symmetry). However, it was determined that a significant amount of computer time was spent integrating over regions where the ion flux was negligible. Therefore, a new approach was tried: the IAED, reflection probability, and slope were evaluated for each reflecting segment, and the integration limits were "pulled in" to span only the range of in-plane and out-of-plane angles where the ion flux was expected to be significant. The IAED was used to set an upper limit on the out-of-plane angle for the entire simulation. The IAED is typically peaked on the macroscopic normal and decays toward zero as the angle increases. An arbitrary cutoff was established at the angle where the IAED dropped to a negligible level. The out-of-plane angle does not change upon reflection from the sidewall, so integrating beyond that cutoff angle would not be productive. Similarly, the reflection probability increases as the incidence angle moves away from normal. The reflection probability could be combined with the slope of the reflecting surface and the relative positions of the reflecting surface and target point to establish a lower limit on the out-of-plane angle (below which the incidence angle on the sidewall would drive the reflected flux to zero, regardless of the IAED). Similar analysis, plus consideration of sidewall shadowing, led to improved integration limits for the in-plane angle as well.

2.4.1 Two-dimensional Approximation

It has been common practice in surface profile simulation to approximate the transport of ions into long trenches by a two-dimensional process. This is justified by observing that an infinitely long trench is symmetric about any cross sectional plane, so an incident particle's longitudinal velocity is unchanged as it enters the trench. It is frequently convenient to evaluate the effects of longitudinal particle motion in advance (perhaps analytically [Singh, *et al.*, 1992]), thus reducing computational time.

However, it is also apparent that this approach must be applied carefully [Dalvie, *et al.*, 1992], and some discussion of the limits of two-dimensional simulation is in order.

With the effect of ion energy and reactant availability eliminated for simplicity, Equation 2.4 becomes:

$$ER = \int_{\alpha} \int_{\psi} Y(\theta_i) IAED(\theta_g) P(\theta_g) (1 - P(\theta_i)) \cos\theta_i \cos\psi \, d\psi \, d\alpha \quad , \quad (2.10)$$

where

$$\cos\theta_i = \cos\alpha_i \cos\psi \quad , \quad (2.11)$$

$$\cos \theta_s = \cos \alpha_s \cos \psi , \quad (2.12)$$

and

$$\cos \theta_g = \cos \alpha_g \cos \psi , \quad (2.13)$$

as shown previously. For the long trench geometry, the integration limits on the out-of-plane angle ψ are constant ($-\pi/2 \leq \psi \leq \pi/2$). This suggests that computational effort could be reduced by performing the inner integral in advance. This is correct only when the integrand is separable (can be separated into a sum or product of functions of α or ψ alone).

While the presence of both $P(\theta_s)$ and $(1-P(\theta_t))$ seems to preclude separation, there are some potentially important cases where this approach may be viable. For spontaneous etching by an isotropic gas with no angular yield dependence or sidewall reflections, both Y and IAD are constant,

$$Y(\alpha, \psi) IAD(\alpha, \psi) \cos \theta_t = Y IAD \cos \alpha \cos \psi , \quad (2.14)$$

and

$$\begin{aligned}
 ER &= Y \text{ IAD} \int_{\alpha} \cos \alpha \int_{\psi = -\frac{\pi}{2}}^{\frac{\pi}{2}} \cos^2 \psi \, d\psi \, d\alpha \\
 &= \frac{\pi}{2} Y \text{ IAD} \int_{\alpha} \cos \alpha \, d\alpha .
 \end{aligned} \tag{2.15}$$

A similar reduction of dimension is usually possible for direct ion flux to the surface but care must be taken to ensure that the IAD is replaced by its in-plane equivalent:

$$\text{IAD}_{2D}(\alpha) \equiv \int_{\psi = -\frac{\pi}{2}}^{\frac{\pi}{2}} \text{IAD}_{3D}(\alpha, \psi) \cos^2 \psi \, d\psi . \tag{2.16}$$

Reflection of incoming ions from feature sidewalls introduces the sidewall and target reflection probabilities through the product $P(\theta_s) (1-P(\theta_t))$. Separation may still be possible, if the feature shape causes θ_t to be close to normal and $P(\theta_t)$ to be zero, but the computational advantage must be considered carefully. For a curved sidewall, θ_s and α are related through θ_{Side} , so the separation process would have to be repeated for each sidewall segment.

2.5 Applications

2.5.1 Microtrenching During Polysilicon Etching

The first application of this ion reflection model was to a process problem observed by engineers at Digital Equipment Corporation. While evaluating a polysilicon gate etching process, they discovered that certain process conditions formed deep notches at the bottom of the etched feature. The problem was subsequently traced to an aggressive overetch step used to clean up polysilicon residues left after the primary trench etch. The primary etch would remove the polysilicon down to the level of the gate oxide, which was very thin. Then the etching conditions (chemistry, power, etc.) were changed to remove any stray residues of polysilicon. The overetch process did not change the shape of the feature significantly (the polysilicon and photoresist walls did not change appreciably), but did occasionally "punch" through the gate oxide in certain locations. Once the oxide was breached, the dramatically higher etching rate of the underlying substrate would cause deep trenches to form. Similar structures have been observed by others in other systems, and the term "microtrench" has been coined to distinguish the small, undesired trenches at the feature bottom from the trench-shaped feature itself.

The microtrenching observed at Digital was unusual in several regards. First and foremost, the location of the microtrenches relative to the feature sidewalls differed from previous reports. While the published work typically showed

microtrenches forming immediately adjacent to the foot of the sidewall, the new process produced microtrenches which were removed from the sidewall by several hundred angstroms. Another interesting characteristic was the existence of asymmetry in some features, where the microtrench on one side would either be smaller than the other or would not exist at all. Finally, changes in the lithographic process used to define the photoresist mask had a profound effect on the extent of microtrenching.

A collaborative venture between Digital and MIT was established to study the microtrenching phenomenon, and ion reflection was evaluated as a possible cause for the microtrench formation (indeed, the ion reflection model described above was developed as part this effort).

The first step in applying the reflection model to this problem was to observe that the overall feature shape did not change during the overetch step. This simplified the simulation greatly, because it eliminated time evolution as a concern. With a gate oxide thickness on the order of 100 \AA , in contrast to film thicknesses and feature dimensions on the order of $5000 - 15000 \text{ \AA}$, the feature could be approximated as essentially static. Second, because the overetch chemistry had been chosen to provide high selectivity of polysilicon to oxide, it was clear that the oxide etching must be a highly ion-driven process. As an initial estimate, the oxide etching

rate was assumed to be proportional to the ion flux, so that

$$Y(E_g, \theta_g, C) = \text{constant} . \quad (2.17)$$

This reduced the process of computing the etching rate for the oxide to simply computing the ion flux across the bottom surface. Determining if and where microtrenches might form would involve analyzing the flux variation: trenches should be expected to form in the regions with the highest fluxes.

Computing the ion flux required two more inputs, as shown in Equation (2.3): the initial distribution of ion angles and energies IAED(E_g, θ_g), and the reflection probability at the sidewall $P(E_g, \theta_s)$. Energy effects were neglected, and the IAED was estimated from the gas pressure, the ion mass, and the previously published studies of Liu, *et al.* [1990] as shown in Figure 2.7.

The reflection probability was more difficult to obtain, because there has been no published study covering reflection of the ions present in this process (primarily Cl^+) from these surfaces (partially chlorinated photoresist and polysilicon). Therefore, the generalized approach of Wilson, *et al.* [1984] was used. They asserted that reflection was related to physical sputtering, in that the commonly observed peak in the physical sputtering yield indicated the onset of ion reflection at angles far from normal. Furthermore, they claimed, the decrease in sputtering yield to zero at angles less than 90° from normal for some materials indicated a condition of total ion

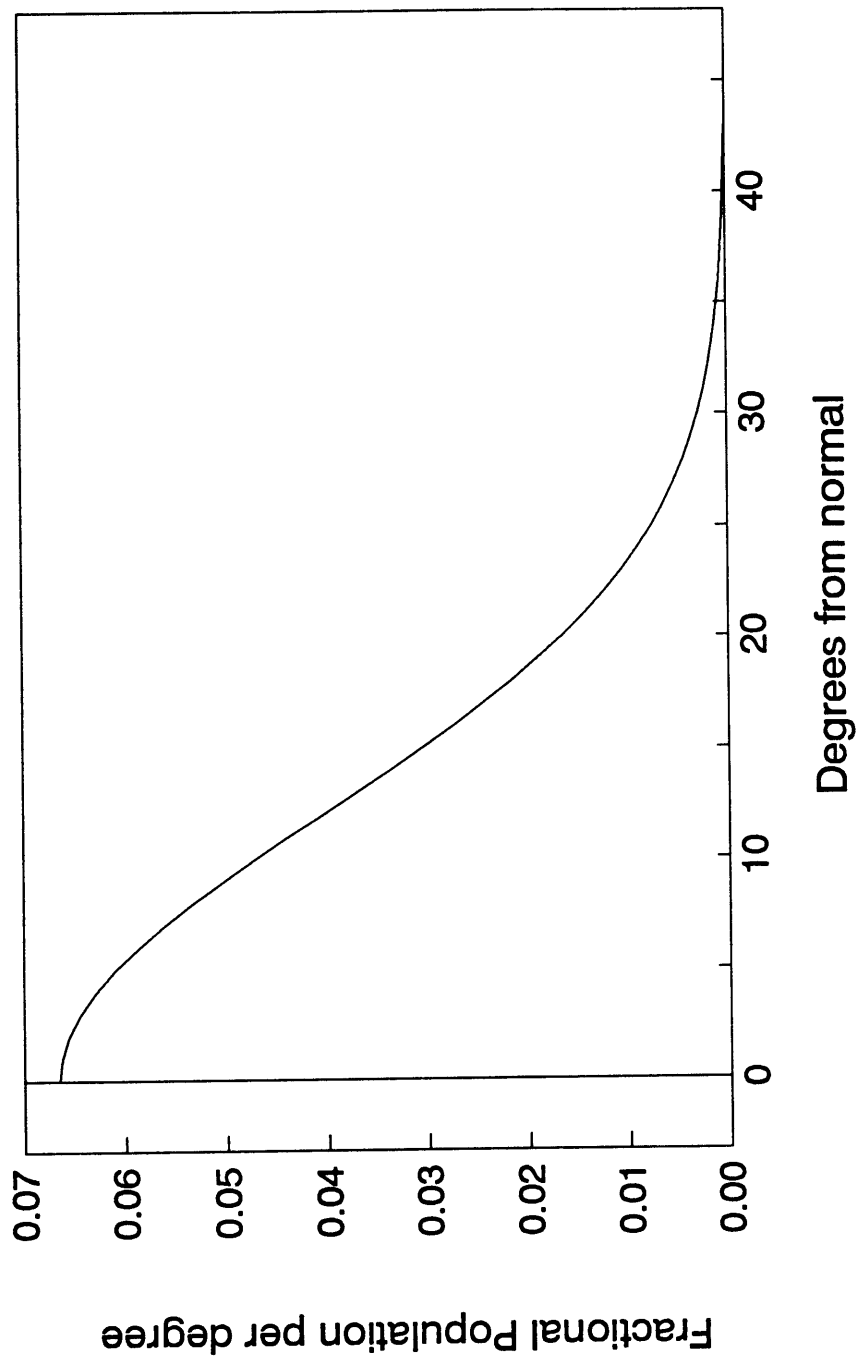


Figure 2.7: Ion Angular Distribution, Fractional Population per degree from macroscopic wafer normal.

reflection. While this view is overly simplistic, it does have intuitive appeal and provides a starting point for estimating the general shape of the reflection probability.

Physical sputtering yields have been studied extensively, but primarily for the inert ions used in ion milling. The most similar (to Cl^+ on polysilicon) system available was Ar^+ on silicon, for which the sputtering yield has been shown to peak near 60° from normal. This established 60° as an initial estimate of the angle at which reflection would commence. Sputtering yield data and intuition suggested that total ion reflection should ensue at grazing incidence (90° from normal), and the probability was assumed to rise linearly from 0 to 1 between 60° and 90° . This function was used to represent both the polysilicon and photoresist surfaces.

These simple inputs were used to estimate the ion flux as a function of position along the feature bottom, and maxima in the flux were found near (but not at) each sidewall. When careful measurements of the sidewall angle were made (from SEM photos), the position of the ion flux maximum was found to match the position of the microtrench within 20% or so. Subsequent decomposition of the total ion flux revealed two important points: first, the maxima were formed by an accumulation of direct flux from the plasma, flux reflected from the photoresist, and flux reflected from the polysilicon (Figure 2.8). Second, the position of the flux maximum (and thus the microtrench) was determined by the relative slopes of the photoresist and polysilicon surfaces. In this process, the two materials had different slopes and the

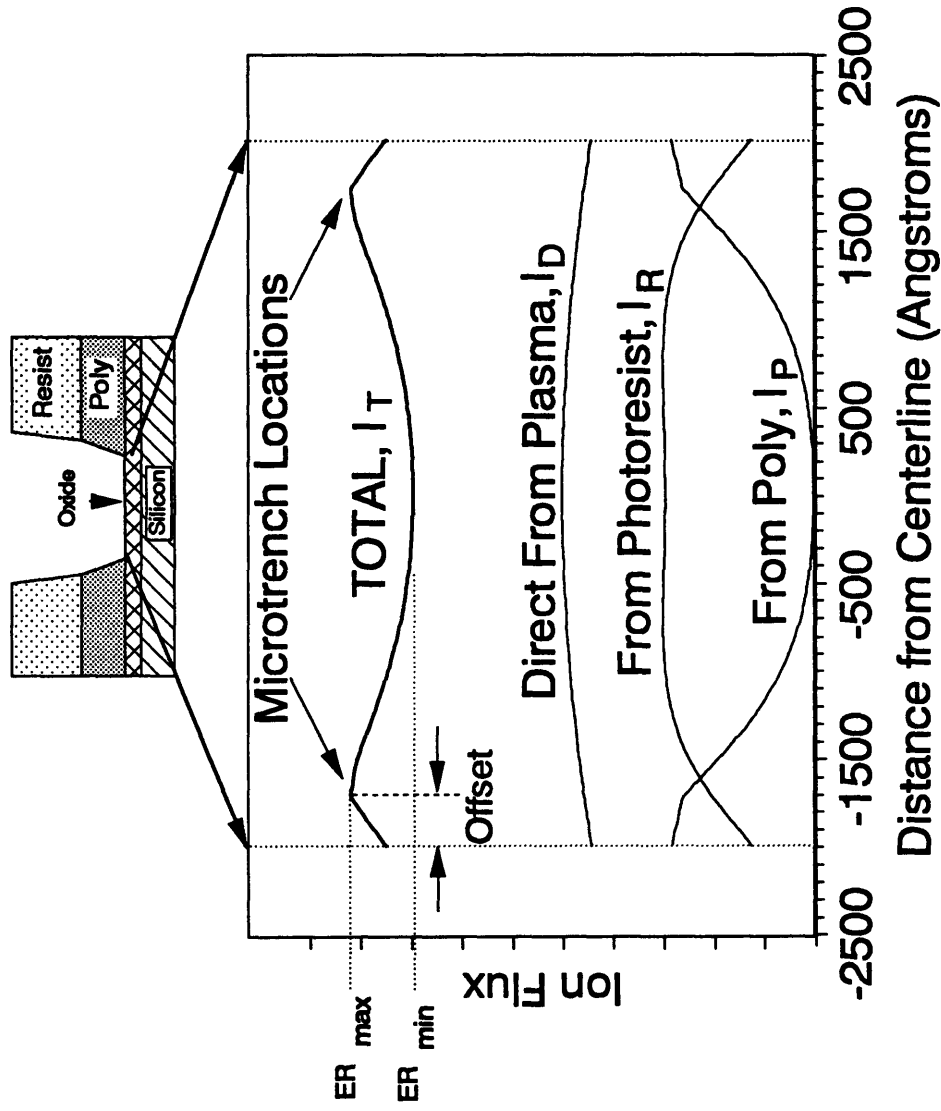


Figure 2.8: Ion flux profile to bottom of surface feature. Total flux is sum of three components: ions arriving directly from plasma, ions reflected from photoresist, and ions reflected from polysilicon.

microtrench was located away from the sidewall. Previous publications showed a single, steeper wall slope and the microtrench directly adjacent to the wall. This has since been explored for other geometries, and the ion flux model indicates, as a general rule, that a sidewall with a single slope (whatever that slope may be) will produce a flux maximum at its foot, while a wall with multiple slopes or curvature will force the microtrench away from the foot. This latter assertion holds regardless of the sign of the curvature (concave, as in the Digital process, or convex).

Both the position and the depth of the microtrench were found to depend upon the sidewall slopes and film thicknesses. Figures 2.9 and 2.10 show the effects of geometry on two parameters characterizing the microtrenching. The first parameter, called " R_{\max} " or the maximum flux nonuniformity, is the ratio of the maximum flux to the flux at the centerline of the feature. Thus, an Enhancement of 15% indicates that the flux at its maximum was 15% higher than the flux at the centerline of the same feature. The second parameter is called the Offset, and describes the distance (in angstroms) separating the maximum in the ion flux from the foot of the sidewall.

The ion reflection model was applied to features produced under various process conditions, and successfully reproduced all of the major process trends. The asymmetric microtrenching was traced to asymmetry in the photolithography (which produced different photoresist slopes on the different sides of the feature). Ion reflection also reproduced the observation that shrinking the feature width caused

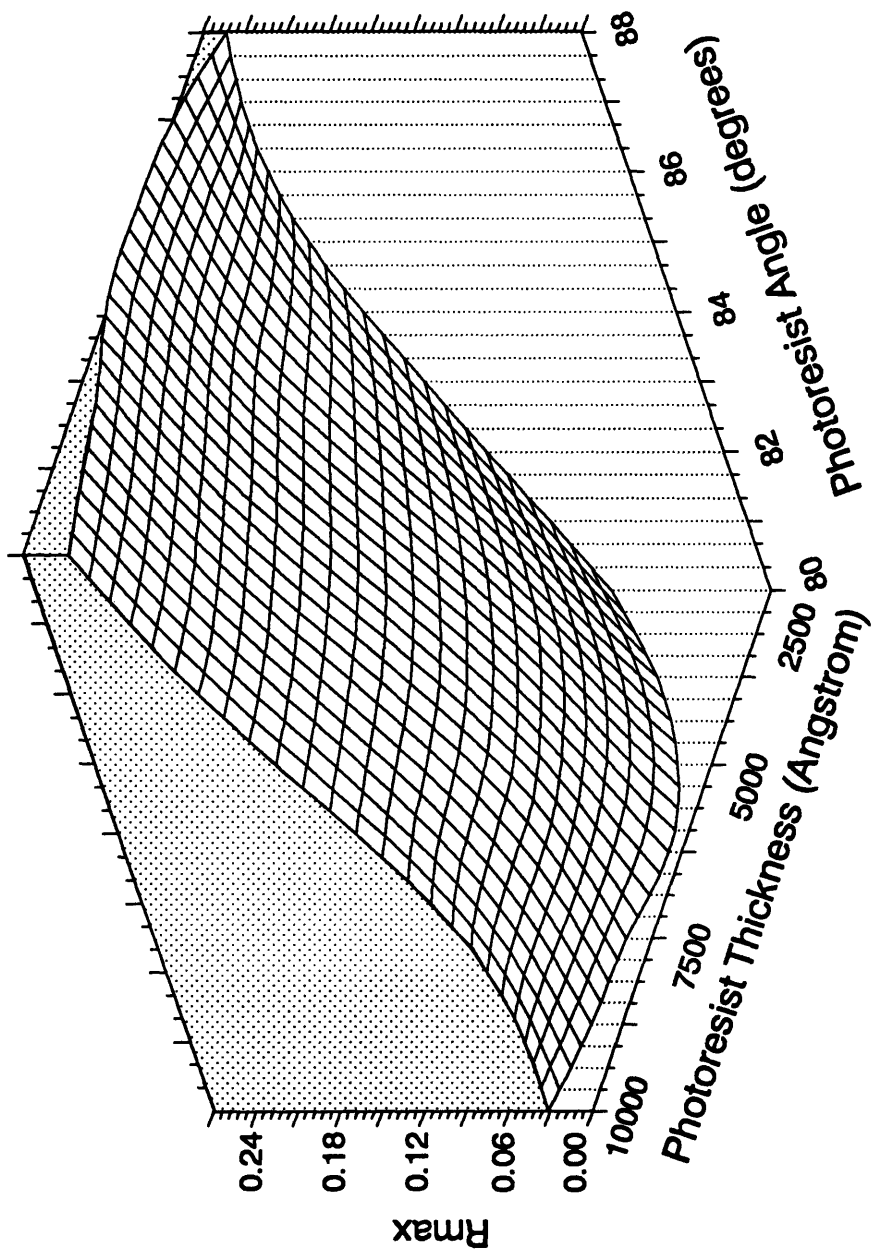


Figure 2.9: Response surface for maximum nonuniformity with varying photoresist thickness and angle.

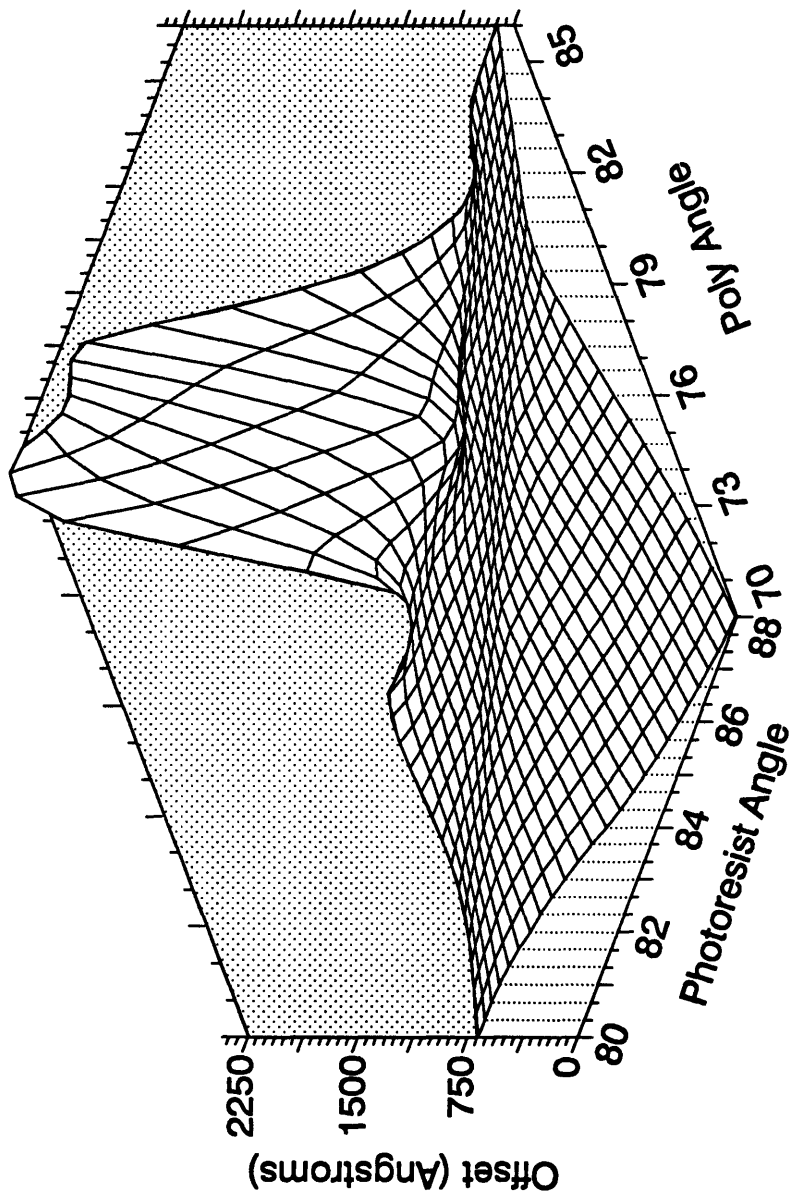


Figure 2.10: Offset (distance from foot of sidewall to microtrench) vs. photoresist and polysilicon angles.

the microtrenches to overlap and coalesce into a single large trench at the centerline (Figure 2.11). Other details, as well as SEM photos, were published in a journal article written jointly with T. J. Dalton and H. H. Sawin of MIT, and S. Swan and D. Corliss of Digital [Dalton, *et al.*, 1993].

Ion reflection was not the only possible mechanism presented for microtrench formation. Others have proposed that microtrenches are formed by surface diffusion of reactants down the sidewall, leading to an excess of the reactant on the bottom and thus a higher ion-enhanced etching rate. However, the unequivocal success of ion reflection in explaining all of the experimental observations, combined with the complete inability of surface diffusion to explain a trench location other than immediately adjacent to the sidewall, led to the conclusion that ion reflection is the dominant cause of microtrenching.

2.5.2 High-density Oxide Etching

A second application of the ion reflection model to an industrial process involved characterization of a high-density oxide etching process. This project, also performed in collaboration with engineers at Digital Equipment Corporation, centered on the etching of contact openings in silicon oxide using an inductively-coupled high-density etching system (the Applied Materials Omega system). The Omega system, like most high-density etchers, employs separate power sources for the main discharge and the wafer bias. The discharge in a high-density system is

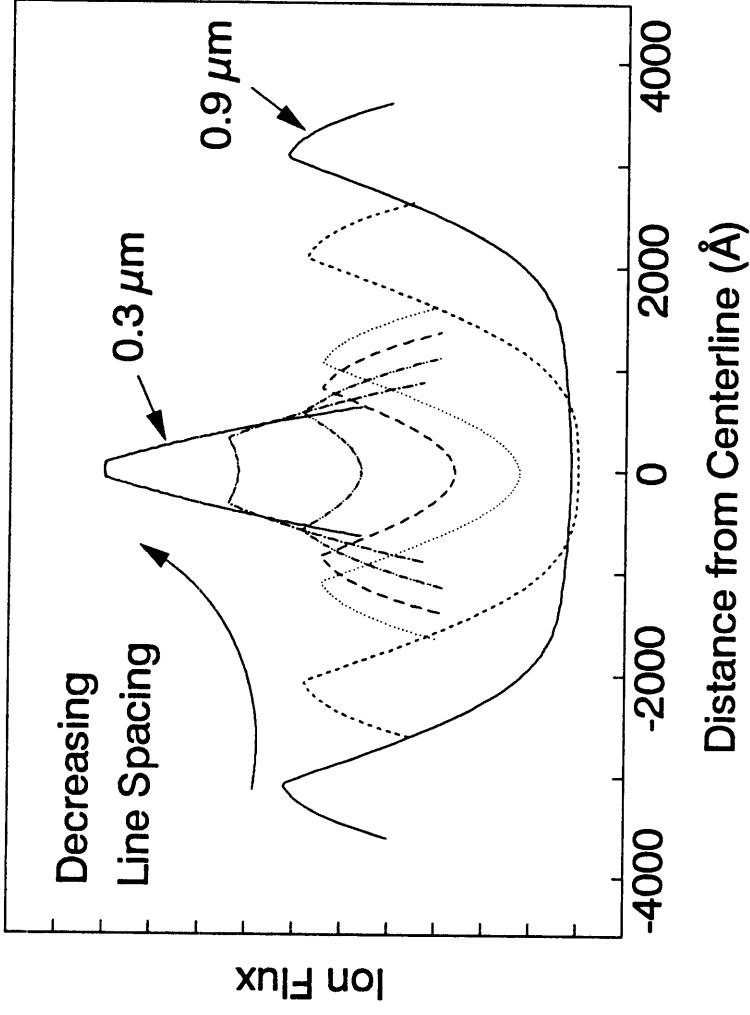


Figure 2.11: Effect of line spacing (open feature width) on bottom ion flux profile. Decreasing feature width causes reflected flux from sidewalls to overlap, leading to a single, centered microtrench.

produced by one of a number of techniques, such as inductive coupling, ECR, or helicon waves, and is characterized by very high plasma density with low plasma potential. As a result, ion currents are typically much higher than RIE processes (up to 10 mA/cm²), while the ion energy is only on the order of 10-20 eV. High ion current is attractive because it provides high etching rate and high throughput. Low ion energy diminishes the subsurface damage caused by collision cascades after ion impingement, but is also lowers the etching rate. Most high-density etchers provide a separate wafer biasing power supply for ion energy control.

The initial investigation into the Omega oxide etching process was motivated by occasional "etch stopping" behavior; under some conditions, etching would proceed for a time and then terminate, without change in the external process conditions. Poor wafer clamping and loss of wafer bias power were proposed as possible causes for etch stopping, so a controlled experiment relating wafer bias to etching performance was proposed. A 1.0 μm -thick mask of Deep-UV photoresist with various feature types (circular vias, long rectangular trenches, and isolated steps adjacent to large open areas) and sizes was applied to wafers with 1.0 μm of deposited oxide and a thin organic Anti-Reflective Coating (ARC). All parts were etched to a fixed fraction of the nominal etch time, with the process terminated before clearing the oxide (and reaching the underlying film). The C₂F₆ discharge was maintained at its normal conditions of inductive power, pressure (2 mTorr), and feed gas flowrate. The wafer bias power was varied in the range from 400 W to 800 W, vs. 750 W for the normal process. The etched depth and shape of all feature types

were found to depend strongly upon the wafer bias.

Not unexpectedly, lowering the wafer bias power lowered the oxide etching rate. Oxide etching has long been understood to be ion-driven. Decreasing the bias power decreases the ion energy flux to the wafer and lowers the etching rate. Changing the wafer bias also affected the sidewall slope, with higher power leading to steeper (more nearly vertical) walls. This is explained by observing that oxide etching in fluorocarbon plasmas frequently involves deposition of polymeric material on the sidewalls. This inhibits undercutting, but can also cause the etched wall to grow "outward" (into the open area) if deposition is excessive. Etching and deposition are in competition, with deposition controlled primarily by discharge conditions. Because the discharge was held nearly constant, decreased etching rate was accompanied by reduced sidewall slope.

The least anticipated and most interesting result of varied wafer bias was its effect on microtrenching. As was stated previously, microtrenches are apparently caused by reflected ions, and ion reflection is expected to occur under most conditions. Therefore, a blind hole etched under almost any conditions should show some microtrenching, especially if the wall is sloped to receive a substantial ion flux near grazing incidence. Indeed, prominent microtrenches were observed on the samples etched with the normal (or "baseline") process. However, samples etched with lower wafer bias showed diminished microtrenching; the microtrenches became progressively shallower as the bias was lowered, and even disappeared at the lowest

power in this experiment. The feature bottoms on the 400 W sample even appeared to turn up slightly.

An ion reflection-based flux model was constructed as a means to understanding the observed microtrenching behavior. Previous work had shown that feature geometry plays a critical role in the ion flux profile; the changes in sidewall slope could have an effect on microtrench formation. As usual, some input assumptions were required. Because the pressure is quite low, the IAD was expected to be very tight. A Gaussian distribution with Full Width at Half Maximum (FWHM) of 1.2° was used. The reflection probability was not known, but the same function used in the previous polysilicon etching project was taken as a starting point. The dynamics of wall motion would have some impact on the ion flux profile, but a brief attempt to determine the mechanism for slope change was not successful. Instead, an empirical relationship between wall slope, position, and time was constructed from the available profile information. The microtrench shape was expected to follow the cumulative ion flux profile to the feature bottom, which was found by adding contributions from 10 different time points in the etching process. This process is illustrated in Figures 2.12 and 2.13.

The calculated ion flux profiles (and thus microtrench shapes) were very different from the experimental observations. First and foremost, the computed level of flux enhancement was far too high. Figure 2.14 shows the ion flux profile for an isolated step (adjacent to a large open area) etched at 800 W. The maximum ion flux

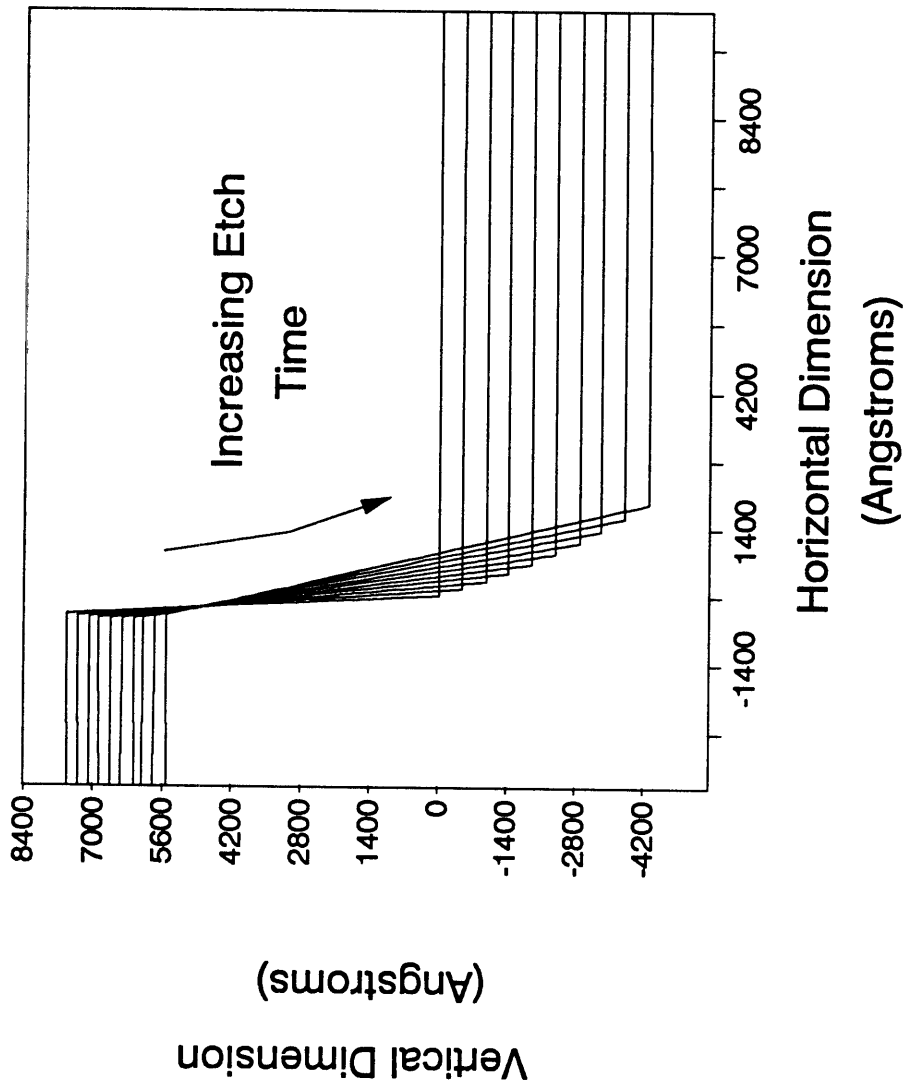


Figure 2.12: Estimated evolution of isolated step etched at 400 W.

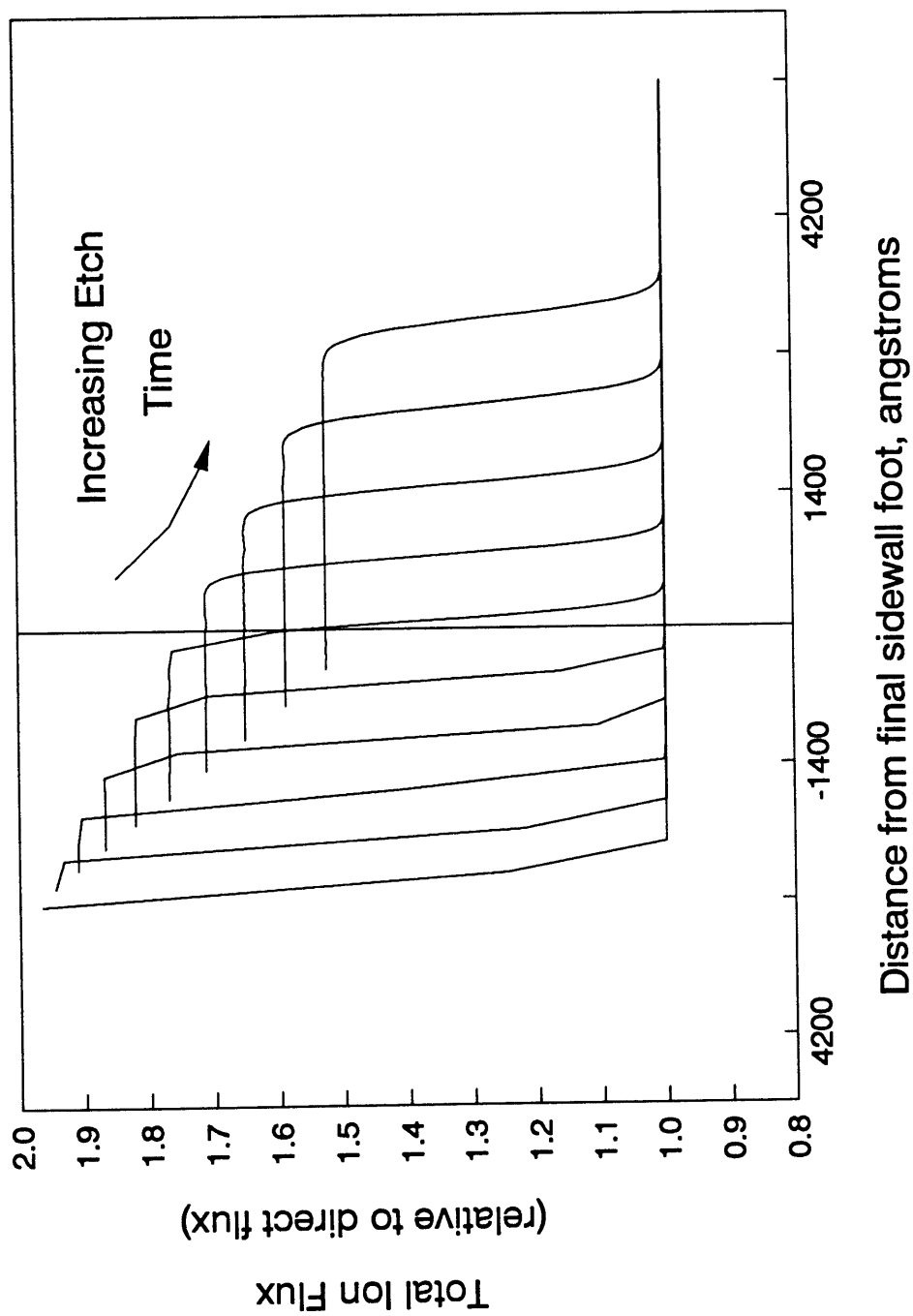


Figure 2.13: Total ion flux to feature bottom vs. distance from final sidewall foot and etching time, for 400 W sample.

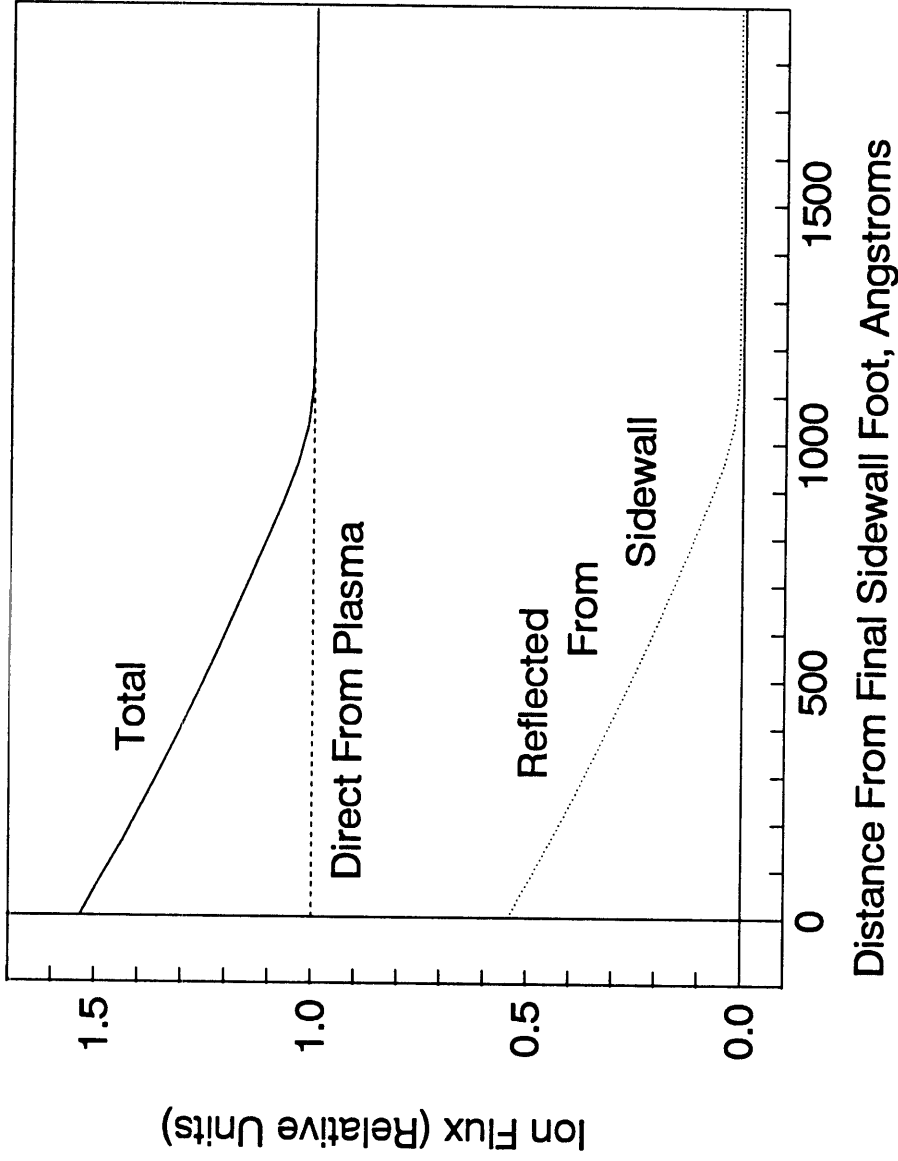
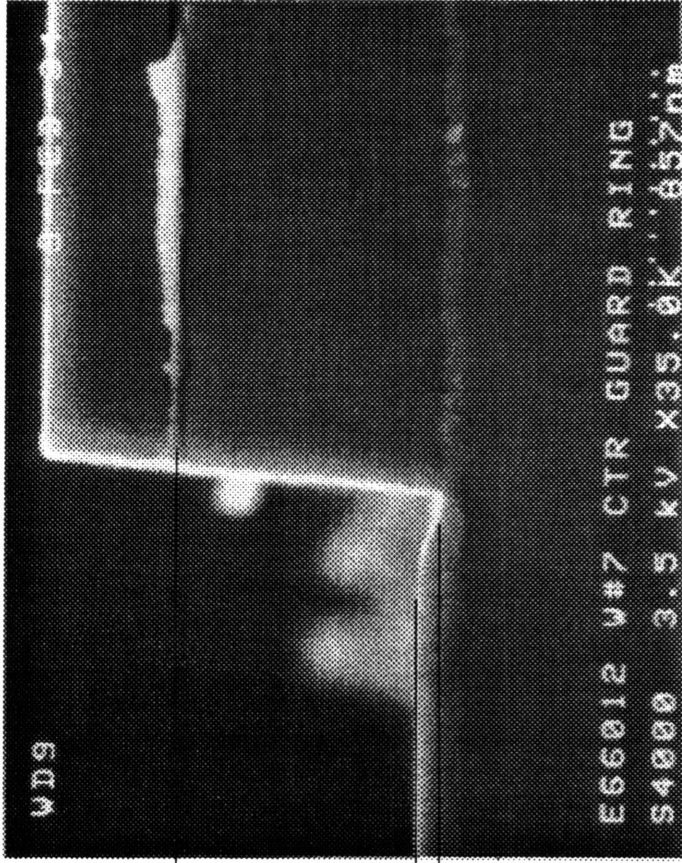


Figure 2.14: Ion flux vs. distance from sidewall foot for isolated step etched at 800 W.

near the sidewall is 53% higher than the direct flux from the plasma. Thus, one would expect the microtrench to be 53% as deep as the etched depth. However, Figure 2.15 shows that the actual trench depth is only about 7% of the etched depth. This disagreement was more pronounced for other process conditions: Figure 2.16 shows the computed ion flux enhancement and measured (from SEM photo) microtrench depths for isolated steps as a function of bias power. The changing sidewall geometry clearly has an effect on the computed ion flux, but the magnitude of the ion flux is simply too high. Varying the input assumptions (primarily changing the characteristic angles for the ion reflection probability function) did not improve the agreement significantly.

It was initially hypothesized that changing sidewall conditions, perhaps buildup of additional polymer material, could be reducing the ion reflection probability. This idea was rejected for two reasons: first, it was difficult to reconcile the accepted reflection theory, which suggests that energy coupling to the wall should be nearly impossible when the ion incidence is very close to grazing, with a reflection probability that saturated at some value other than unity. Second, even if reflection were completely inhibited at low power, the feature bottom would be flat (because the IAD is tight enough to eliminate shadowing effects for the observed wall slopes). Yet the 400 W sample seemed to show some upward curvature near the sidewall. This left a dilemma: the reflected ion fluxes were too strong, but no reasonable adjustment to the input assumptions could reproduce the observed behavior.



Oxide etched
depth $\approx 9100 \text{ \AA}$

Microtrench
depth $\approx 650 \text{ \AA}$

Figure 2.15: SEM photo of isolated step etched at 800 W.

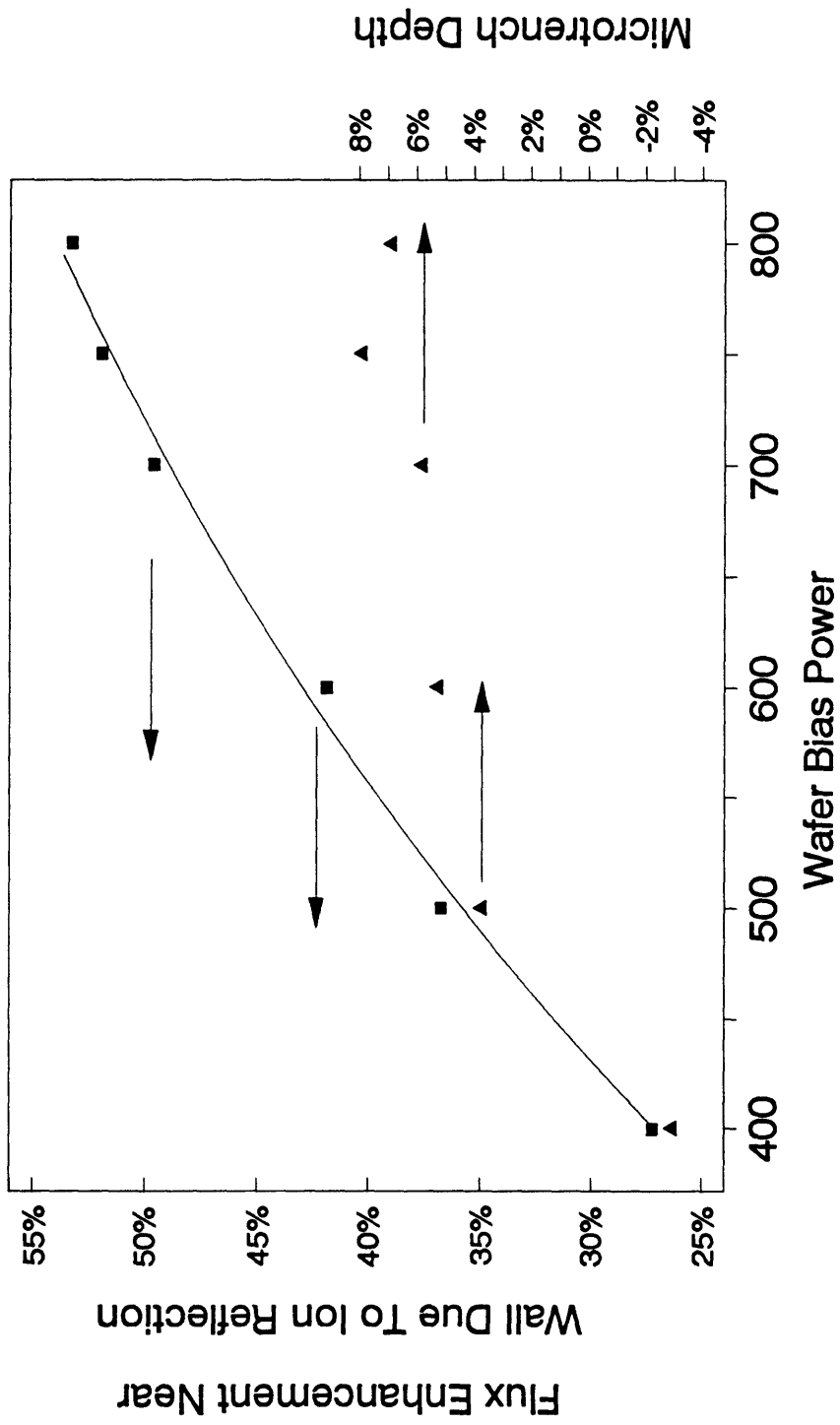


Figure 2.16: Microtrench depth and flux enhancement due to ion reflection vs. wafer bias power.

Reconsideration of the presumed etching mechanism produced an alternative explanation. The microtrench depth was originally equated with the enhancement of ion flux. This would be true if and only if the etching yield per ion were constant, so that reflected ions and direct (from the plasma) ions were equivalent. But the etching yield may depend strongly upon the ion energy, and ions might lose some of their energy upon reflection. This idea led to a reinterpretation of the reflection probability as an expression not just of the number of ions reflected at a given incidence angle, but as a figure that also included the equivalent yield of those ions. If energy losses were non-zero, then an apparent reflection probability of less than unity would be plausible.

The observed microtrench depths were compared to the computed flux enhancement and used to derive an equivalent reflected ion etching yield for each process condition. For example, the microtrench depth for the sample shown in Figure 2.15 was approximately 7% of the etched depth, while the computed flux enhancement for that geometry was 53%. This suggested that the yield for reflected ions was approximately 13% of that for direct ions. Similar analysis for each bias power produced the curve shown in Figure 2.17. The equivalent yield of reflected ions seems to follow a simple trend, dropping with bias power, except that it is negative for the lowest power.

The negative apparent yield for reflected ions would appear to present an insurmountable barrier, if it were not for some recently published work by Oehrlein,

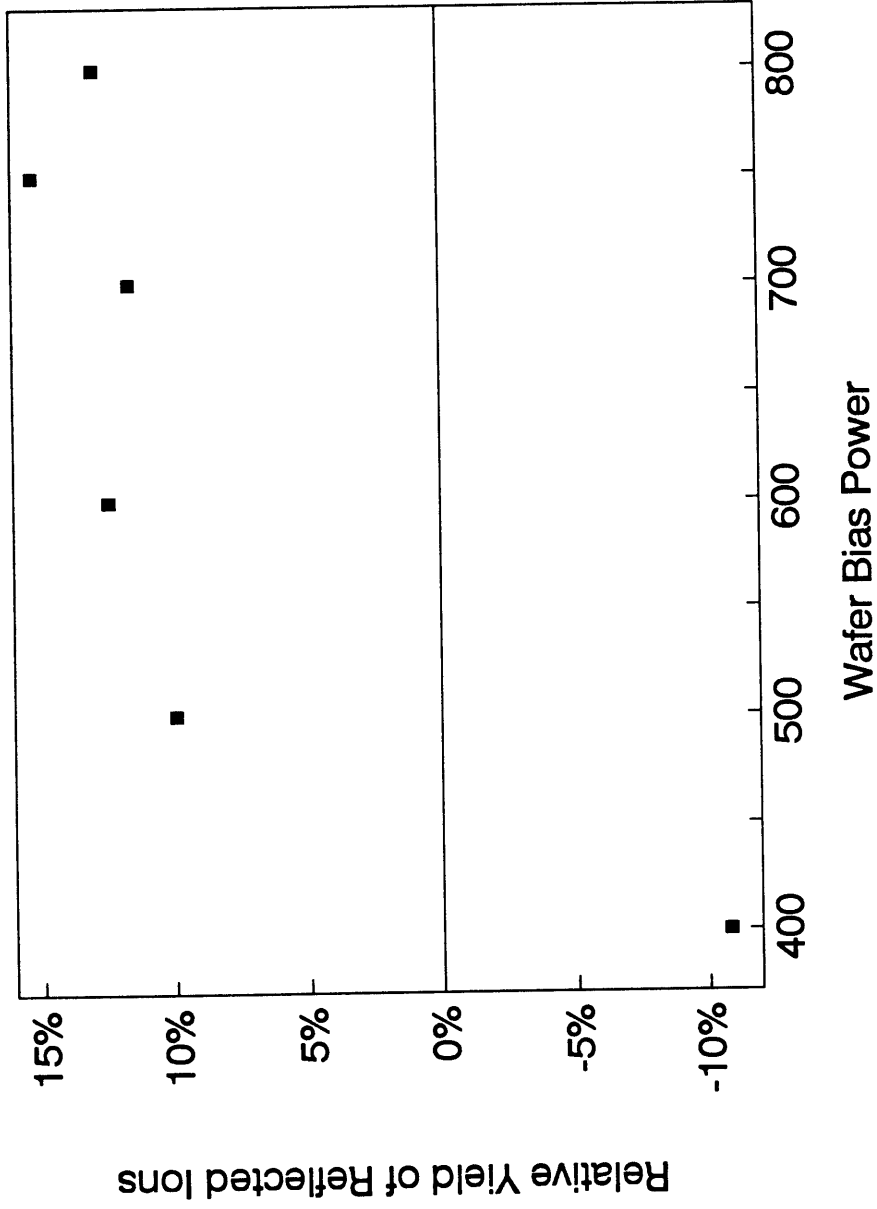


Figure 2.17: Relative yield of reflected ions (vs. direct ions), as estimated from observed microtrench depths, vs. wafer bias power.

et al., [1994] showing that CF_x ions at very low energy can actually lead to deposition. A facsimile of their data for yield vs. ion energy from a CF_4 ECR plasma is shown in Figure 2.18. The yield/energy space is divided into three regimes: in the lowest energy regime, the ions catalyze or otherwise contribute to polymer deposition. At very high energy (> 100 eV), normal etching occurs and the yield increases with the square root of energy. The intermediate energy range, which Oehrlein has termed the "suppression" regime, involves a transition between deposition and etching. As a consequence, the apparent etching yield changes rapidly from a small negative value (deposition) to a high positive value (etching). The feed gas is different in this work (C_2F_6), but a similar mechanism may be at work. Shibano, *et al.* [1993] have reported similar behavior for discrete beams of CF_x ions.

Oehrlein's data could provide an explanation for the observed microtrenching behavior, if the energy loss upon reflection were sufficient to move the ion energy from the etching regime into the suppression regime. Ions with lower initial energies (at lower bias power) would move farther into suppression, and the very low bias ions might even enter the deposition regime. This hypothesis was evaluated in the following manner. First, an estimate of the initial ion energy for each process condition was developed by assuming the ion energy to be approximately proportional to bias power, and noting that Applied Materials has informally reported the ion energy to be around 180 eV at 750 W. Next, the initial ion energy was used with Oehrlein's curve to determine an etching yield for direct ions. Third, the reflected ion equivalent yield derived from microtrench measurements was used

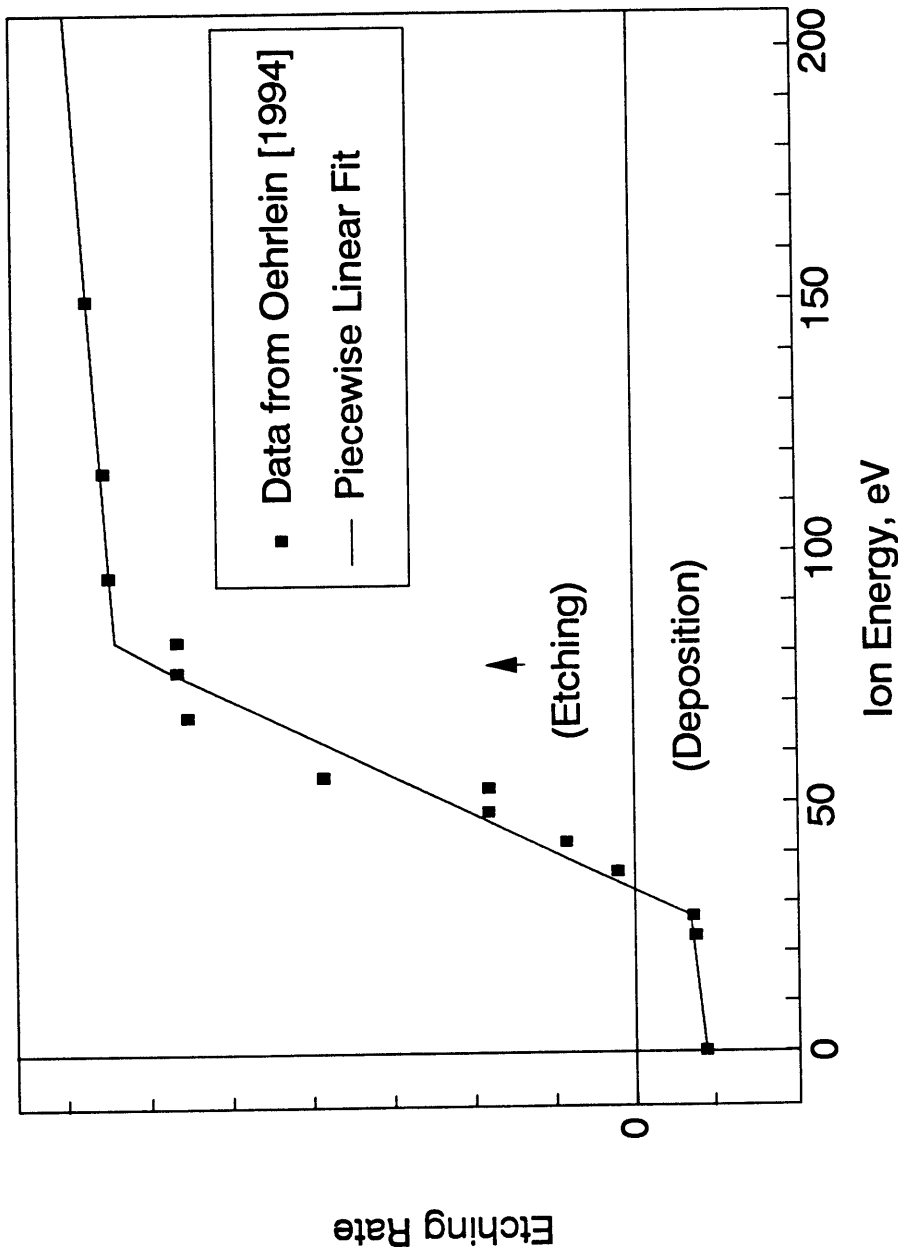


Figure 2.18: Etching rate vs. ion energy for CF_4 etching of SiO_2 in an ECR, from the published work of Oehrlein, *et al.*, [1994].

with Oehrlein's data to estimate the reflected ion energy.

This procedure is illustrated in Figure 2.19 for the 800 W sample. At 800 W, the initial energy is estimated to be 192 eV, which corresponds to a certain etching yield. The reflected ion equivalent yield for this condition is 13% (from Figure 2.17), meaning that each reflected ion is expected to liberate 0.13 times as many surface atoms as a direct ion. Returning to Oehrlein's data shows that this yield corresponds to energy for the reflected ions of 39 eV. This process was repeated for each process condition, producing the trends shown in Figure 2.20.

Figure 2.20 shows not only the estimated initial and reflected energy, but also the energy loss coefficient for each bias power. While the bias power and ion energies vary by a factor of 2, the energy loss coefficient remains roughly constant in the range of 70%-80%. 80% energy loss seems high, but is within the range of reported values [Cuthbertson, 1993] and is consistent across a wide range of process conditions. The constancy is encouraging; a changing loss coefficient would be more difficult to explain in terms of sidewall conditions.

Other researchers have studied a similar system and report different conclusions. Joubert, *et al.* [1994] applied Oehrlein's data to oxide etching in an ECR system. They invoked surface charging and subsequent ion energy loss to explain RIE lag in their system. However, they failed to mention or account for microtrenches clearly present in their work.

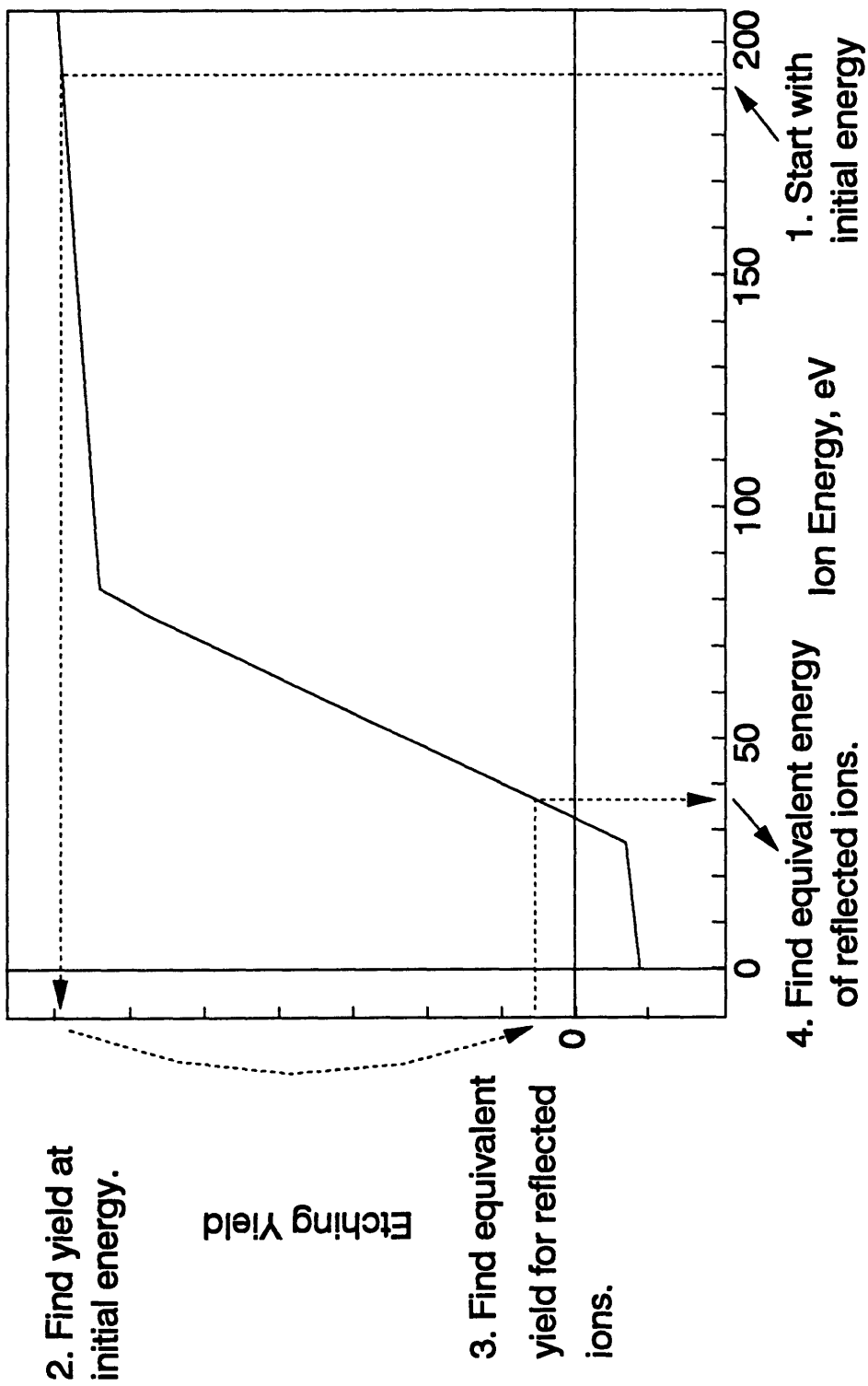


Figure 2.19: Procedure for estimating energy of reflected ions.

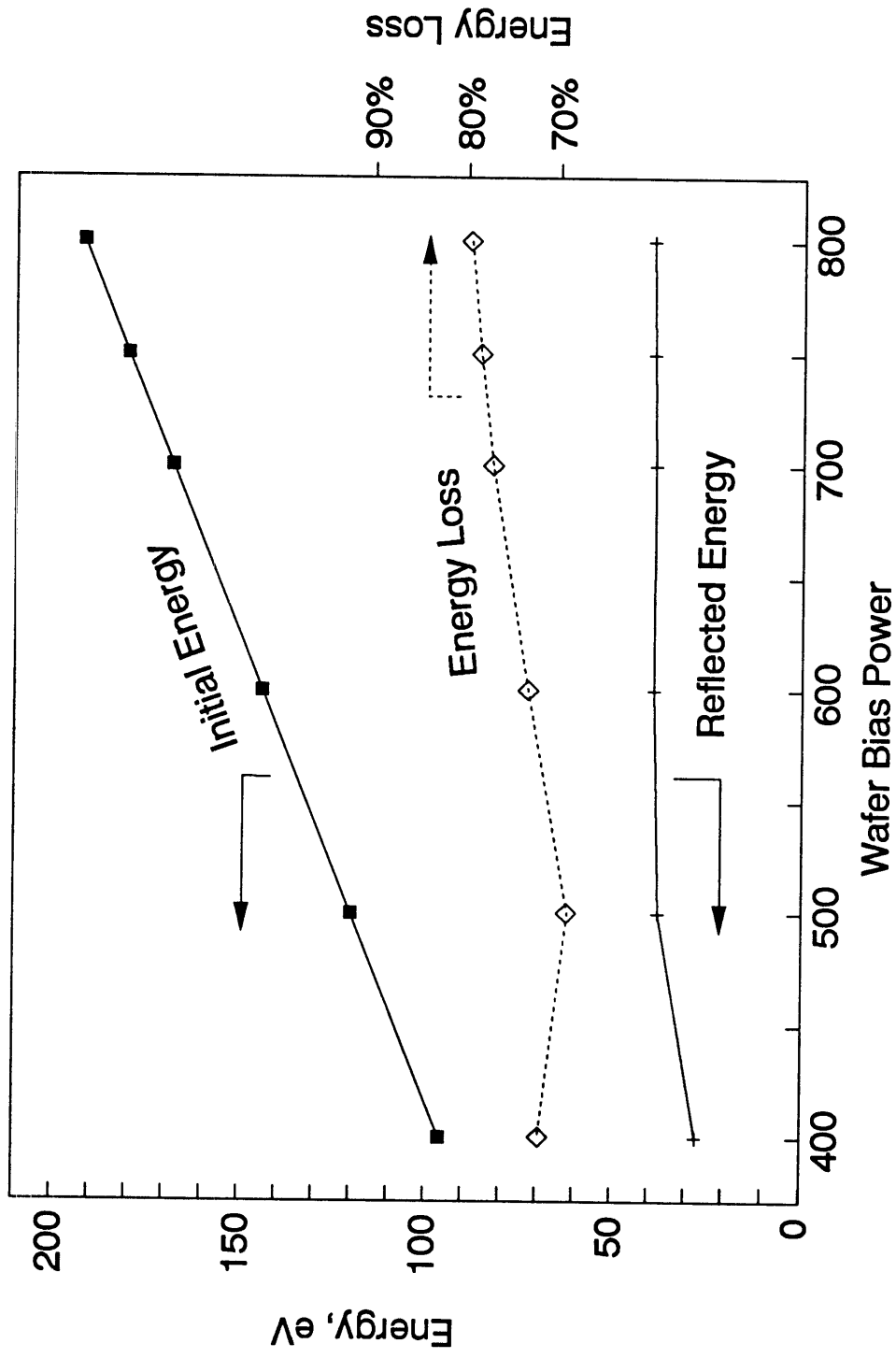


Figure 2.20: Estimated ion energies before and after reflection, and energy loss coefficient, vs. wafer bias power.

There may be other rational explanations for the process variations found in this experiment, and there are certainly some unresolved questions regarding the mechanism for wall slope change. However, the remarkable performance of this relatively simple model suggests that ion reflection with a constant energy loss is at least a plausible explanation for the observed microtrench variations.

Chapter 3

Ion Transport: Surface Charging

3.1 Introduction and Mechanism

In addition to the dispersion and reflection models discussed in the previous Chapter, the consideration of ion transport in features included analysis of localized surface charging. Specifically, it was proposed that imbalance between the local ion and electron flux could give rise to significant electric fields within or near the feature, thus modifying the trajectories of ions in the vicinity.

The theory of feature-scale surface charging begins with the observation that electrons cross the plasma sheath during a short portion of the RF cycle when the sheath field is low. Therefore, their trajectories should not change greatly during the sheath crossing, and they should approach the wafer with an angular and energy distribution that roughly mimics their behavior in the bulk. Electrons in the bulk are known to follow a Boltzmann or Druyvestern energy distribution with a characteristic energy (kT) of a few eV and an isotropic directional distribution. In contrast, ions experience high average fields during their traverse of the sheath, thus acquiring highly directed energies up to several hundred eV.

When the ions and electrons enter a surface feature (such as a photoresist

mask), the difference between their angular distributions leads to a local imbalance of flux. The total numbers of electrons and ions entering the feature should be equal, but they strike the surface in different regions. The isotropically directed electrons deposit preferentially upon the upper sidewalls, while the ions tend to travel farther into the feature before striking the sidewalls and feature bottom. If the walls are strong insulators, then an imbalance in flux can lead to trapped charge accumulating on the surface. Charge on the surface will induce electric fields within the feature, which will modify the trajectories of charged particles subsequently entering the feature (Figure 3.1).

If the walls are assumed to be perfect insulators, then diffusion (and recombination) of the charges can be neglected. In this case, charge will accumulate until the ion and electron fluxes are forced into alignment at every point along the surface. Both the ion and electron trajectories will be significantly perturbed, with ions pulled toward the sidewalls and electrons repelled from the upper regions of the wall. The relative change in trajectory for the two types of carriers will be determined by their initial energies. Ion and electron energies are typically within a factor of 10 to 100, so the perturbation of ion flux may be substantial.

The distribution of charge and the electric field structure within the feature were expected to be quite complex. Because of this, it was not possible to estimate the importance of this mechanism *a priori*. On the other hand, integration of this mechanism with the existing ion dispersion and reflection models would have been

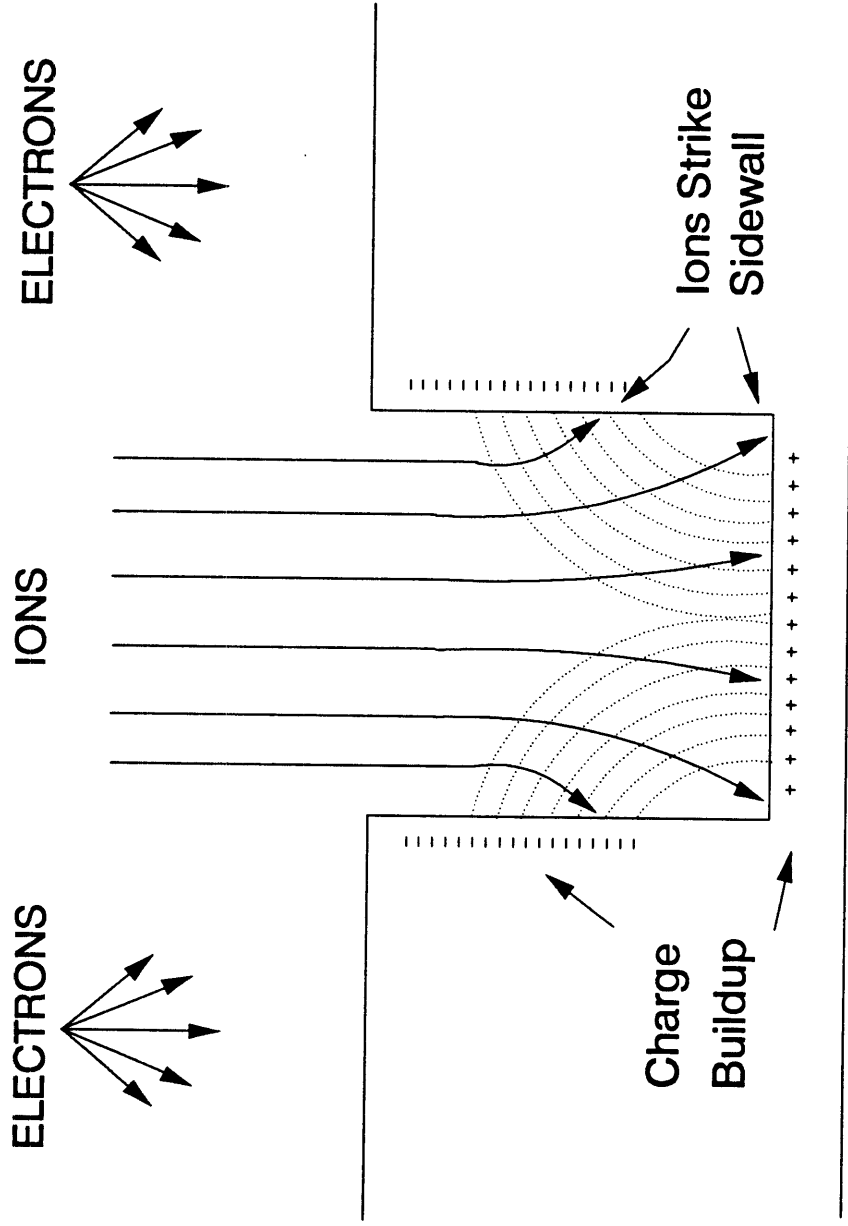


Figure 3.1: Mechanism for ion deflection by charging of feature surfaces. Different ion and electron trajectories lead to buildup of charge on sidewalls. Induced electric fields skew subsequent ion trajectories.

expensive in both effort and computational time. This led to a decision to construct a simple, worst-case surface charging model which could be applied to a few simple cases and used to estimate the relative importance of this mechanism.

The assumptions for the initial exploration of surface charging were chosen to provide the maximum opportunity for a significant effect on the ion flux and to contain the simulation cost. The ions were assumed to be perfectly directed along the macroscopic surface normal with a uniform energy of 100 eV. The electrons were defined to follow the Boltzmann energy distribution with kT set to 5 eV. The sidewalls and feature bottom were taken to be perfect insulators, and the walls were made vertical. Feature aspect ratios (depth/width) of 1, 2, and 4 were explored. These conditions were expected to represent the upper limit on the importance of feature-scale surface charging for the reactive ion etching systems in common use at the time (1990).

3.2 Numerical Methods

The objectives of the initial simulations can be stated as follows: find the distribution of surface charges (or potentials) which force the ion and electron fluxes into alignment, and analyze the resultant ion flux distribution along the surface. Determining the required charge distribution is a highly non-linear problem: the surface potential distribution both stems from and influences the ion and electron flux distributions.

This problem may be viewed as an application of the Vlasov kinetic equation,

$$\frac{\partial f_s}{\partial t} + \vec{w} \cdot \frac{\partial f_s}{\partial \vec{r}} + \frac{q_s}{m_s} (\vec{E} + \vec{w} \times \vec{B}) \cdot \frac{\partial f_s}{\partial \vec{w}} = 0, \quad (3.1)$$

which governs the motion of charged particles in the absence of collisions [Bers, *et al.*, 1987]. In Equation 3.1, $f_s = f_s(\vec{w}, \vec{r}, t)$ is the distribution function for the charged particles of mass m_s and charge q_s , \vec{w} is the velocity vector in three dimensions, \vec{r} is the position vector, and the subscript s identifies each class of charged species (i.e., electrons or ions). Equation (3.1) would be written twice, once for the electron distribution function f_e and once for the ion distribution function f_i . This Equation could be solved in conjunction with Maxwell's equations to find the distribution function at each point within the surface feature. For this case, where there is no magnetic field, the relevant Maxwell equation may be written as [Bers, *et al.*, 1987]

$$\epsilon \nabla \cdot \vec{E} = \rho = \rho_{\text{ext}}, \quad (3.2)$$

where ϵ is the permittivity of the medium, ρ is the charge density given by

$$\rho(\vec{r}, t) = \sum_s q_s \int f_s d^3w, \quad (3.3)$$

and ρ_{ext} is an "external source" of charge density which would give rise to the imposed electric field.

Application of Equations (3.1) to (3.3) to the problem of surface charging within a feature would proceed as follows. The first step would be to define a domain for the solution. An obvious choice is shown in Figure 3.2, where the domain is bounded by four surfaces.

The first surface (1 in Figure 3.2) is placed a few feature widths above the wafer surface and forms an artificial boundary between the plasma sheath and the region of the feature. The length scale of the feature is small enough relative to the sheath width that the electron and ion distributions are (almost) fully developed by the time they reach Surface 1, so f_e and f_i can be taken as fixed inputs along that boundary.

The second surface is the actual surface of the wafer. The desired boundary condition at this location is a balance of time-averaged ion and electron current densities:

$$\bar{J}_e(\bar{r}_2) = \bar{J}_i(\bar{r}_2) , \quad (3.4)$$

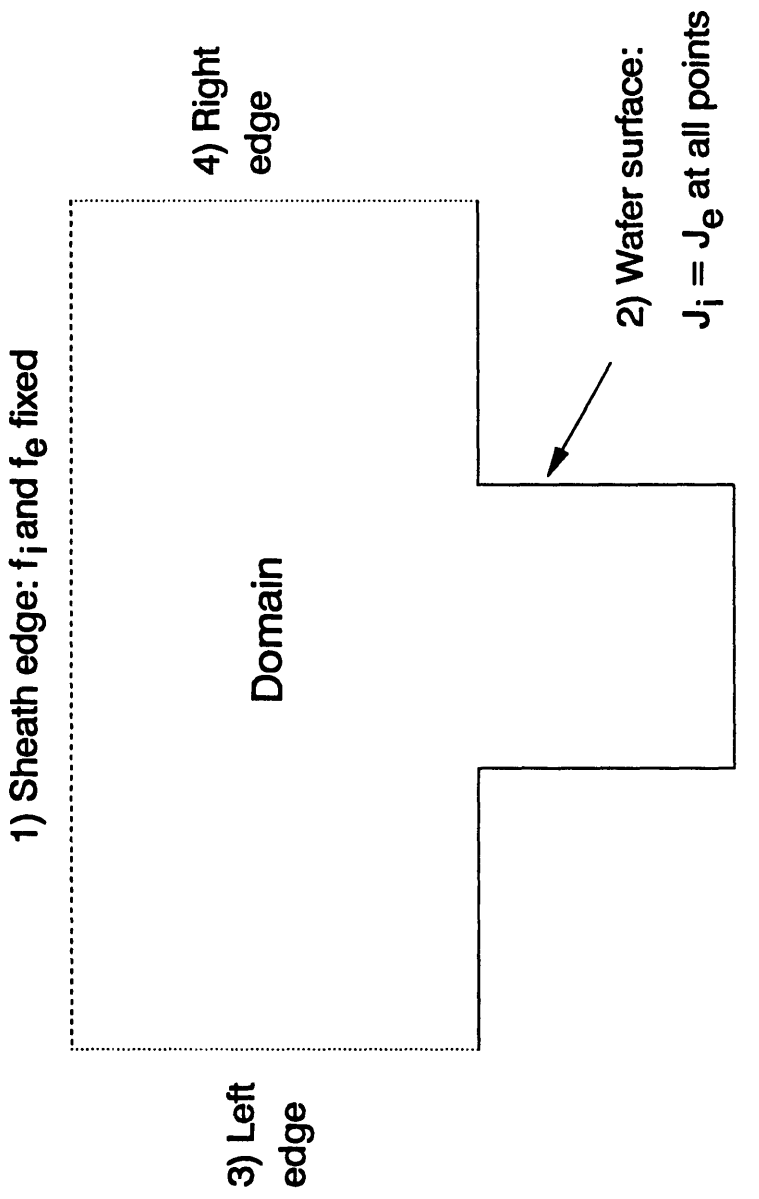


Figure 3.2: Computational domain and boundary conditions for charging of surface features.

where the instantaneous species current density is given by

$$\vec{J}_s(\vec{r},t) = q_s \int \vec{w} f_s d^3\vec{w} \quad (3.5)$$

[Bers, *et al.*, 1987].

The final surfaces, 3 and 4, form lateral boundaries for the computational domain. If the surfaces are placed far enough from the feature, then simple symmetry conditions will apply along both of them.

The electric field in Equation (3.2) stems from two sources: the primary contribution is from the accumulated charge on the surface, while a minor component would arise from the penetration of sheath fields into the computational domain.

The system of equations and boundary conditions presented above applies to the general, time-dependent problem with arbitrary charge density (provided that the particle density remains low enough for collisions to be negligible). However, the specific system under study in this case allows several important simplifications.

First, an estimate of the charge deposited in one RF cycle by a typical processing plasma indicated that several thousand cycles would be required to

accumulate enough charge to reach the desired steady state. Therefore, the time-varying components of the surface charge and distribution functions could be neglected.

Second, the charged particle density near the surface was observed to be low relative to the chosen feature dimensions. The ion density near the wafer for a typical RIE process is on the order of 10^{10} - 10^{11} cm^{-3} , or about 1 ion per 100 cubic microns. This density is clearly low enough that electrostatic interactions between particles can be ignored.

Finally, the very small dimensions of the surface feature (and hence the computational domain shown in Figure 3.2) compared to the sheath width made it clear that the contribution of the sheath field would be minor. Typical feature widths are on the order of microns, while sheath widths for the RIE systems in use at the time of this study were in the millimeter range. Therefore, the penetration of sheath fields into the computational domain could be neglected.

These simplifications reduced the problem to a (simpler) matter of balancing the instantaneous electron and ion currents to the wafer surface, with the trajectories of the particles initially set by the plasma sheath physics and subsequently determined by the electrostatic fields induced by accumulated surface charge.

For reasons of convenience for this initial study, an iterative solution scheme

mirroring the physical process was adopted. Each iteration consisted of three steps: computing the electrostatic fields in and near the feature from the previously accumulated charge, tracking representative ion and electron trajectories to determine the instantaneous flux distribution¹, and adding the local flux imbalances to the accumulated charge. The first iteration began with an uncharged surface, and the iterations proceeded until the instantaneous fluxes were within 2% of each other on average across the surface.

The major computational components were determination of the electric field profiles and the particle trajectories. The public-domain ion lens analysis program SIMION [Dahl and Delmore, 1988] was selected for these tasks. SIMION operates by solving Laplace's equation,

$$\nabla^2 \psi = 0, \quad (3.6)$$

with user-defined boundary conditions, then using the resultant potential distribution to integrate the trajectories of discrete particles. SIMION has been used extensively in this group for design of plasma diagnostic equipment, and its accuracy was considered acceptable for the needs of this surface charging study. The physical assumptions for initial particle trajectories and surface properties were sufficiently

¹ Bers, *et al.* [1987], have mentioned that the method of characteristics is a common method for solving Vlasov's equation, and that f_s is constant along characteristics which correspond to individual particle trajectories.

gross that minor numerical inaccuracies (if there were any) would be inconsequential.

Use of an established package eliminated much of the programming, debugging, and testing effort that would have been required with an original code, but introduced certain pre- and post-processing requirements. First, SIMION accepts input only in the form of electrodes, with each electrode segment defined by its coordinates on a spatial grid and its voltage (potential). The number of electrodes was limited only by the number of grid points, so defining a surface with a varying local potential was not difficult. However, conversion of the surface charge to potential required some effort. This was accomplished in three steps. First, a reference potential of 0 V was defined at a point on the top surface, removed from the edge of the feature by a distance equal to its width. This approach was justified by the expectation that the flux imbalances would be confined to the immediate vicinity of the feature mouth. Next, Gauss's law and superposition were used to find the total electric field induced by the collection of charges along the surface. Finally, the electric field along the surface was integrated to yield the potential at each point. These potentials were then used to create an electrode definition file for input to SIMION. Convenient application of Gauss's law required an assumption that the dielectric constant of the surface material and the vacuum were the same; however, this assumption affected only the scaling relationship between charge and potential, and did not alter the final potential distribution.

An artificial electrode at 0 V was placed at a distance of a few times the

feature width above the top wafer surface (Surface 1 in Figure 3.2). This electrode provided a boundary condition for SIMION's field computation in the space above the feature mouth; the potential was set to 0 V. This electrode could be thought of as a boundary separating the electric field in the sheath from the fields introduced by surface charging.

The second input required by SIMION was the initial position, direction, and energy for each particle. All particles entered through the electrode at the sheath edge. The ion beam was simply represented by a collection of particles emerging from the artificial electrode at intervals along its length, each with initial energy of 100 eV and initially directed toward the wafer surface. The electrons, on the other hand, were distributed over both energy and direction. These distributions were approximately represented by arrays of electron beams at 15 different directions and 5 discrete energies. The directions began at the wafer normal and were spaced at even intervals thereafter, with the relative populations at each initial direction incorporated during post-processing. The 5 energy levels were chosen by dividing the total flux striking the artificial electrode (from the plasma side) into 5 equal groups and assigning a single average energy to each group.

Post-processing was required because the only machine-readable output from SIMION was a "dialog" file containing information about all portions of the calculation. One of the parameters reported for each charged particle was the coordinates of its point of collision with the surface. Extracting this information from

the dialog file produced a set of landing sites for each particle beam (the ion beam and each of the 75 different electron direction and energy combinations). The initial particle positions were evenly spaced along the sheath boundary, but the distance (along the feature surface) between landing sites varied. The spacing of the landing sites was used to compute the flux to each surface point by dividing the initial spacing into the distance between corresponding landing sites. For example, if two adjacent particles landed twice as far from each other as they started, then the equivalent flux (particles/length) between their landing sites would be half the initial flux. The total electron flux was found by adding the contributions from each of the beams, after adjusting for the relative fluxes at the different initial directions.

The instantaneous ion and electron fluxes were compared, with any imbalance added to the previously accumulated charge imbalance. The accumulated charge density at each point on the surface after iteration n was found by

$$\rho^n = \rho^{n-1} + k(J_i^n - J_e^n) , \quad (3.7)$$

where k was a manually-adjusted "tuning" parameter used to control oscillations.

The cycle described above was repeated until the imbalance between ion and electron fluxes along the surface dropped to less than 2% rms. The solution typically required several hundred iterations for each feature aspect ratio, but the adjustment of k in Equation (3.6) was clearly sub-optimal and may actually have increased the

number of iterations required.

Subsequent analysis of the potential distributions suggested that the total accumulated charge would be supplied within a few thousand RF cycles. This time is negligible compared to the length of an etching process, so the steady-state charge imbalance and its influence on ion flux distributions can be presumed to persist throughout the process.

3.3 Results and Conclusions

Figure 3.3 shows the steady-state surface potential distribution obtained for a feature with aspect ratio 2 (with depth equal to twice the width). As initially expected, the potential is generally negative near the upper sidewall and positive near the feature bottom. However, some unexpected structure emerged from the simulation. First, the maximum potential was not found at the feature centerline, but was actually located at the corner where the sidewall meets the bottom. This may be rationalized by considering the degree of perturbation required to redirect ions from the feature bottom. Ions initially approaching the centerline require only a small disturbance to move them away from it. However, those ions are turned toward the outer portions of the bottom, thus increasing the positive flux to those regions. A fairly high positive charge is required to deflect ions beyond the corner and onto the sidewall.

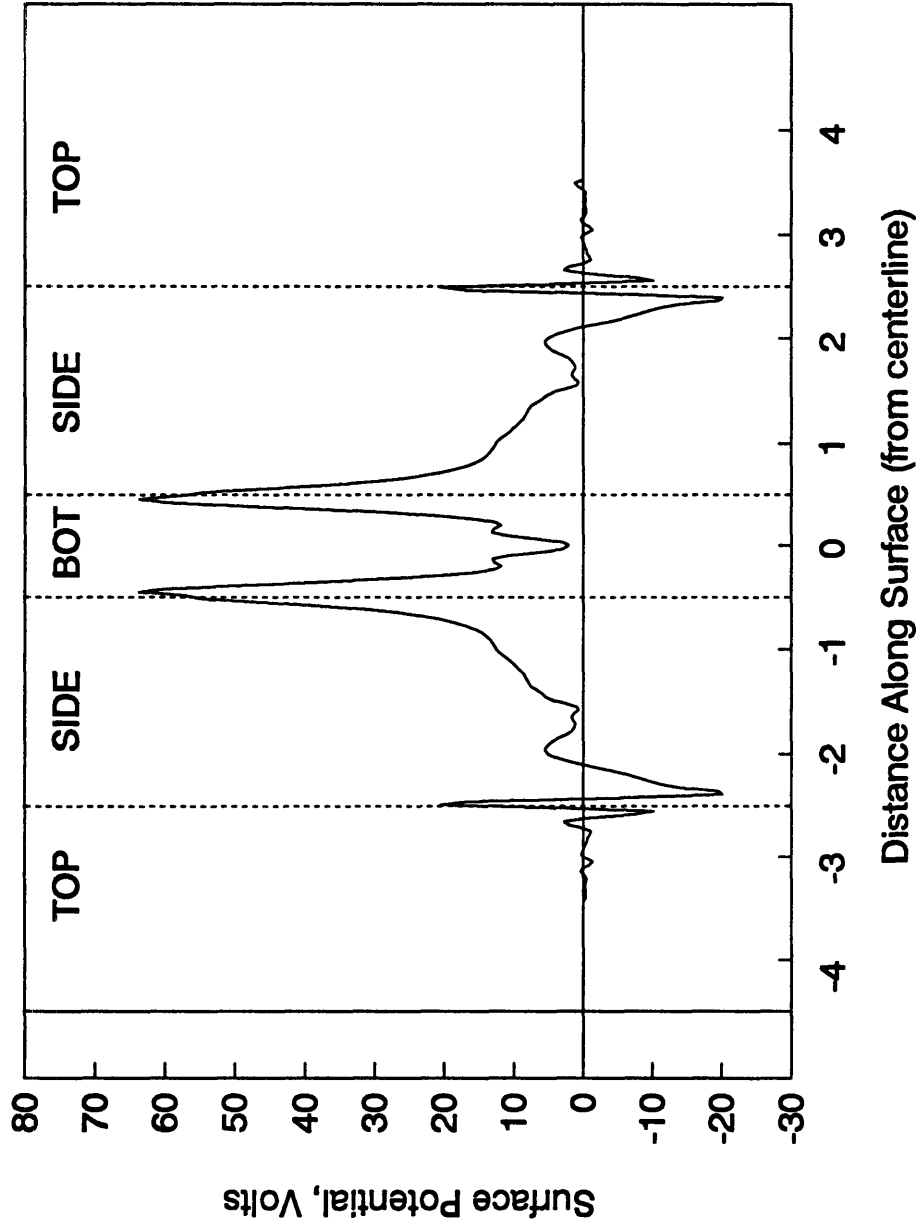


Figure 3.3: Final surface potential for trench with aspect ratio 2. Horizontal axis is distance measured along surface from centerline.

The potential distribution also showed some unexpected features near the corner joining the top surface and the upper sidewall. The upper wall was generally negative, but the top surface near the feature mouth showed some positive charge accumulation. The potential distribution near the top corner also displayed some "ringing," where the potential oscillated between positive and negative. The origin of these effects are not known, but they are thought to stem from an imperfect problem statement. With no surface charge diffusion allowed, the desire to equalize ion and electron fluxes on both sides of the sharp corner may be unrealistic.

The use of discrete electrodes as inputs to SIMION has also been identified as a possible source of error in the final potential distributions. Because the electrodes forming the surface have discrete potentials, the interfaces between them would correspond to discontinuities in the potential and singularities in the electric field. In practice, this problem is not as severe as it may seem because the electrode potentials are impressed upon the same spatial grid used by SIMION for the field computation. Therefore, the numerical field gradient is bounded (by the difference in potentials and the spacing between grid points) and singularities should be contained. However, rapid changes in the surface potential near sharp corners could certainly upset the electric field calculation near the top corner and may have contributed to the odd effects observed there.

Figure 3.4 shows the effect of aspect ratio on the final surface potential. The potential profiles were all qualitatively similar to the one shown in Figure 3.3. The

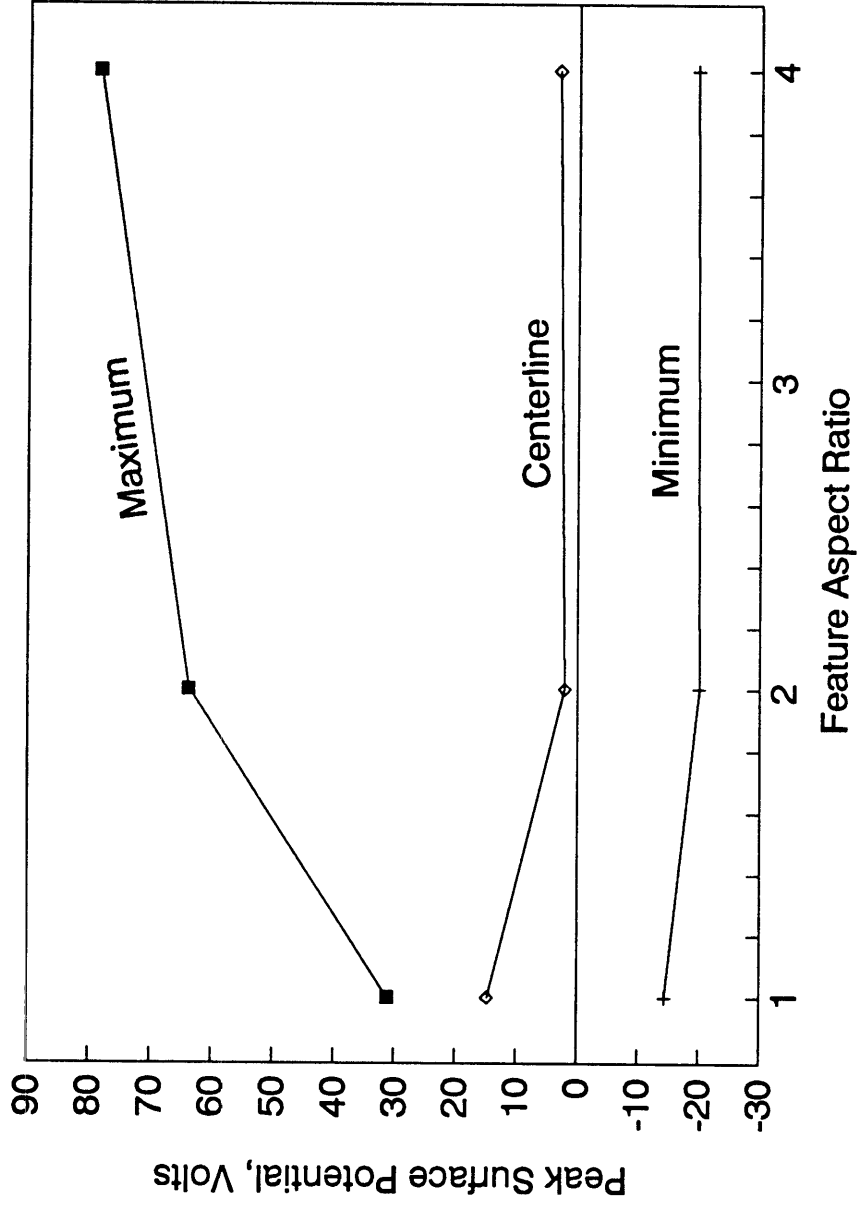


Figure 3.4: Variation of extreme surface potentials with feature aspect ratio. Maximum potentials are found near the foot of the sidewall. Minima are near the upper sidewall.

highest potential was found near the bottom-sidewall intersection, while the minimum occurred on the upper sidewall.

More interesting than the potential distribution are the effects on ion trajectories and flux distributions. Figure 3.5 shows the ion flux as a function of position along the surface for features of three different aspect ratios. In all cases, the reference point is taken as the centerline at the bottom and the feature widths are fixed at 1 length unit. The ion flux is markedly different from what would be expected for these structures in the absence of surface charging. Specifically, a significant portion of the ions are redirected from the feature bottom to various parts of the sidewalls. This would have two consequences: the etching rate on the sidewalls would be increased, and the etching rate on the feature bottom would be decreased. Figure 3.6 shows the effect of feature aspect ratio on the loss of ions from the bottom to the sidewall. For a feature with depth/width aspect ratio of 4 (the highest such ratio considered in this study), nearly 70% of the ions entering the trench land upon one or the other sidewall, and the average ion flux across the bottom is reduced by 70%. The consequences for feature profile are clear: deflecting ions away from the trench bottom would decrease the etching rate of high aspect ratio features (thus exacerbating the RIE lag problem), while attracting ions to the sidewalls would contribute to such problems as undercutting or barreling.

It should also be noted that the surface potentials along the feature bottom are high relative to the initial ion energy. An ion passing from the sheath to a point

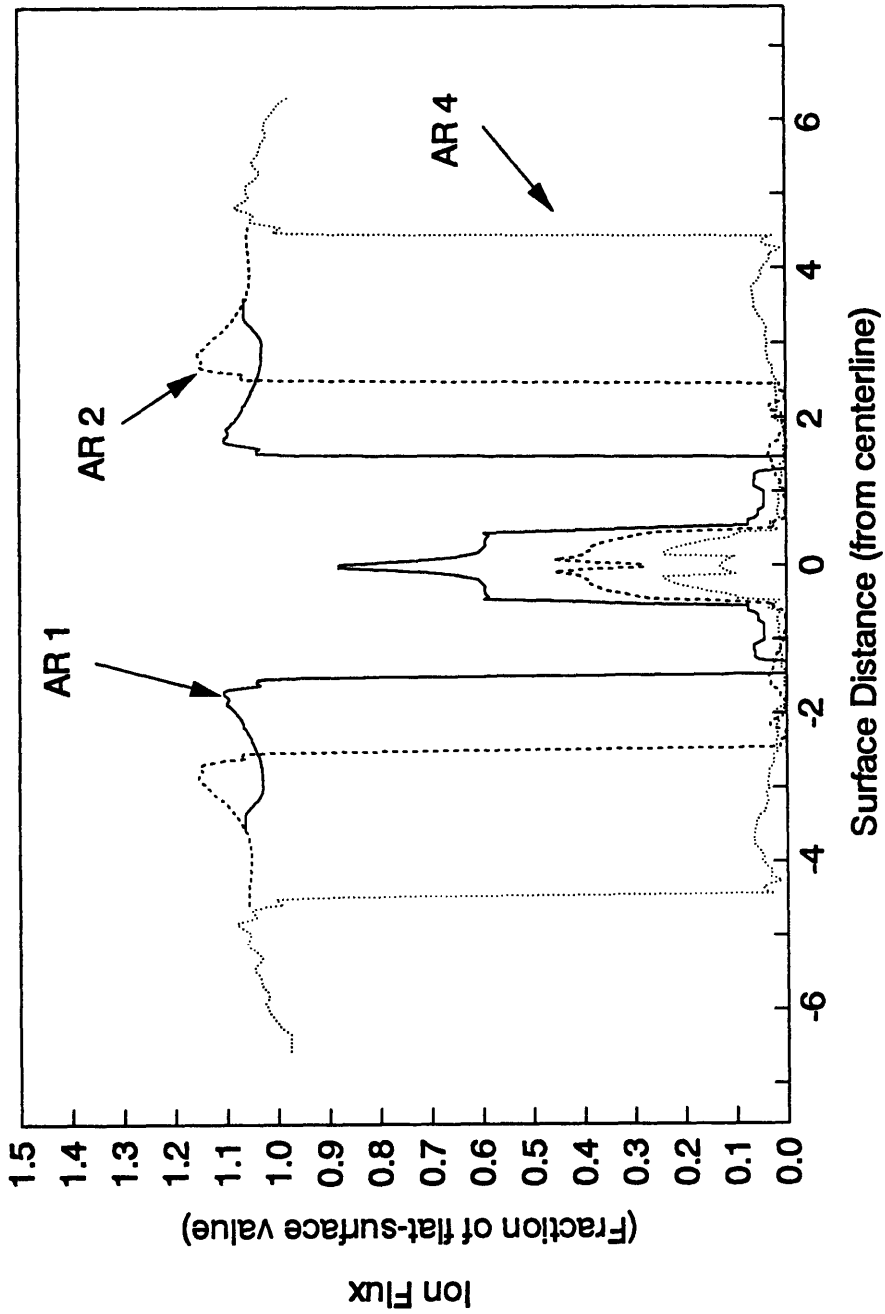


Figure 3.5: Ion flux to feature surface for different aspect ratios (AR). All features are 1 horizontal axis unit wide. AR 1 feature has wall height 1, AR 2 has wall height 2, and AR 4 has wall height 4.

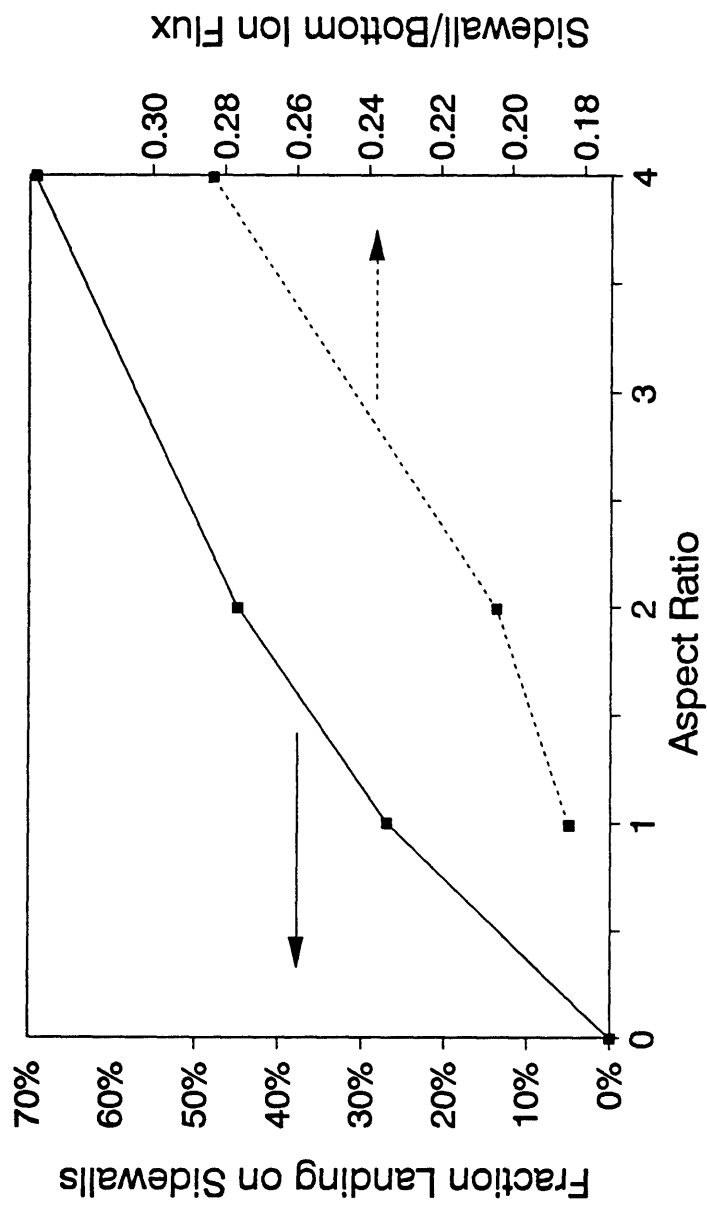


Figure 3.6: Effect of feature aspect ratio (depth/width) on loss of ions to the feature sidewalls. As the aspect ratio increases from 0 to 4, the fraction of ions striking the walls (as opposed to the bottom) increases from 0 to nearly 70%. The average flux along the wall at that aspect ratio is nearly 30% of the bottom flux.

on the surface must lose (or gain) energy equivalent to the potential where it lands. This would reduce not only the ion flux but also the energy flux to the feature bottom. Ion energy is frequently of comparable importance to flux, so the effects on etching behavior may be magnified. Joubert, *et al.* [1994] have utilized this facet of surface charging in their analysis of oxide etching behavior in deep circular vias.

The predicted changes in ion flux profile suggest that the process ramifications of surface charging may be substantial. However, it must be noted that the predictions made above are only as valid as the assumptions upon which the charging model depends. The assumed ion and electron angular distributions are optimistic; ions are known to reach the surface with some off-normal velocity component, so the initial charge imbalance is probably lower than that used here. Furthermore, the assumption of a perfectly insulating surface is also open to question. For one thing, the predicted potential gradient across the sidewall ranged as high as 45 V for the aspect ratio 1 feature. If a typical feature width of 1 micron is assumed, then the corresponding electric field along the wall would exceed 40 million volts per meter. This is near the breakdown limit of many materials.

A more likely possibility is that finite surface conduction would diminish the actual potential buildup. This was evaluated by computing an upper limit for the potential drop across the sidewall for typical ion currents and various surface conductivities. Conduction through the bulk was lumped into the surface conductivity for simplicity. For RIE systems in current use, the ion current arriving from the

plasma is on the order of 0.1 mA/cm^2 . If all of the ion current entering a $1.0 \text{ }\mu\text{m}$ -wide trench were assumed to deposit at a single point on the centerline of the feature bottom, and the balancing electron current were assumed to deposit at the uppermost point on the sidewall, then the potential drop across the feature surface as a function of the aspect ratio and surface conductivity would follow the behavior shown in Figure 3.7. Figure 3.7 clearly shows that potential gradients of the order found in this study could only be sustained if the surface conductance were lower than 5×10^{-14} Siemens (surface resistivity greater than 2×10^{13} ohm). While this is within the reported range for some microelectronic materials, it is not altogether clear that this resistivity could be maintained in the charge- and photon-rich plasma environment.

The ultimate conclusions of this study were mixed. It appears that surface charging of this type may be important in situations where the aspect ratio is high and the sidewall materials are very strong insulators. On the other hand, the material property requirements are quite strict and it is not possible to state with certainty that real materials would exhibit the necessary characteristics in an etching plasma. Direct experimental evidence for charging of this type is weak [Gottscho, *et al.*, 1992], suggesting that the effects are not widespread.

One conclusion that was reached with certainty was that surface charging is a very difficult numerical problem, and would greatly increase the computational cost of profile simulation. Not only is the charging effect non-linear, as discussed earlier,

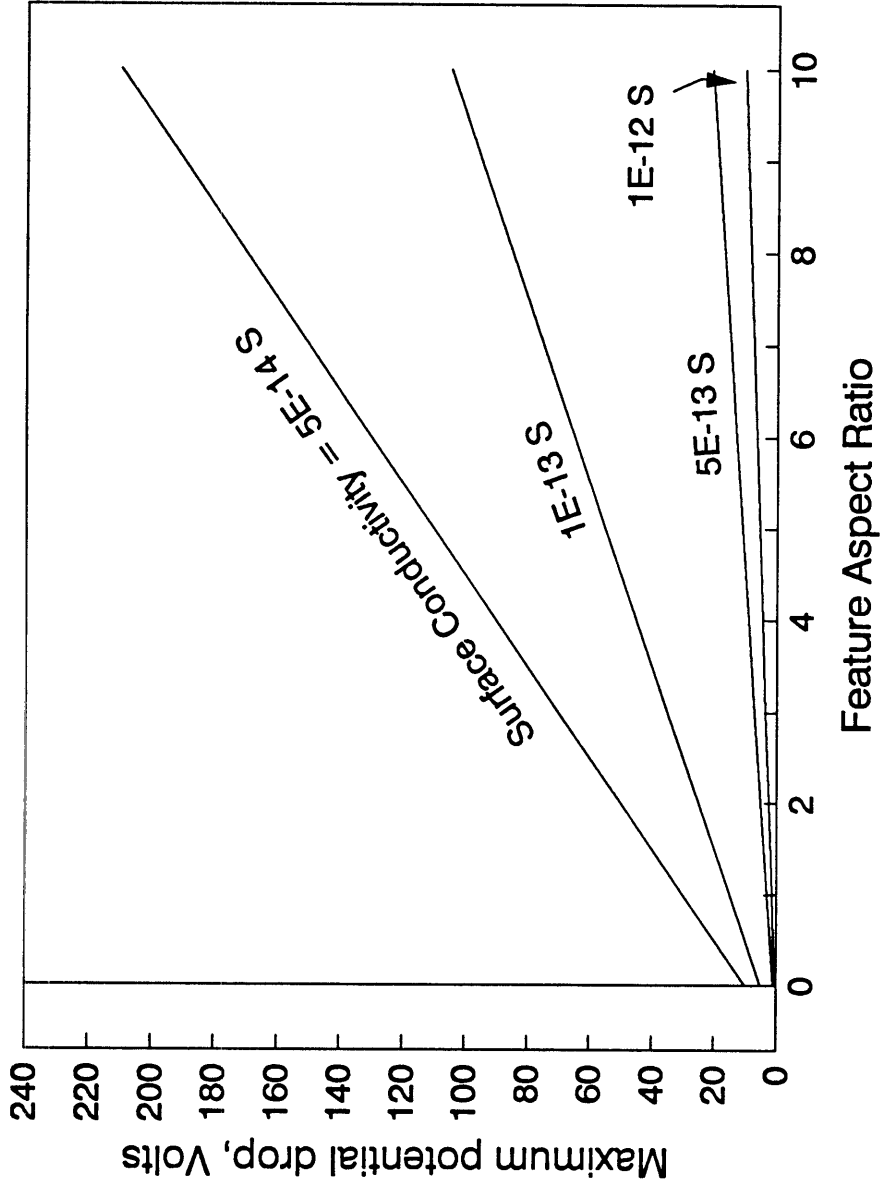


Figure 3.7: Maximum potential difference along surface for simplified conductance model, as a function of feature aspect ratio and surface conductivity in Siemens (Amps/Volt).

but it introduces what are termed "medium" interactions. Particle motion at the low pressures used in etching processes is typically taken to be ballistic: particles travel in straight lines between surfaces, with no changes in direction or energy while passing through the vacuum phase (the "medium"). Surface charging, on the other hand, introduces electric field effects on the particle trajectory, which in turn complicate the computation of fluxes along the feature surface. The high cost was not justified for such an obscure process mechanism, and surface charging was dropped from consideration after this initial exploration.

Chapter 4

Reactant Transport

4.1 Introduction and Mechanisms

The ongoing trend toward higher device density and the use of trench capacitors in modern semiconductor memories have focused increased attention on the plasma etching of features with high aspect ratios. The aspect ratio is defined as the ratio of depth to width for a trench (or depth/diameter for a circular hole), and has been shown to be the most important geometric parameter for plasma etching of small features. High aspect ratio features are particularly susceptible to the "RIE lag" (or "Aspect Ratio Dependent Etching" [Gottscho, *et al.*, 1992]) effect, wherein the etching rate is lower at the bottom of narrower features.

RIE lag has frequently been attributed to dispersion of ions in the plasma sheath and "shadowing" of the ion flux to the feature bottom by the mask [Pilz, *et al.*, 1989] [Jurgensen and Shaqfeh, 1989] [Ulacia F., *et al.*, 1988]. However, the principal effect of ion bombardment is to accelerate the reaction of gaseous species (typically halogens) with the surface [Coburn and Winters, 1979] [Coburn, 1982]. Therefore, it is reasonable to expect the transport of reactants to have some effect on the etching of high aspect ratio features.

Coburn and Winters [1989] introduced the topic of reactant transport in 1989, but were limited to a very simple model by the available data on ion transport and surface reaction kinetics. The time since their publication has seen much progress in these areas. It is now possible, for certain etching systems, to perform a quantitative examination of reactant transport in deep trenches and its influence on the etching rate.

The following sections explain the formulation of a model for the etching rate in deep trenches and explore the relative importance of reactant and ion transport under practical processing conditions.

The motion of neutral reactants into surface features during reactive ion etching is generally assumed to occur by one of two mechanisms. The first is surface diffusion, wherein species arriving from the plasma are adsorbed on the upper sidewalls and subsequently diffuse along the walls to the bottom. This mechanism has been proposed as a cause of microtrench formation during trench etching with chlorine [Sato and Arita, 1987]. However, recent experiments suggest that surface diffusion is insufficient to sustain etching in deep trenches [Singh, *et al.*, 1992], and surface diffusion will not be considered further.

The second and apparently dominant transport mechanism is Knudsen diffusion within the feature. Neutral species from the plasma strike and diffusely scatter from or adsorb upon exposed surfaces, including the upper sidewalls. The

scattered species and a portion of the adsorbates are re-emitted and travel across the feature to the other sidewall. The gas pressure under typical conditions is low enough that the mean free path is much larger than the feature dimensions and transport between surfaces is collisionless; the particles do not experience a significant number of gas-phase collisions while traversing the feature [Coburn and Winters, 1989]. Furthermore, the angular profiles for diffuse scattering and thermal emission follow the "cosine law," wherein the emission probability varies as the cosine of the angle from the surface normal. Therefore, a substantial fraction of the emitted species travel deeper into the feature. The cycle of scattering and/or adsorption/desorption is repeated until the particle either reacts with the feature wall or escapes back into the plasma.

The effect of Knudsen diffusion on reactant flux to the bottom depends upon the rate of reaction within the feature. If the reaction probability approaches zero, the density of reactants striking each surface becomes constant (independent of position within the feature or feature depth). The flux of reactants at the feature bottom decreases as the reactant loss rate within the feature increases. This flux decrease is caused by both the reaction on the sidewalls and the limited conductance of a high aspect ratio trench [Coburn and Winters, 1989].

4.2 Transport Model and Numerical Methods

Models for Knudsen diffusion in surface features have been presented in the

past [Singh, *et al.*, 1992]. The first step is discretization of the surface into short line segments and determination of the "visibility graph." The visibility graph describes which segments may interchange material directly; if the view from the i th segment to the j th segment is blocked by another part of the surface, then none of the material emitted from i may reach j unless it first lands upon a mutually visible segment k (or series of segments k_n).

The published models appear to follow Gebhart's method for diffuse gray radiative heat transfer [Gebhart, 1971], which accounts for both direct ($i \rightarrow j$) and indirect ($i \rightarrow k_1 \dots k_n \rightarrow j$) material exchange through a matrix of "Absorption Factors." Formulation and inversion of this matrix yields the "re-emission source strengths [Singh, *et al.*, 1992]", or reactant fluxes, for each surface segment.

This work utilizes an iterative but more intuitive method. The first iteration comprises computation of the direct flux from the plasma to each segment. The material arriving at each segment is divided into two components, one that is retained and one that is scattered or re-emitted. The re-emitted fraction is distributed over the visible segments, where it is again divided into retained and re-emitted portions. The process is repeated until all of the material has either been retained on feature surfaces or escaped to the plasma.

Each iteration comprises three steps:

1) Computation of the arriving flux at each segment

$$\begin{aligned} (a_i Q_i)^{(1)} &= \text{flux from plasma (first iteration)} \\ (a_i Q_i)^{(n)} &= \sum_j F_{ij} \epsilon_j^{(n)} \quad (\text{other iterations, } n > 1) \end{aligned} \tag{4.1}$$

where Q_i is the flux impinging upon the segment (typically atoms or moles per $\text{cm}^2 \text{ s}$), and a_i is the segment area. $\epsilon_j^{(n)}$ is the amount of material emitted from j in the current iteration (n) and F_{ij} is the direct interchange factor from the j th to the i th segment (the fraction of $\epsilon_j^{(n)}$ which impinges directly upon the i th segment). The flux from the plasma is assumed to be isotropic at the feature opening.

2) Addition of a portion of $a_i Q_i$ to the material already adsorbed on segment i during the previous iterations (1 through $n-1$):

$$\begin{aligned} S_i^{(1)} &= \gamma_i (a_i Q_i)^{(1)} \\ S_i^{(n)} &= S_i^{(n-1)} + \gamma_i (a_i Q_i)^{(n)} \end{aligned} \tag{4.2}$$

where S_i is the amount of adsorbed material on segment i and γ_i is the local sticking coefficient.

3) Calculation of the amount of material to be emitted in the next iteration:

$$\epsilon_i^{(n+1)} = (1 - \gamma_i) (a_i Q_i)^{(n)} \quad (4.3)$$

This process is repeated until the total material emitted from all segments drops below a pre-defined tolerance:

$$\sum_i \epsilon_i^{(N+1)} < \text{tolerance} \quad (4.4)$$

after the final iteration N.

After the last iteration, the total flux which struck each segment is calculated from the total adsorption and the sticking coefficient:

$$Q_i = \frac{S_i^{(N)}}{a_i \gamma_i} . \quad (4.5)$$

The only input to this model, other than feature geometry, is the set of sticking coefficients γ_i . The sticking coefficient need not be constant throughout the feature, and includes all of the loss terms for the species in question. The sole

mechanisms for reactant consumption within a feature are reaction and recombination. A simple mass balance shows that γ_i is identical to the sum of the reaction and recombination probabilities.

The numerical implementation of the foregoing algorithm for this project was straightforward. The first step was computation of the interchange factors F_{ij} for the current surface profile. Appendix C contains derivations of the interchange factors for rectangular trench geometry. Once the interchange factors were stored and the sticking coefficients determined from the particular kinetic model, the reactant transport was computed by the iterative scheme mentioned above. The tolerance was typically held to 0.1% or so, and convergence achieved within a few dozen iterations.

The method described above was initially adopted because it mimicked reality and was easy to test for accuracy. However, it also turned out to be more computationally efficient for the combination of chemistry, resolution, and computer hardware used in this study. The number of iterations required to reach the defined tolerance depended upon the feature geometry and the sticking coefficients. Obviously, more iterations were required with low sticking coefficients and when the visibility between feature surfaces was high.

The direct approach, in contrast, would require only three logical steps to achieve an "exact" answer. These steps were: 1) construct a matrix relating the emission terms for each segment to each other, 2) invert that matrix, and 3) back-

substitute to obtain the answers, accurate to within the precision of the machine. This method was evaluated for some typical etching conditions and found to be more expensive, for three principal reasons: the required accuracy is relatively low, reaction probabilities are relatively high, and the visibility between feature segments is frequently limited. For a feature consisting of N segments, the direct method would require on the order of N^3 operations. The iterative method required approximately $n^2 \cdot I$ operations, where n is not the total number of segments but the total number which interact with one or more other segments, and I is the number of iterations to acceptable convergence. The number of interacting segments n is clearly less than N (because the initial profile always includes a few segments along the flat upper surface), and I was typically between 25 and 100 for reasonable reaction probabilities and tolerances. A reasonable representation of the surface requires N to be several hundred (particularly when the surface includes microtrenches or other fine structures), so I is typically much less than N and $n^2 \cdot I$ is less than N^3 .

Consideration of a different chemical system or use of a computer with vector capability (which can provide a great increase in speed for linear algebra) may alter the balance between direct and iterative methods. A modification of the direct method will be discussed in a subsequent section of this chapter. However, all results presented here were obtained iteratively.

4.3 Application: Fluorine Etching of Deep Trenches in Silicon

The principal input to the reactant transport model is the surface reaction probability. This is best obtained from a model relating the etching rate to the local reactant (and ion) flux conditions. The only such model available at the time of this work was the fluorine/silicon etching study presented in D. C. Gray's thesis [Gray, 1992] and in a journal publication with other members of this group [Gray, Teppermeister and Sawin, 1993]. Gray's kinetic model was used to test the transport code and to study the effect of reactant transport on etching of deep trenches.

4.3.1 Surface Reaction

Reactive ion etching has long been understood to involve several different chemical and physical pathways for conversion of solid surface material to volatile products [Winters and Coburn, 1985]. However, attempts to create numerical models of the overall etching process have been hampered by poor understanding of the chemical reaction networks, kinetic rate parameters, and interactions between the various etching mechanisms. Harper, *et al.* [1981], proposed (and Gray followed) the decomposition of the etching rate into the sum of three components:

$$ER_{\text{total}} = ER_{\text{thermal}} + ER_{\text{physical}} + ER_{\text{ion enhanced}} \quad (4.6)$$

The first component, ER_{thermal} , refers to the spontaneous etching of silicon by fluorine atoms in the absence of ion bombardment. ER_{physical} comprises the physical sputtering of surface atoms by energetic ions alone. The third and final term, ER_{ion}

enhanced, accounts for the greatly enhanced etching observed during simultaneous reactant and ion exposure.

Gray, *et al.* [1993], utilized such an approach to obtain a self-consistent model for the etching of silicon by fluorine over a wide range of conditions. The thermal and physical etching rates are assumed to retain (approximately) their baseline values, and the ion-enhanced component is adjusted to yield the correct total rate. Self-consistency is achieved by incorporating surface fluorination effects in a reactive site model.

The thermal reaction rate was taken from the data of Flamm, *et al.* [1981], as

$$ER_{\text{thermal}} = k_0 Q_F \exp\left(\frac{-E_a}{k_b T}\right), \quad (4.7)$$

where Q_F is the incident flux of fluorine atoms on the surface, E_a is the activation energy (reported as 0.108 eV), and k_0 is a constant. Conversion of Flamm's data to the incident flux basis used in Equation (4.7) yielded a value for k_0 of 0.03. The thermal etching rate given here has the units of incident fluorine flux, typically ($\text{atoms cm}^{-2} \text{ s}^{-1}$).

Ion enhanced etching has been conjectured to proceed by a number of different chemical mechanisms with etch products of varying stoichiometry. Gray, *et*

al. [1993], concentrated on two primary products: fully fluorinated (SiF_4), and partially fluorinated or unsaturated products (including SiF , SiF_2 and SiF_3). They used XPS (X-ray Photoelectron Spectroscopy) to analyze the product distributions under various conditions, and found that the average stoichiometry of the unsaturated products could be well represented by assuming SiF_2 as the dominant component. This is consistent with earlier studies [Tu, *et al.*, 1980]. They next defined the number ratio of unsaturated to saturated products as the "branching parameter," and used this figure to account for all unsaturated product generation. The branching parameter was found to depend primarily upon ion energy.

Gray, *et al.* [1993], also observed the ion-enhanced etching rate to depend not only upon ion flux, but also upon the fluorination state of the surface. In the presence of an incident fluorine flux, a partially fluorinated layer forms on the surface [Chuang, 1980] [McFeely, *et al.*, 1984], and the yield of silicon removed per incident ion increases in proportion to the fractional surface coverage. $\text{ER}_{\text{ion enhanced}}$ is thus the product of four terms:

$$\text{ER}_{\text{ion enhanced}} = \beta_2 (1 + b) C_F I \quad (4.8)$$

β_2 is the yield of saturated product (SiF_4) per incident ion, b is the branching parameter described above, C_F is the fractional surface fluorination (coverage), and

I is the incident ion flux. The variation of β_2 and b with ion energy were reported as

$$\beta_2 = 0.687(\sqrt{E, \text{eV}} - 2) \quad (4.9)$$

and

$$b = 0.009\sqrt{E, \text{eV}} . \quad (4.10)$$

The fractional surface fluorination was reported to follow

$$C_F = \frac{0.2 R}{0.2 R + 2\beta_2(1 + b)} \quad (4.11)$$

where

$$R \equiv \frac{Q_f}{I} . \quad (4.12)$$

Gray, *et al.* [1993], used independent ion and radical beams to explore the etching behavior over a wide range of flux ratios (from zero to several thousand). However, atomic fluorine concentration measurements by Kiss and Sawin [1992] and d'Agostino, *et al.*, [1981] suggest that practical values for R range from a few hundred

to a few thousand.

The etching yield and branching parameter are expected to vary somewhat with ion incidence angle [Mayer, *et al.*, 1981]. However, the details of this variation were not available and the angular dependence were neglected.

The final etching component, ER_{physical} , was taken as

$$ER_{\text{physical}} = p_0 I (1 - C_F) \quad (4.13)$$

where p_0 is the yield of silicon atoms per incident ion, I is the incident ion flux, and the term $(1 - C_F)$ is added to account for depression of physical sputtering by surface fluorination. Only bare (unfluorinated) surface silicon atoms are available for conversion directly to volatile Si, so increasing fluorination of the surface is expected to block the physical sputtering pathway. For this work, p_0 was assumed to follow the energy dependence given by Gray [1992]

$$p_0 = 0.0337(\sqrt{E, \text{eV}} - \sqrt{20}) \quad (4.14)$$

and the angular dependence reported by Catana, *et al.* [1972],

$$\frac{P_0(\theta_t)}{P_0(0)} = 3.2696 \cos \theta_t + 13.1059 \cos^2 \theta_t - 15.3755 \cos^4 \theta_t, \quad (4.15)$$

where θ_t refers to the angle of incidence from the local surface normal.

Equations (4.7) - (4.15) provided the means to calculate the total etching rate at any point on the surface as a function of the local ion and fluorine fluxes, the ion energy, and the surface temperature. The ion and reactant flux models are described below.

4.3.2 Ion Flux

The transport of energetic ions into surface features has been shown in previous Chapters to involve several phenomena, including ion dispersion in the plasma sheath, reflection or scattering from inclined surfaces, and charge accumulation on insulating surface materials. In this case, all surfaces are assumed to be silicon of moderate conductivity so charging effects may be neglected. This leaves ion dispersion and reflection as the important processes affecting the ion flux within surface features.

Ion dispersion has been discussed extensively by others [Thompson, *et al.*,

1988] [Liu, *et al.*, 1990], and there is a general consensus that the degree of angular dispersion depends in a complex fashion upon the gas composition and pressure, the discharge frequency, and the discharge power. In this work, the Ion Angular Distribution (IAD) is assumed to be of the following simple form:

$$\frac{dI(\theta_g)}{dA} = c \exp\left(\frac{-\theta_g^2}{2\sigma^2}\right) \quad (4.16)$$

where $dA = \sin\theta \, d\theta \, d\phi$ for the spherical coordinate system, c is a normalizing constant, θ_g is the angle from the macroscopic wafer surface normal, and σ is termed the "standard deviation" of the IAD. The variation of Equation (4.16) with θ_g and σ and comparison to the reported IAD's of Liu, *et al.* [1990], are shown in Figure 4.1.

The reflection of ions from feature surfaces has been described by Wilson, *et al.* [1984], as a function of incidence angle. They proposed that the range of incidence angles θ_s from 0 (normal) to $\pi/2$ (glancing) may be divided into three regimes. In the first regime, bounded by 0 and an angle $\hat{\theta}$ ($0 \leq \theta_s \leq \hat{\theta}$), all incident ions embed in or adsorb upon the surface and there is no reflection. In the intermediate regime, including angles between $\hat{\theta}$ and θ_R ($\hat{\theta} \leq \theta_s \leq \theta_R$), the reflection probability increases linearly from 0 to 1. For angles in the final regime, where $\theta_R \leq \theta_s \leq \pi/2$, the reflection probability is 1 and all incident ions are reflected. The values of $\hat{\theta}$ and θ_R are not generally known, but may be estimated

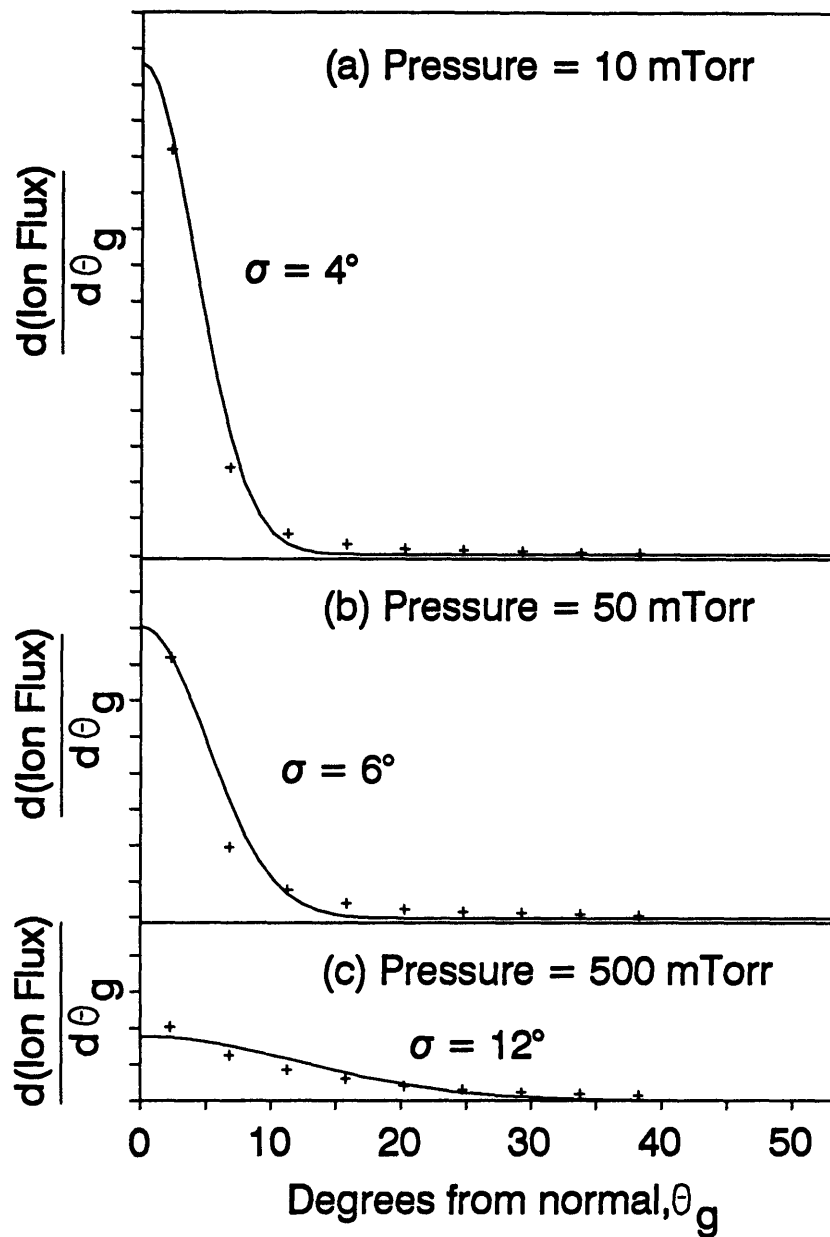


Figure 4.1: Ion Angular Distributions from Liu, *et al.* , [1990]

from physical sputtering yields. For silicon, these angles have been roughly estimated [Dalton, *et al.*, 1993] as $\hat{\theta} = 60^\circ$ and $\theta_R = 90^\circ$.

The influence of ion dispersion and reflection upon ion fluxes within surface features has been discussed elsewhere [Dalton, *et al.*, 1993]. However, there is one issue which warrants further discussion here: the number of reflections experienced by each ion. As shown in Figure 4.2, it is possible for an ion reflected from one sidewall to subsequently experience a glancing collision with the other wall if the ion has a high out-of-plane angle or if the feature aspect ratio (depth/width, abbreviated "AR") is high. The number of multiply-reflected ions could be significant in very deep trenches.

Figures 4.3 and 4.4 illustrate the effect of multiple sidewall reflections upon the ion flux to the bottom of rectangular trenches for several representative IAD's and feature aspect ratios. The horizontal axis in each figure is the position along the feature surface, including the bottom and a small portion of each sidewall. The vertical axis shows the ratio of the local ion flux to that which would land on a flat surface. The parameter NR refers to the number of reflections included in computing the ion flux to the trench bottom. The first case, NR = 0, computes only the direct ion flux from the plasma. The profile labeled NR = 1 adds the ions undergoing one reflection; NR = 2 also includes doubly-reflected ions, and so on.

It is apparent that the total flux is dominated by those ions arriving directly

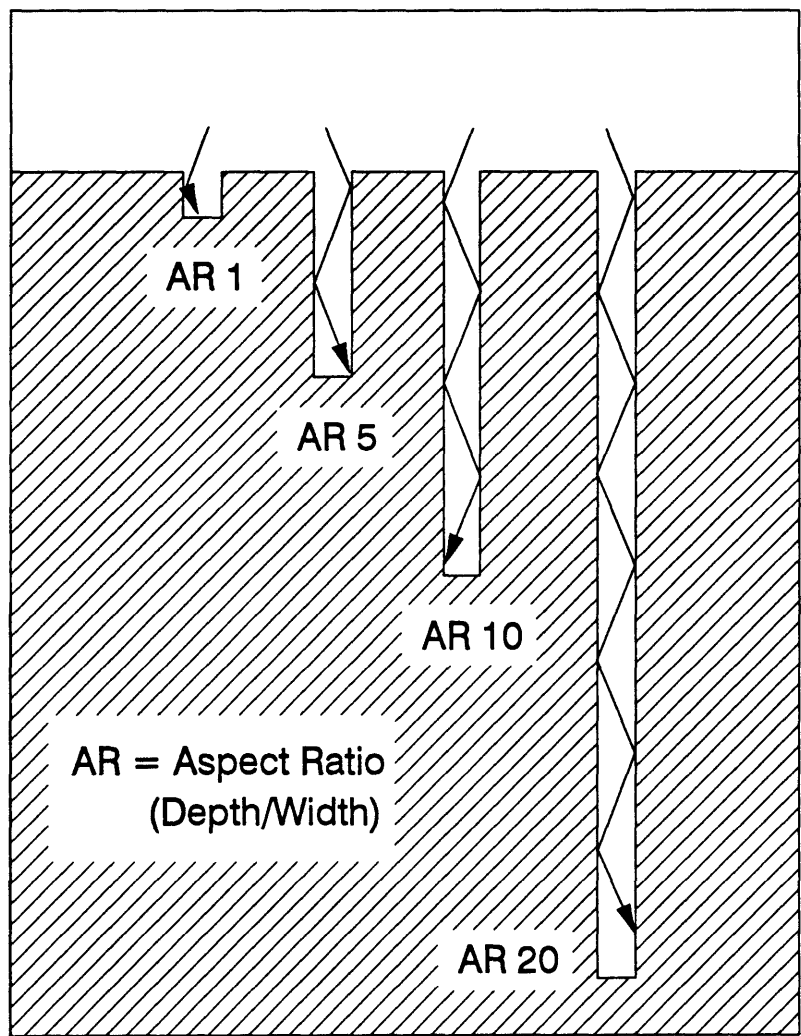


Figure 4.2: Illustration of multiple ion reflection in rectangular trenches of varying aspect ratio (depth/width).

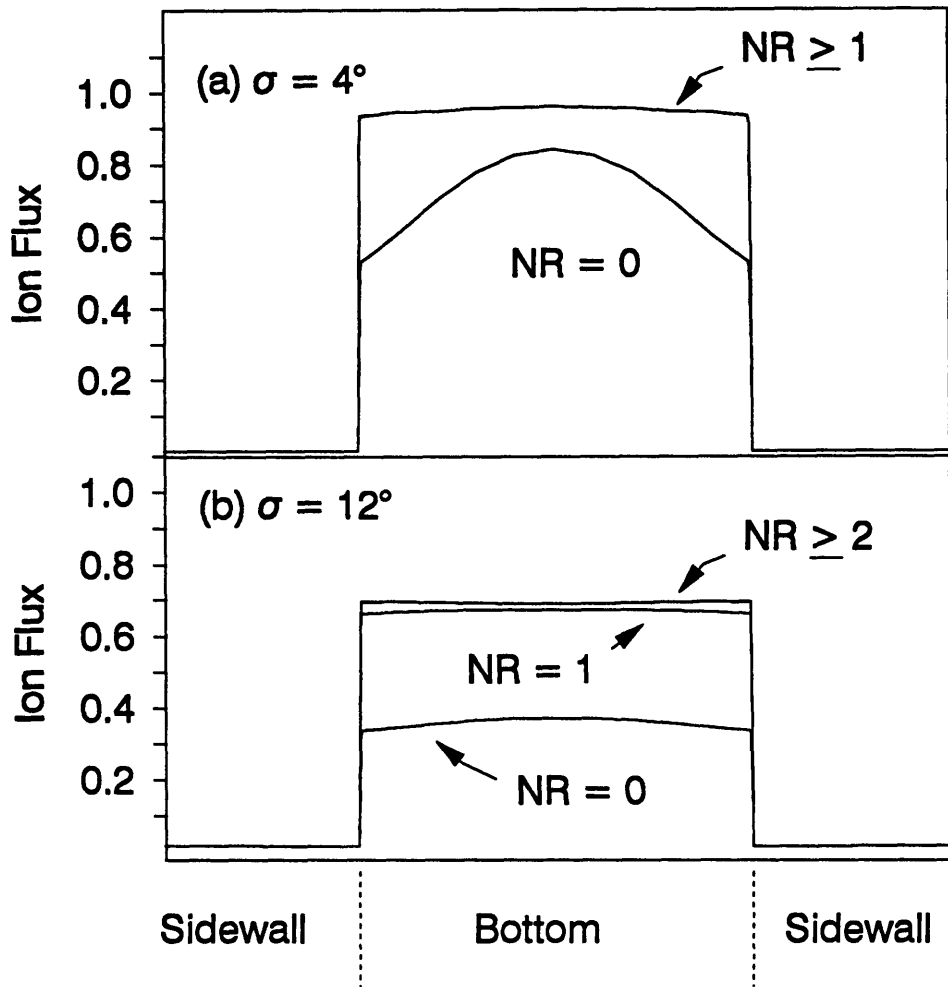


Figure 4.3: Profile of ion flux to the bottom of a trench with aspect ratio 5. σ is the IAD standard deviation, and NR is the number of reflections considered.

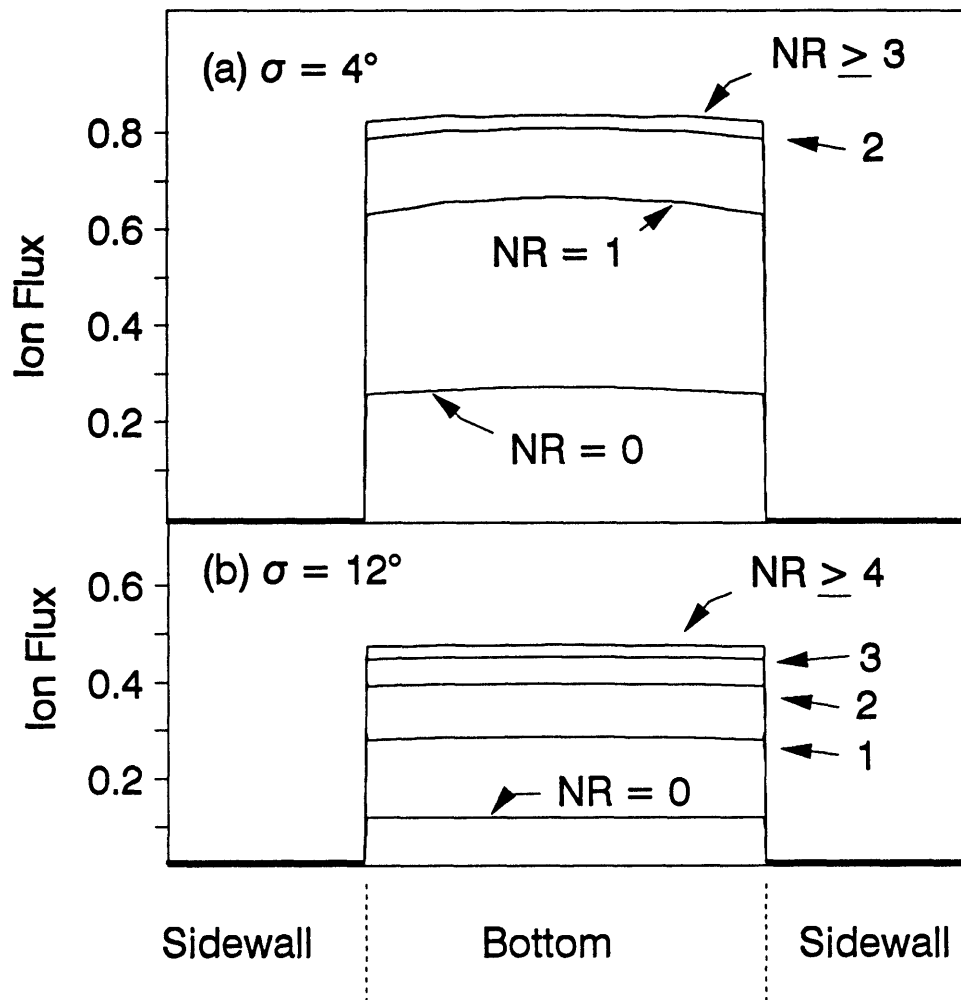


Figure 4.4: Profile of ion flux to the bottom of a trench with aspect ratio 20. σ is the IAD standard deviation, and NR is the number of reflections considered.

from the plasma and those experiencing only one reflection during transit. The importance of singly-reflected ions is apparent in Figure 4.3a, where the addition of reflected ions not only increases the total flux but also dramatically improves the flux uniformity. The smoothing effect of singly-reflected ions offsets the shadowing of direct flux, and suggests that reflected ions are important in deep trench etching processes. At high aspect ratios, the direct ion flux is fairly uniform (Figure 4.4). However, the number of reflected ions is high enough that the reflected flux is higher than the direct flux to the feature bottom.

The importance of ion reflections is quantified in Figure 4.5, which shows the error which would be incurred by truncating the ion flux calculation after a given number of reflections. For example, in Figure 4.5a, the curve for AR (aspect ratio) 20 shows $\text{Error} \approx 0.68$ at $\text{NR} = 0$. This indicates that considering only the direct flux to the bottom would underestimate the total flux by nearly 70%. The error drops quickly as the number of reflections increases, so that a model accounting for three or four collisions would be sufficient for highly accurate values of the total ion flux.

For computation of the etching rate, however, it is only necessary to consider multiply-reflected ions if they contribute to etching. The contribution of an ion to etching is determined by its energy. It seems unlikely that ion-sidewall collisions are perfectly elastic, so the ion must lose some of its energy during reflection. After a certain number of collisions, the energy will drop below the threshold for etching enhancement. While there is a general belief that an ion may retain sufficient energy

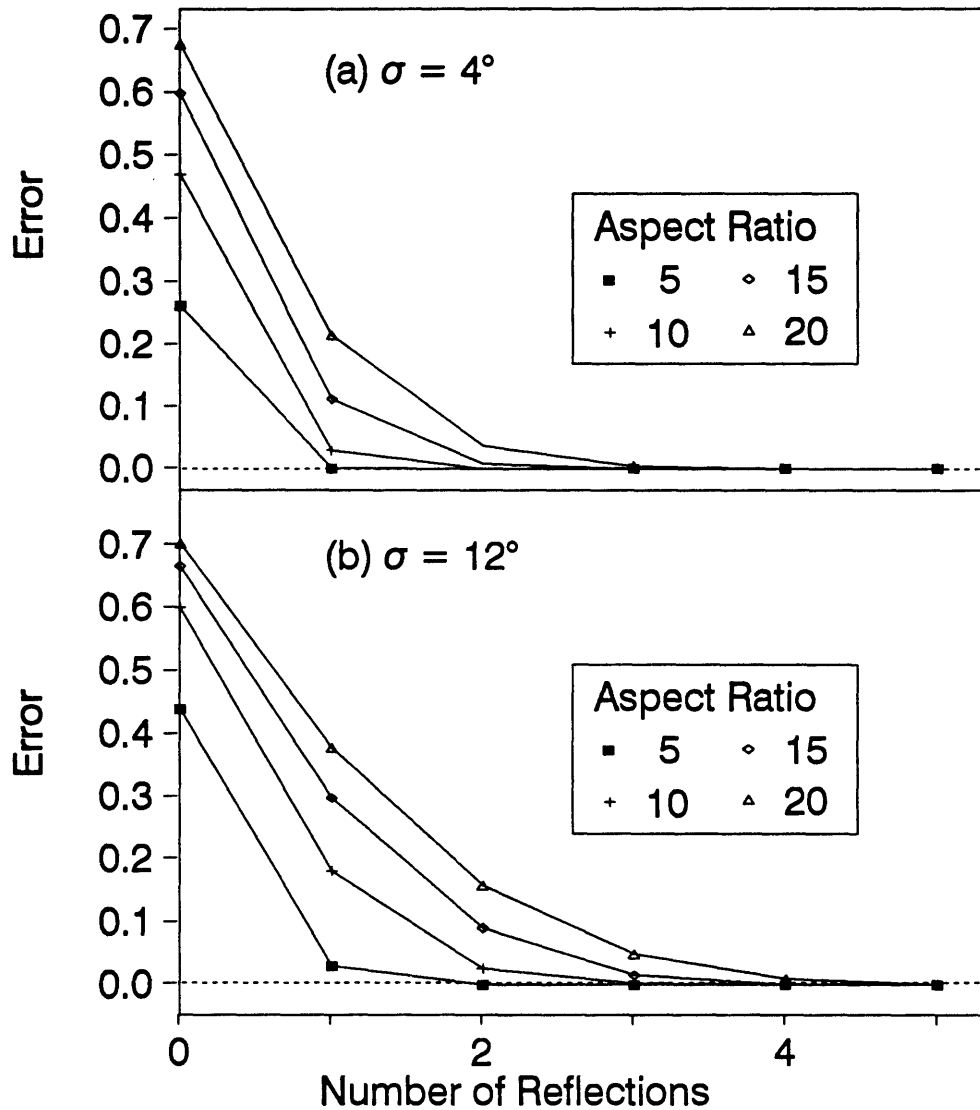


Figure 4.5: Comparison of error in computed ion flux to the number of reflections considered for different IAD's and Aspect Ratios.

to enhance the etching rate after the first glancing sidewall collision, the energy loss during reflection is not understood well enough to accurately predict the maximum number of reflections. In addition, the partial loss of ion energy and microscopic roughness of the surface would both tend to make the scattering more diffuse, further reducing the flux of energetic ions to the feature bottom. Therefore, this work has been limited to a "single-bounce" model, wherein ion trajectories are tracked only up to the second collision. After the second glancing collision, the ion is assumed to have lost most of its energy and to have no influence on the etching of any further surfaces it strikes. Furthermore, an ion reflected from a given surface is assumed to have no effect upon etching of that surface.

4.3.3 Reactant flux

Once the surface reaction kinetics and ion flux have been defined, computation of the reactant flux within the feature requires determination of the local sticking coefficients. As was mentioned earlier, γ_i is identical to the fluorine reaction probability, which is proportional to the local etching rate. The reaction probability and sticking coefficient γ_i may be found as the sum of thermal and ion-enhanced components γ_t and γ_{ie} .

The thermal reaction component γ_t is constant throughout the feature, and given by the data of Flamm, *et al.* [1981], as

$$\gamma_t = 4 \frac{ER_{\text{thermal}}}{Q_F} = 0.12 \exp\left(\frac{-E_a}{k_b T}\right). \quad (4.17)$$

The specific value of γ_t depends upon temperature, but ranges from 6×10^{-5} at -100° C to 4×10^{-3} at 100° C. The total reaction rate and sticking coefficient on the feature sidewalls will be dominated by the thermal component, so a low sidewall sticking coefficient might lead one to expect reactant transport to be unimportant. However, Coburn and Winters [1989] have pointed out that reactant supply at the feature bottom may still be transport limited, even at zero sidewall reaction, if the hole is deep and the reaction probability at the bottom is large.

The reaction rate on the feature bottom or any other surface exposed to a high ion flux will be determined primarily by the ion-enhanced reaction component. As shown in Equations (4.8) to (4.12), the ion-enhanced etching rate depends upon the local ion and fluorine fluxes (as well as the ion energy), and can be expected to depend strongly upon the feature geometry. Gray, *et al.* [1993], reported values for what they termed the "sticking coefficient," but their definition is somewhat different from that used here. For this work, the ion-enhanced sticking coefficient is found

from the reaction probability for fluorine by

$$\gamma_{ic} \equiv \frac{R_{\text{ion enhanced}}}{Q_F} = \frac{4\beta_2 \left(1 + \frac{b}{2}\right) C_F I}{Q_F} \quad (4.18)$$

where $R_{\text{ion enhanced}}$ is defined as the rate of fluorine consumption and is not equal to $ER_{\text{ion enhanced}}$ (the rate of silicon liberation) because there are two reaction products ($\text{SiF}_{x=2}$ and SiF_4). On a flat surface, under typical conditions of ion energy and flux and fluorine partial pressure, Equation (4.18) yields ion-enhanced reaction probabilities on the order of 0.01 - 0.3 (Figure 4.6).

Within a surface feature, it is evident that Equations (4.2), (4.5), and (4.18) form a logical circle: Equations (4.2) and (4.5) relate Q_F to γ , and Equation (4.18) relates γ to Q_F (through C_F). Therefore, the computation of sticking coefficients and reaction rates must be iterative: a set of estimated sticking coefficients is used to solve the reactant transport problem for local fluorine fluxes, then the local reaction rates are used to compute new sticking coefficients. This process is repeated until the sticking coefficients become constant, typically within a few iterations. The final reaction model thus contains two layers of iteration: variation of the local sticking coefficients to reach self-consistency, and iteration of the surface emission for each set of sticking coefficients.

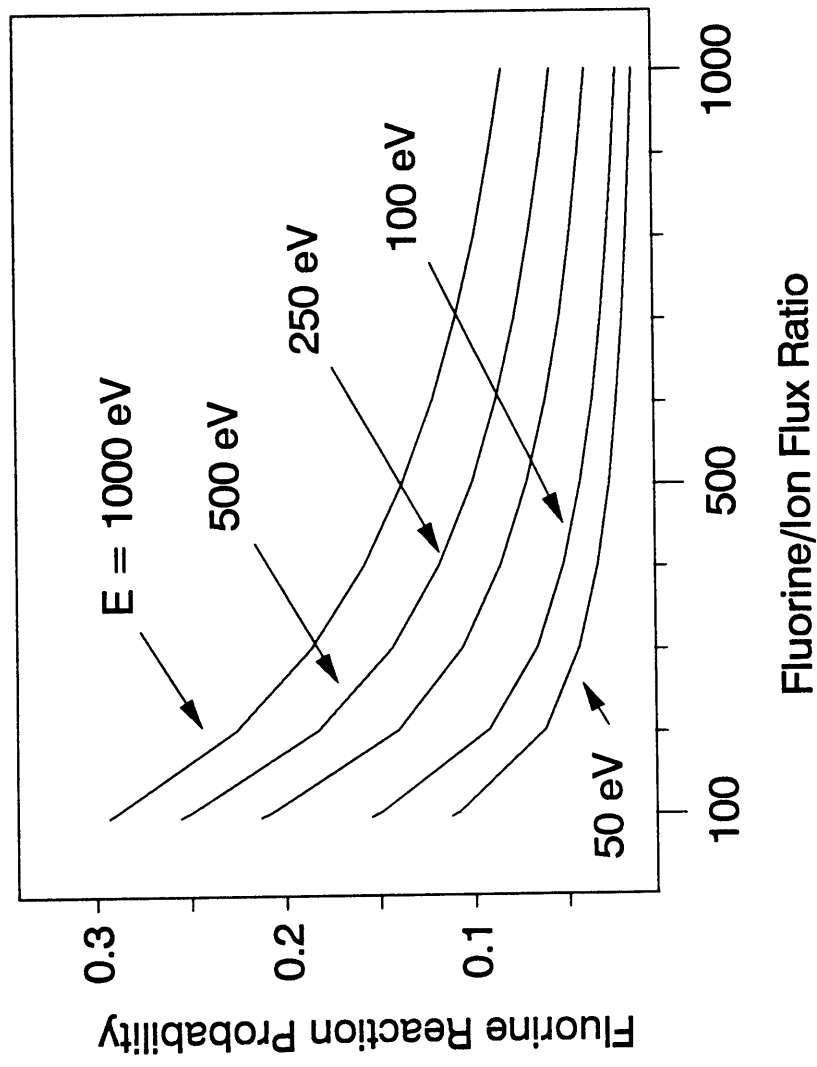


Figure 4.6: Fluorine reaction probability predicted by the model of Gray [1992].

4.3.4 Results

Coburn and Winters [1989] had previously examined the influence of reactant transport on reactive ion etching. They reported the diminution of reactant flux to the feature bottom with increasing aspect ratio. While their analysis provided an important introduction of this topic, they were forced to make several simplifying assumptions.

First, as they were careful to point out, the reaction probability under ion-enhanced etching conditions was "essentially unknown" at the time of publication, so they arbitrarily chose the range 0.1 - 1.0. As was shown in Figure 4.6, typical probabilities for fluorine etching of silicon are somewhat lower. Figure 4.7 shows that the effect of aspect ratio on reactant flux is much less pronounced at lower reaction probabilities.

Second, Coburn and Winters [1989] neglected the effect of aspect ratio on the ion flux to the feature bottom. It has since been shown that dispersion of ions in the plasma sheath leads to a reduction of ion flux at the feature bottom [Lee and Zhou, 1989], and that this effect worsens with increasing aspect ratio [Gottscho, *et al.*, 1992]. Figure 4.8 shows the effect of aspect ratio on ion flux, reactant flux, and total etching rate at the feature bottom for the following typical conditions: Ion Flux 1 mA/cm², Ion energy 100 eV, Fluorine atom partial pressure 3.1 mTorr ($Q_F/I \approx 250$), Substrate temperature 75° C, IAD standard deviation 4°.

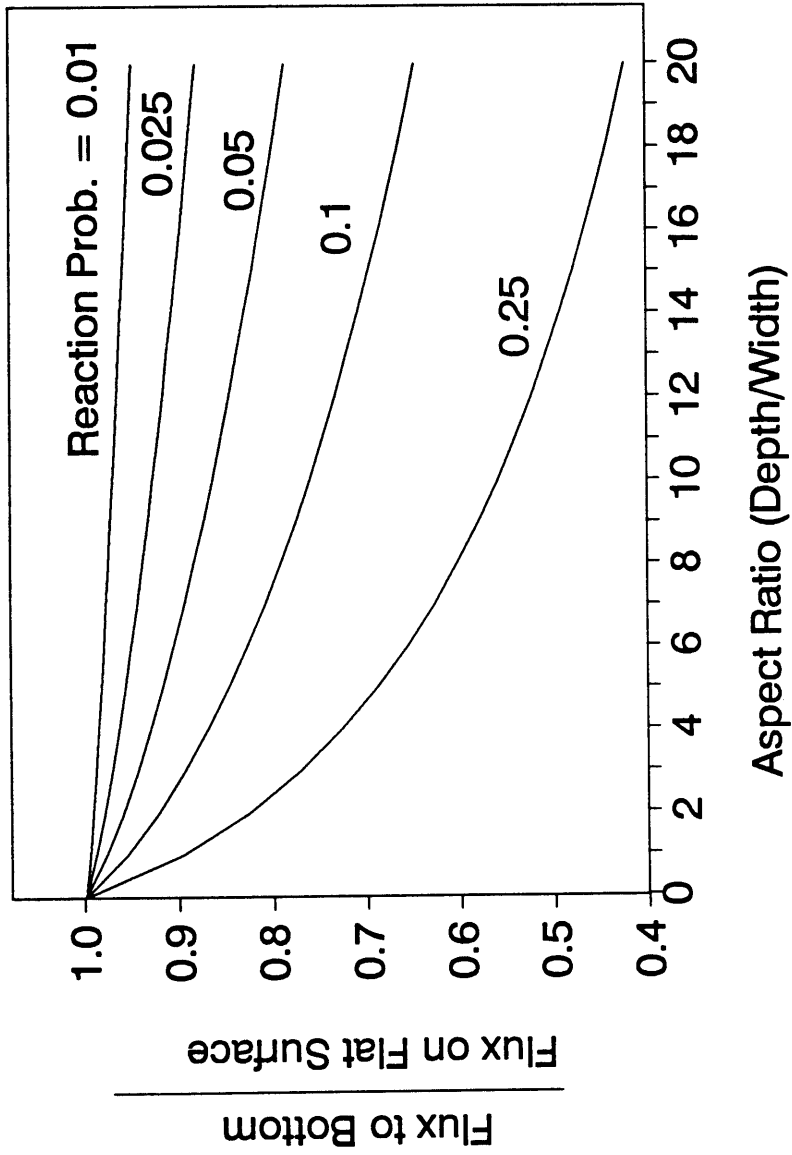


Figure 4.7: Effect of neutral transport to the bottom of a rectangular trench at reaction probabilities in the range reported by Gray [1992].

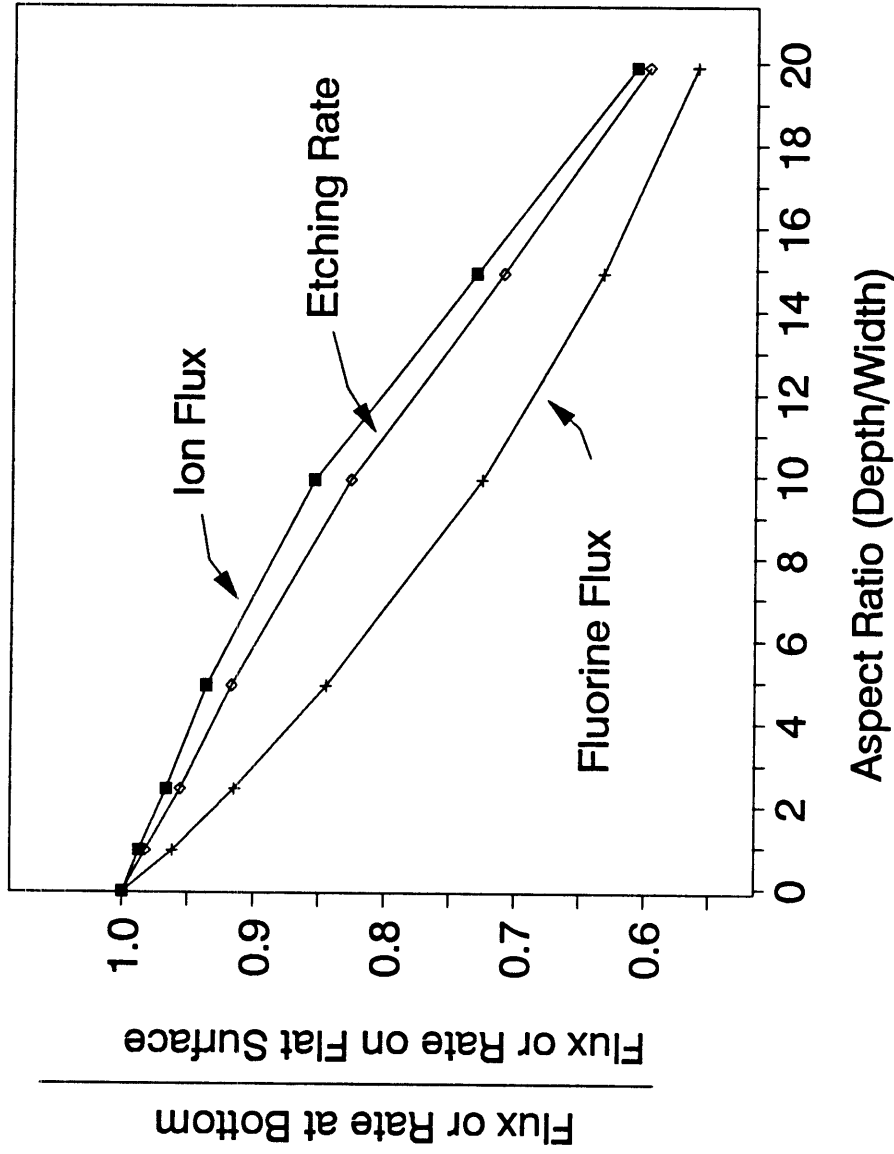


Figure 4.8: Effect of aspect ratio on fluorine flux, ion flux, and etching rate at the bottom of a rectangular trench.

Although the fluorine flux to the bottom decreases more rapidly than the ion flux at all of the aspect ratios shown, the etching rate closely follows the ion flux. This is because the etching rate under these conditions is dominated by the ion-enhanced component, which is nearly linear in ion flux but relatively insensitive to fluorine flux. The transport of fluorine into the feature has some effect (otherwise, the etching rate would decrease in exact proportion to the ion flux), but reactant transport appears does not appear to be important in this situation.

The curve of etching rate ER vs. aspect ratio AR in Figure 4.8 lies between the ion flux I and the reactant flux Q_F , with its greater similarity to the I curve indicating the greater relative influence of ion transport on the etching rate. While Figure 4.8 is instructive, characterizing the relative importance of reactant and ion transport by a single parameter would simplify comparisons to other process conditions. This suggests the definition of a "Reactant Transport Importance Parameter", or "RTIP", from the areas separating the curves of I, Q_F , and ER vs. AR:

$$RTIP \equiv \frac{\int_{AR=0}^{20} |(I - ER)| dAR}{\int_{AR=0}^{20} |(I - Q_F)| dAR} . \quad (4.19)$$

The RTIP varies from 0 (if the curve of ER vs. AR lies directly upon the curve of I) to 1 (if ER vs. AR coincides with Q_F). This definition was chosen primarily for

convenience, but it also indicates the total effect of reactant transport throughout an etching process (because the feature aspect ratio grows with etching time). A higher value of the RTIP indicates that the etching rate depends more strongly upon reactant flux.

The relative importance of reactant transport under conditions other than those shown in Figure 4.8 can be assessed by considering the aspect ratio dependence of the etching rate at the feature bottom:

$$\frac{dER}{dAR} = \left(\frac{\partial ER}{\partial Q_F} \frac{dQ_F}{dAR} \right) + \left(\frac{\partial ER}{\partial I} \frac{dI}{dAR} \right) \quad (4.20)$$

Reactant transport will be more important than ion transport when

$$\left| \frac{\partial ER}{\partial Q_F} \frac{dQ_F}{dAR} \right| > \left| \frac{\partial ER}{\partial I} \frac{dI}{dAR} \right| \quad (4.21)$$

and *vice versa*. Note that both Q_F and I decrease with increasing aspect ratio, so dQ_F/dAR and dI/dAR are negative. Neglecting the relatively small contribution of

physical sputtering, Equations (4.6) - (4.12) give:

$$\frac{\partial ER}{\partial Q_F} = k_0 \exp\left(\frac{-E_a}{kT}\right) + \beta_2(1 + b)I \frac{\partial C_F}{\partial Q_F}, \quad (4.22)$$

where

$$\frac{\partial C_F}{\partial Q_F} = \frac{1}{I} \left[\frac{0.2}{0.2R + 2\beta_2(1 + b)} - \frac{0.04R}{(0.2R + 2\beta_2(1 + b))^2} \right], \quad (4.23)$$

and

$$\frac{\partial ER}{\partial I} = \beta_2(1 + b) \left[\frac{0.2R}{0.2R + 2\beta_2(1 + b)} \right]^2. \quad (4.24)$$

These Equations provide a means to relate the relative importance of reactant transport to process conditions:

IAD - The Ion Angular Distribution has a strong effect on dI/dAR . As the ion dispersion decreases and the IAD becomes tighter, the magnitude of dI/dAR decreases. The influence of ion transport on etching rate decreases,

and reactant transport becomes more important. In the extreme limit of no ion dispersion, as modeled by Coburn and Winters [1989], dI/dAR would be equal to zero and the etching rate would be controlled entirely by reactant transport. Published studies of ion dispersion in plasma sheaths [Thompson, *et al.*, 1988] [Liu, *et al.*, 1990] [Ulacia F. and McVittie, 1989] indicate a lower practical limit for the parameter σ in Equation (4.16) of about 1.25° [Dalvie, *et al.*, 1992].

Temperature - Higher temperature increases the thermal reaction probability, with several effects on reactant transport. First, the thermal component of $\partial ER/\partial Q_F$ is increased. Second, higher consumption of fluorine through sidewall etching may contribute to depletion of the fluorine flux to the feature bottom. Finally, as Coburn and Winters⁷ pointed out, dQ_F/dAR is also controlled by the feature conductance. Increasing the thermal reaction probability at the feature bottom also depresses the local fluorine flux, so that the etching rate may not increase as rapidly as might be expected from the reaction probability. This effect is shown in Figure 4.9, where the ratio of feature bottom to flat surface etching rates decreases with temperature. Although the etching rate increases in both locations, increased reactant consumption within the feature causes the bottom etching rate to lag behind the flat-surface value. This effect is more dramatic at higher aspect ratio, higher ion energy, and lower fluorine/ion flux ratio.

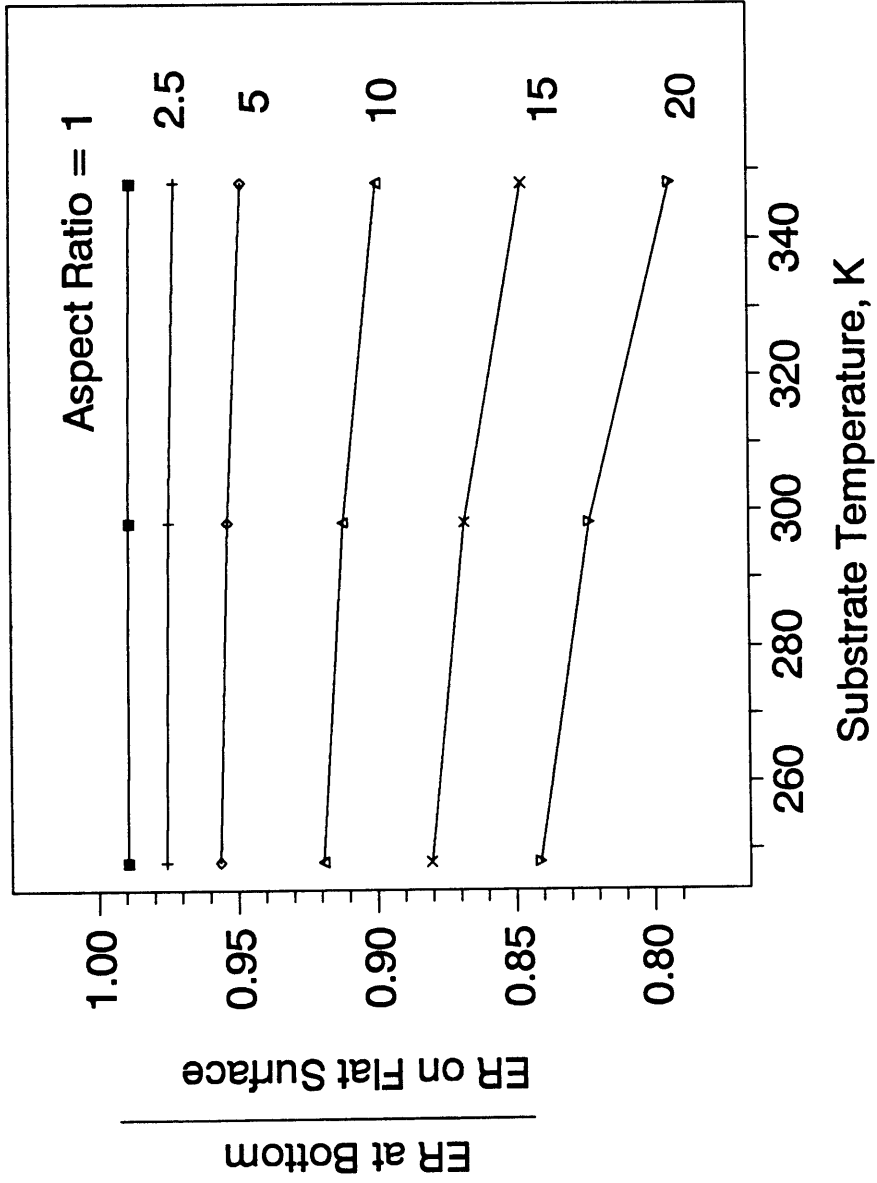


Figure 4.9: Effect of substrate temperature on bottom surface etching rates for trenches of varying aspect ratios.

The variation of RTIP with IAD and temperature is shown in Figure 4.10.

Flux Ratio - The balance between ion and reactant transport limitations is also dependent upon the flux ratio R (Q_F/I). As R decreases, C_F and $\partial ER/\partial I$ are reduced. There is a simultaneous enhancement of $\partial ER/\partial Q_F$, increasing the importance of reactant transport.

As Q_F nears zero, the thermal and ion-enhanced rates will drop and the total etching rate will be dominated by physical sputtering. This will clearly reduce the importance of reactant transport, but typical process conditions are not expected to give such low flux ratios ($R < 2$).

Ion Energy - The primary effect of increasing ion energy is to increase the ion-enhanced etching yield (Equations (4.9) and (4.10)). However, increasing the yield also decreases the fractional surface fluorination, which in turn enhances the influence of reactant flux. Figure 4.11 summarizes the variation of RTIP at typical values of Flux Ratio and Ion Energy.

These four parameters were chosen because they are the natural independent variables for etching rate calculations. Extension of the trends reported above to practical process inputs (such as power, pressure, etc.) is awkward. For example, increasing the pressure increases the ion flux [Allen, *et al.*, 1986], which would suggest an increase in the importance of reactant transport. On the other hand,

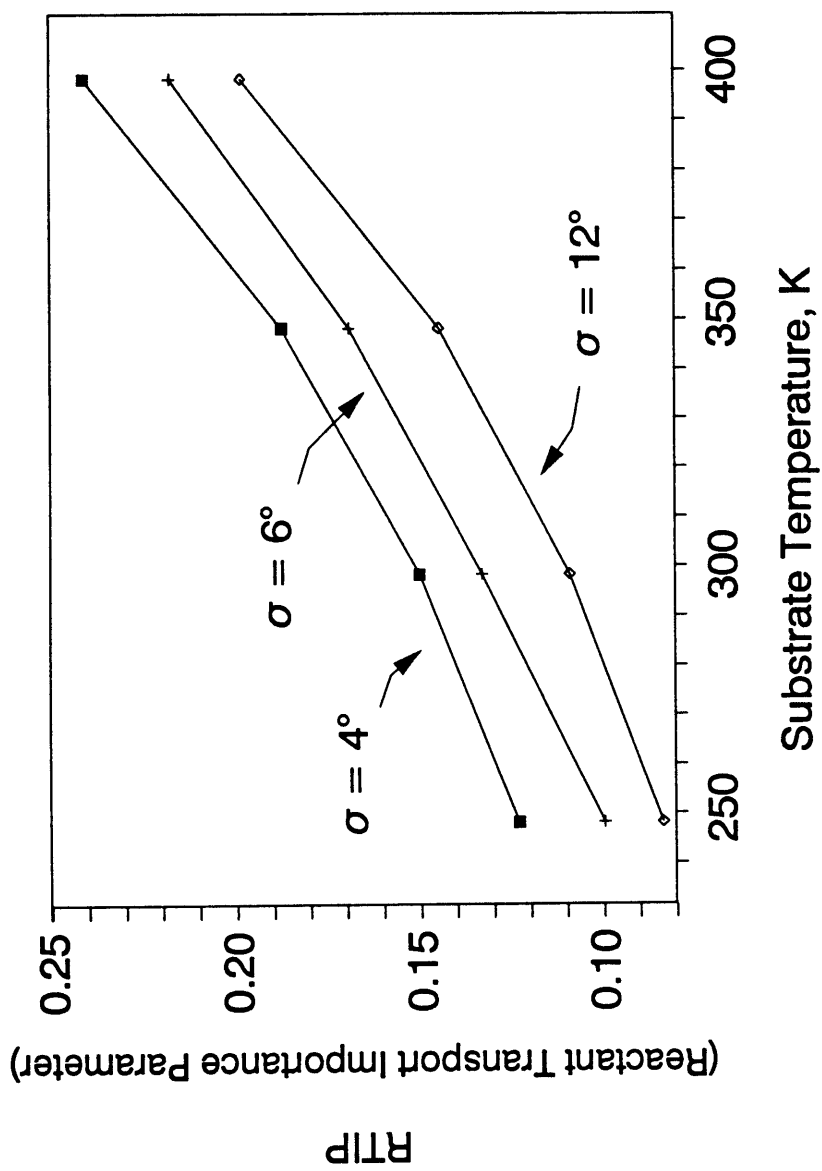


Figure 4.10: Effect of substrate temperature and IAD on the relative importance of reactant transport.

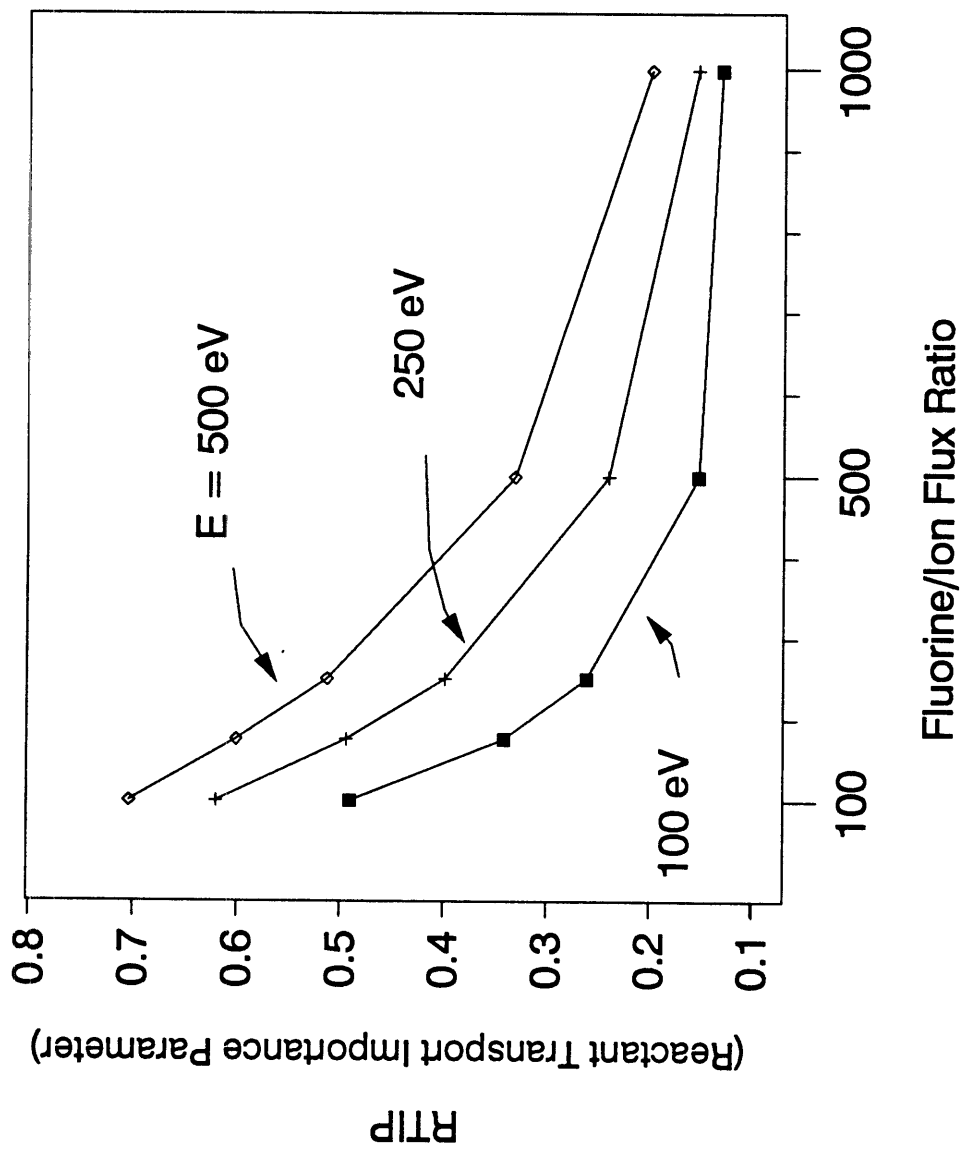


Figure 4.11: Effect of fluorine/ion flux ratio and ion energy on the relative importance of reactant transport.

increasing pressure also decreases the ion energy [Allen, *et al.*, 1986], increases the reactant flux [Ryan and Plumb, 1986] and broadens the IAD [Liu, *et al.*, 1990], all of which would tend to diminish the role of reactant supply in determining etching rate.

4.4 Combined Model for Reaction and Reactant Transport

One of the more interesting conclusions of the trench etching study was the fact that the sticking coefficients could not be specified in advance because the reaction probability depends to some extent upon the reactant flux. This problem was overcome by iterating the sticking coefficients through a successive substitution scheme: the reaction probabilities found at the end of the first iteration became the inputs for the second, and so on. However, this experience raised the question of whether it might be more efficient to use a standard iterating technique, such as Newton's method, to achieve more rapid convergence.

To this end, a Newton's method solution scheme was formulated for Gray's [1992] reaction model. The analysis begins by observing that, at steady state, the emission from each surface segment is related to the flux arriving at it by the sticking coefficient

$$e_i = (1 - \gamma_i) a_i Q_i , \quad (4.25)$$

and that the total flux arriving at a segment is formed from the sum of material leaving other segments and material arriving directly from the plasma

$$a_i Q_i = \sum_{j \neq i} F_{ij} \epsilon_j + a_i Q_i^{\text{direct}}, \quad (4.26)$$

where a , Q , γ , ϵ , and F_{ij} retain their previous definitions (from Section 4.2), and the meaning of Q^{direct} should be clear.

If the solution has not reached convergence (if Q and γ are not in balance throughout the feature), then a residual term may be defined as

$$R_i = -a_i Q_i + \sum_{j \neq i} F_{ij} (1 - \gamma_j) a_j Q_j + a_i Q_i^{\text{direct}}. \quad (4.27)$$

The values of a , F_{ij} , and Q^{direct} are all fixed by the geometry of the feature and the plasma conditions and may be treated as constants. The remaining equation has two unknowns (or sets of unknowns), γ and Q , but they may be related through the reaction model. For Gray's model [Gray, 1992],

$$\gamma = \gamma_t + \gamma_{ie}, \quad (4.28)$$

$$\gamma_t = 0.12 \exp\left(\frac{-E_a}{k_b T}\right) \quad (4.29)$$

and is constant throughout the feature,

$$\gamma_{ic} = \frac{4\beta_2 \left(1 + \frac{b}{2}\right) C_F I}{Q}, \quad (4.30)$$

and

$$C_F = \frac{0.2 \frac{Q}{I}}{0.2 \frac{Q}{I} + 2\beta_2(1+b)}. \quad (4.31)$$

Combining produces an expression for R in terms of Q,

$$R_i = -a_i Q_i + \sum_j F_{ij} a_j \left(1 - \gamma_t - \frac{0.8\beta_2(1+\frac{b}{2})I_j}{0.2Q_j + 2\beta_2(1+b)I_j} \right) Q_j + a_i Q_i^{\text{direct}}, \quad (4.32)$$

and differentiation produces the terms required for Newton's method:

$$\frac{\partial R_i}{\partial Q_i} = -a_i \quad (4.33)$$

and

$$\frac{1}{F_{ij} a_j} \frac{\partial R_i}{\partial Q_j} = 1 - \gamma_i - 0.8 \beta_2 \left(1 + \frac{b}{2}\right) I_j \left[\frac{1}{0.2 Q_j + 2 \beta_2 (i+b) I_j} - \frac{0.2 Q_j}{(0.2 Q_j + 2 \beta_2 (1+b) I_j)^2} \right]. \quad (4.34)$$

The advantage of Newton's method over the fully iterative scheme described earlier depends upon the relative computational cost of linear algebra. Newton's method is expected to reduce the number of sticking coefficient iterations required to reach self-consistency, and completely eliminates iteration from the transport problem for each set of sticking coefficients. However, each step requires a matrix inversion (or the equivalent), which was previously shown to be excessively costly for the systems studied and computers used in this work. Use of a more advanced computer may reduce the cost of linear algebra sufficiently to justify use of Newton's method, and the above formulation is presented for use if such circumstances arise.

Chapter 5

Surface Advancement

5.1 History and Requirements

The fundamental task of surface advancement is to utilize knowledge of the present surface topography and the etching rate along the surface to predict the surface topography after etching. The etching rate may vary along the surface, depending upon such factors as feature geometry, surface composition, and plasma conditions. Analytical descriptions of this variation are obtainable in a few trivial situations, but numerical costs will generally limit the availability of etching rate data to a finite number of discrete locations along the surface (and a finite number of discrete times during the process). Building a simulation code generally requires choosing a discretized representation of the surface and some scheme or algorithm for advancing that representation.

The most familiar surface advancement algorithm was introduced as part of the original SAMPLE code developed at UC-Berkeley in the late 1970's [Jewett, 1979] [Oldham, *et al.*, 1979], wherein the surface is represented by a string of points connected by straight line segments. Each point is advanced in time along the local surface normal, which is approximated by the bisector of the inwardly-pointing normals to the two adjacent segments. The point velocity is taken as the average of

the two segment etching rates (Figure 5.1). This "Angle Bisector" algorithm and its derivatives are popular because advancing the surface along the normal is consistent with popular intuitions about surface evolution, and because no *a priori* knowledge of the etching rate behavior is required.

Although intuitively satisfying and easy to implement, the Angle Bisector method suffers certain penalties when applied to ion etching systems. The time integration step must be small enough to ensure that the surface evolution is gradual; the movement of points during each time step must be small relative to their separation. This is because the slope of each segment is determined by the relative positions of the end points. If the etching rate is a strong function of slope (or ion arrival angle), errors in the point locations at one time step result in errors in the etching rates at the next. If the time step is too large, the profile may become unstable as shown in Figure 5.2.

One popular variation on the Angle Bisector theme is to use the straight segments between points to define the surface normals; the segments are advanced parallel to themselves at their individual etching rates, with the new point locations determined from the intersection of adjacent segments [Neureuther, *et al.*, 1979] (Figure 5.3). This technique is more stable in corner regions, but suffers from one very important limitation: segments may grow or shrink, but there is no systematic method for introducing segments with new slopes. Therefore, the final surface can not contain any slopes which do not appear in the initial surface. The most dramatic

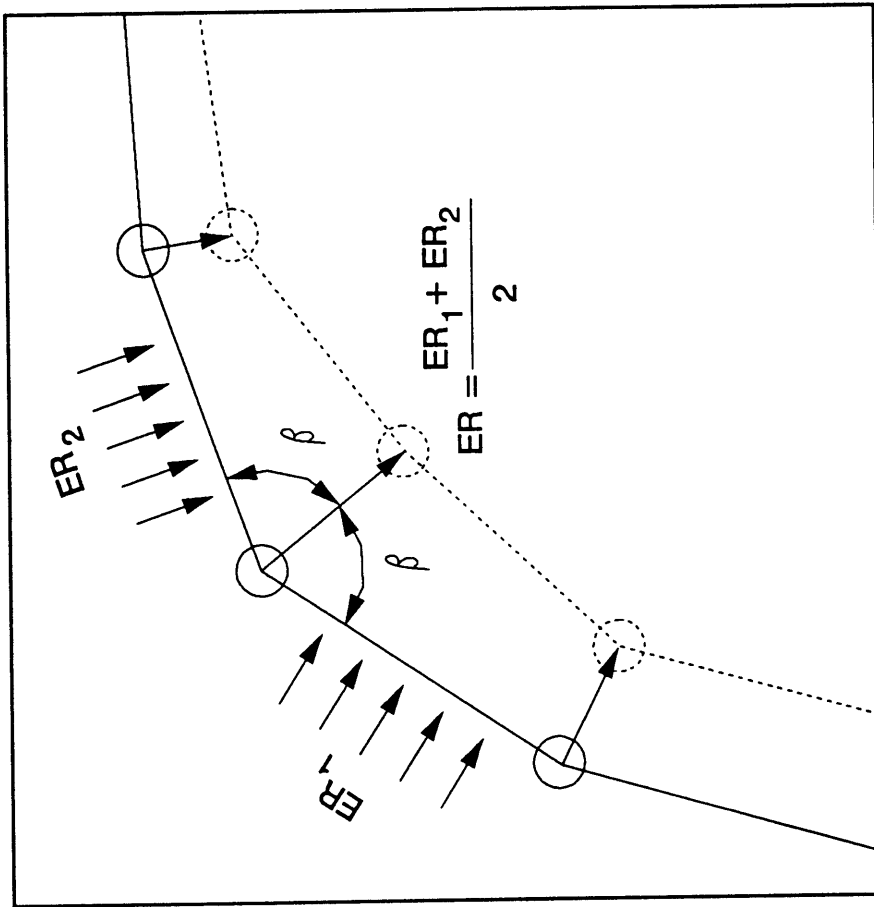


Figure 5.1: The Angle Bisector algorithm. Each point is moved inward along the line which bisects the angle between adjacent segments at a velocity equal to their average etching rate.

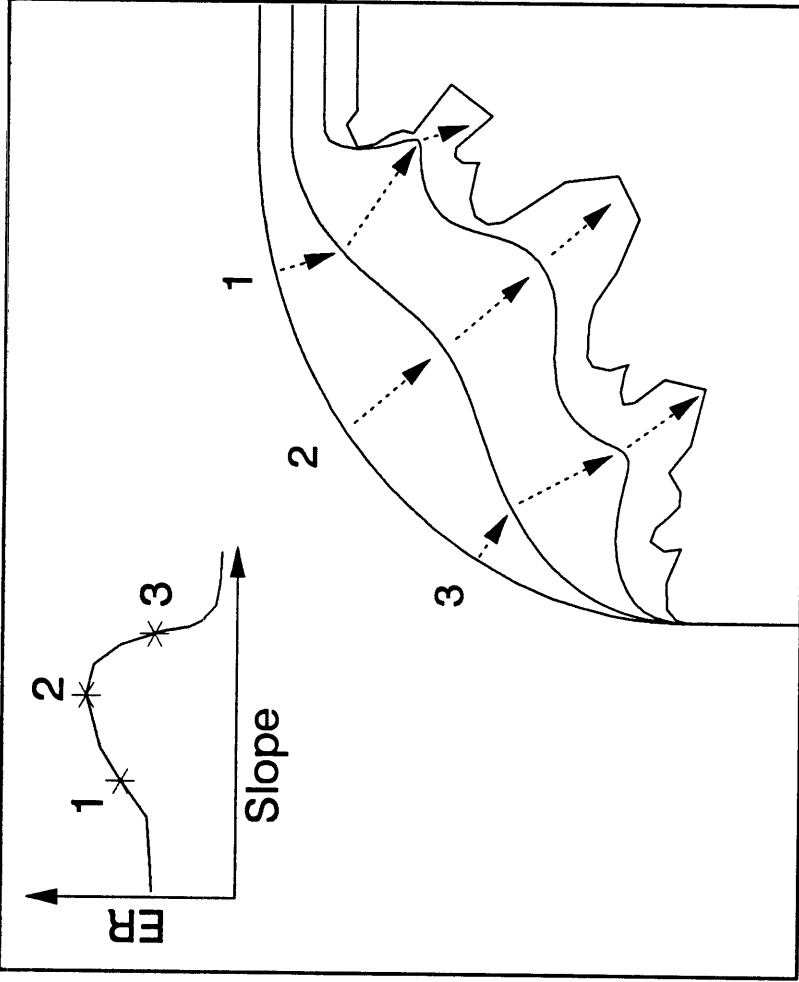


Figure 5.2: Instability of the Angle Bisector algorithm due to excessive time step and strong slope dependence of etching rate.

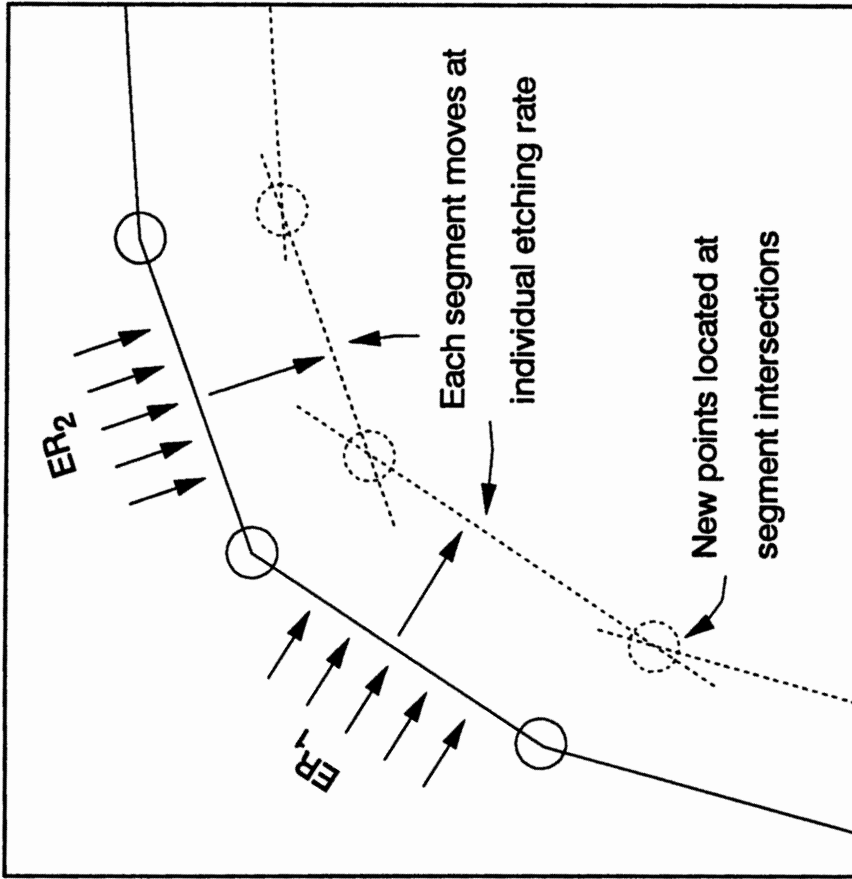


Figure 5.3: Segment advancement algorithm. Each segment is moved parallel to itself by a distance equal to the local etching rate. New points are placed at intersections of relocated segments.

illustration of this point is the etching of an initially flat surface at a varying rate. The expected result is a sloped surface, but advancing the initial segments parallel to themselves introduces discontinuities (Figure 5.4).

Several researchers have improved the efficiency and accuracy of their simulations by first describing the etching rate analytically and then using the Method of Characteristics to determine equations governing point motion [Smith, *et al.*, 1987] [Shaqfeh and Jurgensen, 1989]. This approach has several advantages: the point trajectories are not limited to the normal direction, and also have a strong mathematical basis. However, widespread application of this method has been limited by uncertainties regarding the treatment of sharp corners and an apparent need to develop an analytical description of the etching behavior.

The foregoing review of the available advancement techniques led to the following list of requirements for the new simulator: the advancement scheme chosen should be simultaneously *accurate, convergent, robust, stable, and efficient*.

Accuracy obviously refers to the requirement that, in the limit of infinite spatial and temporal resolution, the final surface profile must match the "correct" result. Ideally, this would be the surface profile produced by an actual etching process, but the predicted profile is determined by both the surface advancement method and the assumed etching rate behavior. Therefore, it sufficient to require that the advancement scheme produce the profile which would be obtained by an

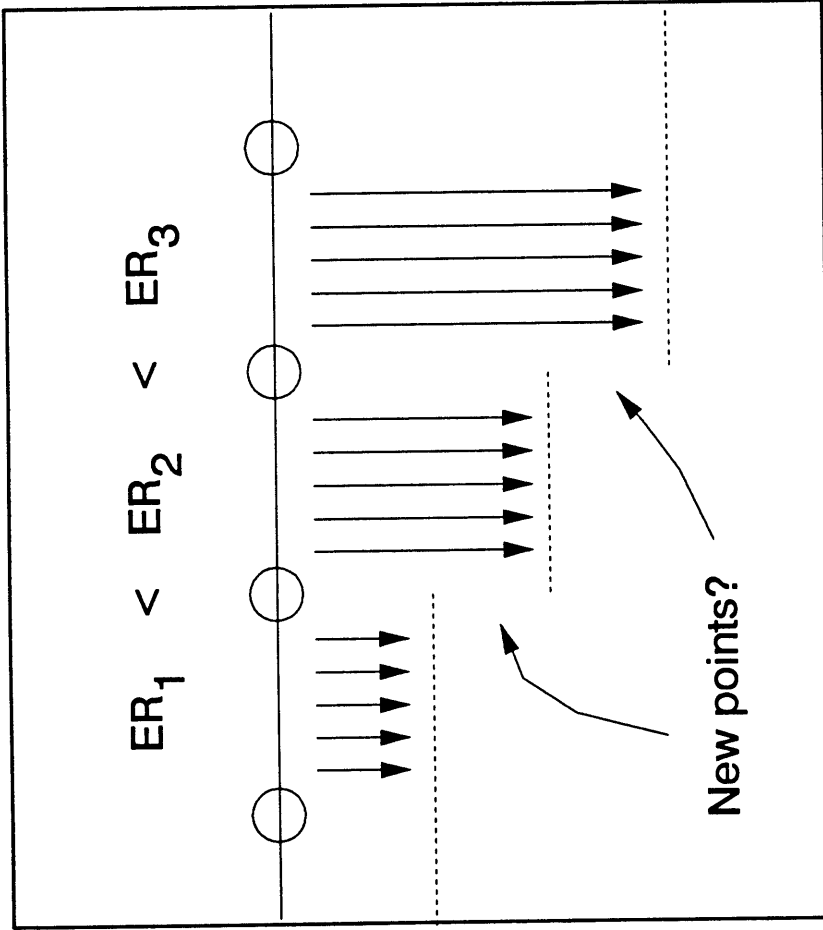


Figure 5.4: Instability of segment advancement algorithm on flat surface with non-uniform etching rate. Advancement of initially collinear segments by different distances introduces discontinuities in final surface.

analytical solution of the appropriate advancement equations (if an analytical solution were obtainable).

Convergence is used in this case to describe the approach of the numerical solution to the limit described above. Not only should the predicted profile approach the ultimate solution as the resolution is increased, but the profile obtained at lower resolution should qualitatively resemble the ultimate shape. Such behavior is essential if credible profiles are to be obtained at reasonable computational cost.

Robustness and stability imply that the code should be functional over a wide range of geometries, process conditions, and resolution levels.

Finally, the requirement of efficiency means that the code should yield profiles of acceptable accuracy at reasonable cost. As will be shown later, the computational cost is dominated by etching rate calculations, so an efficient advancement scheme should require a minimum of these. This suggests that the chosen method should be able to advance the surface profile using etching rate data from a minimum number of points along the initial surface, and that the computed direction of surface evolution should be valid for as long an etching time as possible.

None of the methods in use at the outset of this project met all of the requirements detailed above. However the following sections discuss an acceptable solution that was found through a collaborative effort with researchers at IBM's

facility in Yorktown Heights, NY.

5.2 Equations for Surface Advancement

In 1991, Satoshi Hamaguchi and co-workers at IBM pointed out that the Method of Characteristics (MOC) could in fact be applied in cases where the etching rate behavior is not known in advance [Hamaguchi, *et al.*, 1993]. Conventional practice up to that time had been to write a single partial differential equation (PDE) for the surface evolution, incorporate the known etching rate into that equation, and then use MOC to decompose the result into a set of ordinary differential equations for computing point trajectories. Hamaguchi *et al.* observed that it was possible to apply MOC to the initial PDE without specifying the etching rate, obtaining a set of ODE's giving the point trajectory in terms of the etching rate and its variation with position and surface slope:

$$\dot{x} \equiv \frac{dx}{dt} = ER \sin(\theta) + ER_{\theta} \cos(\theta) , \quad (5.1)$$

$$\dot{y} \equiv \frac{dy}{dt} = - ER \cos(\theta) + ER_{\theta} \sin(\theta), \quad (5.2)$$

and

$$\dot{\theta} \equiv \frac{d\theta}{dt} = -ER|_{\theta} \quad (5.3)$$

ER is the etching rate, θ is the local surface inclination angle, and l is the arc length, or distance along the surface from some reference location. The subscripts on ER refer to partial differentiation of the etching rate with respect to θ or l . The derivation of these equations is reproduced in Appendix D.

Equations (5.1) to (5.3) define a characteristic trajectory for any point on the initial surface. Equations (5.1) and (5.2) specify the motion of the point, while Equation (5.3) describes the change in local surface slope as the point advances (through time) along its trajectory. The quantity $ER|_{\theta}$ refers to the change in ER along the surface, with slope held constant, and could be estimated by computing the etching rate with the flux conditions of adjacent points (Figure 5.5).

$ER|_{\theta}$ (and $\dot{\theta}$) are non-zero if the etching rate is explicitly dependent upon position along the surface. This is common in plasma etching situations, if there is geometric shadowing of a portion of the ion flux to the surface or if the etching rate is limited by transport of a reactant into the feature.

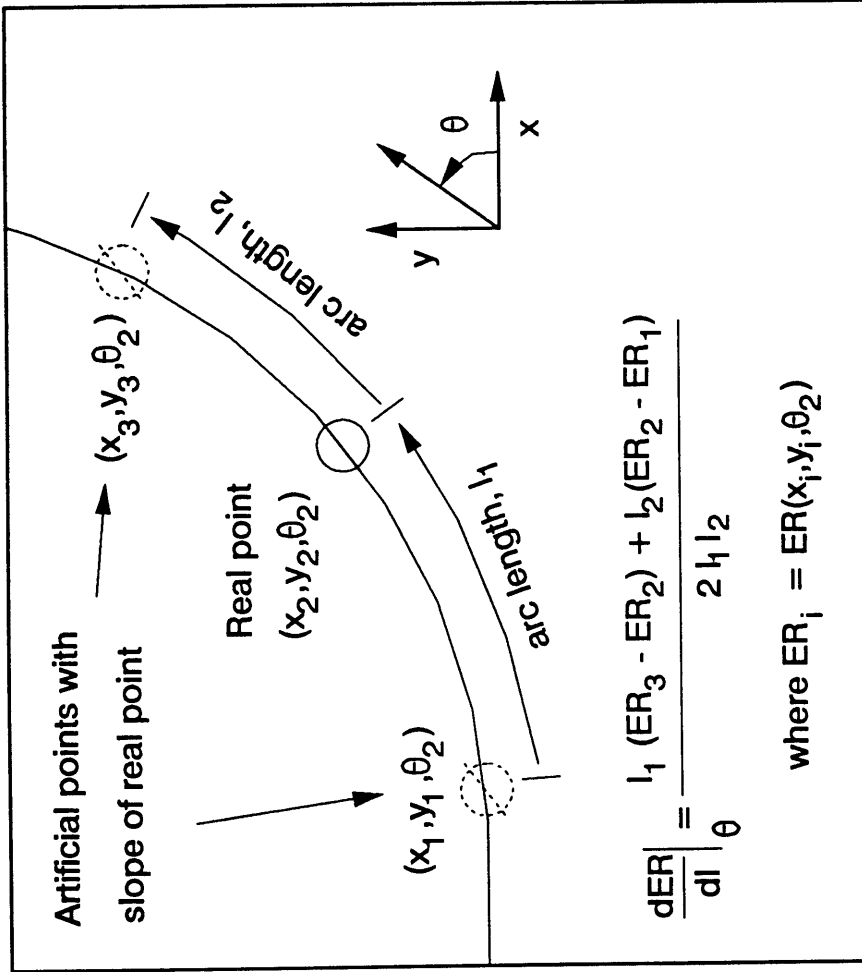


Figure 5.5: Computation of ER_l . Artificial points with same slope as real point are introduced at adjacent locations along the surface. Centered finite difference is used to estimate derivative.

There are some practical situations where spatial variations in etching rate are negligible. For example, ion milling of a non-reentrant surface with a highly collimated beam results in an etching rate that depends only upon the surface slope (ion milling will be discussed in more detail in a later section). In such a case, Equations (5.1) - (5.3) are simplified greatly. ER_t is equal to zero, θ for each point is constant in time, and the characteristic trajectories reduce to straight lines. The orientation of the characteristic trajectory relative to the surface normal depends upon the sign of ER_θ , as shown in Figure 5.6a. The trajectory lies to the counterclockwise from the inwardly-pointing normal for points with $ER_\theta > 0$, on the inward normal when $ER_\theta = 0$, and clockwise from it when $ER_\theta < 0$. This is consistent with the common intuition that planes of higher etching rate grow at the expense of others. Figure 5.6b shows the governing equations and surface motion for the Angle Bisector method for comparison.

A further simplification is achieved if the etching rate is not dependent upon the slope, as in isotropic etching. With ER_θ equal to zero, Equations (5.1) and (5.2) reduce to motion along the surface normal, as in the Angle Bisector method. The Angle Bisector algorithm thus provides the correct solution for isotropic etching problems, such as photoresist development (the algorithm's original application [Oldham, *et al.*, 1979]).

5.3 Treatment of Sharp Corners in the Initial Profile

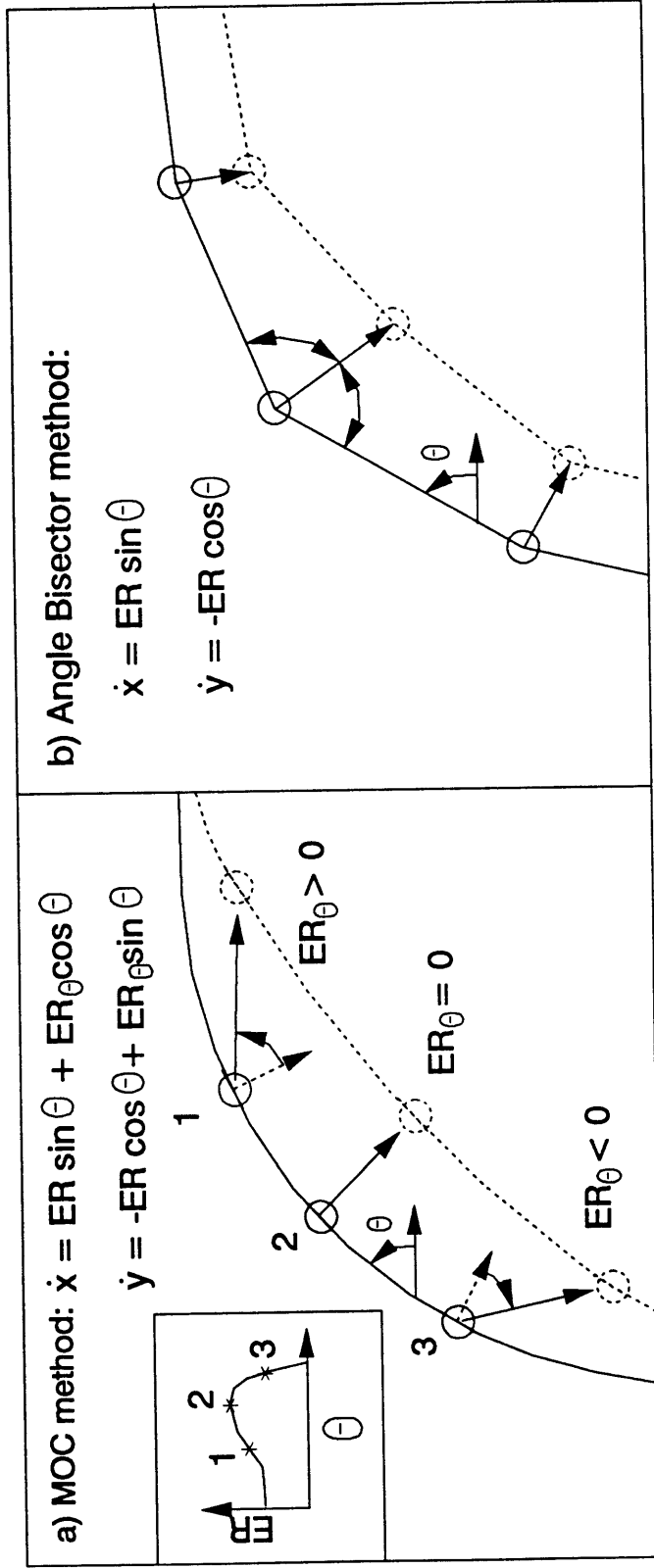


Figure 5.6: Comparison of Method of Characteristics with Angle Bisector method for etching rate which varies with surface slope. a) Variation of characteristic direction with ER_{θ} . Trajectories vary from inward normal according to sign of ER_{θ} . b) Angle Bisector method. Trajectories always follow inward normal.

The development presented above provides a method for advancing smooth surfaces. However, real surface profiles contain regions where the surface slope changes abruptly, such as at the top or bottom corner of a feature sidewall¹. Such corners are frequently referred to as "shocks," because the discontinuous change in surface slope is mathematically analogous to the changes in gas pressure and velocity found in shock waves.

The treatment of shocks has been a major source of difficulty in profile simulation. When the slope changes abruptly, the surface normal is poorly defined and the Angle Bisector algorithm produces unrealistic profiles as shown in Figure 5.7. Furthermore, there are many instances in which initially sharp corners expand into smooth surfaces during etching. One common example of this is the isotropic etching of a rectangular trench. Because etching proceeds uniformly in all directions, the sharp interior corners at the base of the trench expand to form smooth, curved surfaces as shown in Figure 5.8a. A related phenomenon is the formation of "facets" on the mask edge during ion milling [Melliar-Smith, 1976] (Figure 5.8b).

Shocks are not unique to ion-enhanced etching, and the mathematical behavior of shocks in other systems has been studied extensively by others over the last several decades [Lax, 1954, 1957] [Lax and Wendroff, 1960]. Ross [1988] demonstrated the applicability of the previous work of Lax [1957], Quinn [1971], and

¹ The issue of slope discontinuity in "real" surfaces will be addressed in Chapter 6; for this discussion, sharp corners are assumed to be points of truly discontinuous slope.

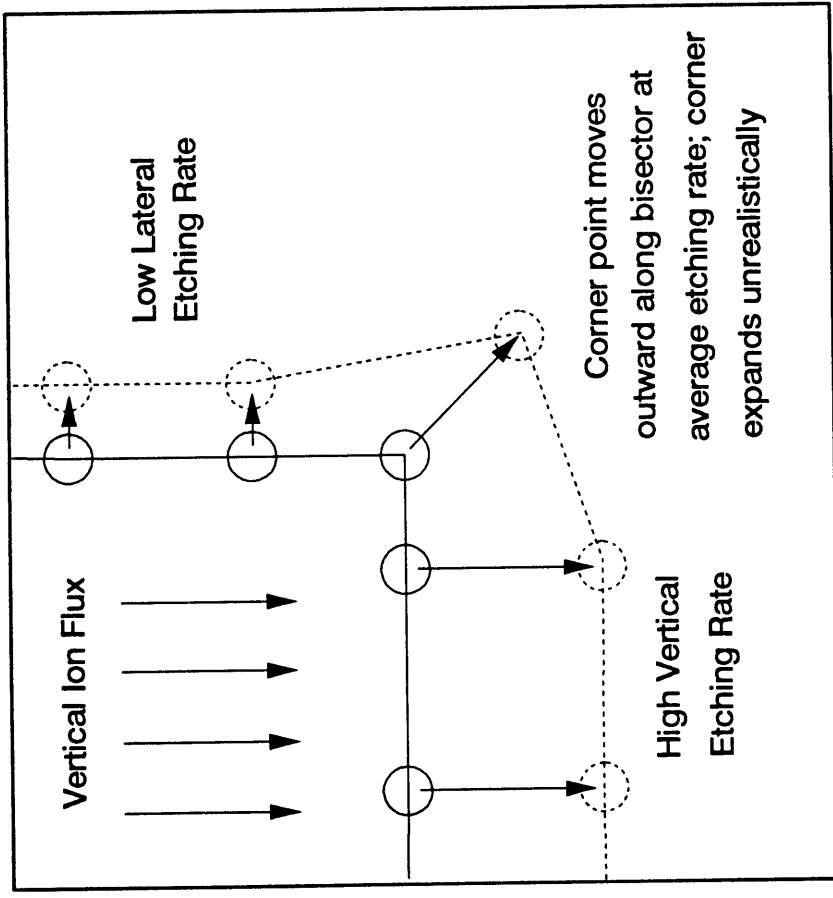


Figure 5.7: Behavior of the Angle Bisector algorithm in sharp corner with different etching rates on adjacent walls. Surface normal is not well defined at the corner, and use of bisector causes unrealistic lateral expansion of the feature.

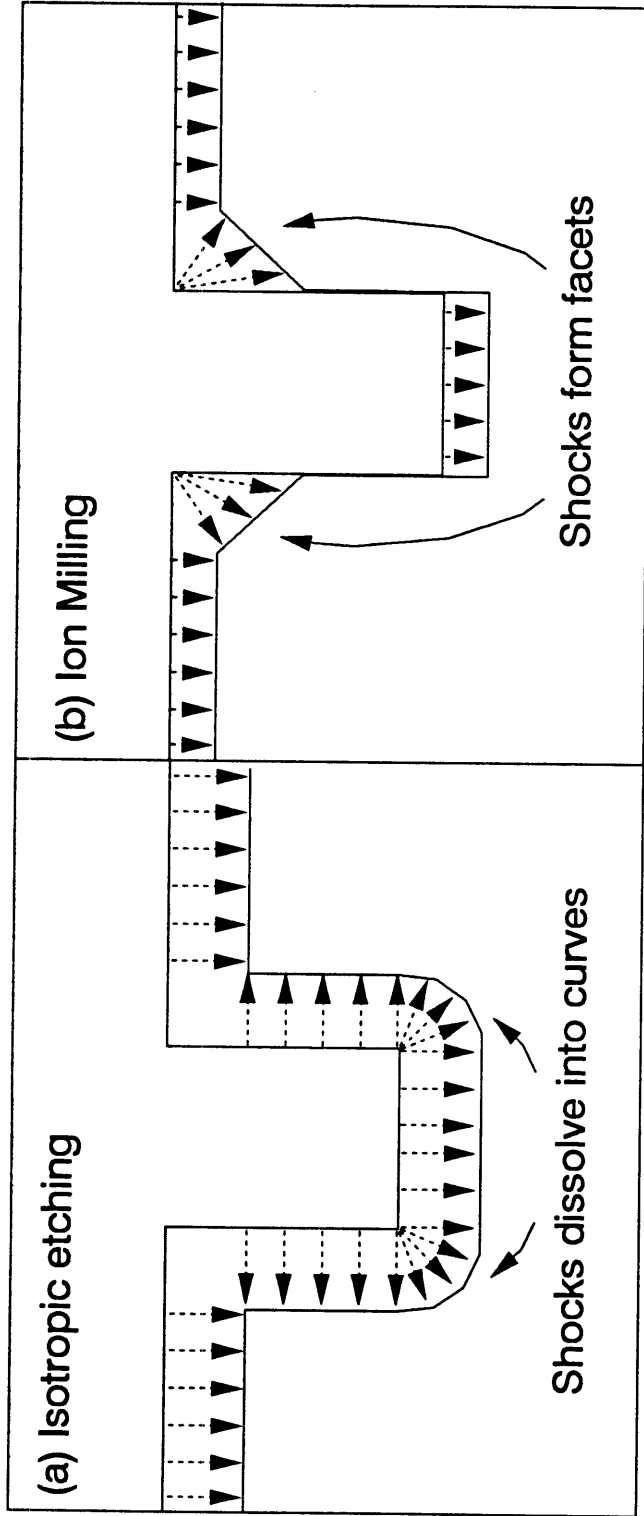


Figure 5.8: Examples of unstable shocks. a) Isotropic etching is uniform in all directions, causing concave shock to expand into smooth curve.
b) High etching yield for off-normal ions under ion milling conditions causes convex shocks to form facets.

others to ion milling. Although little of Ross's presentation was new or unique, it makes a convenient starting point for this discussion because it represents the first widely distributed application of hyperbolic conservation laws to ion-based etching processes.

The most important contribution of hyperbolic equation theory to modeling of ion etching is the entropy condition, which requires there to be a unique, stable, minimum-energy profile joining any pair of surface slopes. If the initial surface does not correspond to the minimum-energy profile (and the chosen mathematical description of the etching process is accurate), then the surface must evolve toward the stable shape as etching proceeds.

Quinn [1971] proposed and Ross related a graphical interpretation of the entropy condition for determining the stable profile, beginning with the definition of a "flux function" proportional to the ion yield (amount of material etched per incident ion). The flux function is given by

$$f(p) \equiv \frac{ER}{\cos(\theta)} - ER\sqrt{p^2 + 1} \quad (5.4)$$

where p is the surface slope ($p = \tan(\theta)$). The stable profile is found by plotting $f(p)$ vs. p over the range of interest, and then constructing an envelope over the curve between the limiting slopes. The choice of convex or concave envelope depends upon

the geometry of the problem: if the surface profile is convex (if the higher of the two slopes is found to the left of the intersection), then the convex envelope over $f(p)$ is used, and *vice versa*. Figure 5.9a shows $f(p)$ and the convex envelope for the intersection of two surfaces at 75° and -75° , using the typical sputtering yield [Catana, *et al.*, 1972] of

$$S(\theta) = 3.2696 \cos(\theta) + 13.1059 \cos^2(\theta) - 15.3755 \cos^4(\theta) \quad (5.5)$$

for illustration.

The envelope over $f(p)$ is used to decide which slopes are present in the stable profile, and which disappear (into shocks). The convex envelope shown in Figure 5.9a coincides with $f(p)$ over two regions, from -50.5° to -45° and from 45° to 50.5° . The stable profile will contain points with these slopes. On the other hand, the convex envelope separates from $f(p)$ over the ranges -75° to -50.5° , -45° to 45° , and 50.5° to 75° . Each of these ranges corresponds to a shock in the stable profile. The stable profile is shown in Figure 5.9b and contains five features: two curved facets and three shocks joining them to each other and to the initial slopes. The facets curve from 50.5° to 45° and from -45° to -50.5° , and the shocks span 75° to 50.5° , 45° to -45° , and -50.5° to -75° .

Figure 5.10 illustrates an important characteristic of systems governed by entropy: the stable profile is unique and independent of the initial shape. In Figure

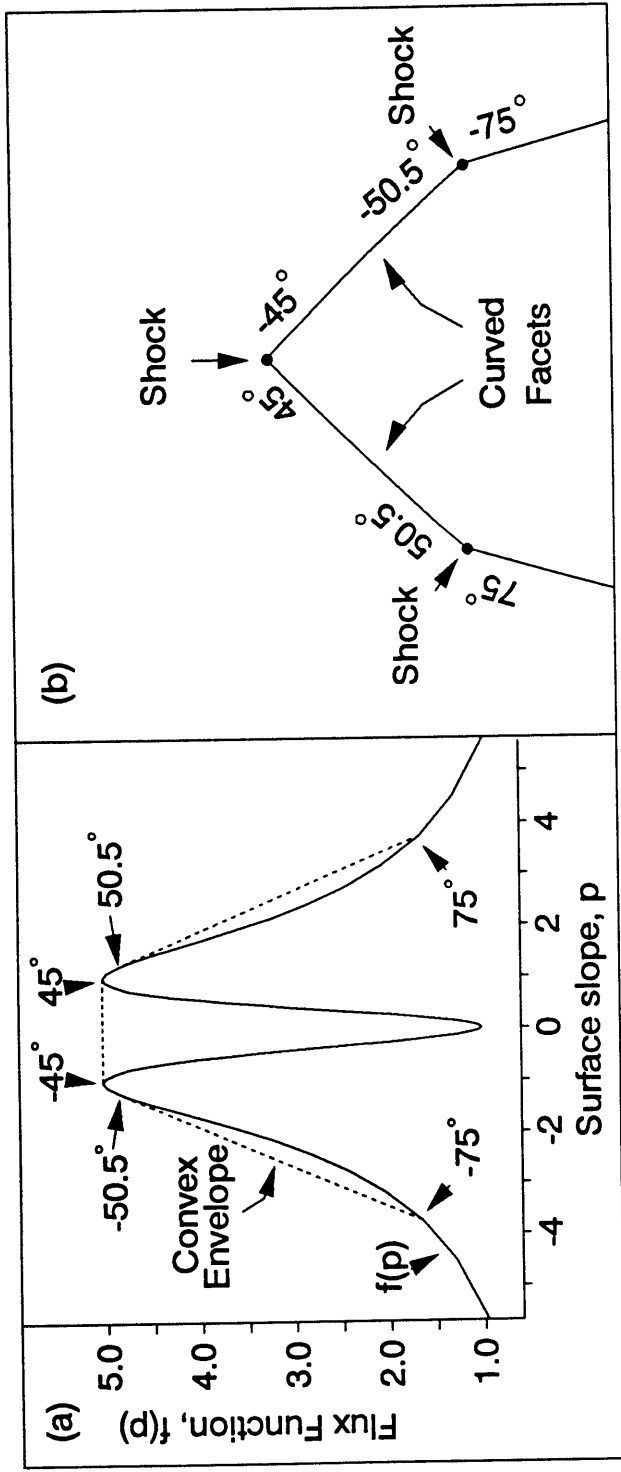


Figure 5.9: Flux function and stable profile for the intersection of two surfaces at 75° and -75° for the typical sputtering yield shown in Equation (5.5). a) Flux function $f(p)$ vs. slope p . Dashed line is the convex envelope over $f(p)$. Ranges of slope where the envelope corresponds to $f(p)$ form smooth curves in the stable profile shown in b). Regions of separation between envelope and $f(p)$ form shocks in the stable profile.

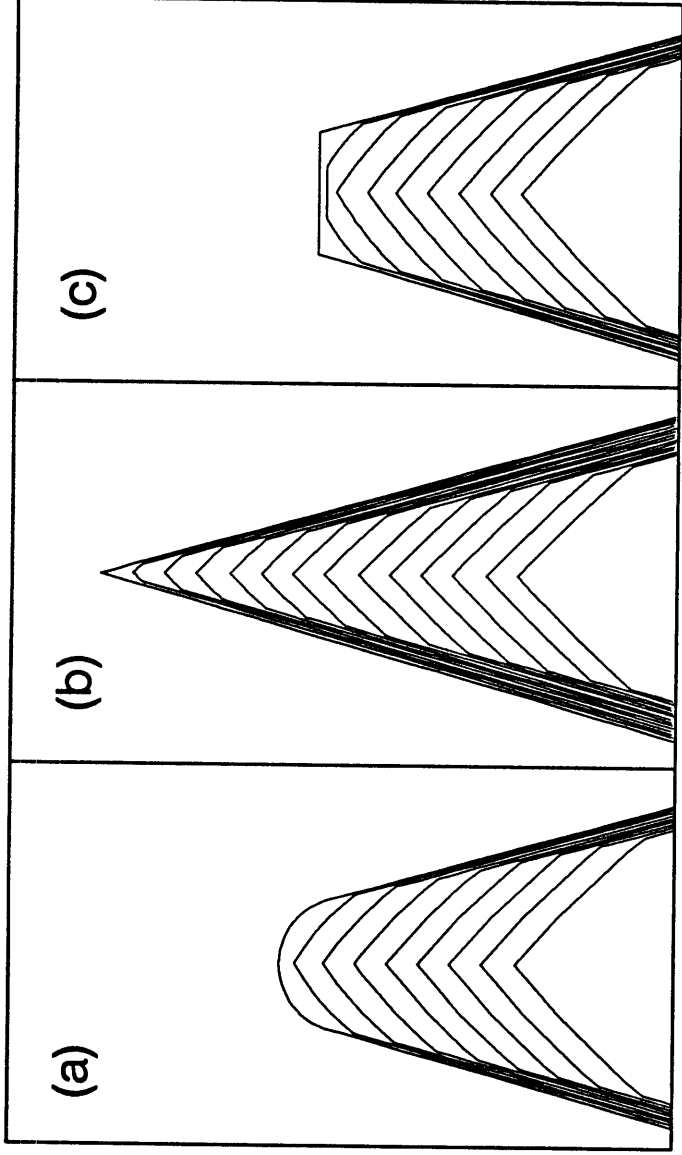


Figure 5.10: Evolution of various initial surfaces joining two inclined planes. Entropy condition requires that stable profile for this combination of planes and etching yield match Figure 5.9b. a) Initially smooth surface collapses to form the expected profile of three shocks and two smooth curves. b) Single shock expands into three. c) Pair of unstable shocks bifurcate and then coalesce to stable profile.

5.10a, an initially smooth surface develops the shocks and facets dictated by the entropy condition. Figure 5.10b shows that a single shock spanning 75° to -75° expands into three shocks and two facets. The initial profile in Figure 5.10c has two shocks, spanning 75° to 0° and 0° to -75° . Each of these shocks initially bifurcates into two shocks (and a curved facet), but two of the new shocks eventually coalesce into one. As the etching time tends toward infinity, all three of the initial shapes in Figure 5.10 evolve toward the same stable profile.

Ross [1988] also discussed a "jump condition" describing the motion of shocks.

A shock spanning angles p_- to p_+ moves according to

$$\dot{x}_s \equiv \frac{dx_s}{dt} = \frac{f(p_+) - f(p_-)}{p_+ - p_-} \quad (5.6)$$

and

$$\dot{y}_s \equiv \frac{dy_s}{dt} = \frac{p_- f(p_+) - p_+ f(p_-)}{p_+ - p_-} . \quad (5.7)$$

These values may also be found from a plot of $f(p)$ and the envelope over it (Figure

5.9a): \dot{x}_s is the slope of the straight line joining $(p_-, f(p_-))$ and $(p_+, f(p_+))$, and

$$\dot{y}_s = p_- \dot{x}_s - f(p_-) = p_+ \dot{x}_s - f(p_+) . \quad (5.8)$$

The analogous equations of motion for a point on a smooth surface may be found by letting p_- approach p_+ , yielding

$$\dot{x} \equiv \frac{dx}{dt} = \frac{df(p)}{dp} \quad (5.9)$$

and

$$\dot{y} \equiv \frac{dy}{dt} = p \frac{df(p)}{dp} - f(p) , \quad (5.10)$$

which are exactly equivalent to Equations (5.1) and (5.2).

Hamaguchi, *et al.*, [1993] have developed a surface advancement algorithm based upon a direct implementation of the entropy and jump conditions. While there is no doubt that this method will yield accurate results, it places certain constraints on the relationship between spatial and temporal resolution: the integration time step must be small enough to prevent the characteristic trajectories of adjacent points

from crossing one another.

This thesis employs an alternative method which is thought to provide more flexible control of computational cost without significant loss of accuracy. The integration time step is set arbitrarily, and the characteristic trajectories of converging points are allowed to cross. This results in the formation of a closed loop, which is subsequently removed in a process commonly known as "delooping" (Figure 5.11). Shocks in the initial profile are treated in the manner proposed by Smith, *et al.* [1987]: using test points at intermediate slopes to map the characteristic locus between the limiting angles and removing any closed loops which form (Figure 5.12). The profile obtained by this technique satisfies the entropy and jump conditions (Appendix E).

Delooping is a legitimate method for increasing the allowable integration time step, so long as the loops are formed by the crossing of properly computed characteristic trajectories. The forgoing discussion should not be interpreted as an endorsement of delooping with other advancement methods, which must be reviewed individually. For example, one popular variation on the Angle Bisector theme is to use the straight segments between points to define the surface normals; the segments are advanced parallel to themselves at their individual etching rates, with the new point locations determined from the intersection of adjacent segments [Neureuther, *et al.*, 1979] (Figure 5.3). The motion of a segment intersection satisfies the jump condition (Appendix F). In the limit of high spatial resolution, where the angle

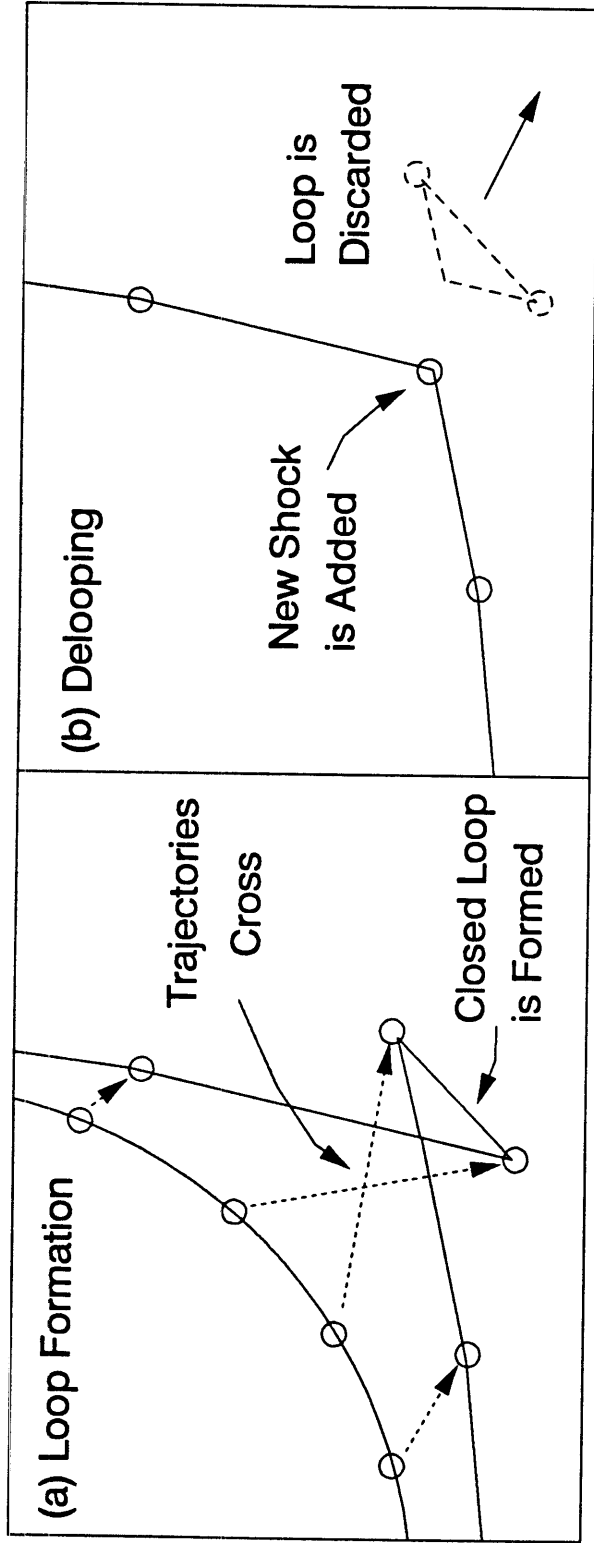


**Figure 5.11: Delooping process. a) Closed loops are formed when characteristic trajectories of adjacent points cross.
 b) Removal of closed loop leaves new shock where the surface profile crossed itself.**

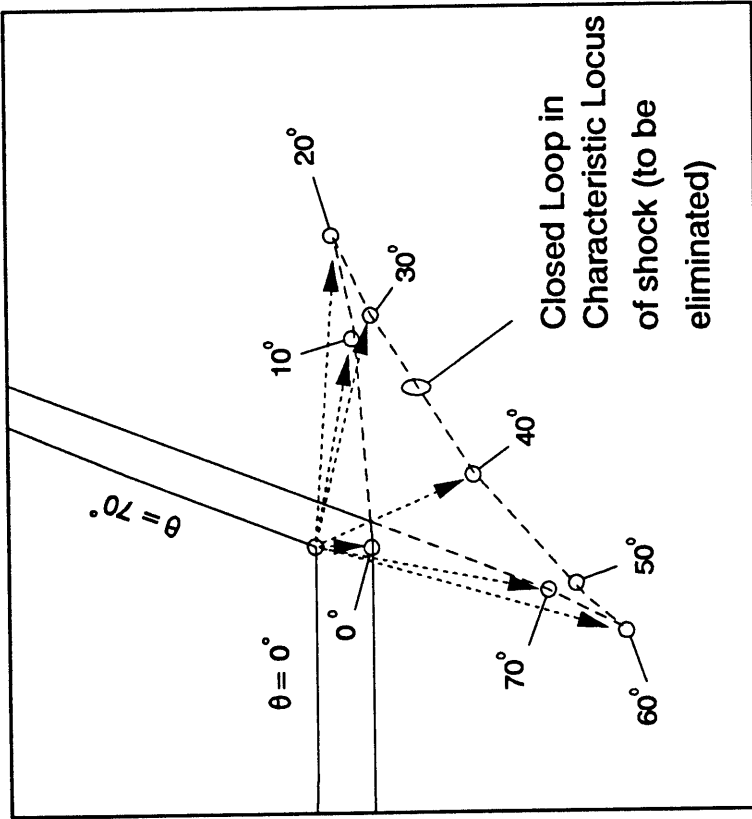


Figure 5.12: Modeling of shocks in initial profile. Characteristic locus is mapped by advancing test points with intermediate slopes from the initial shock location. Any closed loops that form are removed from the final profile.

between adjacent segments approaches zero, segment intersections obey Equations (5.1) and (5.2).

However, bringing the segment advancement method into compliance with the entropy condition requires additional effort. Applying segment advancement near a shock may generate a closed loop (Figure 5.13a), but simply removing this loop will not yield the correct profile. This is because the segment advancement technique preserves the segment slopes, and any slope required for the stable surface must be present in the initial profile. Therefore, the proper procedure for shocks is to approximate the sharp corner with a large number of short segments forming an arc. Subsequent advancement of this profile with a small time step provides the expected result (Figure 5.13b).

Increased time step is of great importance in simulation. The total simulation cost is now dominated by computation of reactant and ion fluxes. The relative advantage of different advancement methods is determined by their efficiency in reducing the number of points and time steps required to model the evolution with acceptable accuracy. Use of delooping with the Method of Characteristics decouples the integration time step from the point separation, thus providing an opportunity for increasing the time step without sacrifice of spatial resolution.

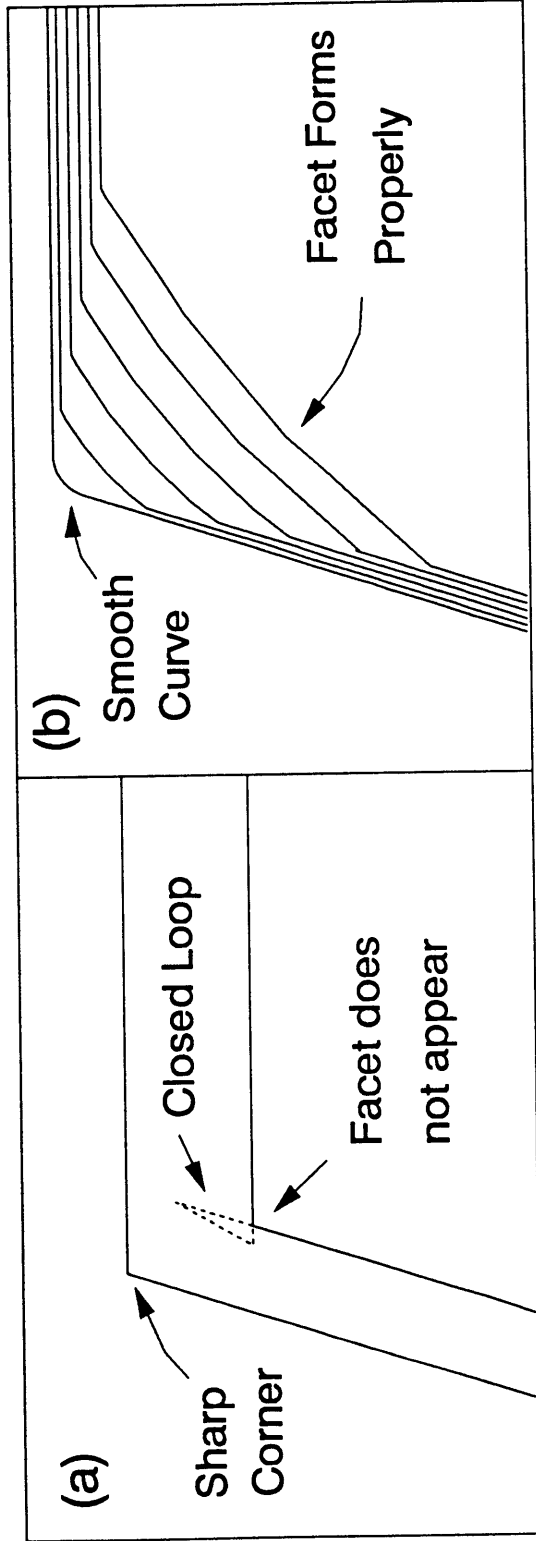


Figure 5.13: Treatment of shocks with segment advancement algorithm.

- a) Attempt to use delooping preserves initial shock.
- b) Proper profile evolution requires replacement of shock with smooth curve, followed by advancement with a small time step.

5.4 Numerical Implementation

Delooping has been combined with Equations (5.1) and (5.2) to produce a computer code for simulation of surface topography evolution. Specifically, the initial surface is represented by a number of points, and those are classified according to whether they lie upon smooth curves or at sharp corners (shocks). Those points lying on smooth curves are simply advanced by a first-order (forward Euler) time integration along the characteristic trajectories defined by Equations (5.1) and (5.2).

Each shock in the initial surface is replaced by a group of points which share a common starting position but have slopes spanning the range covered by the initial shock. These test points are then advanced according to Equations (5.1) and (5.2). Any loops formed in the resulting surface are removed in the manner described previously. New shocks are generated whenever the change in slope at a given point exceeds a user-defined tolerance.

This approach may be applied to any initial surface, requiring only that ER and ER_{θ} be calculable at each point. The accuracy of the resulting profile is controlled by adjusting the integration time step, the spacing of points along the initially smooth surface regions, and the angular resolution used at the initial shocks. Equation (5.3) is not used in this implementation because the local slope at each point after advancement is found from the relative position of the adjacent points, so independent tracking of θ is not necessary.

5.5 Application to Ion Milling

Ion milling processes are reasonably well understood and provide a convenient example for demonstration of profile evolution algorithms. Ion milling is typically conducted at low pressures, so the ion beam is assumed to be completely collimated and directed along the macroscopic surface normal. For non-reentrant surfaces (surfaces where no region is blocked from the ion beam), the etching rate depends only upon the local slope through the sputtering yield $S(\theta)$.

The sputtering yield usually shows a prominent maximum at some angle between 30° and 60° from normal. The local etching rate is equal to the sputtering yield times the ion flux (proportional to $\cos\theta$), so it also exhibits an off-normal maximum. Figure 5.14 shows typical sputtering yield and etching rate curves. The off-normal maximum in sputtering yield leads to the phenomenon known as faceting, wherein an initially sharp convex corner (such as the one at the top of a trench sidewall) may expand into an inclined plane (Figure 5.8b). The formation of facets is one of the most common experimental observations in ion milling [Melliard-Smith, 1976], and has been modeled extensively by others [Ducommun, *et al.*, 1974] [Smith, *et al.*, 1987] [Katardjiev, *et al.*, 1988] [Katardjiev, 1988]. Figure 5.15 illustrates the simulation of this process by the new algorithm.

Ducommun, *et al.*, [1975] have also published quantitative data for the simulated and experimental etching of a stepped structure. The initial profile consists

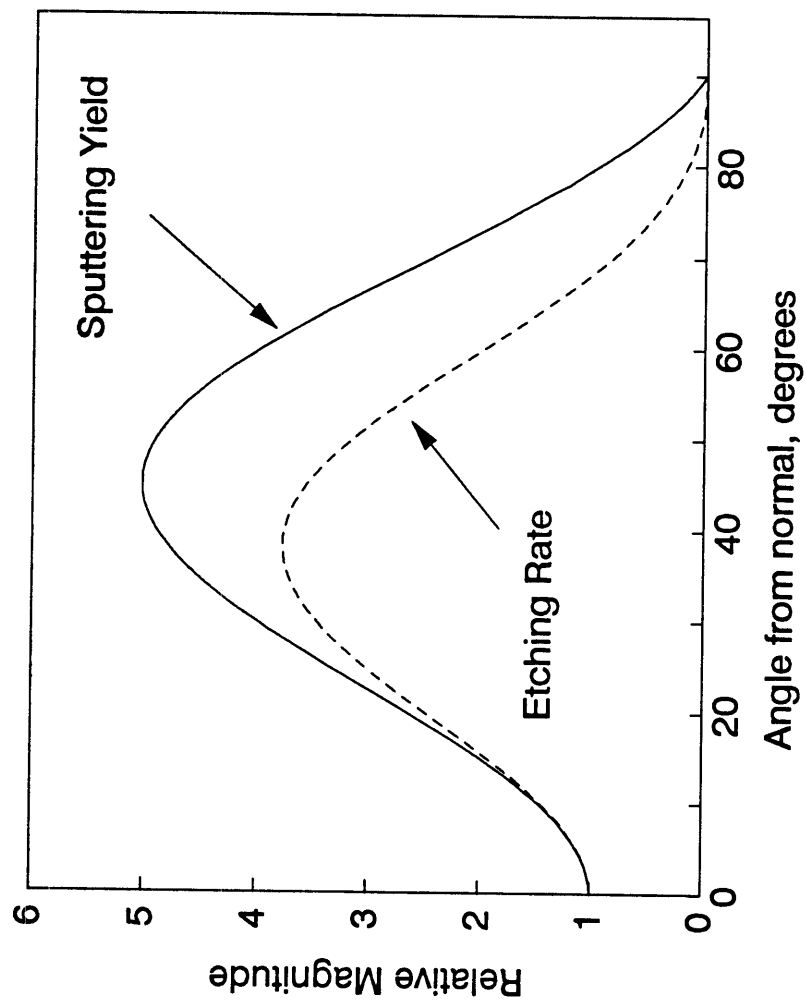


Figure 5.14: Example ion sputtering yield and etching rate curves for ion milling, from Equation (5.5).

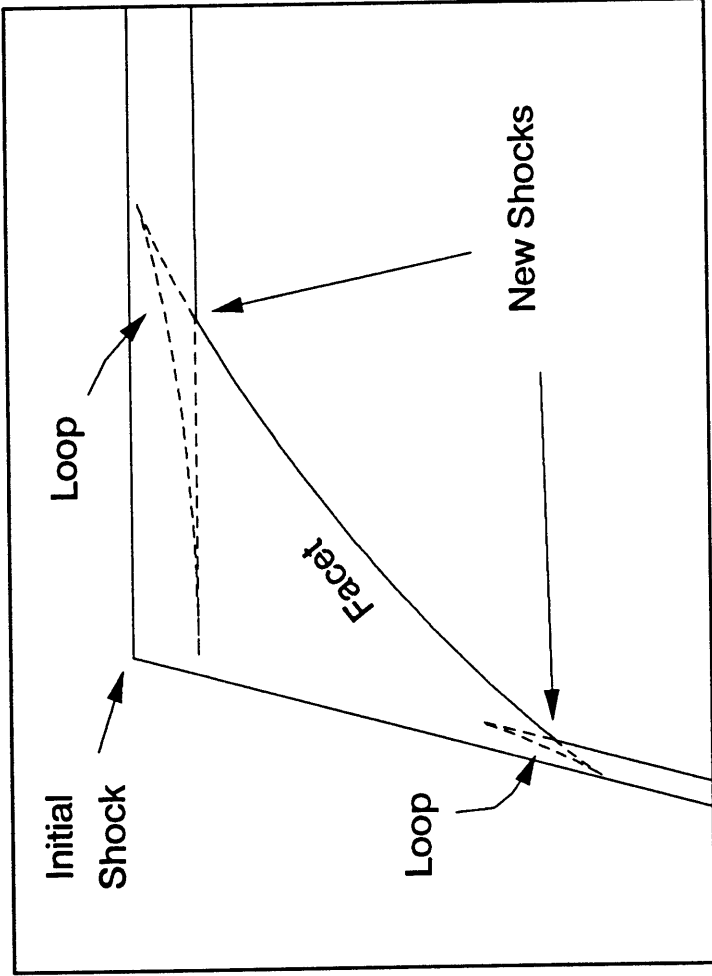


Figure 5.15: Facet formation at convex shock under ion milling with typical sputtering yield. Single shock expands to form two shocks separated by a smooth facet. Facet is commonly assumed to be planar, but actually curves slightly.

of an inclined plane joining two horizontal planes, with a small notch extending below the lower horizontal surface at the foot of the inclined step. The initial profile and simulation of the time evolution by the new method appear in Figure 5.16. In addition to SEM photos and surface profile illustrations, their work contains measurements of shock locations and angles, and the facet slope and length at several etching times. Figure 5.17 compares the reported values to those predicted by the new algorithm, and the agreement is well within the uncertainty. Katardjiev [1988] has also repeated Ducommun's simulation, with similar agreement. Such consistency is not unexpected, as both Katardjiev's and Ducommun's equations of motion can be rearranged to match Equations (5.1) and (5.2).

One additional point is raised in Figure 5.16: at long etching times, the step disappears and the surface approaches the smooth horizontal plane. This is in spite of the fact that the initial slope of the sidewall (80°) is well above the sputtering yield maximum (65° for the sputtering yield used by Ducommun [1975]). Common intuition, and the published work of Stewart and Thompson [1969], predict that the stable shape would be an inclined plane at 65° translating across the surface indefinitely.

This contradiction is one of three interesting phenomena observed in this study. All of these stem from the entropy condition's requirement that certain shocks of high slope range expand into smaller shocks and curved surfaces. Although the qualitative behavior does not depend upon the specific variation of sputtering yield

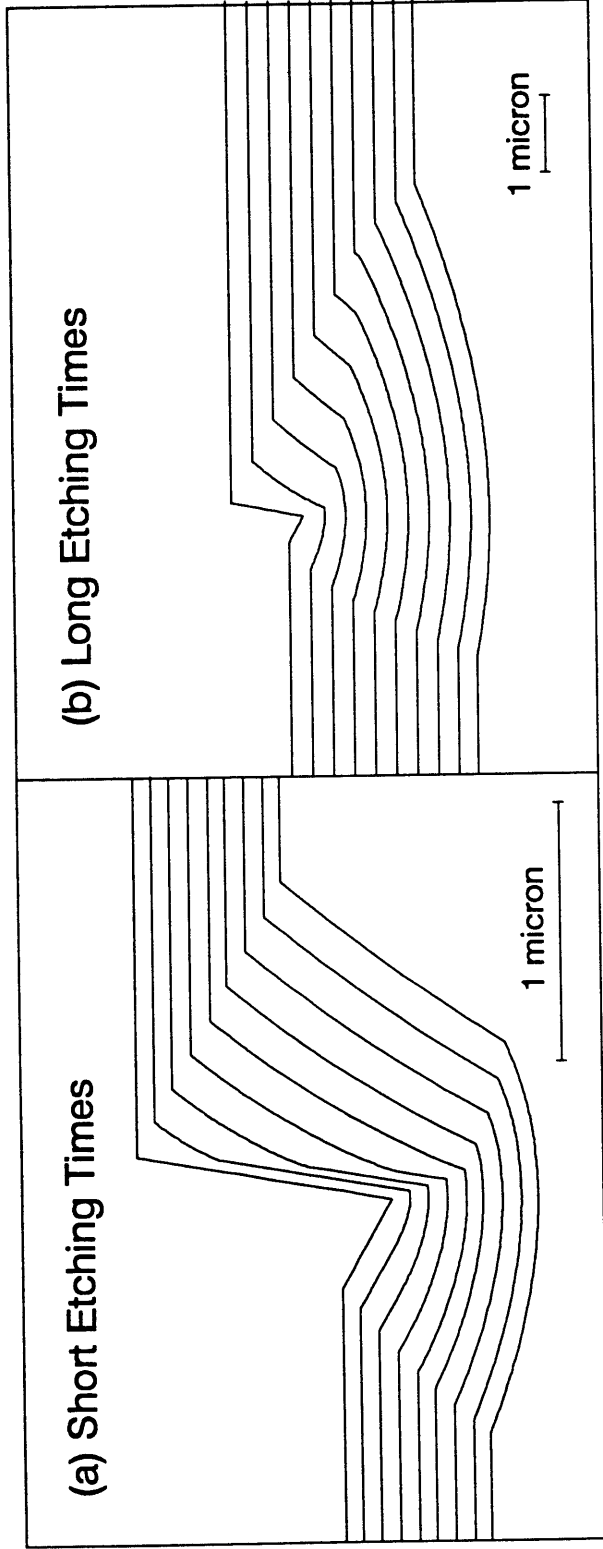


Figure 5.16: Simulated evolution of initial profile described by Ducommun, *et al.*, [1975]. Both sections show evolution of the same initial structure under the same conditions. a) shows initial etching (up to approximately 10 minutes) in greater detail, while b) illustrates approximately 1 hour of etching.

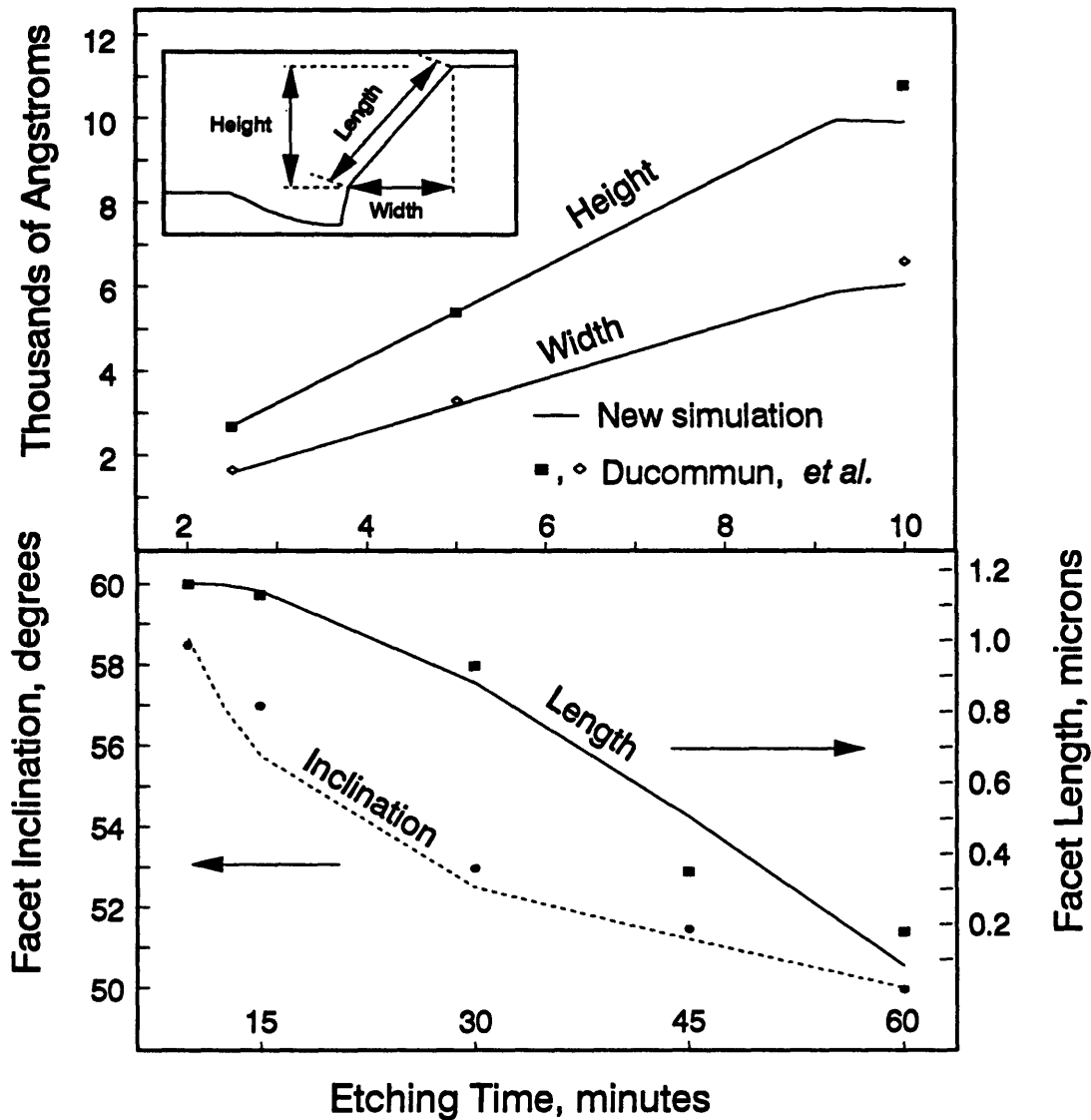


Figure 5.17: Comparison of simulation shown in Figure 5.16 to dimensions reported by Ducommun, *et al.*, [1975]. Symbols are reported values, while lines are extracted from new simulations.

with angle, the following discussion uses the typical yield introduced in Equation (5.5) for illustration.

The first case involves the ion milling of a 90° concave corner, such as the one found where a horizontal trench bottom meets the vertical sidewall. Because the sidewall receives no flux from an ideal ion beam, the etching rate there is zero. The bottom is flat and perpendicular to the ion beam, so its etching rate should be uniform. Thus, one might expect the bottom to progress vertically downward, retaining its 90° intersection with the sidewall.

Figure 5.18 illustrates the actual evolution of this structure under the sputtering yield shown in Equation (5.5) and Figure 5.14. Figure 5.18 was created using the new advancement algorithm, but a similar profile may be obtained by application of Hamaguchi's shock-tracking method [Hamaguchi, *et al.*, 1993] or the segment advancement technique described earlier. Points with slopes between θ_1 and 90° emerge from the initial shock, leaving a new shock with slopes between 0° and θ_1 and a small curved section on the sidewall. Furthermore, all of the points in the curved region and the new shock have negative values of \dot{x} , indicating that the width of the curved region will grow indefinitely in time. In the case of a deep trench, the two sidewalls will both grow inward and the trench width will decrease as etching proceeds and the trench will eventually be "pinched off". This phenomenon was previously observed by Smith, *et al.* [1987].

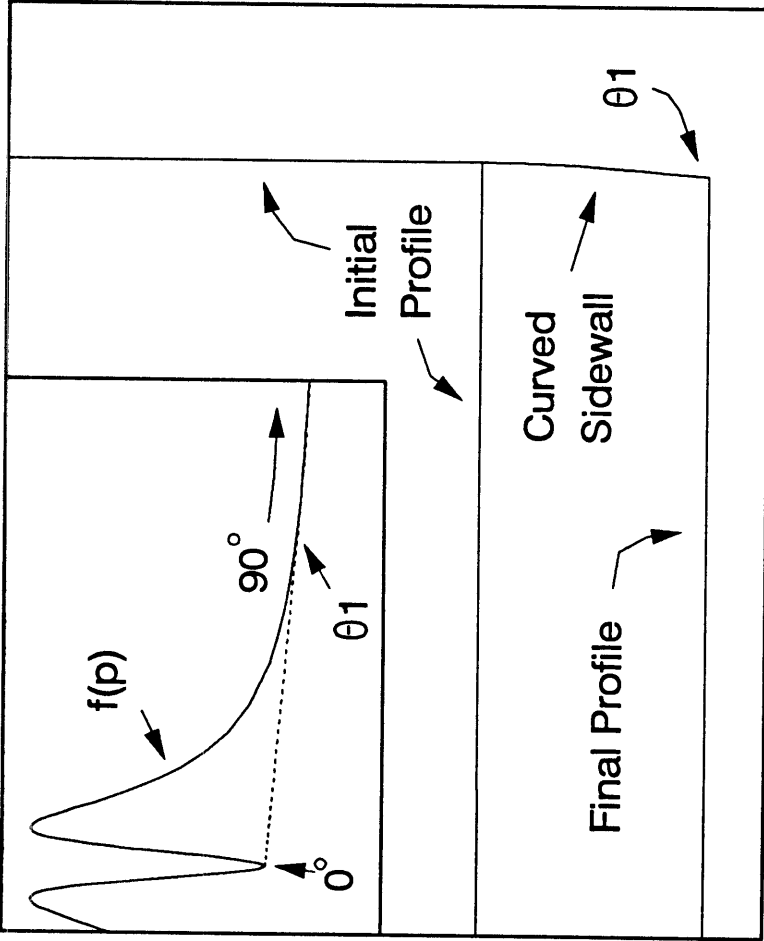


Figure 5.18: Evolution of 0° to 90° concave shock under ion milling with sputtering yield from Equation (5.5). Single shock expands to form a curved sidewall and a less abrupt shock. Inset shows flux function $f(p)$ with concave envelope over it.

θ_1 depends in a general fashion upon the shape of the etching yield curve: if the etching yield approaches zero closer to normal ion incidence, then θ_1 will be smaller. If the etching yield remains high over a broad angular range and approaches zero abruptly near grazing incidence, then θ_1 will be larger. For example, the ion milling yield curve introduced in Equation (5.5) gives a θ_1 of approximately 84.4° , while a yield proportional to $\cos\theta$ (the energy perpendicular to the surface) would produce a θ_1 of 45° . Figure 5.19 shows the impact of these yields on trench etching. θ_1 can only reach 90° if the yield is constant across the entire angular range.

Of course, the reality of plasma etching is far more complicated than the simple variation of etching rate with slope modeled here. Such phenomena as ion dispersion in the sheath and ion reflection from the sidewall may have some compensating effect, and the importance of sidewall passivation has been well established.

The second interesting situation also involves a concave shock, this time between a horizontal surface and an inclined facet at an angle close to the sputtering yield maximum. This structure would arise during the complete removal of a surface protrusion by ion milling [Ducommun, *et al.*, 1974]. In this case, the initial shock between 0° and 45° expands to form a curved bottom terminated by a shock between 8.4° and 45° . Furthermore, the vertical motion (\dot{y}) of the points on the curved bottom is less than that of either the horizontal surface or the inclined plane, so the curved surface becomes increasingly prominent as etching proceeds (Figure 5.20).

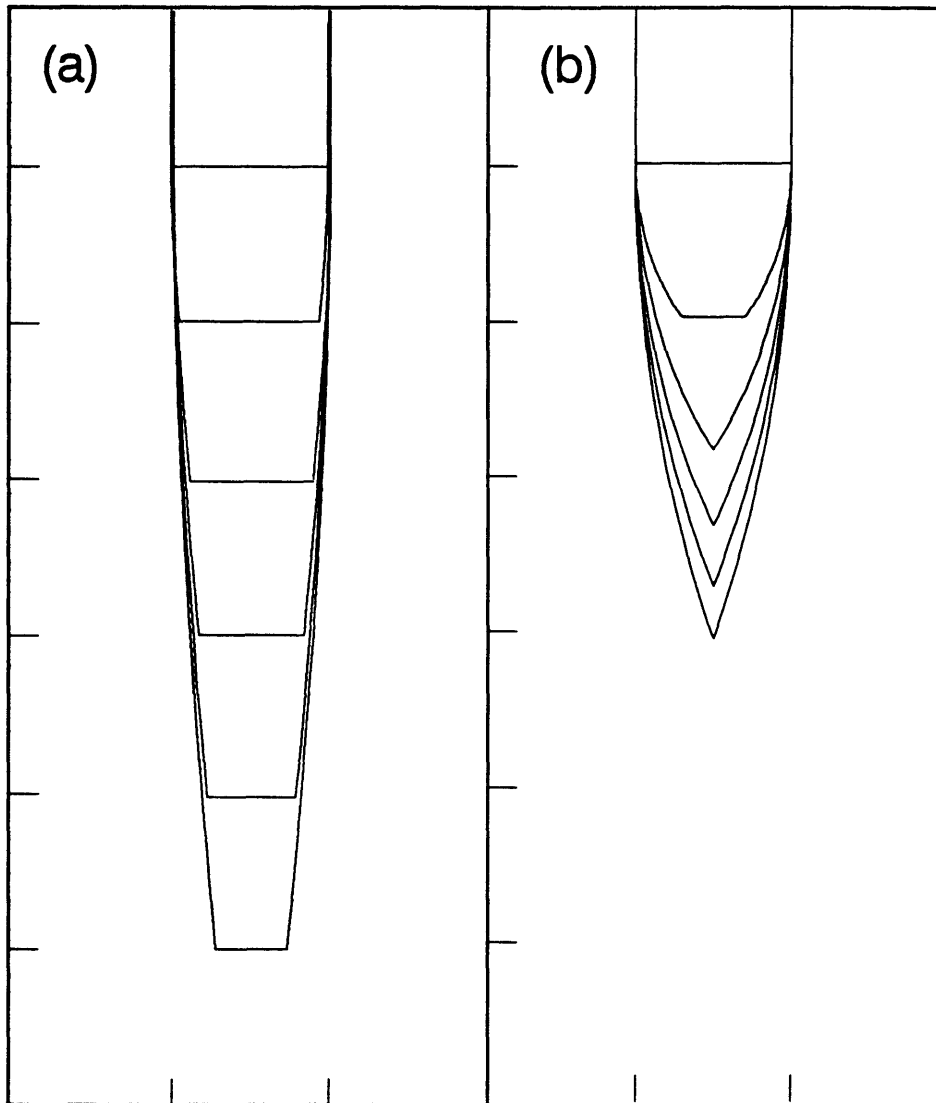


Figure 5.19: Effect of shock expansion on deep trench etching for two sputtering yield functions. Trench width decreases as depth increases.

a) Sputtering yield from Equation (5.5).

b) Yield proportional to $\cos \theta$.

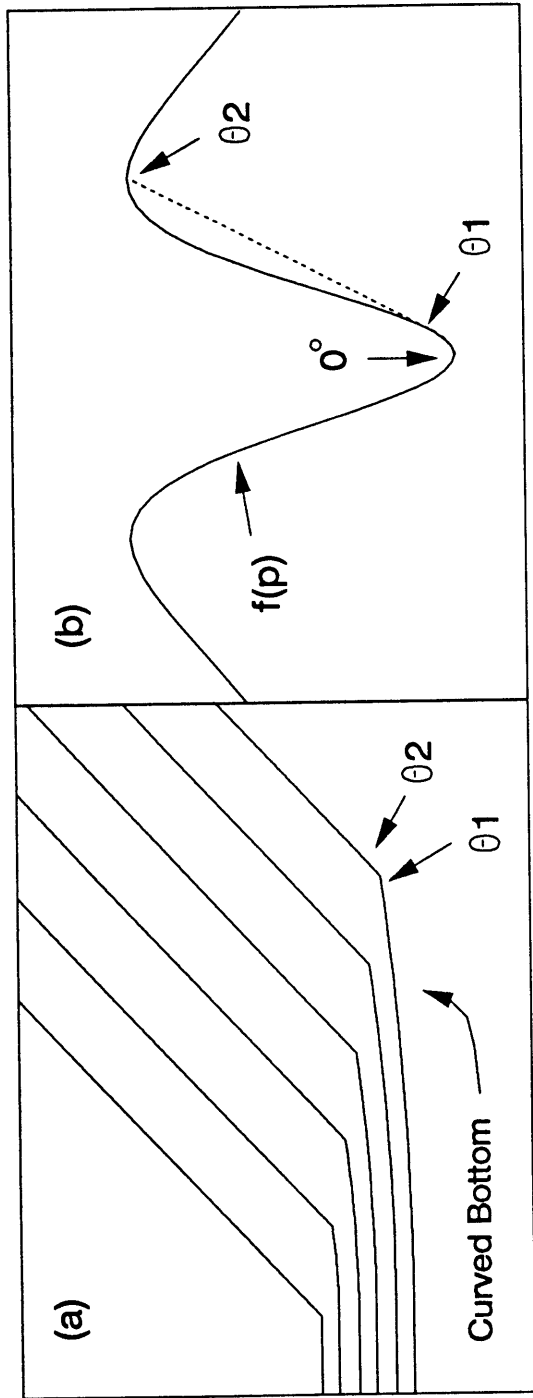


Figure 5.20: Expansion of 0° to 45° concave shock under ion milling with typical sputtering yield, Equation (5.5). In contrast to Figure 5.18, a shock of this angular range expands to form a less abrupt shock and a curved feature bottom.

Ducommun, *et al.*, [1974] have also studied this situation. While their text does not explicitly mention curvature of the bottom surface, the figures accompanying the paper suggest that curvature appeared in their simulations as well.

The final anomaly, which was in fact contradicted by the early report of Stewart and Thompson [1969], concerns the stability of a vertical surface step joining two semi-infinite horizontal planes. Stewart and Thompson predicted that the convex corner at the top of the step would form an inclined facet which would grow until it spanned the entire distance between the two horizontal planes. The surface shape would then be stable, with the facet translating laterally across the eroding surface as etching proceeded. This is consistent with common intuitions regarding the behavior of steps and facets.

Figure 5.21 shows the time evolution of this structure as predicted by the new algorithm. Once again, the sputtering yield function described in Equation (5.5) has been used for illustration, but the fundamental behavior of the step is not dependent upon the specific yield curve. The initial structure has two shocks, a concave corner connecting the left horizontal plane (at 0°) to the vertical (90°) sidewall and a convex corner joining the sidewall to the other horizontal (0°) plane.

As the etching begins, the angular range of the concave shock (S1 in Figure 5.21) changes in the manner discussed above (Figure 5.18). This shock moves to the left along the horizontal plane, leaving a curved sidewall. The etching rate of the

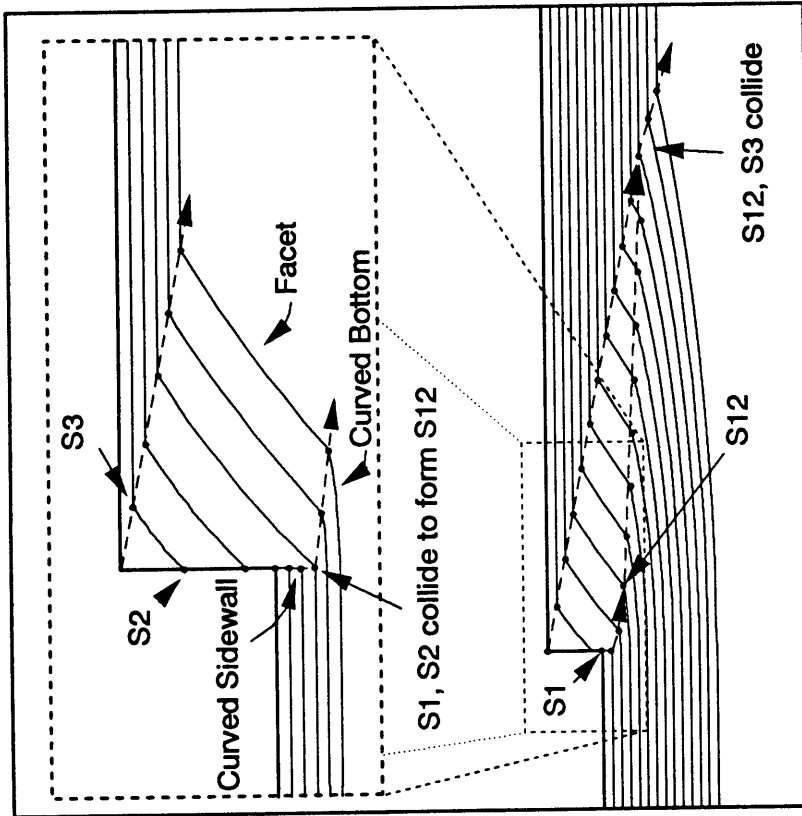


Figure 5.21: Evolution of a sharp step joining two horizontal planes. Shocks in the initial profile immediately expand to form a facet and a curved sidewall. As etching proceeds, the facet expands until it joins the lower horizontal plane, after which the lower surface curves upward and the facet shrinks. At long etching time, the surface approaches a horizontal shape.

horizontal planes is not zero, so they move vertically in time as well.

Simultaneously, the convex shock at the top of the sidewall bifurcates into two shocks joined by a curved facet (as shown previously in Figure 5.15). The first of these (S2) moves down the vertical sidewall. The second shock (S3) moves to the right along the upper horizontal plane.

S2 has a higher velocity than S1 and eventually overtakes it. The collision leaves a single, concave shock similar to the one shown in Figure 5.20. Not only is a shock of this angular range not stable, but the direction of the shock motion changes. The new shock, S12, moves down and to the right, but with a vertical velocity lower than that of the facet (or the other shock S3). Etching proceeds until S12 reaches the top of the facet and combines with S3.

The collision of S12 and S3 leaves only one shock and a curved region connecting the new shock to the lower horizontal plane. The new convex shock is not stable, either, and its left slope declines asymptotically toward 0° as the etching time approaches infinity.

The sequence described above leads to an interesting conclusion: the only stable surface is horizontal. This result is independent of the initial step shape: inclined planes, sigmoidal curves, and other steps all eventually approach the smooth shape observed for the square step (Figure 5.22). In order for a structure to be

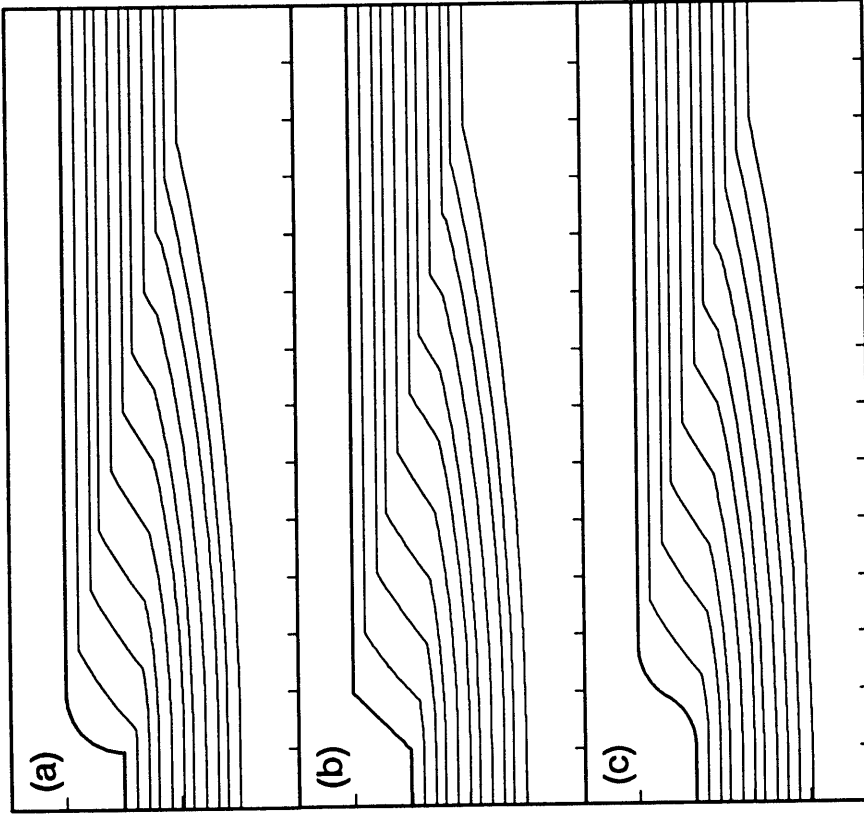


Figure 5.22: Evolution of various steps joining two horizontal planes. Dimensions and locations of facets vary with the initial profile, but all surfaces eventually approach the horizontal shape observed for the sharp step (Figure 5.21).

stable, both \dot{x} and \dot{y} would have to be constant for all slopes contained within the feature. Equations (5.1) and (5.2) show that this is possible only if the sputtering yield is constant over the included angular range. This is clearly impossible under ion milling conditions, where $S(\theta)$ and $ER(\theta)$ display prominent maxima.

5.6 Convergence

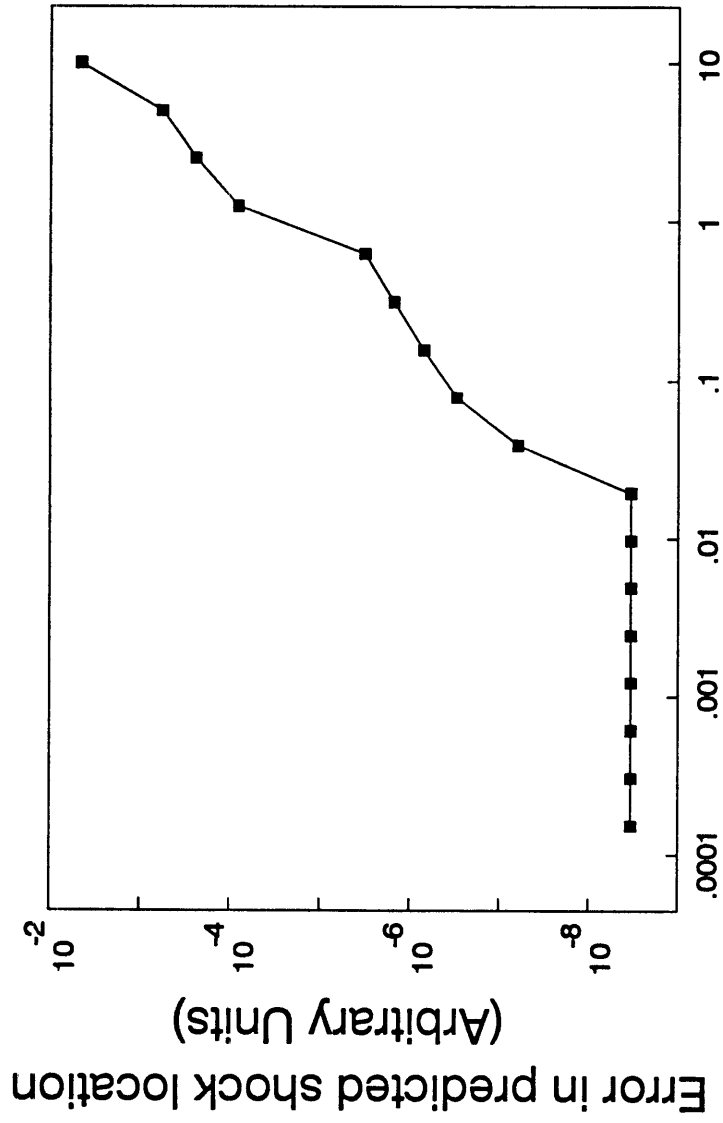
As with most numerical methods, the algorithm described above involves certain approximations. First, the smooth surfaces are approximated by series of discrete points. Second, the continuous variation of slope at shocks is approximated by a group of points at uniformly spaced intermediate slopes. Finally, the first-order (forward Euler) time integration scheme replaces the actual (smooth) trajectory with a sequence of straight line segments. Each of these approximations introduces some error into the final profile, and the credibility of the predicted profile depends strongly upon the convergence behavior of the numerical method. In other words, if a predicted profile is to be believable, there must be some method for estimating the maximum error in each of its components.

This section addresses the issue of error in the predicted profile by considering the convergence of the profile as the spatial and temporal resolution is increased. The resolution of this advancement method is determined by three parameters: the distance between discrete points used to represent smooth curves in the initial profile, the angular separation between test points used to simulate shock behavior,

and the time step used for advancement (integration). Each of these will be considered in turn.

The distance between points on smooth curves is not, by itself, a convergence issue. This is because Equations (5.1) and (5.2) are independent for each point, so the individual point trajectories (and hence the profile error) for a single time step are independent of resolution. However, the etching rate usually depends upon the surface slope, which is determined for each point by its location relative to the adjacent points. Therefore, separation between points may lead to errors in the computed slope at each point, which in turn may cause the etching rate (and ER_0) to be computed incorrectly, and may finally give rise to errors in the point trajectories and predicted profile. This effect is expected to be most important in regions where the curvature changes rapidly.

The angular resolution at shocks has a more direct impact on the predicted profile, because delooping places the final shock location at the intersection of two straight line segments (as shown in Figure 5.12). If the angular resolution is low, then the predicted shock location (and limiting angles) may be incorrect. Figure 5.23 shows the effect of increasing angular resolution on the error in shock location. This plot was prepared using a concave shock initially spanning 0° to 90° (horizontal to vertical), etched for an arbitrary time with the etching rate given in Equation 5.5. The true shock location was computed according to the method described by Ross [1988]. The delooped shock position became progressively more accurate as the



Angular separation of test points (degrees)

Figure 5.23: Convergence of predicted shock location with angular resolution.

As the angular resolution is increased (angular separation between test points is decreased), the error in the predicted shock location decreases to the machine precision.

angular resolution was increased, until the separation between test points was approximately 0.02° (4500 test points for the sample shock). Below that limit, with the chosen time step and single precision arithmetic, the successive improvements in resolution were smaller than the machine precision for point location. Consequently, no further improvement in accuracy was seen. If accuracy greater than 1 part in 10^8 were (for some unimaginable reason) required, then higher precision arithmetic and storage could be used.

The final source of error in the advancement algorithm is in the time integration between profiles. The chosen method (forward Euler) is well-established, and widely reported to converge linearly in time step. That is, halving the time step should halve the error (when the time step is sufficiently small). Of course, the time step is only important in determining the etched profile when the trajectories are curved, i. e. when ER_1 and $\dot{\theta}$ are non-zero. For this test, the admittedly contrived case of

$$ER = cl \tag{5.11}$$

(where c is a constant and l is the arc length along an initially horizontal line) was used. The profile was advanced through a fixed time with varying time steps, and the resultant profile was compared to the expected sloped line. The error was expressed in terms of the area between the predicted and expected curves, and the variation

of error with time step is shown in Figure 5.24. Not surprisingly, the convergence is linear.

5.7 Conclusions

A new method for simulating surface topography evolution during plasma etching has been developed and demonstrated. The new algorithm satisfies the entropy and jump conditions dictated by the mathematical theory of hyperbolic nonlinear equations (and previously applied to ion milling by Ross [1988]), and improves upon the conventional surface advancement methods in several ways. It simultaneously captures the efficiency of point methods on smooth surfaces and the accuracy of shock tracking methods at sharp corners. It is stable for longer time steps than such methods as the Angle Bisector algorithm, and is expected to minimize the number of points required to accurately model a given surface. It is flexible enough to be compatible with the sophisticated reaction models presently emerging, requiring only that the etching rate be differentiable in slope and space.

Comparison of the popular Angle Bisector and segment advancement algorithms has shown that they are both accurate in certain situations. However, neither of these methods can be expected to produce correct profiles over the broad range of conditions found in plasma etching.

This work has also highlighted some common misconceptions regarding the

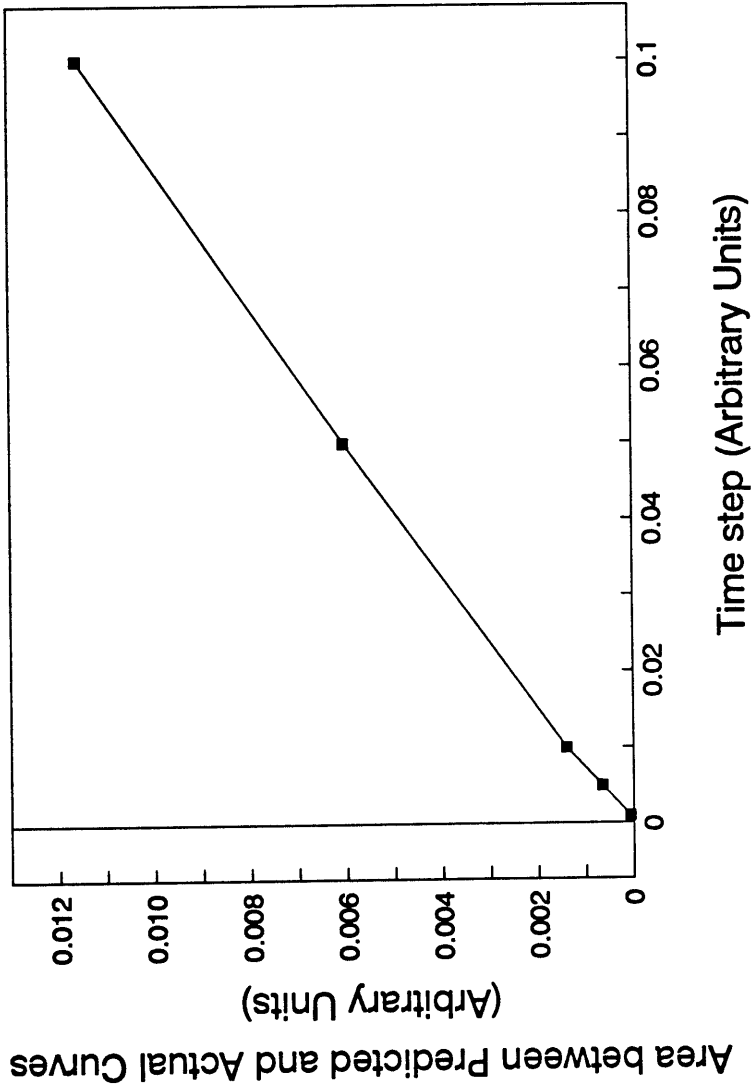


Figure 5.24: Convergence of curved trajectories with time resolution. The area between predicted and expected profiles decreases in linear proportion to the time step.

stability of surface features under prolonged etching. In particular, the instability of sharp concave corners would appear to limit the manufacturability of the very deep structures needed for advanced DRAMs. This underscores the need for further development of detailed models for etching physics and chemistry, and combination of those models with carefully characterized numerical methods to enable truly predictive simulations.

Chapter 6

Model Integration

The previous Chapters have described the development of several components of a surface topography evolution model. Construction of a complete simulator for application to problems of practical interest would require that the individual parts be joined together. Efforts were made to ensure that the separate components would fit together readily, but there were some unforeseen issues that arose during integration. This Chapter discusses some of those issues and possible solutions.

6.1 Ion Flux to Sharp Corners

One of the principal advantages of the surface advancement algorithm presented in Chapter 5 was its ability to track the formation and motion of sharp corners in the surface profile. The only requirement for accurate advancement was the ability to describe the etching rate at the corner as a function of slope. This did not appear to be a difficult requirement, as the etching rate for a real system should vary continuously with slope between the rates observed at points adjacent to either side of the shock.

Reactive ion etching is primarily driven by the ion flux. The simplest kinetic description for RIE is to equate the etching rate with the ion flux. Therefore,

simulation of shock evolution under RIE using the advancement scheme from Chapter 5 requires computation of the ion flux as a function of slope at the shock. Models for computing the direct and reflected ion flux to an arbitrary point on the surface profile were described in Chapter 2.

Integration of the ion flux and surface advancement models was not as simple as anticipated. The difficulty arose from consideration of two facts: 1) shocks are frequently found at the ends of long straight surface segments (particularly at the start of processing), and 2) ions reflected from a planar surface (or straight wall segment in 2-D) cannot strike any other point on that surface. As a consequence, the reflected flux to the shock at the end of a straight segment receives no contribution from that segment. Yet a point infinitesimally removed from the shock on either side receives the full reflected flux from the segment on the opposite side. Discontinuities in the ion flux (and etching rate) appear at each shock.

The discontinuous ion flux is not caused by an approximation in the surface representation. The spatial discretization used throughout this work divides the surface into straight segments, thus assuring that every shock lies at the intersection of two straight segments. But straight wall segments do occur in real systems, so a more accurate discretization would not necessarily eliminate flux discontinuities.

The true error lies in a mismatch of the length scales for the actual surface and its numerical representation. Real surfaces do not contain shocks; the slope of

a real surface is continuous down to the atomic level, by which point diffusion processes eliminate etching rate discontinuities. Shocks in the numerical representation of a surface are approximations introduced to accommodate the limited resolution of digital computers. If sufficient resolution and computing power were available, the true surface could be modeled in molecular detail (and, of course, surface advancement algorithms would be unnecessary).

A practical solution requires the introduction of curvature to the numerical model. There are two methods for this: the first, which is conceptually simpler and was actually used in this work, involves replacing every shock on the surface with a small circular arc joining the two wall segments (Figure 6.1). Implementation is relatively straightforward, and the surface advancement is also simplified (because the new surface consists solely of "smooth" sections).

The difficulty with curving the surface is that it introduces an error in the final location of points which originate in the shock. Moving points from the shock to an arc displaces both their initial and final positions from the correct values. In some cases, the error could accumulate between time steps as the shock forms, is replaced by an arc, reforms in the next time step, is replaced again, and so on. The displacement error is related to the radius chosen for the circular arc. But the radius cannot be reduced indefinitely, because points along the arc must remain distinguishable. Additional difficulties arise when the distance between converging shocks (as in Figure 5.21) approaches the chosen arc dimension.

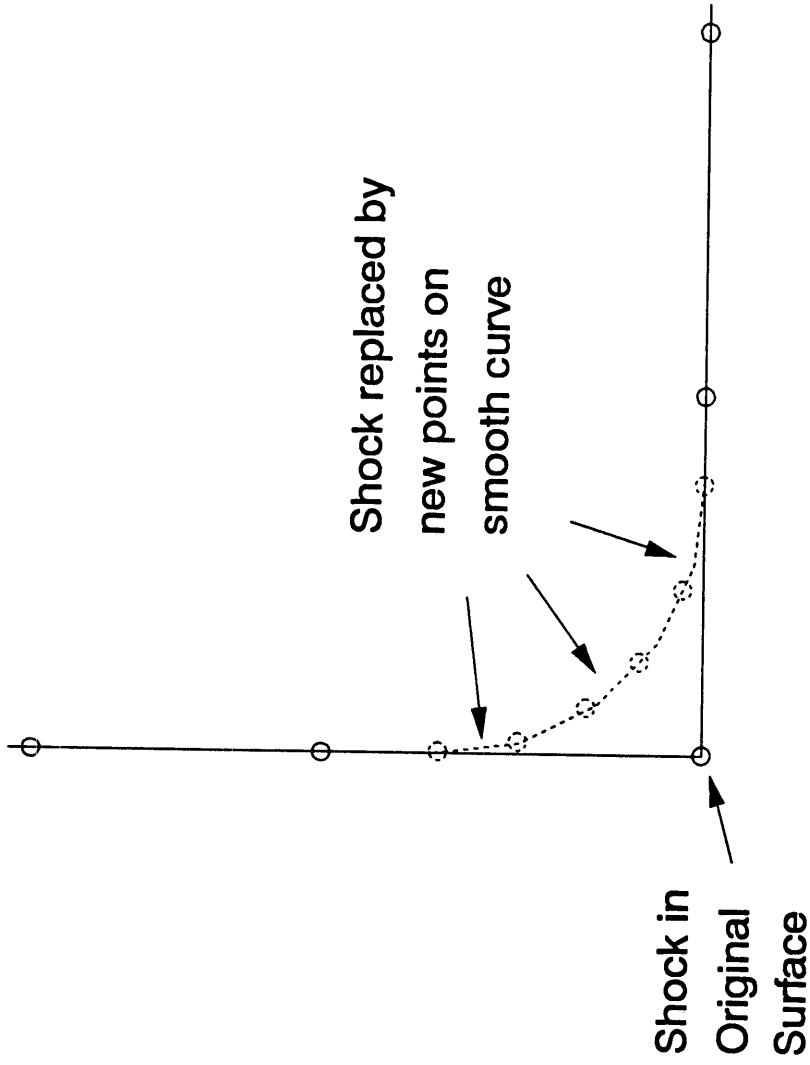


Figure 6.1: Replacing shocks with smooth curves to avoid ion flux and etching rate discontinuities.

A second approach, which was not implemented because of greater complexity but which may remove the limitations on arc radius, would be to temporarily displace each point from the shock during the ion flux computation. The simplest approach would be to introduce a circular arc as before and compute the ion flux to a series of artificial points on that arc. The ion fluxes to the artificial points would then be applied to the actual points in their actual positions (in the shock). This approach also entails some error, but this error is caused by spatial variations in the ion flux and should be smaller than the displacement error introduced by breaking up the shocks.

Both of these methods introduce some errors. The distinction between the two techniques can be stated as follows: the first approach (curving the shocks) solves the wrong problem, but does so correctly. The second provides an incorrect solution to the correct problem. The choice of which to implement depends upon the available resolution and the labor cost of coding.

6.2 Etching Rate vs. Slope

The second major integration issue also arose from the information requirements of the surface advancement algorithm. The characteristic equations for

point motion (Equations (5.1) and 5.2)),

$$\dot{x} = ER \sin\theta + ER_{\theta} \cos\theta \quad (6.1)$$

and

$$\dot{y} = -ER \cos\theta + ER_{\theta} \sin\theta , \quad (6.2)$$

showed that the trajectories depend upon both the etching rate (ER) and its derivative with respect to surface inclination angle in the 2-Dimensional plane containing the surface profile (ER_{θ}). As was discussed in Chapter 4,

$$ER_{\text{total}} = ER_{\text{thermal}} + ER_{\text{physical}} + ER_{\text{ion enhanced}} , \quad (6.3)$$

or

$$ER = ER_T + ER_{PS} + ER_{IE} , \quad (6.4)$$

where

$$ER_{PS} = \iint_{\hat{A}} \frac{dI}{dA} Y_{PS} dA , \quad (6.5)$$

and

$$ER_{IE} = \iint_{\hat{A}} \frac{dI}{dA} Y_{IE} dA . \quad (6.6)$$

The term \hat{A} refers to the solid angle of plasma and sidewall visible to the point in question. ER_0 also comprises three components:

$$\frac{\partial ER}{\partial \theta} = \frac{\partial ER_T}{\partial \theta} + \frac{\partial ER_{PS}}{\partial \theta} + \frac{\partial ER_{IE}}{\partial \theta} . \quad (6.7)$$

The thermal etching rate is isotropic, so

$$\frac{\partial ER_T}{\partial \theta} = 0 , \quad (6.8)$$

while

$$\frac{\partial ER_{PS}}{\partial \theta} = \iint_A \left[\frac{\partial}{\partial \theta} \left(\frac{dI}{dA} \right) Y_{PS} dA + \frac{dI}{dA} \frac{\partial Y_{PS}}{\partial \theta} dA + \frac{dI}{dA} Y_{PS} \frac{\partial}{\partial \theta} (dA) \right], \quad (6.9)$$

and

$$\frac{\partial ER_{IE}}{\partial \theta} = \iint_A \left[\frac{\partial}{\partial \theta} \left(\frac{dI}{dA} \right) Y_{IE} dA + \frac{dI}{dA} \frac{\partial Y_{IE}}{\partial \theta} dA + \frac{dI}{dA} Y_{IE} \frac{\partial}{\partial \theta} (dA) \right], \quad (6.10)$$

The relationship between A and θ depends upon the coordinate system chosen. The derivative of ion flux is found from

$$\frac{dI}{dA} = IAD(\theta_g) P(\theta_s) (1 - P(\theta_t)) \cos \theta_t, \quad (6.11)$$

as shown previously in Equation (2.3). The gas-phase and sidewall incidence angles θ_g and θ_s depend only upon the position of the target point and not upon its slope. The 3-Dimensional ion arrival angle at the target point, θ_t , depends upon the 2-D

surface inclination θ in a manner that depends upon the chosen geometry and coordinate system. In general,

$$\frac{\partial}{\partial \theta} \left(\frac{dI}{dA} \right) = IAD(\theta_s) P(\theta_s) \left[(P(\theta_s) - 1) \sin \theta_t - \frac{\partial P(\theta_s)}{\partial \theta_s} \cos \theta_t \right] \frac{\partial \theta_t}{\partial \theta}, \quad (6.12)$$

which is complicated but readily computed if the reflection probability P is differentiable. The derivative of ion etching yield with respect to slope,

$$\frac{\partial Y(\theta_s)}{\partial \theta} = \frac{\partial Y(\theta_s)}{\partial \theta_s} \left(\frac{\partial \theta_s}{\partial \theta} \right), \quad (6.13)$$

includes the variation of yield with ion arrival angle. This variation is well understood for physical sputtering (Y_{PS}), but not known for ion-enhanced etching (Y_{IE}). Ion-enhanced etching dominates industrially important processes, so the lack of yield vs. angle data is an important issue. Other researchers have assumed the yield to be independent of angle, but such an assumption is weak without direct evidence.

6.3 Surface Reaction Kinetics

As the discussion of reactant transport in Chapter 4 showed, the relationship

between ion flux, reactant flux, and etching rate influences not only the etching behavior at individual points but also the transport of reactants throughout the feature. The ion and reactant fluxes within a feature can vary by several orders of magnitude from point to point. Therefore, an understanding of the reaction rate over a broad range of parameters will be essential for analysis of etching in surface features. Furthermore, the preceding section of this Chapter established the need for knowledge of the (ion arrival) angular dependence of etching rate.

Several researchers have invested substantial effort in the measurement of etching kinetics, and it was originally hoped that the information needed for profile simulation would be available in the literature. This section explores the availability of such data and its suitability for use in profile simulation.

6.3.1 History

The synergistic ability of ions and radicals to increase the etching rate was demonstrated by Coburn and Winters in their famous XeF_2/Ar^+ experiment [Coburn and Winters, 1979] [Winters and Coburn, 1985]. They measured the etching rate of a silicon sample during exposure to XeF_2 vapor and/or an Ar^+ ion beam. When the XeF_2 vapor alone was used, they observed a small etching rate (because XeF_2 reacts spontaneously with Si at room temperature). Using just the Ar^+ beam also produced a low etching rate (corresponding to the physical sputtering of Si atoms through momentum transfer). However, applying both the ion beam and the XeF_2 vapor

simultaneously produced a much higher rate than was obtained with either beam alone. This behavior is common in ion-enhanced etching processes: radicals alone induce chemical reaction, but at a rate that is limited by activation energy barriers; ions alone provide energy but can only remove surface atoms by the less efficient physical sputtering mechanism; radicals and ions together give rapid reaction to volatile products.

The specific reaction pathways involved in etching by ions and radicals are not fully understood [Winters and Coburn, 1985]. For most purposes, however, the details are not necessary as long as the etching behavior is known for the expected operating conditions. For this reason, Harper, *et al.* [1981], chose to describe the total etching rate as the sum of the three components ER_T , ER_{PS} , and ER_{IE} , as shown in Chapter 4 and Equation (6.4).

Gray, *et al.* [1993], utilized such an approach to obtain a self-consistent model for the etching of silicon by fluorine over a wide range of conditions. The thermal and physical etching rates are assumed to retain (approximately) their baseline values, and the ion-enhanced component is adjusted to yield the correct total rate. Self-consistency is achieved by incorporating surface fluorination effects in a reactive site model.

The reactive site model was used to account for interactions between the ion-driven mechanisms (ER_{PS} and ER_{IE}), and is justified as follows: in the absence of

reactive radicals, the surface is "clean" and consists solely of silicon atoms (Figure 6.2a). Under these conditions, the only pathway for ion-based etching is physical sputtering. Increasing the radical concentration (or flux to the surface) slightly results in the formation of some silicon-fluorine bonds, changing the surface composition to a mixture of pure silicon and SiF_x (x typically 1-3). The partially reacted surface atoms are more readily converted to SiF_4 during subsequent radical and ion bombardment, thus opening the more efficient ion-enhanced pathway and increasing the yield of silicon atoms removed per incident ion (Figure 6.2b). At high radical flux, all exposed silicon atoms are fluorinated, all etching proceeds via the ion-enhanced mechanism, and the yield per ion reaches its peak value (Figure 6.2c). Further increases in radical flux have little effect. Other research has confirmed both the saturation of silicon etching yield at high fluorine flux [Tu, *et al.*, 1981] [Gerlach-Meyer, 1981], and the presence of a fluorinated layer on the silicon surface during plasma etching [Chuang, 1980] [McFeely, *et al.*, 1984].

The reactive site approach has enough intuitive appeal to suggest that it may be applicable to other systems. In particular, the current industrial processes for etching silicon involve conversion of silicon to multiply-halogenated species (such as SiF_4 , SiCl_4 , etc.). It is difficult to believe that such reactions could proceed without the initial formation of some sort of halogenated surface layer, so the qualitative behavior of the ion etching yield vs. radical flux should be similar for most systems. However, what is needed for profile simulation is an identification of the important factors in determining the etching rate, and a quantitative description of the

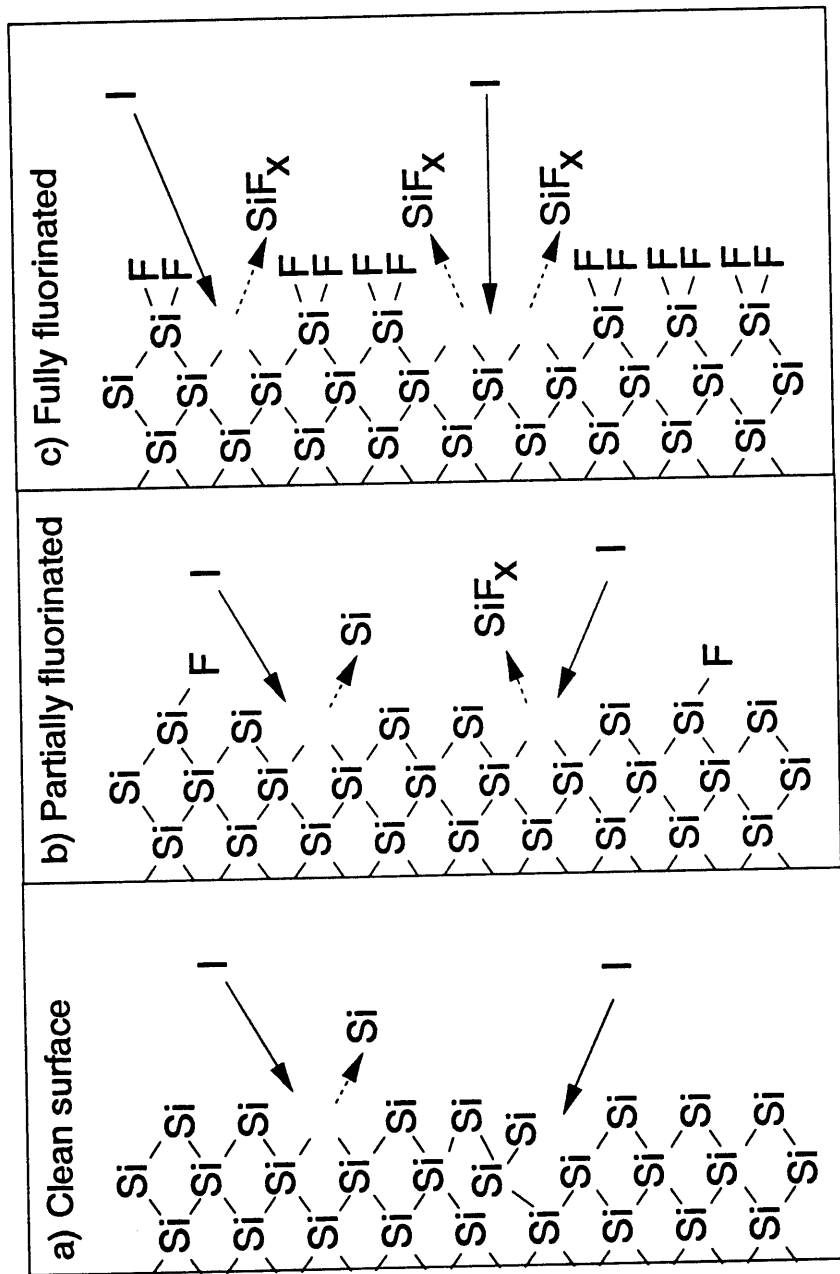


Figure 6.2: Effect of reactant availability on ion etching yield. In a), the surface is clean and physical sputtering is the only etching mechanism. In b), some surface sites are fluorinated and some reactive etching takes place. In c), the surface is fully covered with fluorine, and all etching is reactive.

relationship between those factors and the etching rate. In the absence of some as yet unavailable unifying theory, the kinetic mechanism and rate parameters must be considered for each combination of surface material and reactive radical. A review of the data available from the published literature comprises the remainder of this section.

6.3.2 Fluorine-based etching of Si and SiO₂

Although current industrial practice is shifting toward the use of chlorine- and bromine-based plasmas, many of the earlier processes utilized fluorocarbon feed gases (such as CF₄) for etching both silicon and oxide. Furthermore, laboratory simulations of fluorine discharges are relatively convenient compared to other halogens. As a consequence, the fluorine system has been studied in more depth and more detail than any other.

Coburn and Winters [1979, 1985, 1987] have conducted a series of experiments aimed at determining the fundamental mechanisms by which ion bombardment influences the reaction of fluorine and silicon. Others, such as Donnelly, *et al.* [1984], Booth, *et al.* [1989], and Butterbaugh [1990] have considered the effect of discharge conditions on etching behavior. Houle [1983, 1986] evaluated the influence of doping on silicon etching. Variations in etching yield with the ratio of radical to ion flux at the surface were reported by both Tu, *et al.* [1981] and Gerlach-Meyer [1981]. Finally, Mayer, *et al.* [1981], have utilized ion beams to consider energy and angle of

incidence effects.

However, the only published work to consider this system in a manner and depth conducive to use in profile simulation was performed by Gray, *et al.* [1993], which has also been discussed in Chapter 4. As was mentioned previously, they followed the lead of Harper, *et al.* [1981] by considering the total etching rate as the sum of thermal, physical sputtering, and ion-enhanced components. The latter contribution was found by subtracting known values for the first two from the measured etching rate.

The thermal reaction rate was taken from the data of Flamm, *et al.* [1981], as

$$ER_{\text{thermal}} = k_0 Q_F \exp\left(\frac{-E_a}{k_b T}\right), \quad (6.14)$$

where Q_F is the incident flux of fluorine atoms on the surface, E_a is the activation energy (reported as 0.108 eV), and k_0 is a constant. Conversion of Flamm's data to the incident flux basis used in Equation (6.14) yields a value for k_0 of 0.03. The thermal etching rate given here has the units of incident fluorine flux, typically ($\text{atoms cm}^{-2} \text{s}^{-1}$).

Ion enhanced etching has been conjectured to proceed by a number of different chemical mechanisms with etch products of varying stoichiometry. Gray, *et*

al. [1993] concentrated on two primary products: fully fluorinated (SiF_4), and partially fluorinated or unsaturated products (including SiF , SiF_2 and SiF_3). They used XPS (X-ray Photoelectron Spectroscopy) to analyze the product distributions under various conditions, and found that the average stoichiometry of the unsaturated products could be well represented by assuming SiF_2 as the dominant component. This is consistent with earlier studies [Tu, *et al.*, 1981]. They next defined the number ratio of unsaturated to saturated products as the "branching parameter," and used this figure to account for all unsaturated product generation. The branching parameter was observed to depend primarily upon ion energy.

Gray, *et al.* [1993] also observed the ion-enhanced etching rate to depend not only upon ion flux, but also upon the fluorination state of the surface. In the presence of an incident fluorine flux, a partially fluorinated layer forms on the surface [Chuang, 1980] [McFeely, *et al.*, 1984], and the yield of silicon removed per incident ion is observed to increase in proportion to the fractional surface coverage. ER_{IE} is thus the product of four terms:

$$\text{ER}_{\text{IE}} = \beta_2 (1 + b) C_F I \quad (6.15)$$

β_2 is the yield of saturated product (SiF_4) per incident ion, b is the branching parameter described above, C_F is the fractional surface fluorination (coverage), and

I is the incident ion flux. The variation of β_2 and b with ion energy were reported as

$$\beta_2 = 0.687(\sqrt{E, eV} - 2) \quad (6.16)$$

and

$$b = 0.009\sqrt{E, eV} . \quad (6.17)$$

The fractional surface fluorination was reported to follow

$$C_F = \frac{0.2 R}{0.2 R + 2\beta_2(1 + b)} \quad (6.18)$$

where

$$R \equiv \frac{Q_F}{I} . \quad (6.19)$$

Gray, *et al.* [1993], used independent ion and radical beams to explore the etching behavior over a wide range of flux ratios (from zero to several thousand). However, atomic fluorine concentration measurements by Kiss and Sawin [1992] and d'Agostino, *et al.* [1981] suggest that practical values for R range from a few hundred

to a few thousand.

The final etching component, ER_{PS} , was taken as

$$ER_{PS} = p_0 I (1 - C_F) \quad (6.20)$$

where p_0 is the yield of silicon atoms per incident ion, I is the incident ion flux, and the term $(1 - C_F)$ is added to account for depression of physical sputtering by surface fluorination. Only bare (unfluorinated) surface silicon atoms are available for conversion directly to volatile Si, so increasing fluorination of the surface is expected to block the physical sputtering pathway. The energy dependence of p_0 was given by Gray [1992] as

$$p_0 = 0.0337(\sqrt{E, eV} - \sqrt{20}) . \quad (6.21)$$

Gray [1992] reported similar behavior for the fluorine etching of SiO_2 , with the following differences:

$$ER_T = .006 Q_F \exp\left(\frac{-.163 \text{ eV}}{k_b T}\right), \quad (6.22)$$

$$\beta_2 = 0.053(\sqrt{E, \text{eV}} - 2) , \quad (6.23)$$

$$b = 0.007\sqrt{E, \text{eV}} , \quad (6.24)$$

$$C_F = \frac{0.02 R}{0.02 R + 2\beta_2(1 + b)} , \quad (6.25)$$

and

$$p_0 = 0.0139(\sqrt{E, \text{eV}} - \sqrt{18}) . \quad (6.26)$$

The energy and flux dependencies of the Si and SiO₂ etching yield are summarized in Figures 6.3 and 6.4.

Gray [1992] also attempted to extract a surface reaction network from his

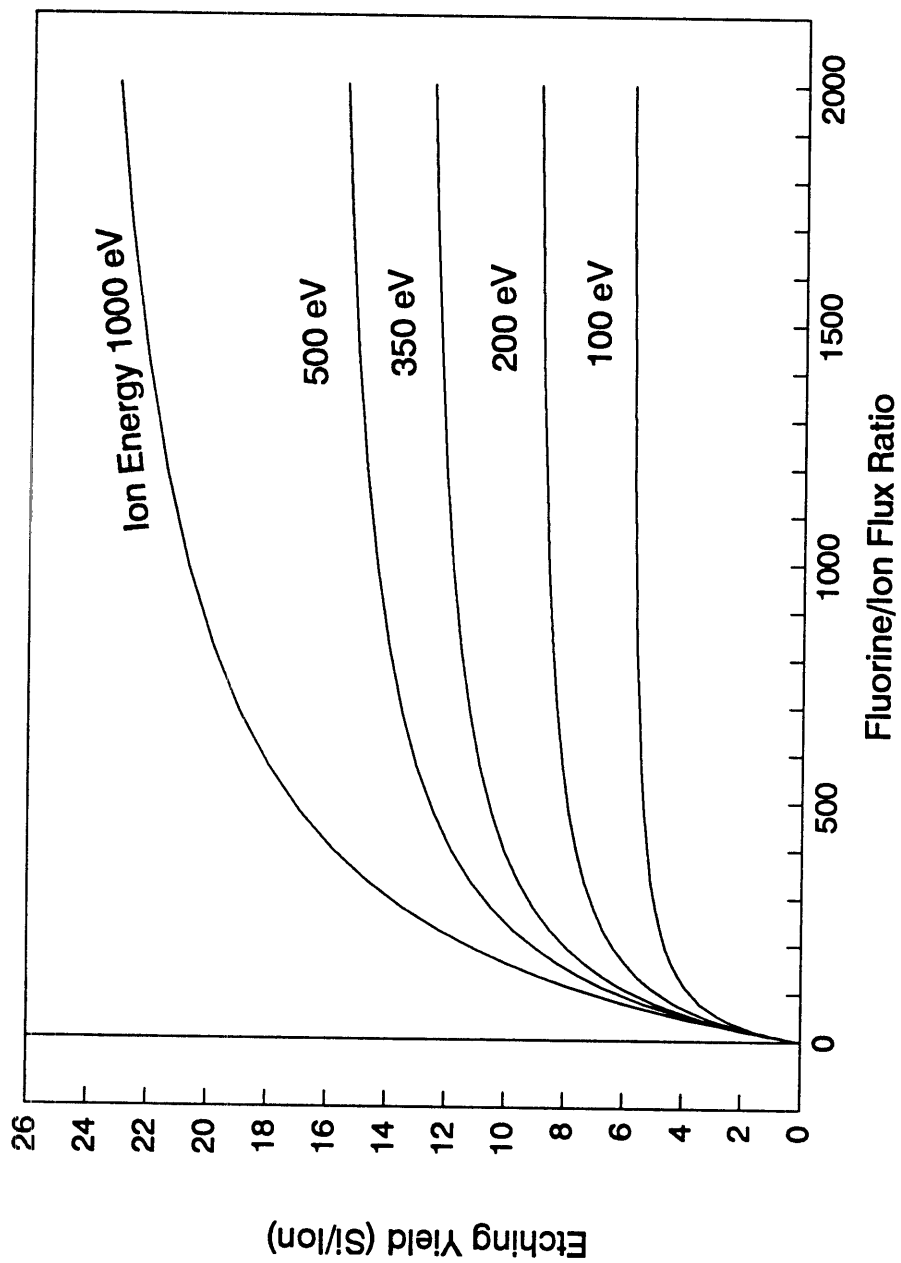


Figure 6.3: Ion-enhanced etching behavior for Silicon and Fluorine, according to Gray, *et al.* [1993]. Etching yield increases with Fluorine/Ion flux ratio, approaching saturation at highest ratios. Yield increases with square root of ion energy.

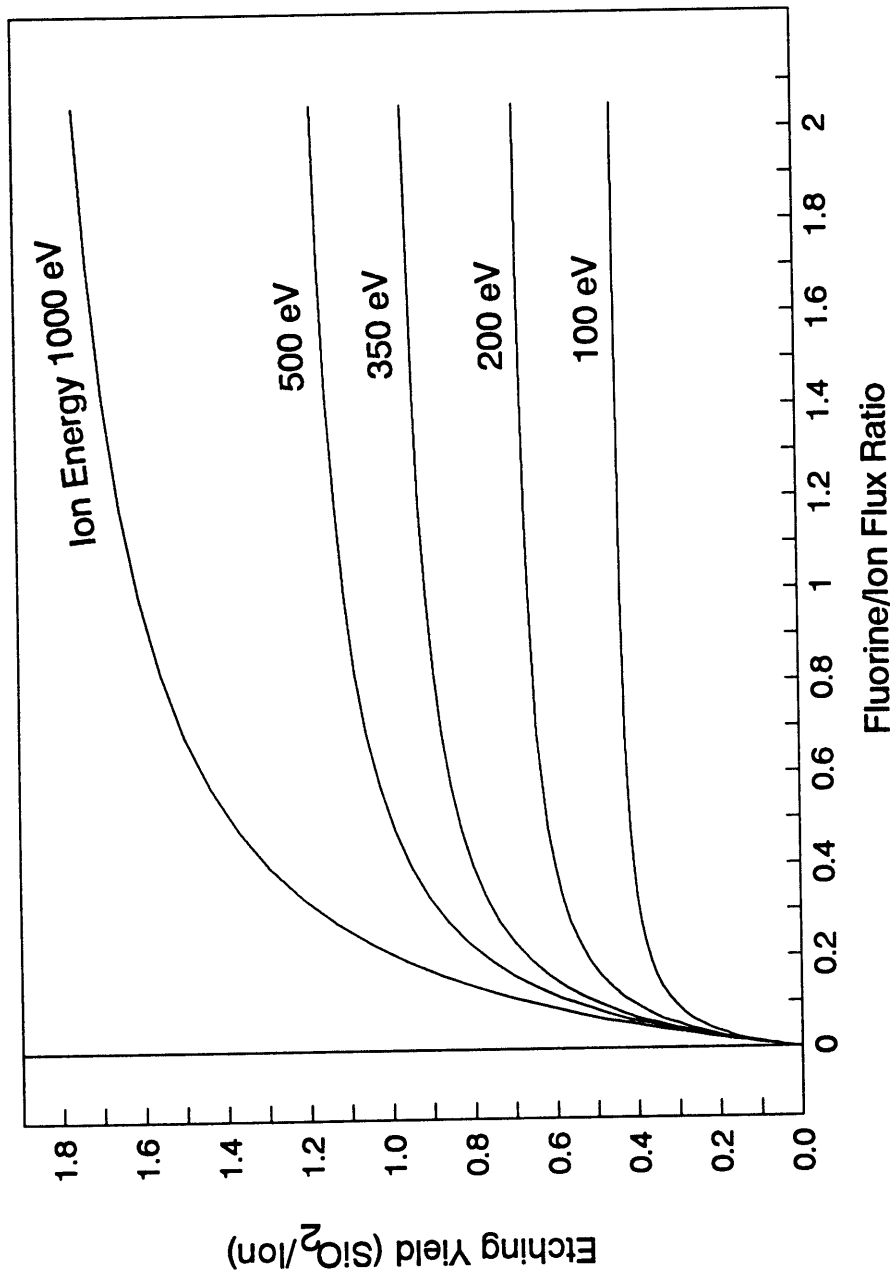
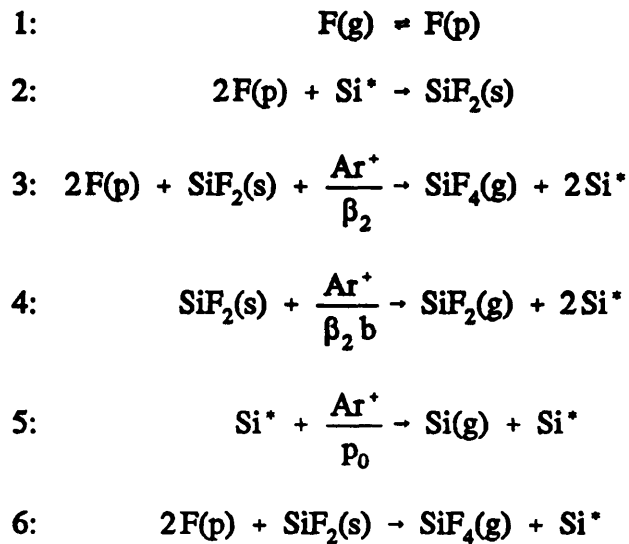


Figure 6.4: Ion-enhanced etching behavior for Silicon Dioxide and Fluorine, according to Gray, et al. [1993]. Etching yield increases with Fluorine/ion flux ratio, approaching saturation at highest ratios. Yield increases with square root of ion energy.

data, obtaining



where (g), (p), and (s) refer to species that are in the gas phase, physisorbed on the surface, or bound to the surface, respectively, and Si^* refers to an available reactive site. This network appears to account for the limiting flux conditions (i.e. Ar^+ or F(g) equal to zero), but the Si^* and $\text{SiF}_2\text{(s)}$ concentrations do not balance at steady state. This problem could be eliminated by adjusting the stoichiometry of Si^* , but it was not possible to reconfigure this reaction set to simultaneously balance at steady state, account for the experimentally observed coverage dependence, and reduce to the thermal or physical sputtering limits. This paradox underscores both the difficulty in identifying fundamental reaction steps, and the acceptability of a carefully derived empirical model. Gray's model is useful for predicting the etching behavior over a broad range of process conditions, even though the underlying reaction pathway is not understood.

6.3.3 Chlorine-based etching of Si

Chlorine-based etching processes for silicon have recently gained importance, owing to their high selectivity (Si over SiO₂) and the emergence of polysilicon as a gate material for MOS transistors. The increased industrial interest in chlorine-based processes has been accompanied by research on various components of the etching process.

Ogryzlo, *et al.*, have measured the thermal etching of silicon with molecular [1988] and, more recently, atomic chlorine [1990]. In both cases, the etching rate increased with molecule or atom flux to the surface, surface temperature, and n-type doping level of the silicon. The Cl-atom work also considered the effect of crystallography, finding higher rates for polycrystalline material.

Both Barker, *et al.* [1983] and McNevin and Becker [1985] have studied Ar⁺-enhanced etching of silicon in Cl₂ backgrounds. Both groups found flux behavior reminiscent of that observed previously [Gray, *et al.*, 1993] for fluorine etching: the etching yield per incident ion initially increased with the Cl₂ pressure, then saturated at high pressure.

Tachi and Okudaira [1986] etched silicon with a beam of Cl⁺, comparing the etching rate to the observed yield for inert ions of similar mass to infer the qualitative behavior of the ion-enhanced reaction. They suggested qualitative

saturation behavior at high neutral fluxes, but did not actually etch under simultaneous ion and radical exposure and did not present enough quantitative data for use in simulation.

In summary, the published data for chlorine etching suggests that the mechanisms are similar to those observed for fluorine, but do not provide the kinetic parameters necessary for accurate simulation at this time. The reason for this can probably be traced to the nature of Cl radicals: they are easy to produce but difficult to maintain in sufficient quantity for kinetic experiments. As shown by Deshmukh and Economou [1993], Cl₂ is readily dissociated in an RF or microwave discharge, but Cl has a very high surface recombination velocity. This makes it difficult to separate the discharge from the sample without losing the Cl atoms (through recombination to Cl₂).

6.3.4 Proposal for Additional Measurements

The last two sections have shown that, although many people have spent years studying the kinetics of plasma etching reactions, none has provided the full range of information necessary for use in profile simulation of currently important processes. While Gray, *et al.* [1993], conducted a thorough study of silicon etching, their use of fluorine as the primary etchant and their failure to explore the effect of ion incidence angle leave their data somewhat lacking. No other researcher has presented such a complete analysis of the ion and reactant flux dependence.

Predictive simulation of surface profile evolution for current processes is not possible without complete kinetic information.

The shortage of kinetic data prompted an adjustment in the strategy of this project. Whereas the original proposal had called for a primarily theoretical/numerical effort, additional model development could not be justified without confirmation of the existing portions. The most logical step, and the one which would make the greatest contribution to the field, was to abandon model development in favor of kinetic measurements. The distinguishing factor in these measurements would be the consideration of ion arrival angle in reactive (ion-enhanced) etching.

Because of its current industrial importance, the system chosen for study was the etching of polycrystalline silicon (polysilicon, or poly-Si) with chlorine. Polysilicon is widely used to form gate electrodes in MOSFETs. Gate definition is one of the most demanding processes in terms of dimensional control and etching selectivity. Chlorine and chlorine-based plasmas are popular for gate definition because they offer high selectivity to the thin oxide under the poly-Si film. Chlorine etching of polysilicon was a natural choice for further kinetic study. The remainder of this thesis is devoted to the construction of equipment for and initial results from that investigation.

Chapter 7

Equipment for Etching Polysilicon with Chlorine

7.1 Reactor Vessel and Vacuum System

7.1.1 Overview

The main reactor vessel and vacuum system were adopted from the previous etching studies performed by D. C. Gray. Detailed drawings and specifications can be found in his thesis [Gray, 1992], but a simplified description is included here.

The main vacuum chamber is based on a cylinder 8" in diameter, as shown in Figure 7.1. The bottom of the chamber is open to a cryogenic pump (model Cryo-Torr 8 from CTI-Cryogenics, Mansfield, MA), while the "back" has been joined to a sample exchange/load lock system. The vertical midplane of the cylinder contains three 3" diameter ports for attaching ion or radical beam sources; hence, the system is commonly referred to as the "3-beam" system. The three ports are oriented such that one of them lies along the outward surface normal of the sample, with the other two displaced by 45° to either side. Only two beams were required for this experiment, so one of the side ports was unused.

The chamber also included two 1.5" viewports designed for the entrance and

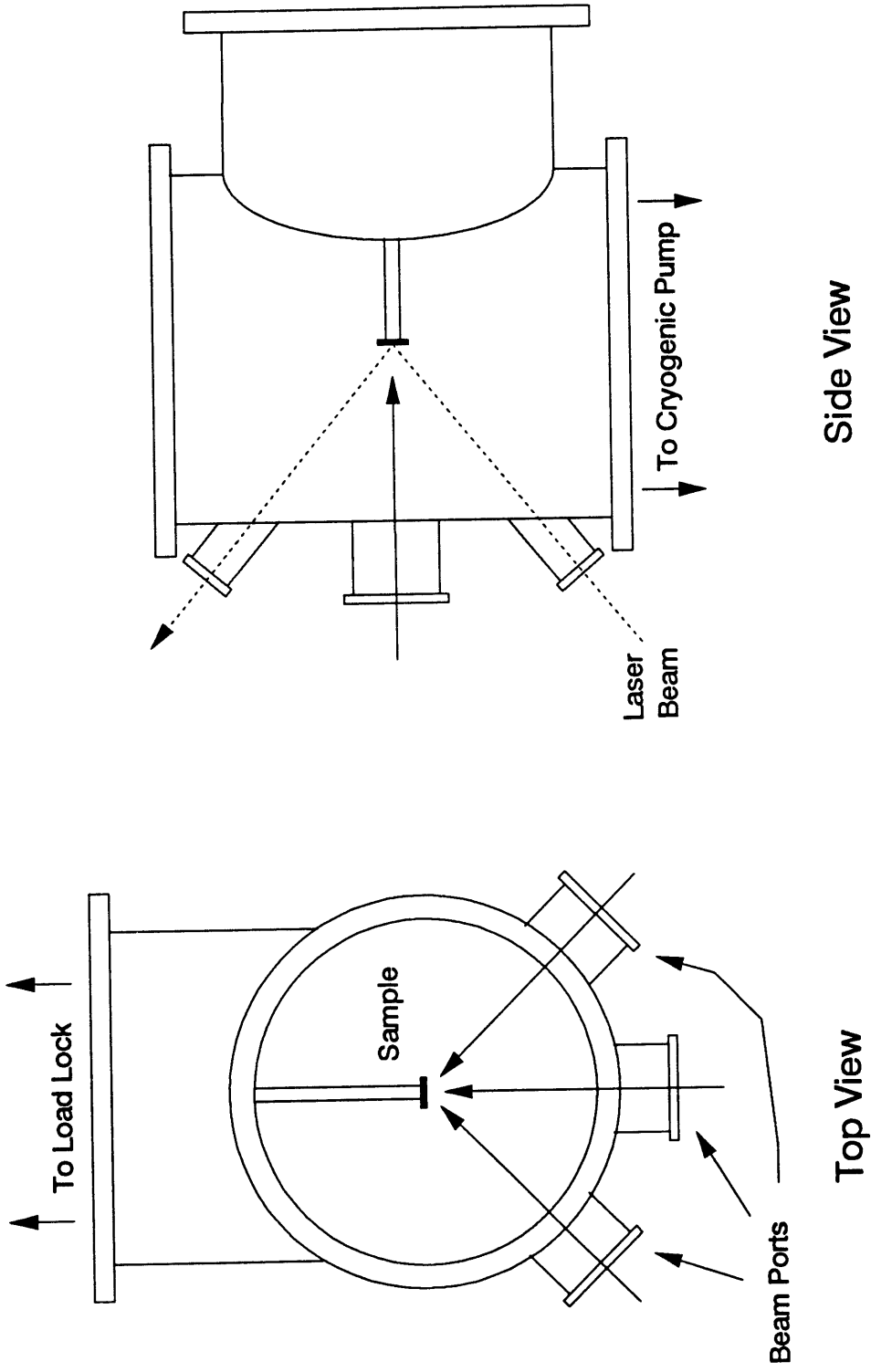


Figure 7.1: Schematic view of multi-beam etching apparatus.

exit of a laser beam reflected from the sample surface. These ports were placed above and below the center beam port, inclined at $\pm 40^\circ$ from the sample normal.

Additional ports and accessories provided visual access, ion gauge pressure measurement, mass spectrometric residual gas analysis, measurement of neutral beam flux, and electrical signals for sample temperature and heater power. These systems have all been described by Gray [1992], and will not be discussed here.

7.1.2 Modifications for Off-normal Ion Incidence

In its original configuration, as reported by Gray [1992], the top of the chamber was occupied by a rotatable mass spectrometer used for etch product identification. This system was removed and replaced with an 8" diameter (by 1" thick) Pyrex window. Not only did this allow better visual access for system operation, but it also provided a means for measurement of etching rate with off-normal ion incidence.

In normal operation, the sample is mounted perpendicular to its holder and the ion beam is directed along the sample normal. The etching rate is measured by laser interferometry, with the laser beam entering through the lower and exiting through the upper optical port (Figure 7.1). However, this scheme restricts the ion incidence angle to normal or 45° off-normal (if the ion beam is admitted through one of the side beam ports). Measurements at other incidence angles were not possible.

Replacing the rotatable mass spectrometer at the top of the chamber with a window provided a means for maintaining laser access while etching at other ion incidence angles. As shown in Figure 7.2, the ion incidence angle could be varied between 13.5° and 36.5° off-normal by changing the sample inclination and allowing the laser beam to exit through the top window. Higher incidence angles could be achieved by admitting the laser through the top viewport: the laser beam would exit through the same viewport for ion incidence of 40° , or through the top window for angles of 53.5° to 76.5° off-normal.

In practice, uncertainties in the sample mounting made *a priori* selection of the ion incidence angle impossible. This difficulty was accommodated by using the laser beam's points of entry (on the upper or lower viewport) and exit (through one of the viewports or the top window) to compute the direction of the sample normal. This direction was compared to the known direction of the ion beam to compute the necessary incidence angle.

Tilting the sample also changed the incidence angle of the atom beam, necessitating a correction of the atom flux measured for the usual sample location. The flux is measured in such a way that the usual atom beam incidence angle of 45° is already accounted for. The correction for other sample orientations was obtained from the sample normal direction and the atom beam direction, with the actual atom

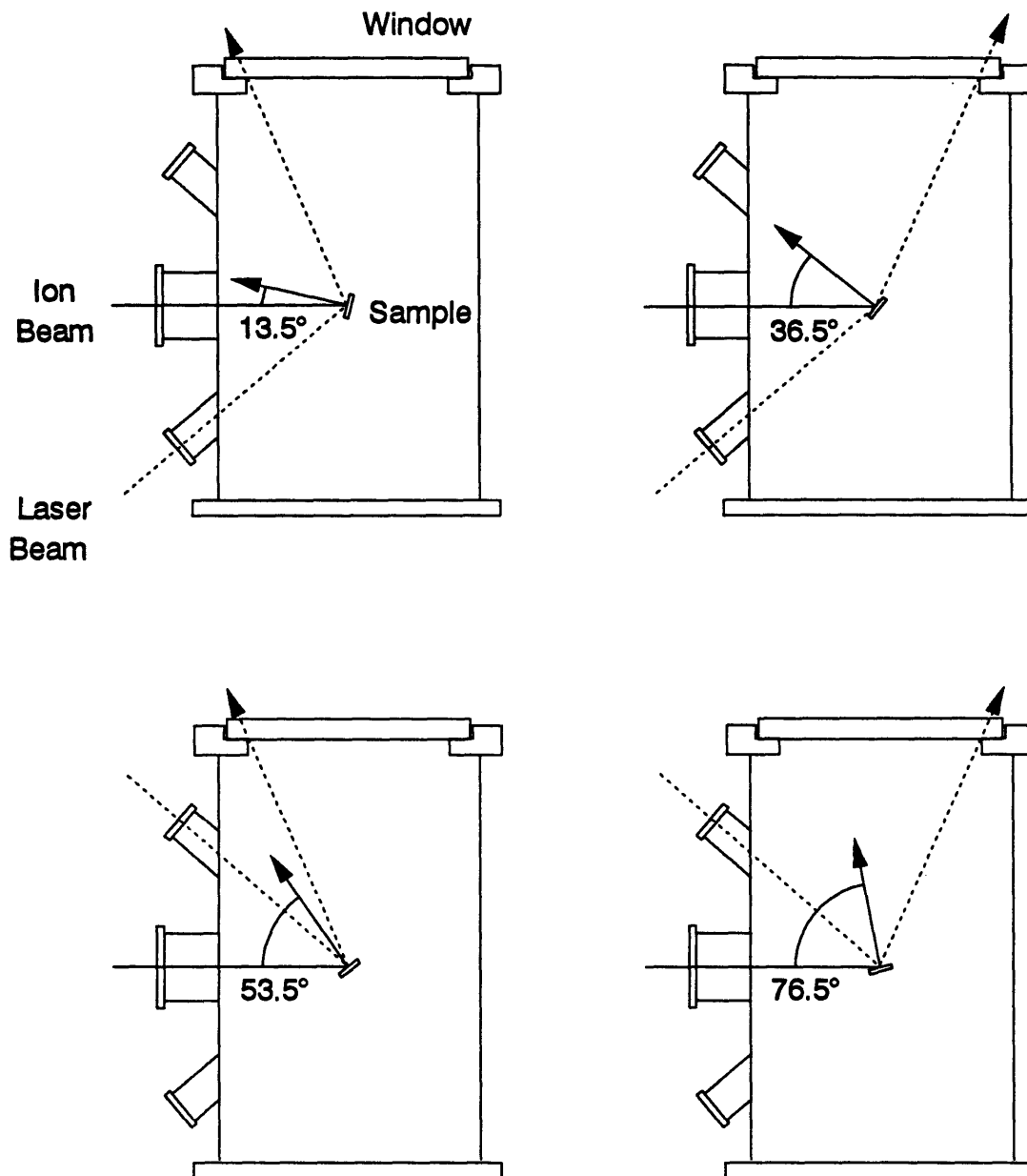


Figure 7.2: Measurement of etching rate at ion incidence angles other than normal. Ion incidence angle is varied by tilting sample. Etching rate is measured by letting laser beam exit through window on top of chamber.

flux given by

$$Q_{\text{Actual}} = Q_{\text{Measured}} \frac{\cos \theta}{\cos 45^\circ}, \quad (7.1)$$

where θ is the angle between the atom beam and the sample normal.

7.2 Ion Flux and Energy Analysis

Ion-enhanced etching rates are most commonly reported in terms of the etching yield, or the amount of surface material removed per incident ion. In order for such measurements to be successful, both the etching rate and the ion flux must be known with reasonable accuracy. Furthermore, the energy of an ion beam produced by the means employed in this study is not well known in advance; common practice requires adjustment of beam acceleration and discharge conditions to produce the desired energy. For these reasons, accurate measurement of the ion flux and energy (flux within a few percent and energy within a few eV) was important to the success of this kinetic study. Installation or construction of an accurate and reliable device for measuring the ion energy and flux was one of the highest priorities.

7.2.1 Measurement Technique

The principle for measuring ion beam flux and energy is relatively simple: if the ion beam is directed toward a conductive plate at some potential V , then only those ions with energy greater than V will reach the plate. Measuring the current as V is varied allows computation of the Ion Energy Distribution (IED) by

$$\frac{dI}{dE} = -\frac{1}{q} \frac{dJ}{dV}, \quad (7.2)$$

where V is the voltage applied to the "collector" plate, J is the current density arriving on the collector, q is the charge per ion, E is the ion energy, and I is the ion flux. Figure 7.3 illustrates the relationship between J , V , and the IED for an example beam.

The total ion flux could be found by simply measuring the total ion current when the collector is grounded, but this approach may not produce an accurate result. If the beam contains a significant number of low energy ions, which may not contribute to etching, then the total current may not be the proper figure for kinetic measurements. Therefore, it is more common to obtain the relevant ion flux by integrating the IED over the range of ion energies where the etching yield is substantial.

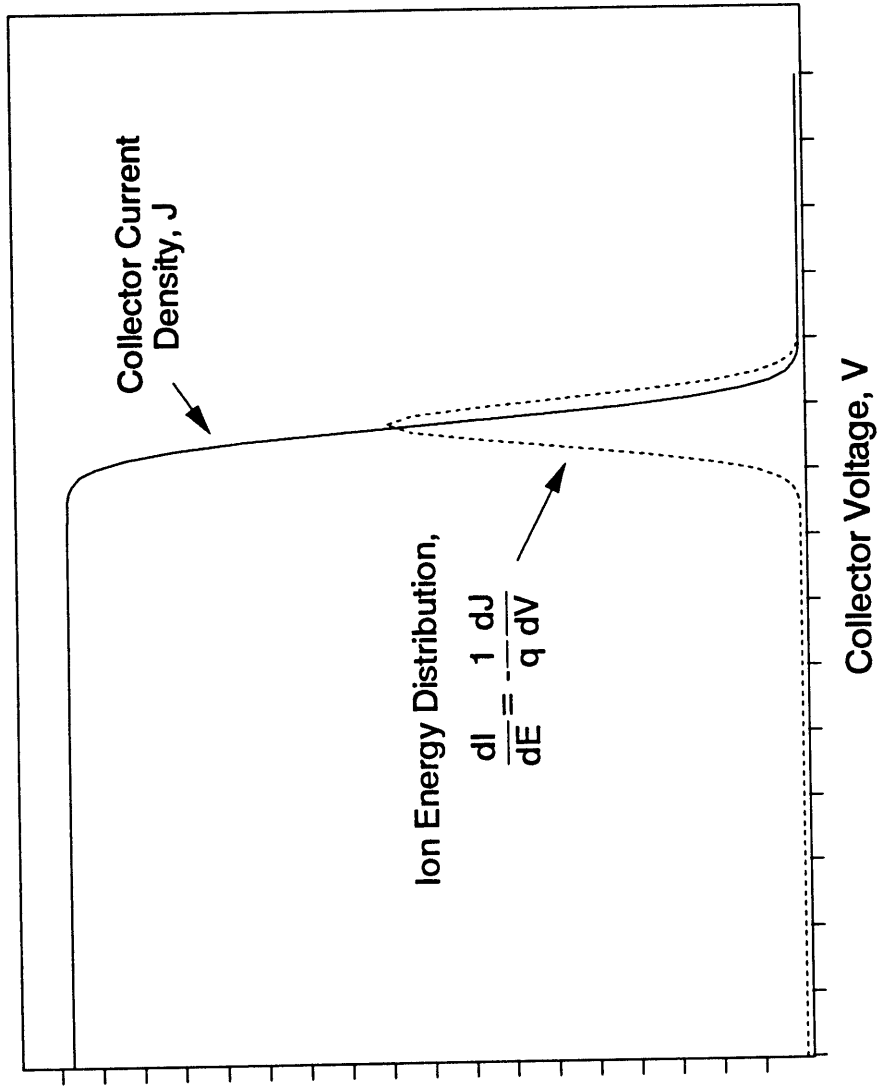


Figure 7.3: Example of current to ion collector and Ion Energy Distribution.

The apparatus for measuring the IED contains a few additional components, because the "ion" beam does not consist solely of ions. The beam is neutralized with electrons to inhibit space-charge spreading during transit from the source to the sample. These electrons must be screened before they reach the collector, or else they would subtract from the measured current. Furthermore, simply placing a biased collector plate in the beam path would induce a complicated field structure within the chamber, possibly perturbing the beam.

For these reasons, the conventional practice for measuring IED's is to use a "gridded" analyzer as shown in Figure 7.4. The outermost grid is held at ground potential to minimize leakage of fields into the chamber and perturbation of the beam. The second grid (called the "electron repeller") is held at a negative potential to remove the electrons from the beam, leaving only ions to reach the collector. The current arriving at the collector is measured as a function of applied bias to provide the IED. The current density (equivalent to ion flux) is found by dividing the collector current by the area of the collector (or, more commonly, the area of a small aperture placed in front of the grounded grid) and the transmittance of the grounded and electron repeller grid material.

The external circuitry required for operation of the gridded energy analyzer is also simple, consisting solely of a pair of power supplies (one each to bias the electron repeller and ion collector) and an ammeter in the collector circuit. This project utilized two different techniques, one using manually-adjusted power supplies

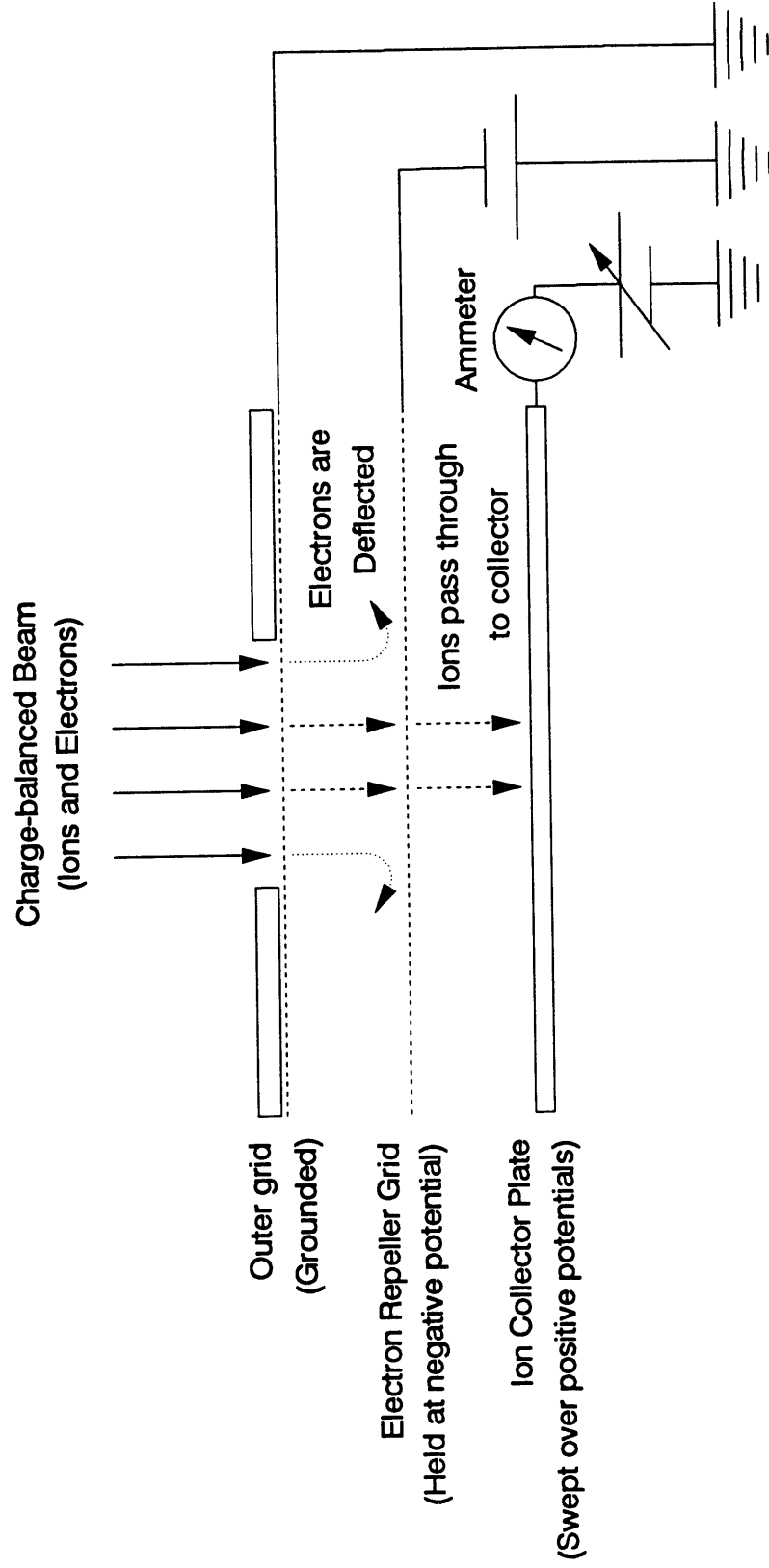


Figure 7.4: Schematic diagram of typical gridded ion energy analyzer.

and manual current measurements as described by Gray [1992], and one using a PC with digital to analog (D/A) and analog to digital (A/D) equipment to sweep the collector voltage and record the current. The PC-based system was more convenient to use but failed before the experiments were complete.

7.2.2 Gibson's Gridded Analyzer

The performance, energy resolution, and transportability (between vacuum systems) of a gridded analyzer depends upon the size and spacing of the grids. G. Gibson [1992] has invested a substantial effort in the design of energy analyzers for application in plasma etching systems, obtaining a very compact analyzer with high energy resolution. The entrance aperture is approximately 0.020" in diameter, and the grids are made of electroformed Nickel with 8 μm square holes and are placed 0.010" apart. The overall dimensions of the analyzer are on the order of 1/4", and energy resolution of less than 0.5 eV has been achieved.

A series of analyzers were constructed for use in this work, according to a modification of Gibson's design, as shown in Figure 7.5. However, the performance of these analyzers was unsatisfactory for several reasons. First and foremost, the current vs. collector bias curves did not follow the expected form (Figure 7.3). A sample of the actual measurement is shown in Figure 7.6. These measurements were adequate for estimating the ion energy, but were totally unsuitable for determining the total ion current with acceptable accuracy.

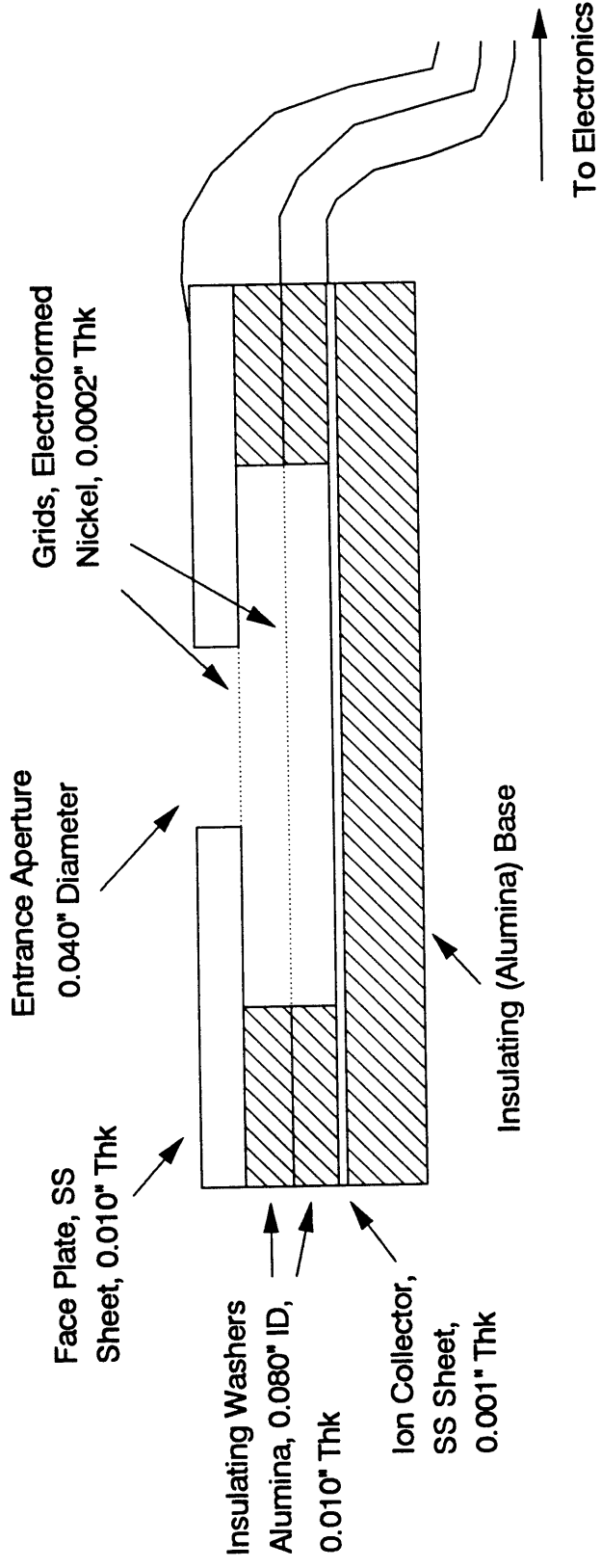


Figure 7.5: Gridded ion energy analyzer adapted from design by Gibson [1992]. Analyzer is cylindrically symmetric; view shown is a typical cross-section.

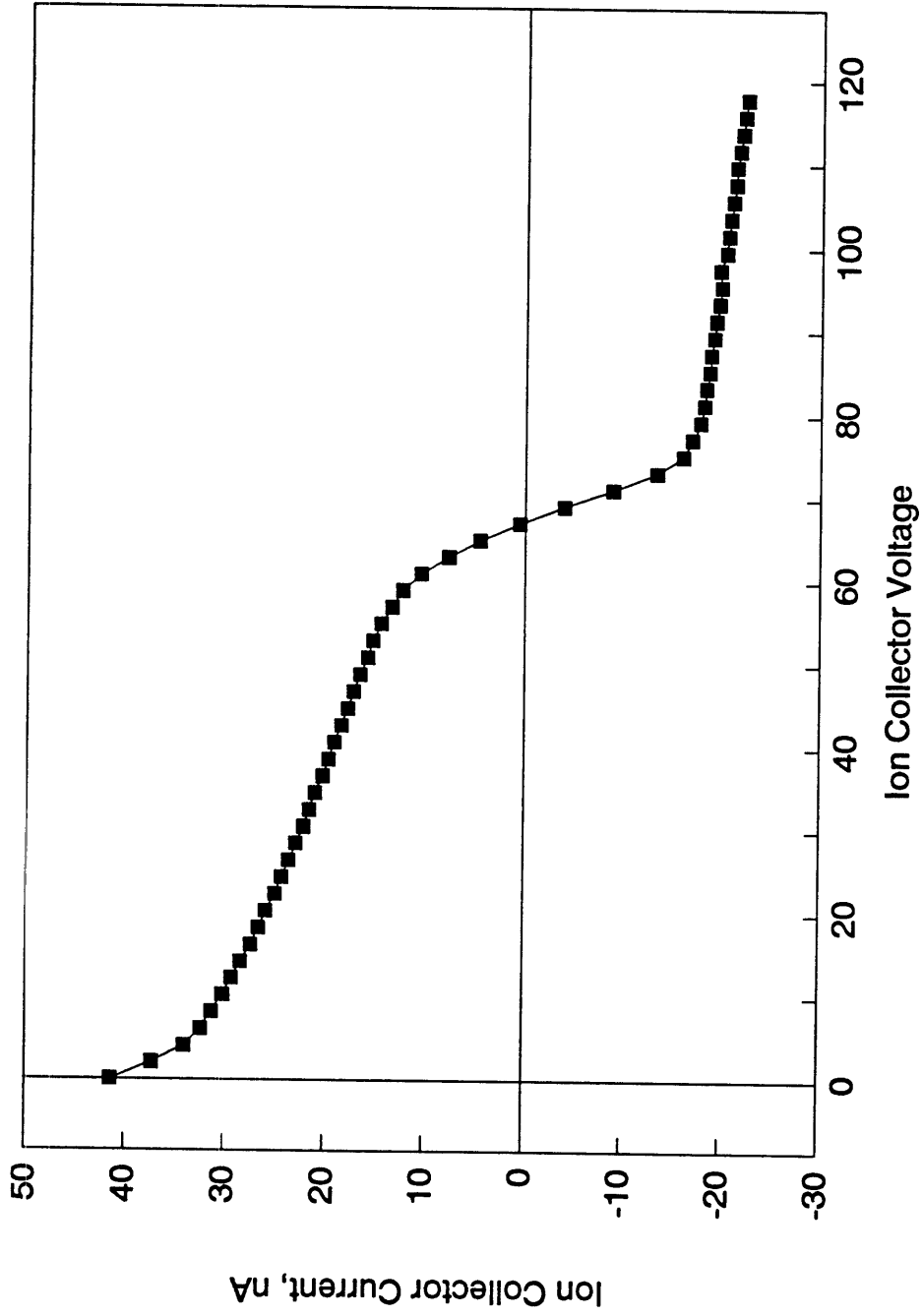


Figure 7.6: Typical ion collector current vs. voltage for original energy analyzer. Beam energy for this example was approximately 70 eV.

Several sources for the discrepancy between actual and expected current-voltage characteristics were explored. One possibility was the small size of the entrance aperture, which led to very low collector currents. The aperture diameter of 0.040" and the overall grid conductance of 13% produced collector currents on the order of a few nanoamps. However, reducing the aperture diameter did not worsen the behavior. Increasing the aperture size was prevented by the limited availability of insulating spacers with larger openings.

Isolation between the grids or the leads connecting to them was considered, because the curve shown in Figure 7.6 is somewhat reminiscent of a "normal" curve superimposed on an ohmic leakage. However, leakage between grids was negligible with the ion beam off, and could not be measured directly with the beam on.

Exposure of the connecting leads to the weak plasma in the vacuum chamber was another plausible source of leakage. Indeed, additional insulation and shielding appeared to improve the measurements. However, extreme difficulties in shielding the area of the vacuum feedthrough made it impossible to either prove that this was the source of the errors or to eliminate the problem.

Other possible causes included charging of the insulating surfaces inside the analyzer itself and charging of insulating deposits on the grids. The latter hypothesis was supported by allowing the repeller grid to "float," which maintained the qualitative character of the measurements but made the downward slope of the curve

even worse. Also, G. Gibson has observed similar behavior under some conditions and has tentatively linked it to deposition of quartz sputtered from the walls of his ECR chamber.

In addition, the analyzers built to this design suffered from poor yield (not all devices worked), poor reproducibility (from person to person) in build quality, and poor correlation between individual analyzers built together, to the same design, and by the same person. Furthermore, the gossamer Nickel grid material limited the useful lifetime of an analyzer to between a few hours and a few dozen hours in the beam.

The persistent difficulties with analyzers of this type, coupled with the fact that the small dimensions and high resolution were not needed for this project, led to the construction of a new analyzer of more conventional design. Because many of the possible causes for the poor measurement quality seemed to be related to leakage between the grids and between their connectors and the plasma, the new analyzer was designed to maximize electrical isolation.

7.2.3 High Isolation Analyzer

The new analyzer design differed from the one used previously in several

different ways:

1) The size was increased dramatically, to improve the signal level. Whereas the previous analyzers had used entrance apertures of 0.020" - 0.040" diameter, the new entrance aperture was 0.1253" diameter (nearly 10 times increase in area).

2) The separation between the grids was increased and the grid supports were redesigned to minimize the opportunities for leakage between grids within the analyzer. The original design used alumina washers encircling the entire active area of the grids. The new design utilized small alumina standoffs in three locations around the periphery of a grid support washer that was several times larger than the open (grid) area.

3) The entire analyzer was surrounded by a grounded metal can, so avoid charging of insulating surfaces in the beam path.

4) The connector leads from the analyzer to the feedthrough were replaced with Microdot™ miniature coaxial cables from Malco (S. Pasadena, CA). This necessitated the purchase of a custom-made feedthrough (to allow two Microdot connectors on a single 1 1/3" Conflat Miniflange).

5) To avoid the possibility that the source of Nickel grid material had been

contaminated, and to improve the grid lifetime, stainless steel grids were used. The chosen material was Buckbee-Mears (St. Paul, MN) #228, which has 0.003" diameter holes etched through 0.002" thick material.

Figure 7.7 shows the new analyzer design. The Microdot connectors were made by Malco and purchased from Ceramseal (New Lebanon, NY). The alumina insulators were purchased from Kimball Physics (Wilton, NH). The Teflon screws (needed to maintain the separation between grids without risk of short-circuit or leakage) were made to order by Berghof America (Concord, CA). The custom feedthrough was built to order by Sycon Instruments of E. Syracuse, NY, and all other components were fabricated by Sharon Vacuum Co. (Brockton, MA).

Figure 7.8 shows a typical current vs. voltage measurement taken with the new analyzer. Several features are evident. First, the currents measured are in the range of microamps, instead of nanoamps for the previous devices. This greatly reduced the sensitivity to noise in the ammeter and electronics. Second, even though the grid separation and hole size were both increased by a factor of nearly 5, energy resolution remains more than adequate for this application (+/- a few eV). Finally and most importantly, the current is nearly flat both below and above the beam energy, and the IED is sharp and free of noise.

The signal levels with the new analyzer are far higher than with the original design. However, the currents are lower and the voltages higher than for the typical

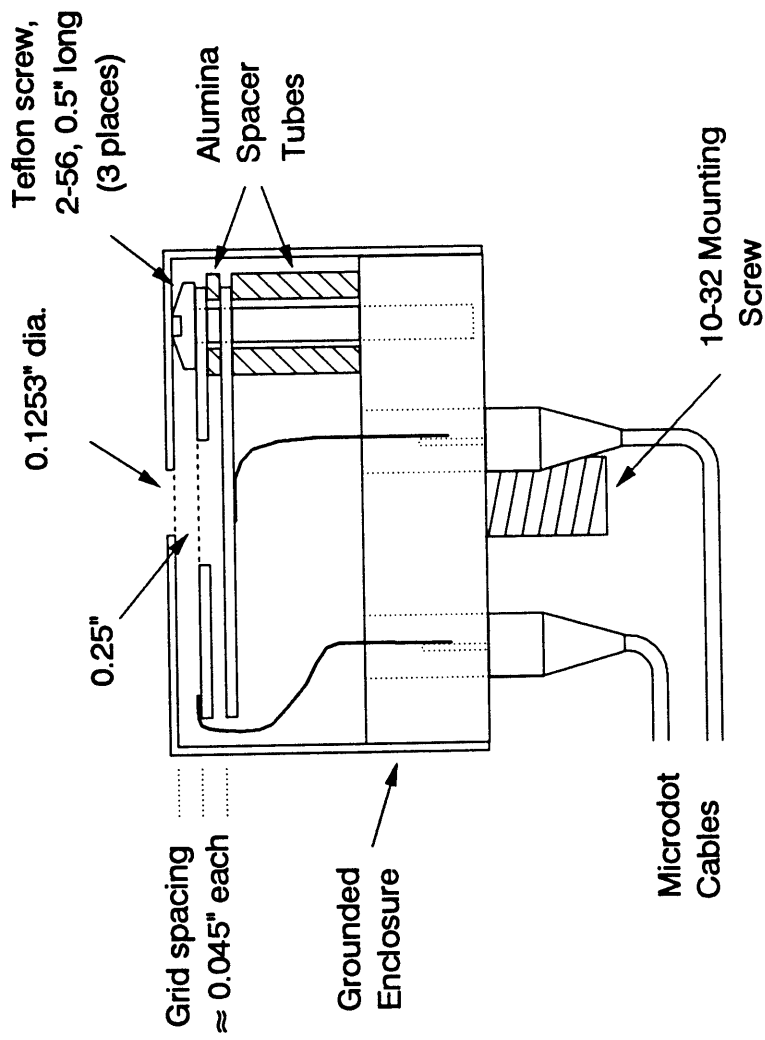


Figure 7.7: Schematic diagram of new ion energy analyzer design. Screw and spacer assembly is repeated three times around periphery (only one shown for clarity).

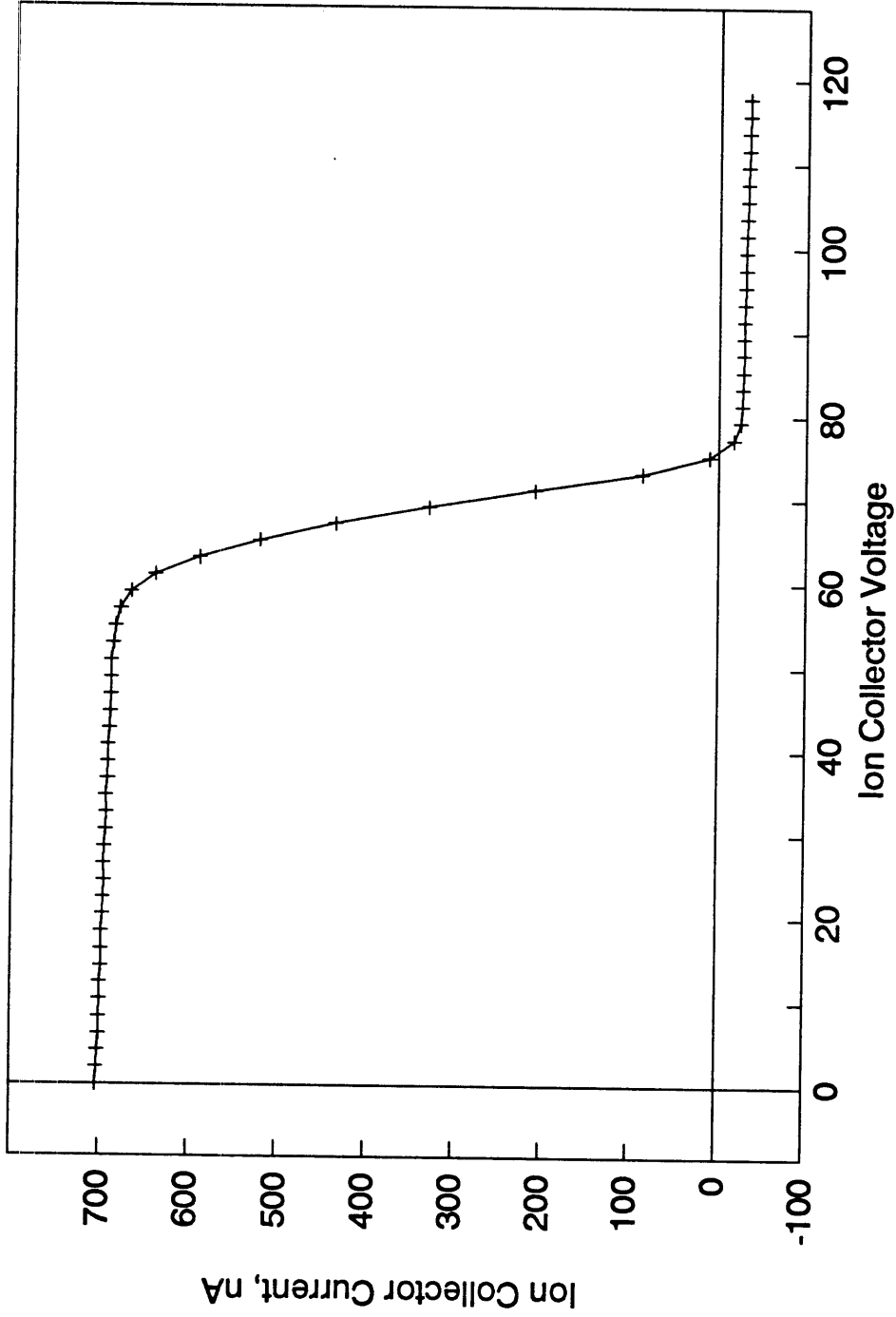


Figure 7.8: Typical ion collector current vs. voltage for revised energy analyzer. Beam for this example was the same as shown in Figure 7.6 (approximately 70 eV).

applications of Microdot connectors. The insulation on Microdot components is rated to only 5 G Ω ohms, and the breakdown voltage is rated to only 1000 V. Ohmic leakage in the current cables was measured on the order of 10-20 G Ω (leakage of \approx 10 nA at 200 V), and the present beam energies are low enough to avoid the rated limits for the cables. However, leakage and breakdown may become issues in the future, if the cables are replaced or if very high beam energies are used.

7.3 Ion Beam Source

The Kaufman ion gun previously used by Gray [1992] suffered from several shortcomings that made it unsuitable for use in this study. First, the flux and energy of Kaufman-source ion beams are closely coupled, so that reducing the energy to the range desired for this work would have made the flux too low to represent current etching processes. Second, the Kaufman-source discharge is not an efficient source for ions from molecular feed gases. Maintaining adequate dissociation generally requires a more intense discharge than the hot-cathode design used in Kaufman sources. Finally, Gray [1992] experienced very short neutralizing filament lifetime, which he attributed to reactive sputtering of the fine filament placed directly in the ion beam. This Section describes the development and characterization of a new ion beam source which overcomes these problems. Much of the initial work for this section was performed by G. C. H. Zau, but has not been published and is thus included here for the sake of completeness.

7.3.1 ASTeX CECR

The major component of the new beam source is the CECR (Compact Electron Cyclotron Resonance) discharge system developed and marketed by ASTeX (Applied Science and Technology, Inc., Woburn, MA). This system uses confining magnets and high microwave power (up to 250 W at 2.45 GHz) to excite a very intense discharge in a small volume.

A schematic drawing of the CECR is shown in Figure 7.9. The discharge vessel consists of a quartz tube approximately 0.9" in diameter and about 6" long. In its standard configuration, the tube is capped at one end (except for a small gas inlet) and open at the other (through a quartz plate with a single hole about 0.5" in diameter). Gas and plasma stream out of the discharge vessel, providing a source of free radicals and ions. The CECR is typically used in research and small-volume production settings, with applications including thin-film and diamond film growth as well as etching.

7.3.2 Modifications for Beam Energy Control

One of the industrially attractive features of ECR and other high-density discharges for plasma etching is the high ion flux at relatively low ion energy. The plasma potential for high-density systems is usually on the order of 15-20 volts above the chamber walls. Industrial etching systems use separate power supplies to bias the

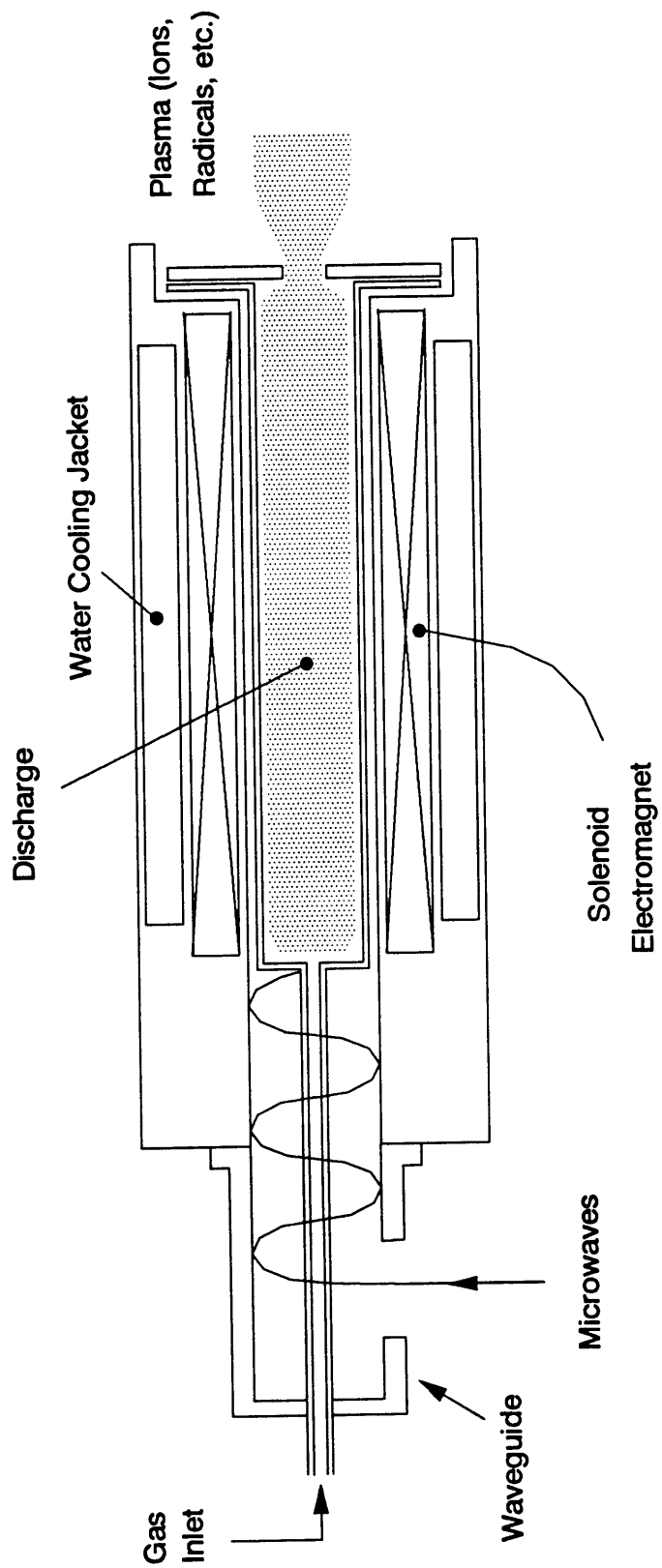


Figure 7.9: Schematic diagram of Compact ECR plasma source.

wafer negatively and increase the ion energy to useful levels.

Biasing the sample in the 3-beam system would be impractical, for several reasons, so some other means for increasing the ion energy was needed. The most practical method was to apply a positive bias to the discharge. This was accomplished by placing a thin (0.003" thick) cylindrical metal surface (or "liner") around the inner periphery of the quartz discharge tube. With any plasma system, the discharge assumes a potential higher than the most positive surface it contacts (provided that surface is of comparable dimension to the other conductive surfaces containing the plasma). Therefore, applying a positive potential to the liner would increase the plasma potential. The energy of the beam at the sample is related to the potential drop between the discharge and the sample, so biasing the plasma would increase the ion energy.

In order to contain the plasma and minimize the stray fields inside the chamber, the open end of the discharge tube was capped by a grounded metal "extraction" grid. The grid material was formed by etching an array of frustum-shaped holes in a thin stainless steel sheet, so it had a finite gas conductance and allowed the pressure to be higher in the discharge region than in the main vacuum chamber. Grounding the grid eliminated any stray electric fields from the chamber (because the chamber was completely surrounded by grounded metal surfaces), and fixed the beam energy as the difference between the plasma potential and ground. The plasma potential varied with the liner bias and the discharge intensity (determined by power,

pressure, and magnetic field strength), so that the ion beam energy was typically in the range of 5 to 20 eV higher than the liner bias (in Volts). The grid was welded over the opening in a thick stainless steel washer to provide support and cooling.

After passing through the extraction grid, the ion beam was neutralized by a hot filament shaped to encircle the beam slightly downstream. The neutralizing filament was made of thoriated tungsten and was heated by passing a current of several amps through it. Electrons emitted from the hot filament would be entrained in the beam, balancing the space charge of the ions and preventing dispersion of the beam during transit to the sample. The neutralizing filament current was one of the most sensitive operating parameters for the ion beam. Figure 7.10 shows the qualitative relationship between ion flux measured at the sample position and filament current. At low current, the supply of electrons was insufficient to prevent space-charge spreading of the beam. At high current, the electron population was excessive and the beam was also dispersed. The optimum neutralizer current varied from run to run, even when the beam conditions (gas flow rate, power, magnet current, and liner bias) were the same.

Figure 7.11 shows the biasing liner, extraction grid assembly and neutralizing filament. Electrical access to the biasing liner was provided by passing a wire through an alumina tube bonded to the grid support washer. The biasing wire was completely encapsulated in alumina tubes and ceramic paste to prevent it from robbing the beam of neutralizing electrons. The dimensions of the biasing liner were not

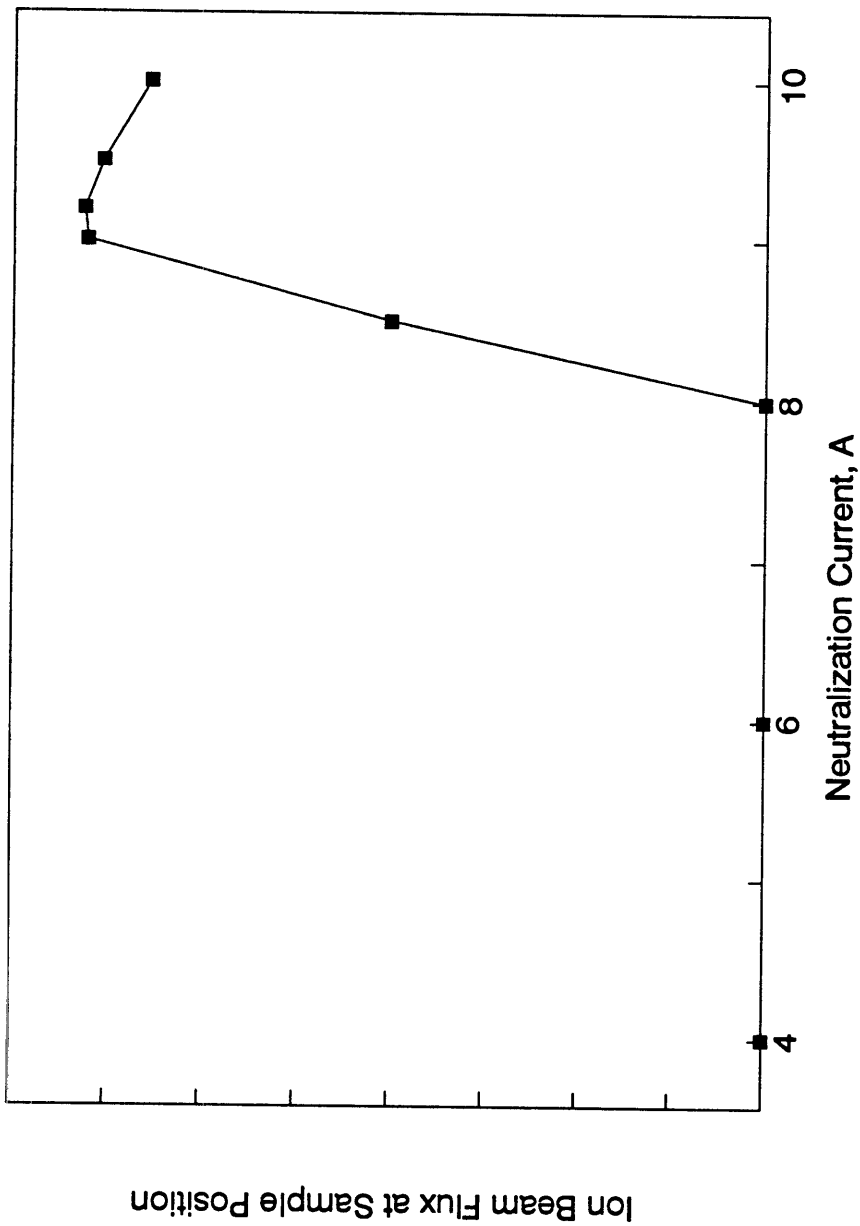


Figure 7.10: Effect of neutralizing filament current on ion beam flux at sample position. Ion beam is dispersed at low filament current. Beam flux increases rapidly above critical current, then rolls off at higher values. Optimum current varies from run-to-run.

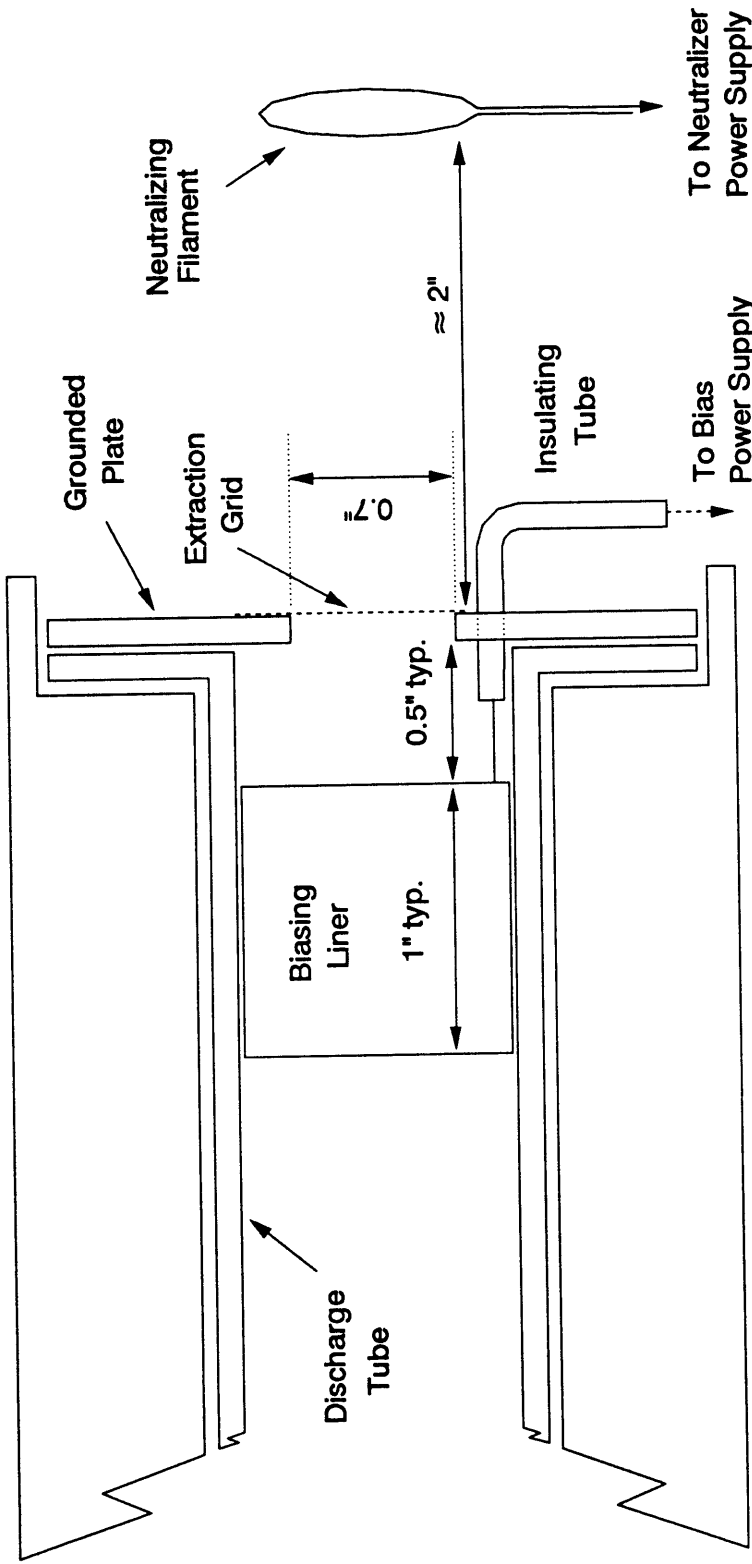


Figure 7.11: Biasing liner, extraction grid, and neutralizing filament. Biasing liner is formed by rolling 0.003" stainless steel sheet into a cylinder which fits snugly in discharge tube. Neutralizing filament is skewed slightly in this view to emphasize that it is a loop encircling the beam.

particularly critical, and Figure 7.11 shows typical values. In general, making the liner wider would tighten the beam IED but would also perturb the discharge more (reducing the ion current). Moving the liner closer to the grid support would be expected to tighten the IED, but also contributed to arcing and leakage between the liner and the grounded grid support washer. Variations of +/- 10% in the width and placement of the liner were found to be tolerable, but the absolute limits were not explored.

This biasing arrangement was effective for controlling the beam energy from the plasma self-bias (5-20 Volts, depending upon discharge conditions) up to a few hundred eV. Figure 7.12 shows typical IED's at various bias potentials. The current (ion flux) varies somewhat with beam energy, but remains substantial over the energy range shown. This should allow more convenient separation of ion energy and flux effects on etching rate than was available in the past. Figure 7.12 concentrates on relatively low ion energies, because typical energies in industrial etching processes have been decreasing. This is due to concerns over subsurface damage from energetic ion bombardment. Energies in the range of 20-200 eV are typical of current practice.

The beam energy available with this system was limited to a few hundred eV, for two reasons. First, sputtering of metal from the grids and support washer led to deposition of a thin metal film on the quartz tube. As this film built up, it would eventually form a bridge between the biasing liner and the grid support. Not only would this increase the biasing current requirements, but it would also affect the ion

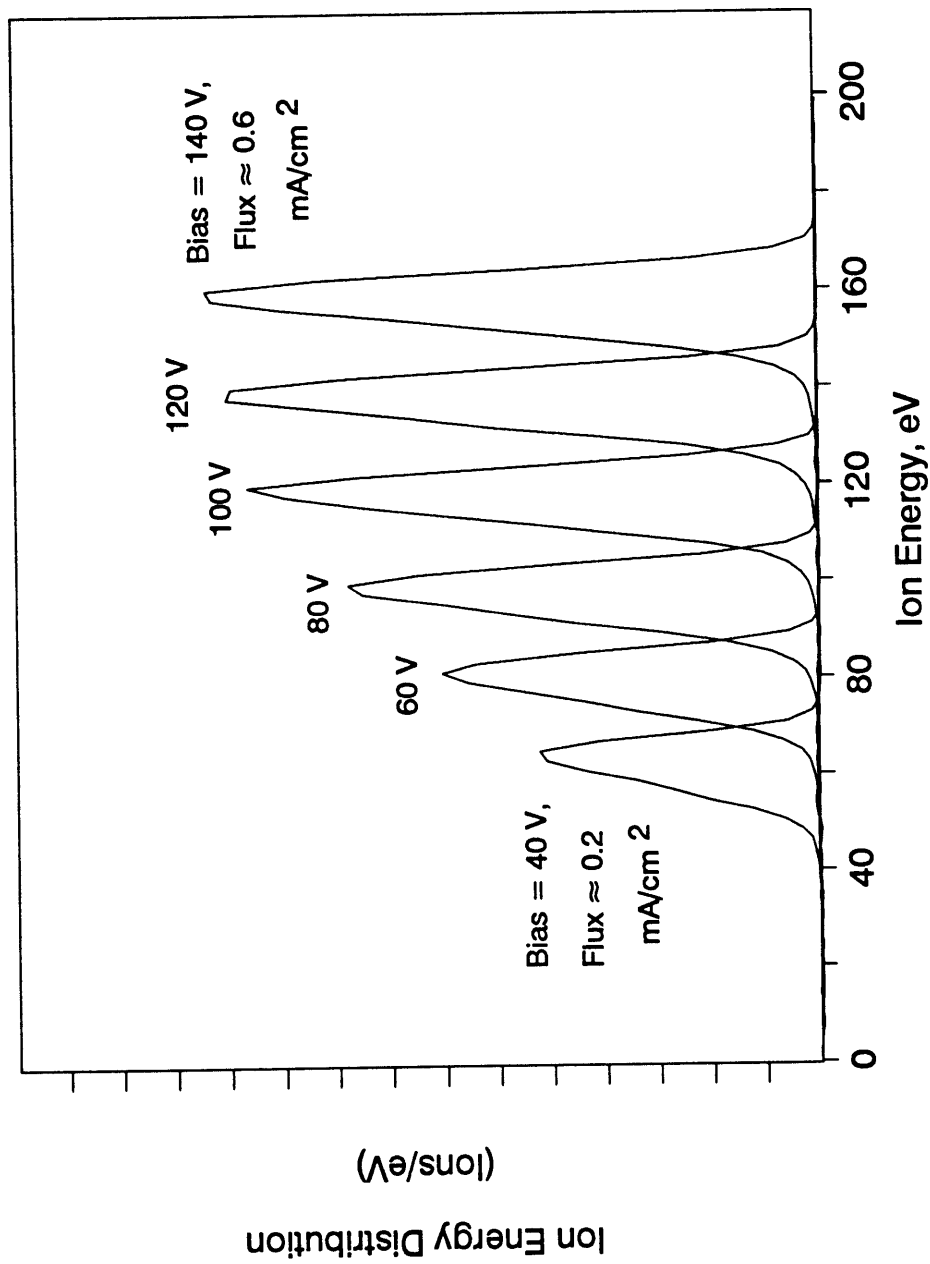


Figure 7.12: Effect of applied plasma bias on ion beam energy and current. Beam energy is typically \approx 20 eV above the applied bias.

energy distribution. Higher ion energies would increase the rates of sputtering and film deposition. The second effect of high bias was arcing between the liner and the grid support. This problem was observed at energies about 350 eV.

The interim solution to film deposition on the quartz tube was to remove and replace the tube frequently (after approximately 50 hours of operation at 100 eV, much more often at higher energy). The tubes could be cleaned a few times by etching the metal deposits off and then flame polishing the surface. This service was performed by G. Finkenbeiner (Scientific Glassblowers, Waltham, MA) at a reasonable cost, but repeated etching eventually degraded the surface to the point that the quartz tube had to be replaced. A revised grid support design, perhaps incorporating an insulating layer on the plasma side, would be a worthy topic for future consideration.

7.3.3 Ion Extraction Grids

The ion extraction grids at the end of the discharge tube needed frequent replacement. Not only was the metal sheet eroded by the ion beam, but some unknown phenomenon caused the grids to swell from their initially flat configuration into a domed shape (Figure 7.13). This deformation was thought to be related to the heating and cooling associated with startup and shutdown of the beam; in any event, the domed grid allowed the ions to emerge from the plasma at a variety of angles and weakened the beam.

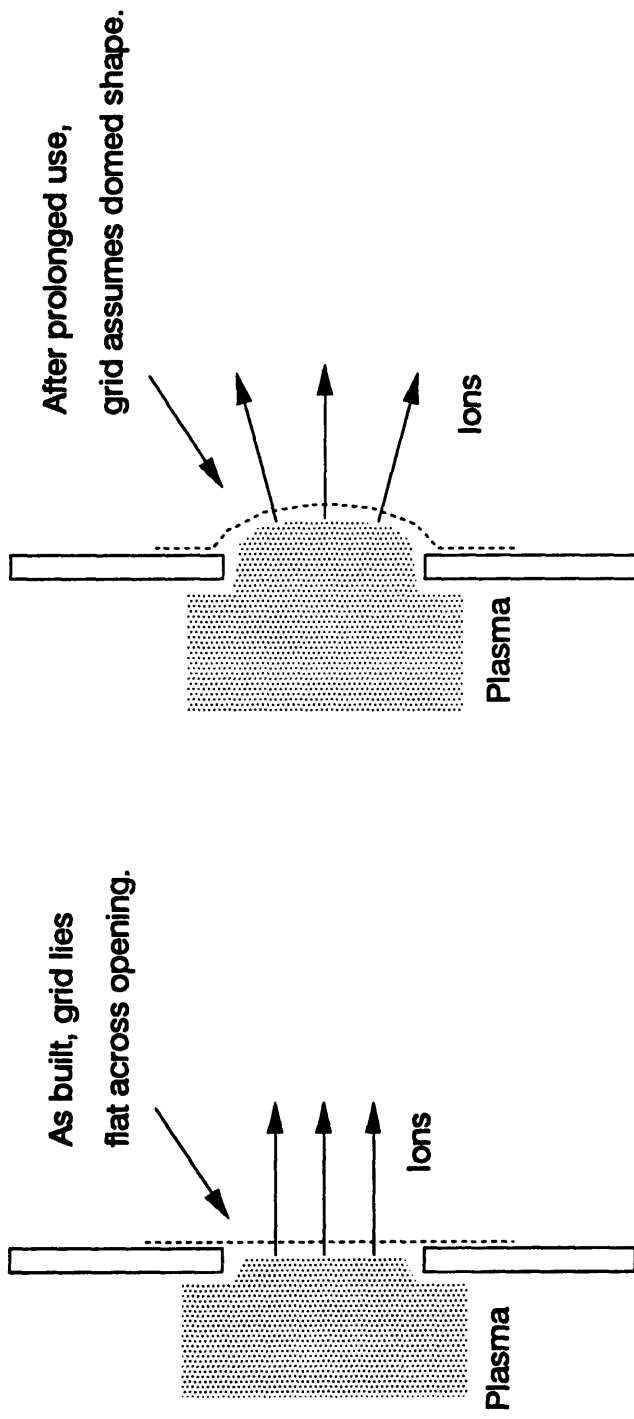


Figure 7.13: Effect of prolonged use on grid shape and ion beam intensity. After use, grid bows outward from plasma to form a dome. Plasma conforms to grid shape, and emerging ions are poorly directed.

Removing and replacing the grids was a simple matter of grinding off the original grid and spot welding a new piece in place. However, the obtainable ion flux varied significantly from grid to grid, even though all samples were cut from the same sheet of material. An initial investigation suggested that the hole size varied across the sheet.

Hole size has long been known to affect ion extraction efficiency from plasma sources. If the grid holes are large compared to the Debye length, then the plasma sheath will conform to the walls of the hole, ions will emerge at many angles, and the beam will be weaker (Figure 7.14). In contrast, holes smaller than the Debye length do not deform the sheath and will restrict the ion emergence angles.

An estimate of the plasma density for the CECR suggested that the grid holes might be large compared to the Debye length, so an investigation of hole size and ion flux was conducted. Smaller holes were expected to be more efficient and allow higher ion fluxes. Unfortunately, smaller holes were not readily available. The Buckbee-Mears #228 material already in use had the smallest holes available in stainless steel of reasonable thickness. A compromise method for obtaining smaller holes was to have the starting material plated with electroless Nickel. The nominal hole size was 0.003", so adding 0.0005" of plating should have reduced the diameter to 0.002". Additional samples with 0.001" plating were also made. One additional size of holes was added by using a section of the electroformed Nickel sheet used previously in ion energy analyzers. The materials and hole sizes available were as

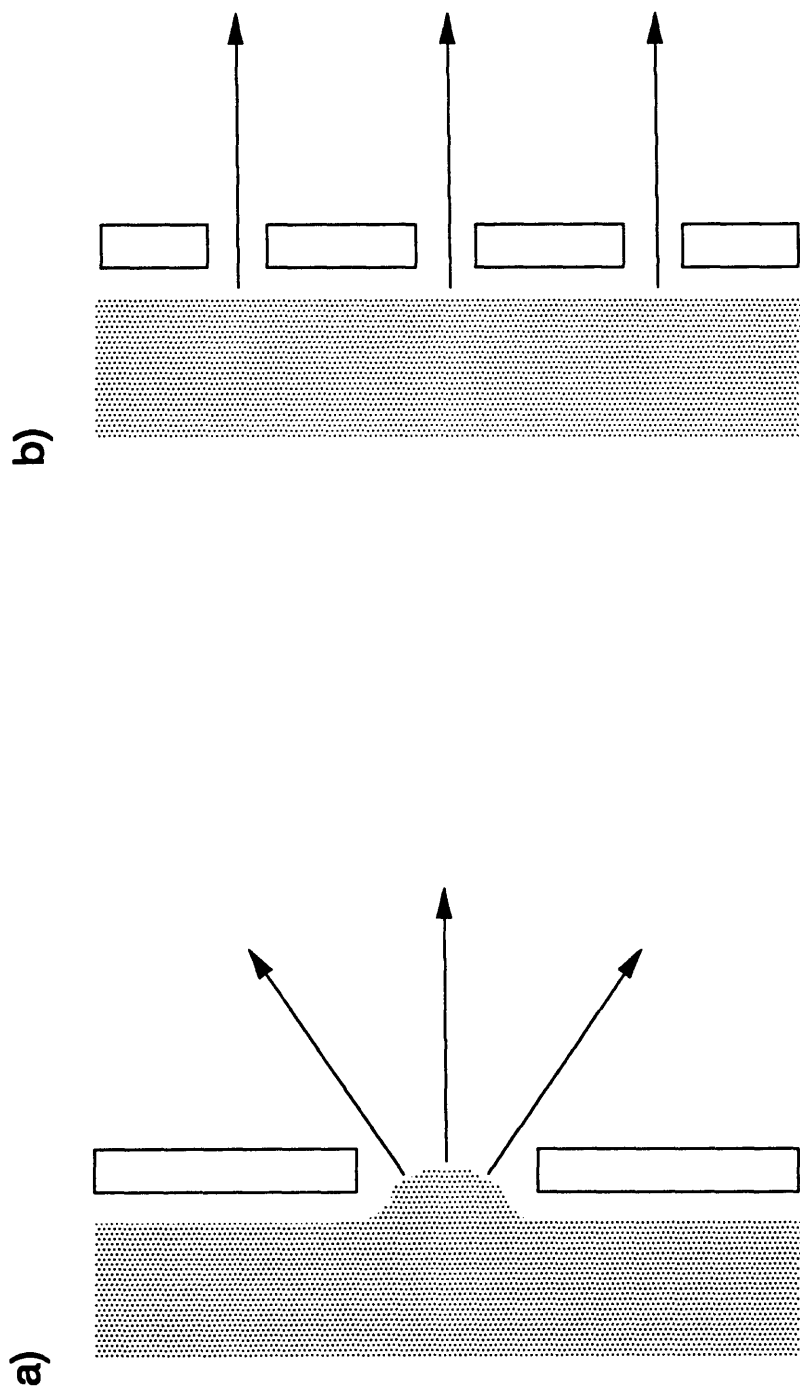


Figure 7.14: Effect of hole size on ion beam intensity. In a), the hole is large enough for the plasma to expand partially into the opening. The emerging ions are poorly directed. In b), the holes are too small for plasma deformation and the ions emerge with one direction.

follow (all materials are from Buckbee-Mears):

<u>Material</u>	<u>Hole dimension</u>
#514 Stainless Steel Sheet, 0.005" thick	0.006"
#228 SS Sheet, 0.002" thick	0.003"
#228 SS with 0.0005" Ni plating	0.002"
#228 SS with 0.0010" Ni plating	0.001"
Electroformed Nickel sheet, 0.0002" thick	0.0003"

Four identical grid support/biasing liner assemblies were constructed, and one of the above grids was attached to each. Each grid was tested by running an Argon discharge at 240 W microwave power with the gas pressure, magnet current, and neutralizer current all optimized to provide the highest ion flux at each of two liner bias levels (50 and 100 V). The gas pressure was adjusted to compensate for the differing conductances of the materials. The maximum ion flux was divided by the open area fraction to develop an efficiency rating for each grid. The electroformed and 0.0010" plated grids were limited to one sample each. Two 0.0005" plated grids and several unplated grids were tested. The hole diameters were measured using an

SEM, and an attempt to correlate the efficiency with the hole diameter was made.

Unfortunately, this experiment was almost completely inconclusive. The largest holes performed poorly, as expected, but the smallest holes did not perform well. The strongest ion beams were found with the normal material (#228, unplated). The 0.0005" plated holes, although only 25% or so smaller (in diameter), produced ion beams nearly 90% weaker. The ion beam produced with the 0.0010" plated material was nearly undetectable, and the electroformed grid was comparable in performance to the 0.0005" plated material. One possible explanation is that plating changed not only the hole size but also the aspect ratio of the holes. The effect of aspect ratio of extraction efficiency is not well known. Furthermore, both the plated and electroformed materials contained Nickel, which has a high permeability and may have had some effect on the magnetic field within the ECR.

No convenient and affordable source of grids with varying diameter but constant aspect ratio in stainless steel could be found. Laser drilling can produce holes of the desired dimensions, but the cost would probably be prohibitive (one grid contains more than 10,000 individual holes). Buckbee-Mears may be able to produce special runs of smaller holes in thinner materials, but also at substantial cost. It is not clear whether further analysis of hole size is warranted. The performance of the present ion beam is adequate; only the variations from grid to grid are not understood.

One positive result of this effort was the nearly accidental discovery that stronger beams could be obtained by placing the grid so that the larger ends of the frustum-shaped holes were toward the plasma. Conventional wisdom, as expressed in Figure 7.14, suggests that the smaller hole should be placed toward the plasma. However, inverting the grid was found to double or triple the beam flux.

7.3.4 Differential Pumping

One of the features added to the vacuum system by Gray [1992] was a differential pumping arrangement for the ion source. A secondary vacuum chamber with a small cryogenic pump was added to the main chamber, and the ion source was attached to the secondary chamber. The two chambers were separated by a conical "skimmer" which allowed the ion beam to pass through but limited the exchange of background gases between the chambers. The perceived benefits of this arrangement were twofold: first, the total gas load to the main chamber (and consequently the background pressure) would be reduced, and second, backmixing of reactive gases from the main chamber to the ion source would be reduced.

The differential pumping arrangement was disabled for this work. Premature saturation of the small pump was linked to excessive pressure in the secondary chamber, subsequently weakening the ion beam at the sample. The aperture in the skimmer was narrower than the ion beam, so removing the skimmer also improved the beam uniformity at the sample.

The added gas load in the main chamber was deemed acceptable, because the gas load leaking in from the ion source was typically smaller than that entering through the atom source. Typical gas flow into the CECR was on the order of 1 sccm, while gas flow through the atom source ranged as high as 5 sccm. In no case did the background gas pressure rise above 10^{-4} Torr.

Backmixing of reactive gas is not a major concern with the new ion source. While Gray [1992] had difficulty with neutralizer filament lifetime from reactive etching, the thicker filament and out-of-beam placement in the new source eliminated this concern. There is some evidence that chlorine entered the CECR under some process conditions (as will be discussed in Chapter 8), but such contamination would only be of concern when the atom and ion feed gases are different. The use of inert ions has been popular for kinetic experiments (including this work), but is hardly representative of industrial practice.

For this work, the benefits of improved ion beam performance and reduced maintenance outweighed the disadvantages of disabling the differential pumping apparatus. Differential pumping may be required for future work, but additional characterization of the ion beam under those conditions will be necessary.

7.4 Chlorine Atom Source

One of the greatest challenges of this project was the production of a beam

of chlorine radicals (atoms). Producing chlorine atoms is straightforward; near total dissociation can be achieved with a simple McCarrol cavity discharge system. Extracting those radicals from the discharge and transporting them to the sample is far more difficult.

Chlorine atoms adsorb readily on a variety of surfaces, leading to high recombination probability for radicals subsequently striking those surfaces. Attempts to produce chlorine atom beams by the conventional upstream discharge method have been thwarted by recombination during transport from the discharge to the sample. Deshmukh and Economou [1993] have reported experiments where the dissociation in the upstream discharge was nearly total, yet the beam arriving at the sample contained less than 10% chlorine atoms (the remainder having recombined to molecular chlorine).

Various researchers have proposed that the recombination probability could be reduced by selecting or treating the material of the tube connecting the discharge to the sample. While this approach has been successfully applied to fluorine atoms [Gray, 1992], none of the published surface preparations were effective or reliable enough for use with chlorine.

G. C. H. Zau explored the various options for producing and maintaining chlorine atoms, and concluded that an entirely new type of source was needed. Details of the source design and construction will be published elsewhere by Zau, but

a brief overview of the source and its application to this project is presented below.

7.4.1 Principles of Operation

The new source design is shown schematically in Figure 7.15. In contrast to the conventional upstream sources, which generate atoms in a discharge outside of the vacuum chamber and then transport them into the system, the new source places the discharge in proximity to (but not in contact with) the sample. Microwave power is transported across the air/vacuum boundary through a differentially sealed coaxial waveguide. Undissociated chlorine gas is fed into a small quartz vessel (ampule) placed at the end of the waveguide.

The ampule is placed so that the gas inside is subjected to the high electric field travelling down the waveguide, sustaining an intense discharge. A small nozzle at the end of the ampule allows some of the dissociated gas to escape and strike the sample. The nozzle dimensions were chosen to limit the number of wall collisions (and opportunities for recombination), so the beam emerging from the ampule is highly dissociated.

The atom source includes two other principle features. First, water cooling is provided both in the center conductor of the waveguide and in a reservoir surrounding the outer conductor near the ampule. The discharge inside the ampule is unusually intense and would cause the ampule to melt if it were not cooled.

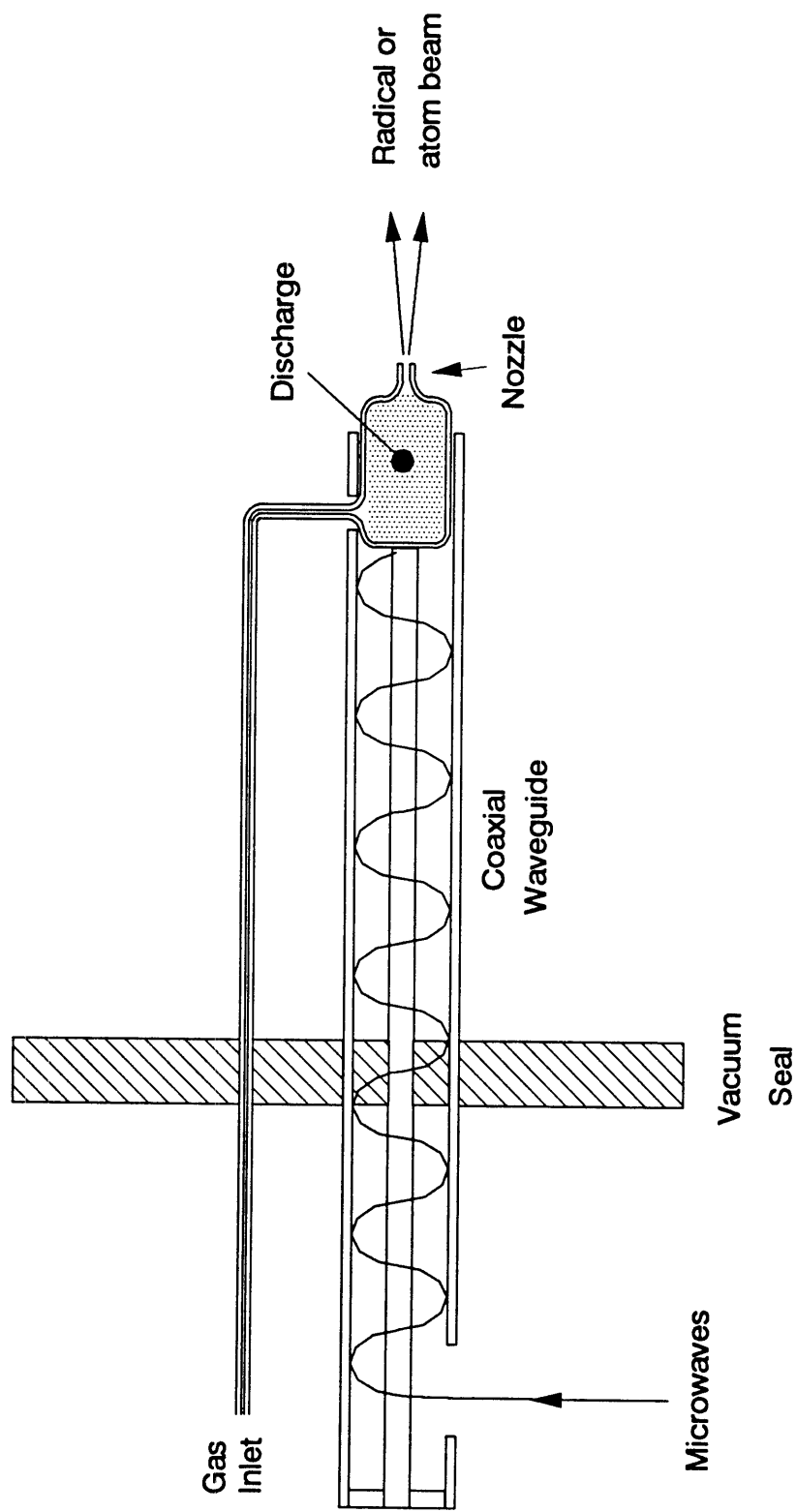


Figure 7.15: Simplified schematic diagram of new radical (or atom) source. Microwaves are carried down coaxial waveguide, passing through vacuum seal and into discharge vessel. Gas flows through separate tube into discharge vessel, where it is dissociated. Radical beam emerges through short nozzle.

The second essential feature is an ignitor lead which touches the face of the ampule at one end and is attached to a high-voltage feedthrough at the other end. A Tesla coil is touched to the outer contact of the feedthrough during discharge startup. The Tesla coil is needed because the electric field in the waveguide is not strong enough to break down the feed gas by itself. Once the discharge starts, conductance through it is sufficient to couple power in from the waveguide.

This source has proven effective for producing chlorine, oxygen, and hydrogen radicals. Similar sources are currently being used in both diamond and copper growth experiments, supplying hydrogen radicals.

7.4.2 Beam Characterization

The first step in applying the new source to chlorine atom production was to measure the dissociation. This was accomplished using a separate vacuum system with a mass spectrometer mounted behind the sample position. With the sample removed, beams arriving at the sample position passed through an aperture into a differentially pumped chamber containing the mass spectrometer. The system also included an oscillating "chopper" which could be used to selectively block the incident beam, thus allowing isolation of the background signal (signal due to residual gases in the differentially pumped chamber).

The dissociated fraction in the beam was estimated by comparing the

magnitude of the Cl₂ (71 AMU) peak on the mass spectrometer with the discharge turned on and off. For example, turning the plasma on under one particular set of discharge conditions reduced the amplitude at 71 AMU by 90% (after subtraction of the background signals). This indicates that the beam under those conditions contained only 10% molecular chlorine, or that 90% of the molecular chlorine had been dissociated.

Figure 7.16 shows the dissociation as a function of feed gas flowrate and applied power. The power was varied by a factor of 5 and the flowrate by a factor of 2, but the dissociation remained in the range of 80% to 95%. The ampule used in this trial had a nozzle 0.5 mm in diameter and 3.0 mm long, for an aspect ratio of 6:1. Decreasing the aspect ratio would decrease the number of wall collisions and possibly reduce the effect of recombination, but the performance obtained at 6:1 was adequate and more extensive characterization was deferred to the ongoing project of G. C. H. Zau.

7.4.3 Modifications for Plasma Containment

The ampule described in the previous section provided an acceptable flux of chlorine atoms to the surface. However, the first etching experiments in the 3-beam system suggested that there was some leakage of plasma out of the ampule and into the region of the sample. This was indicated primarily by the appearance of a visible glow outside of the ampule, and also by heightened silicon etching rate for the atom

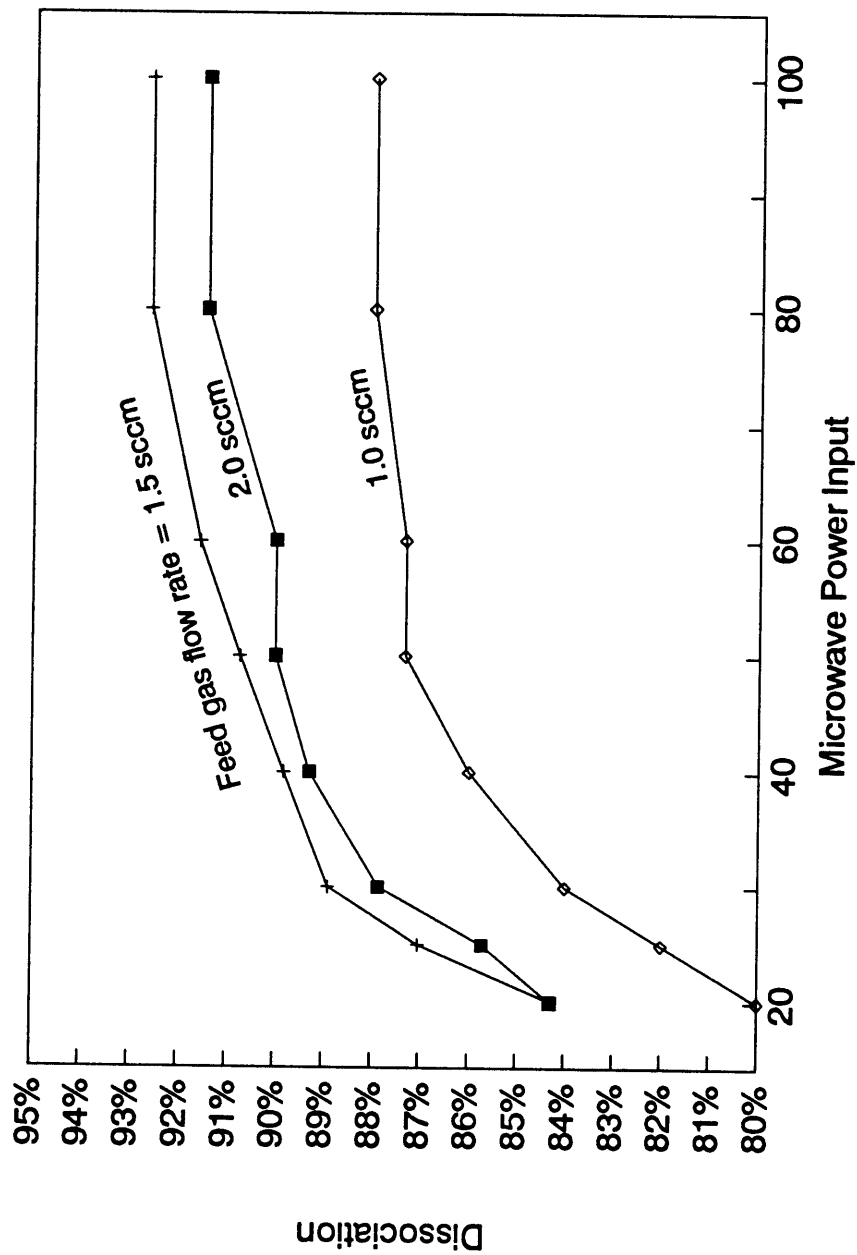


Figure 7.16: Effect of microwave power and feed gas flow rate on dissociation of chlorine in the new atom source. Gas flow changes by a factor of 2 and power changes by 5 times, but dissociation remains between 80% and 95%.

beam.

The intensity of the external discharge varied with the gas flow rate. The glow was strongest at low flow rates (0.2-0.4 sccm), weakened with increasing flow, and disappeared entirely above about 1.5 sccm. Figure 7.17 shows the etching rate of polysilicon as a function of flow rate. Note that the ion beam was not active during these measurements, so the observed etching rate should have indicated the effect of spontaneous (or thermal) etching by Cl atoms alone. Ogryzlo, *et al.* [1990], have measured the spontaneous etching of silicon with Cl atoms in a downstream etcher. Their data indicate that the etching rate under the flux conditions of Figure 7.17 should increase linearly with flowrate, reaching a value of approximately 5-7 Å/min at the highest flowrate shown. The much higher etching rates observed, and the "backward" behavior with increasing flowrate, suggest that the etching was enhanced by the external discharge.

The ampule design was modified to provide better confinement of the plasma. The primary change was to decrease the hole diameter from 0.5 mm to 0.25 mm. A secondary effect of this modification was a change in the fabrication technique: whereas the 0.5 mm nozzle had been formed by drawing a piece of larger tubing, the 0.25 mm hole required laser drilling. The laser drilling equipment required a planar sample, so the new nozzle was formed by drilling a hole in a flat plate, which then became the front wall of the ampule. Figure 7.18 shows a schematic comparison of the two designs. The thickness of the flat plate was set at 1.5 mm to maintain the

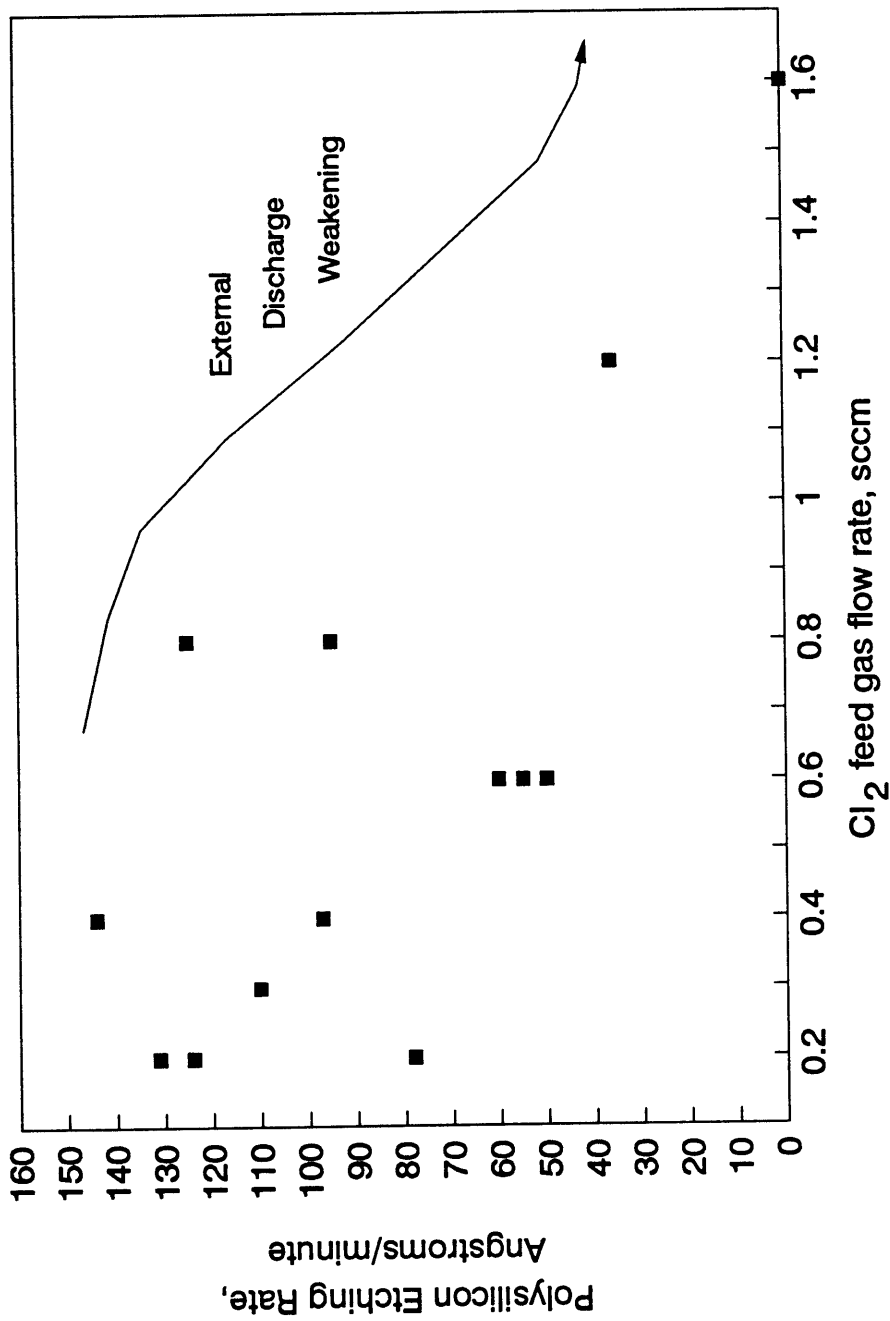


Figure 7.17: Polysilicon etching rate with atom source alone, using original ampule and nozzle design. Expected etching rate for these conditions was less than 10 Å/min.

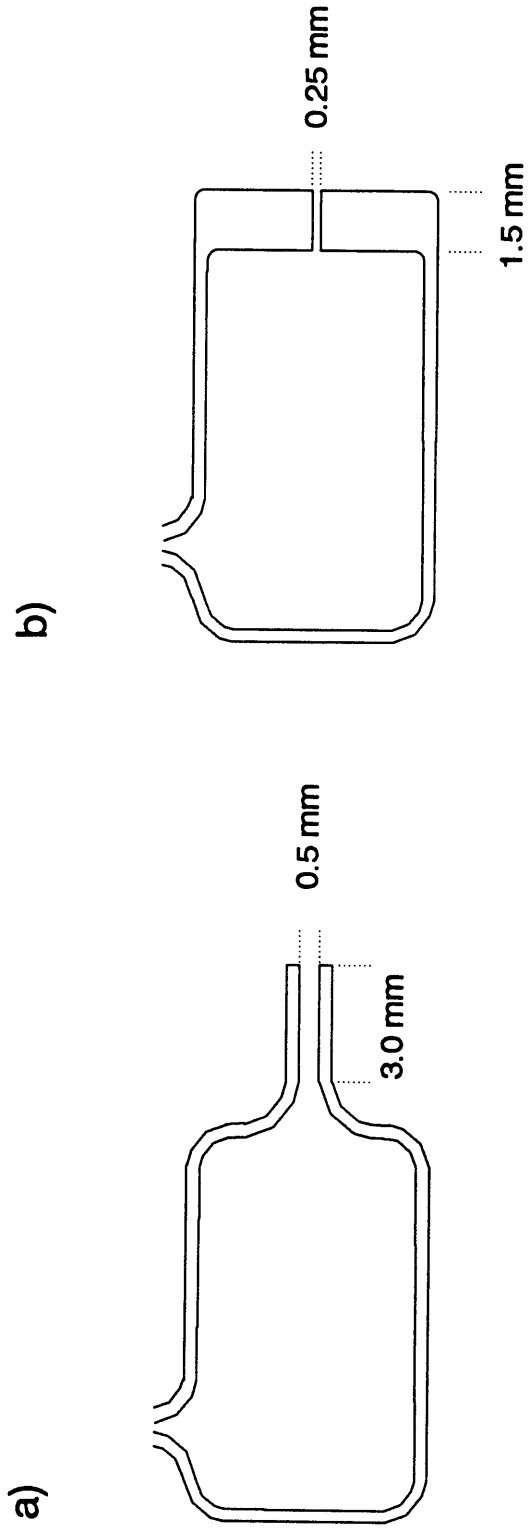


Figure 7.18: Comparison of original and revised nozzle designs. a) Original ampule, with drawn nozzle 0.5 mm in diameter and 3.0 mm long. b) Revised ampule, with 0.25 mm nozzle drilled in 1.5 mm plate. NOTE: Drawings are not to scale. Actual ampule is roughly 8 mm in diameter and 12 mm long.

nozzle aspect ratio of 6:1.

Reducing the nozzle diameter inhibited the leakage of plasma by increasing the loss of ions and electrons to the nozzle walls. Sheaths form along all surfaces in contact with the plasma, so sustaining a plasma through the length of the nozzle (and outside of the ampule) would require a diameter great enough to permit the formation of sheaths on both sides while still leaving a substantial volume of quasi-neutral bulk plasma. As the nozzle diameter approaches the sheath dimensions, the remaining bulk volume decreases. When the loss of charged particles to the walls exceeds the rates of ionization in the nozzle and transport into the nozzle, then the plasma is extinguished before reaching the main chamber.

Etching rate measurements and visual observation with the new ampule design verified that the plasma was contained. However, decreasing the nozzle dimensions had the undesired effect of increasing the discharge pressure, which apparently influenced the dissociation. This topic will be discussed further in Chapter 8.

Chapter 8

Polysilicon Etching Experiments

8.1 Kinetic study

8.1.1 Plans

The fundamental purpose of these experiments was to determine the kinetic rate parameters for the ion-enhanced etching of polysilicon with chlorine. The etching rate was expected to depend upon at least five major inputs, including the ion energy, ion flux, radical flux, substrate temperature, and possibly the ion incidence angle. A complete kinetic study would have to vary all of these parameters independently over broad ranges.

Fortunately, the previous work of Gray, *et al.* [1993], and others could be used to focus this study on the parameters most likely to be important. The major conclusion of the previous silicon/fluorine etching study was that the ion etching yield at a given energy and temperature depended more upon the ratio of radical to ion flux than upon the absolute fluxes. The yield (surface material removed per ion) increased rapidly with radical flux when the ratio of radical to ion flux was low, and leveled off or "saturated" when the ratio was high. The total etching rate was proportional to ion flux at any ratio, but the constant of proportionality varied with

flux ratio.

There is a reasonable theory for the saturation of ion etching yield at high flux ratio for ion-enhanced etching with halogens. As was shown in Figure 6.2, increasing radical flux could lead to increased halogenation of the surface, which would improve the ability of energetic ions to promote etching. At very high radical flux, the surface would be completely covered and small variations in the total flux would have no effect.

There was some support for the applicability of this mechanism to etching with molecular chlorine [McNevin and Becker, 1985], but conclusive evidence with chlorine atoms was unavailable. Therefore, the first order of business in this study would be to analyze the dependence of etching yield upon ion or radical flux and flux ratio. This would involve three questions: would the yield depend more strongly upon flux ratio than absolute flux, would the yield saturate at a high flux ratio, and (perhaps most importantly) would saturation occur within the range of fluxes achievable with the ion and atom sources described in Chapter 7?

Gray, *et al.* [1993], also verified that ion energy was an important factor in determining the etching yield. However, the observed variation with energy was simple (yield roughly proportional to square root of energy), consistent with previous theories, and ultimately less interesting than other effects. Investigation of the energy dependence for chlorine etching could be deferred to a later point in this study.

Substrate temperature was also given a low priority. The activation energy for ion-enhanced etching is provided by ion bombardment. Ion energies range from a few dozen to a few hundred eV, while the thermal energy for typical processing temperatures is a small fraction of an eV. The effect of substrate temperature on ion-enhanced etching reactions is usually mild.

Ion incidence angle was considered vital to this study for two reasons. First, the modeling effort described in Part I showed that the variation of yield with incidence angle could be very significant in determining etched feature shape. Second, no previously published work had studied the effect of incidence angle directly. Measurement of the ion-enhanced etching yield at different incidence angles would be both novel and informative.

One final parameter not mentioned above was the ion type. Many published studies, including the work of Gray, *et al.* [1993], have combined reactive radicals with inert ions (typically argon). This is justified by hypothesizing that the primary purpose of the ion is to supply energy and/or momentum. Under this assumption, an inert ion would be equivalent to a reactive ion of similar mass and energy. The validity of such an assumption is not entirely clear; etching studies with molecular ions have produced effects dramatically different from what would be obtained with inert ions [Oehrlein, *et al.*, 1994].

The high-density CECR source used in this study would make selection of the

ion type a simple matter of changing the feed gas and adjusting the plasma bias. This would allow the first comprehensive, side-by-side comparison of inert (argon) and reactive (chlorine) ions in concert with chlorine radicals.

The above considerations led to the following plan of action: the initial work would utilize argon ions, to facilitate comparison with Gray's [1992] fluorine etching study. The sample temperature would be held at a moderate level (50° C), and the ion energy would be fixed at 100 eV. The effect of chlorine atom to argon ion flux ratio on etching yield at normal ion incidence would be examined first. If the anticipated saturation behavior was observed, then the next set of experiments would vary the ion incidence angle. The next step would replace the argon ions with chlorine, maintaining the energy at 100 eV and the temperature at 50° C and varying the flux ratio and incidence angle. The final effort would briefly examine the effects of ion energy and substrate temperature.

8.1.2 Etching with Chlorine Atoms and Argon Ions: Effect of Flux Ratio

As discussed above, the first step of the kinetic study utilized chlorine atoms and argon ions. The ion energy was fixed at 100 eV, the sample temperature was held at 50° C, and the ions struck the sample at normal incidence. The ion-enhanced etching rate was defined by Gray [1992] as the total etching rate minus the thermal and physical sputtering components. The latter contributions were assessed by successively turning off the ion and atom beams. Although etching was apparent, the

rates were too low to be measured in a reasonable time. Therefore, the ion-enhanced etching rate was approximated by the total rate.

A typical etching rate experiment proceeded as follows. First, the sample was loaded and allowed to reach an approximately steady temperature. The thermal mass of the sample holder and lag in the control system caused the temperature to vary somewhat; however, the temperature excursions during processing were typically less than $\pm 3^{\circ}\text{C}$.

Once the sample reached the desired temperature, the atom source was activated and allowed to stabilize at the chosen flow rate. Although the atom source was operable with feed gas flows between 0.07 and 5.0 sccm, ignition was only possible between 0.1 and 0.2 sccm. Ignition was difficult at any flowrate, typically requiring 5 to 15 attempts at different flow rates and tuning positions. Consequently, the process of igniting and stabilizing the atom source could consume as much as 15 minutes.

After the atom source was stabilized, the CECR discharge was ignited. Once again, the operating pressure was different from the level required for ignition, but the ignition process was repeatable. The final steps in activating the ion beam were to turn on the plasma bias and adjust the neutralizer current.

A small, exposed wire placed near the sample was used as an ion current

monitor. Although the current collected by the wire did not compare well with the ion flux measured using the energy analyzer, the wire did provide a convenient method for optimizing the neutralizer current and monitoring the beam during each run. After a variable induction period (up to several minutes for some samples), etching would ensue.

The etching rate was measured by plotting the laser interferometer output on a chart recorder. The time between successive extrema was monitored; the measurement was considered acceptable if the rate was stable over an etched thickness of about 2000 Å. The initial film thickness was 5000 Å, so it was frequently possible to analyze two etching conditions per sample (by changing the atom source gas feed rate).

After the polysilicon film was etched through, the atom source was shut down and the sample removed from the chamber. The ion beam was left running during this time, and the ion energy analyzer was rotated into the sample position for a current and energy measurement. This approach eliminated any uncertainty in the ion flux; although the ion beam was reasonably stable during each run, the current varied somewhat from run to run.

Several runs were completed, with the ion and radical fluxes adjusted to vary their ratio. Varying the radical flux was more convenient, requiring only an adjustment to the feed gas mass flow controller. In contrast, adjusting the ion flux

required changing the discharge conditions (power and pressure), then empirically finding the bias voltage necessary to achieve the desired ion energy. The ion beam was initially set to a fairly high flux (approximately 0.5 mA/cm², or 3.0 x 10¹⁵ ions/cm²-s), and the atom beam flux varied over the available range (from about 2.2 x 10¹⁵ to 1.5 x 10¹⁷). The etching yield increased with radical flux from 0.25 to 1.1. Next, the ion flux was reduced by lowering the discharge power and a new series of samples were etched at various radical fluxes. This procedure produced new data points at higher flux ratios, while also providing some overlap with the previous data set (at higher ion flux).

The ion and atom fluxes were adjusted over their maximum ranges. The etching yield rose less rapidly as the flux ratio was increased, but it did not reach a constant value. It was apparent that the available range of flux ratios was insufficient. The atom flux could be varied by a factor of about 70, but adjusting the discharge conditions allowed only about 3 times total variation in the ion flux. Changing the grid material (to the 0.0005" plated sample mentioned in Section 7.3.3) allowed a further reduction in the ion current, but the maximum flux ratio was only 650. Attempting to increase the atom flux further (by increasing the Cl₂ feed gas flow rate) actually decreased the ion etching yield. This decrease was accompanied by a visible reduction of the glow intensity, suggesting that excessive pressure inside the ampule was weakening the discharge and lowering the dissociation efficiency.

Figure 8.1 shows the ion etching yield as a function of flux ratio for normal

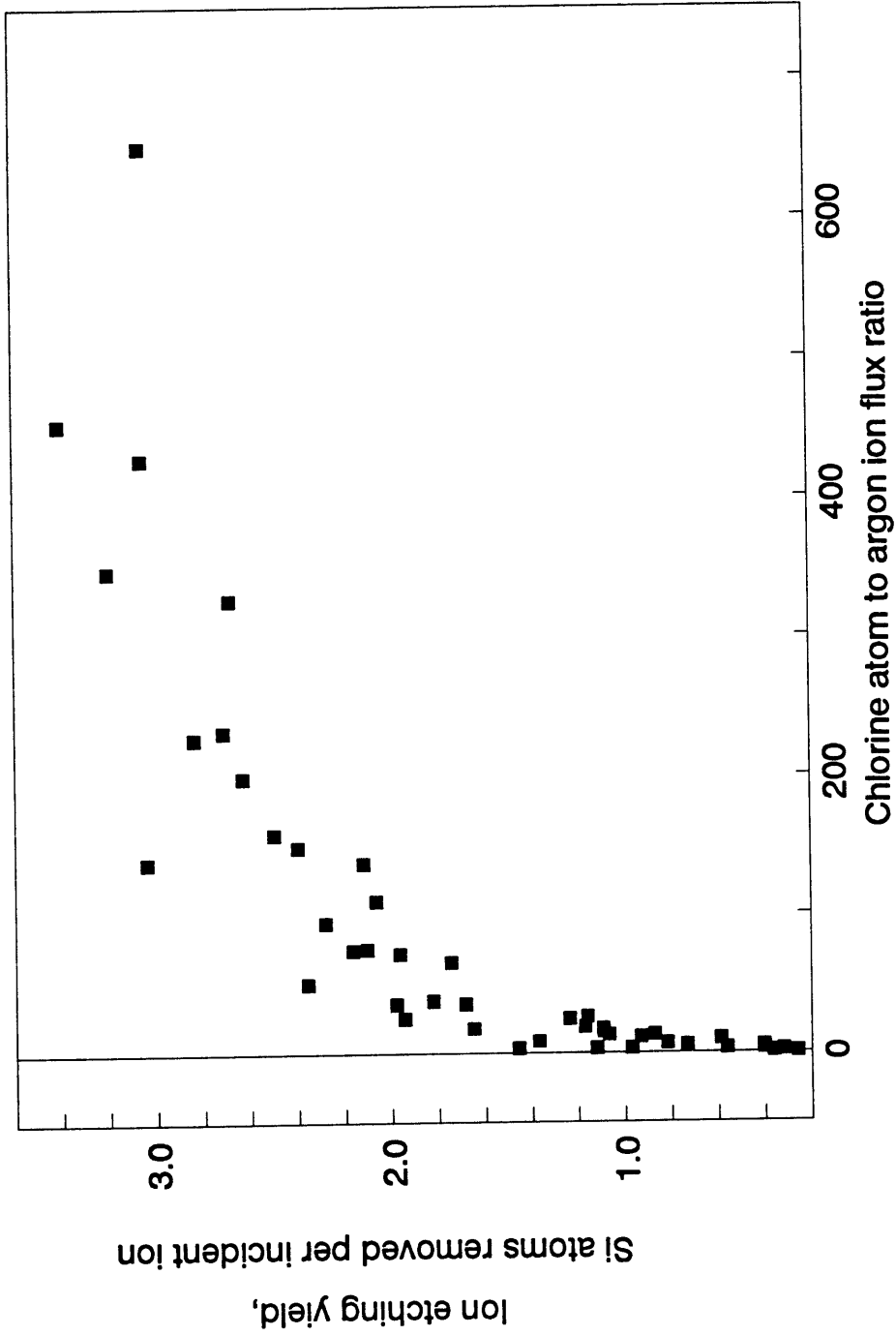


Figure 8.1: Variation of ion etching yield with chlorine atom/ion flux ratio. Maximum flux ratio of 650 corresponds to maximum atom flux with minimum stable ion flux.

incidence. The etching yield continued to increase, even at the highest flux ratio, so saturation was not achieved. On the other hand, the diminished rate of etching yield rise with flux ratio is consistent with the expected behavior. Additional measurements at higher flux ratios would be valuable. Proposals for future work are discussed in Section 8.1.4.

8.1.3 Etching with Chlorine Atoms and Argon Ions: Effect of Ion Incidence Angle

After the initial investigation of etching yield vs. flux ratio, the effect of ion incidence angle was explored. Samples were mounted at different inclinations as discussed in Section 7.1.2, and etched with varying flux ratios. Nominal ion incidence angles were 20°, 30°, 40°, and 60° from normal, but variations in the fabrication of sample mounts and the attachment of samples to the mounts caused deviations of +/- 3° from nominal.

Figure 8.2 shows the effect of flux ratio on etching yield at various incidence angles. The range of flux ratios in Figure 8.2 is broader than the one shown in Figure 8.1. This was caused by degradation in the ion extraction grids (Section 7.3.3). Deformation of the grids over time led to lower ion fluxes, thus allowing higher flux ratios to be reached. Unfortunately, the inevitable failure of the grid prevented a comprehensive study at high flux ratio.

Figure 8.2 clearly suggests that the etching yield is lower at incidence angles

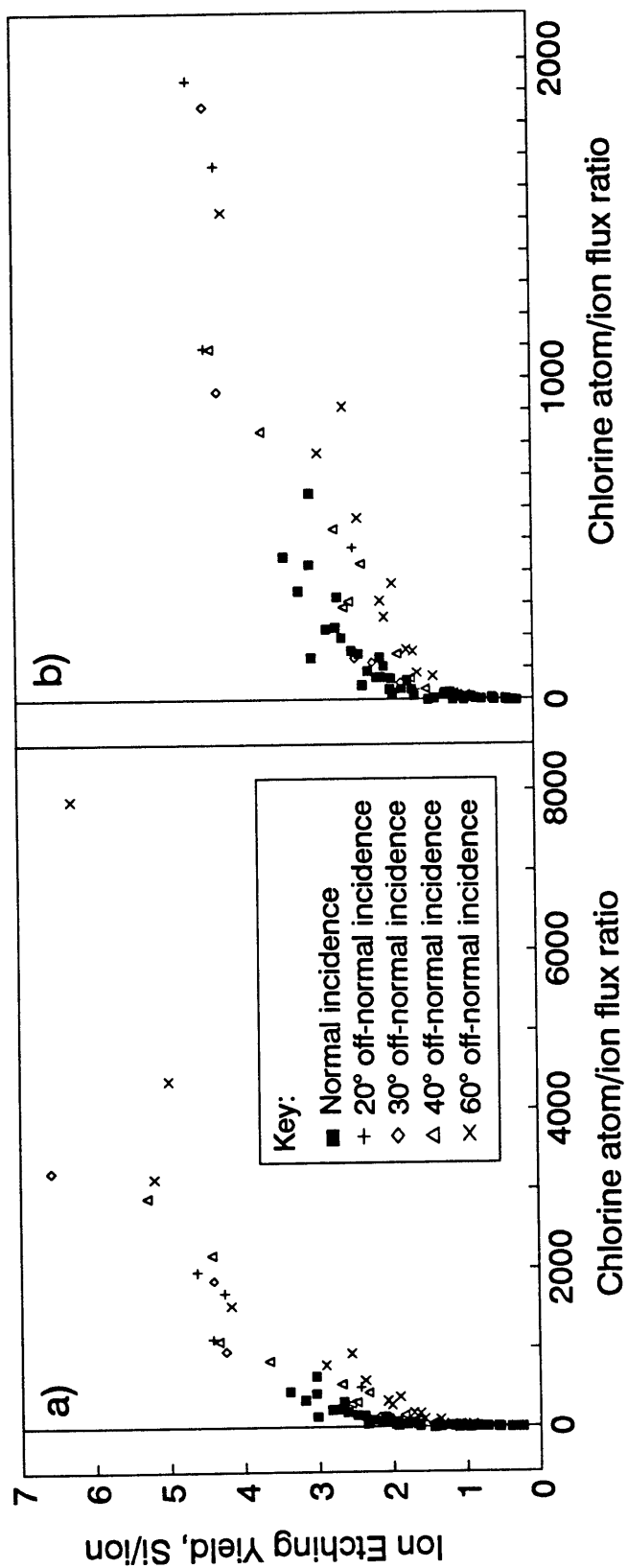


Figure 8.2: Variation of ion etching yield with chlorine atom/ion flux ratio and ion incidence angle. a) covers full range of flux ratios, while b) expands the lower flux ratio range for clarity. Reported incidence angles are approximate (+/- 3° typical).

far from normal. Accurate analysis is prevented by the sparsity of data, but the etching yield at 60° ion incidence may be as much as 35% lower than at normal incidence. This is a far more dramatic variation than had been assumed by others [Ulacia F. and McVittie, 1989]. This topic bears further consideration in the future.

8.1.4 Problems and Suggestions for Future Work

The kinetic study outlined above was cut short by devastating equipment failures and another project's need for the multibeam system. These problems notwithstanding, the complete study would have exceeded the scope of this thesis. The remaining experiments will be completed by another student (apparently P. C. Chang) in the future. This section outlines difficulties experienced during this initial program, makes suggestions for improvements to the equipment, and identifies certain opportunities for follow-on studies.

The major experimental difficulties stemmed from the immature design of the atom source. While some interesting results have been achieved, the source used in this work can not be considered more than a prototype. An extensive effort in design and characterization of the source will be required before reliable operation is assured.

The principal mechanical deficiency of the source is the vacuum seal design. The current design utilizes a pair of Teflon bushings pressed into the space between

the inner and outer conductors of the waveguide. The space between the bushings is pumped to rough vacuum, as shown in Figure 8.3. While this approach has been effective, the very tight fit needed for adequate vacuum sealing adds both cost and inconvenience to the construction and maintenance of the source. The mechanical fabricating firm employed for construction of this source (Sharon Vacuum Co., Brockton, MA) has resorted to a trial-and-error approach to manufacturing the bushings and assembling the source. The most recent examples have been assembled by passing liquid nitrogen through the center conductor before sliding it and the bushings into the outer conductor tube. Even with cooling, the resistance to assembly was great enough to causing bending of the center conductor.

The cumbersome assembly process for the vacuum seal makes routine maintenance of the source impossible. A simple cleaning of the center conductor (to remove surface corrosion induced by long-term exposure to reactive gases) would require returning the source to the fabricator for installation of new bushings.

Simultaneous vacuum sealing and microwave insulation is challenging, and there is no obvious solution. One promising possibility would be to replace the single intermediate vacuum stage with several stages by dividing the space between the conductors into several compartments with independent pumping of each. Increasing the pumping speed to the intermediate stage might also allow adequate sealing with a more relaxed fit between the bushings and the conductors.

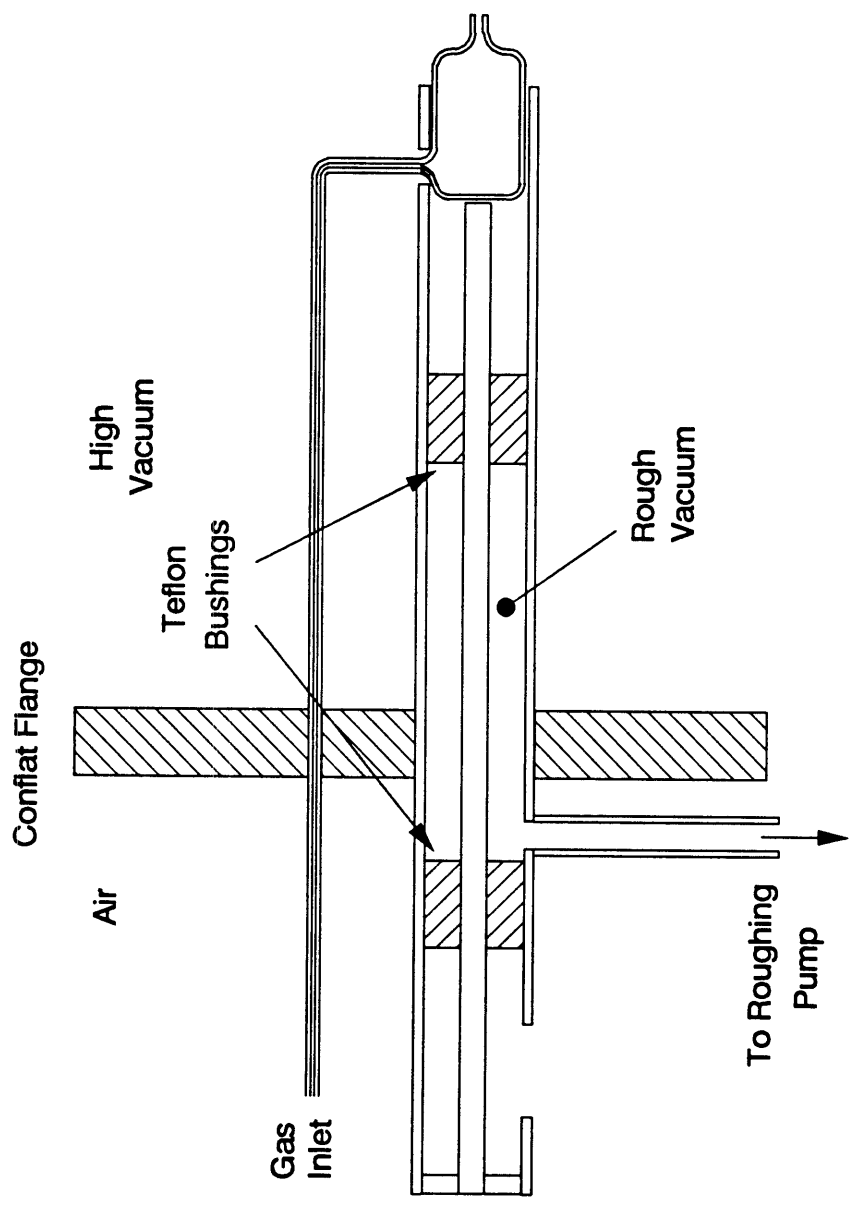


Figure 8.3: Current design for atom source vacuum seal. Teflon bushings in annulus of waveguide define an intermediate compartment, which is maintained at rough vacuum by a mechanical pump.

The other major problem with the atom source was the limited flux to the sample position. Increasing the atom flux above the present level would allow both higher flux ratios and higher overall etching rates. Higher rates would be more representative of industrial practice, and the consequent reduction in etching time would make the experiments more convenient and more reliable (by reducing the opportunities for drift in ion and atom fluxes).

The initial characterization shown in Figure 7.16 was performed before any etching experiments were completed. Not only was the nozzle diameter subsequently changed from 0.5 mm to 0.25 mm, but the need for high flux ratios required an increase in the feed gas flow rate from 2 sccm to 5 sccm. Higher flow rates would have been desirable, but the initial kinetic study presented some indications that the consequent increase in ampule pressure reduced the dissociation efficiency.

There are, in general, three ways to increase the atom flux to the sample: 1) increase the total flux emerging from the source, 2) change the nozzle design to make the emerging beam more directional, and 3) move the atom source closer to the sample. The latter alternative, although conceptually simplest, is limited by clearance problems in the chamber. Moving the present atom source closer to the sample would cause it intrude upon the ion beam. Not only might this affect the direct ion flux to the sample, but it would also raise the possibilities of sample contamination by material sputtered from the atom source and corruption of the ion energy distribution by reflection of ions from the atom source.

The most promising opportunities would appear to be in the ampule and nozzle design. Gray and Sawin [1992] have analyzed the behavior of tubular beam sources at high flux. Several of their conclusions may be applicable to this system as well. First, they introduced a dimensionless parameter η which controls the emission profile of the source (and hence the flux profile of the beam). η is defined as the ratio of source diameter to the mean free path for gas molecules near the tip of the source:

$$\eta = \frac{a}{\lambda_{\text{tip}}} . \quad (8.1)$$

Kinetic theory relates the mean free path to the local pressure by

$$\lambda_{\text{tip}} = \frac{kT}{\sqrt{2} \pi \sigma^2 P_{\text{tip}}} , \quad (8.2)$$

while Gray and Sawin [1992] have shown that

$$P_{\text{tip}} = \frac{4kTN}{\pi v a^2} . \quad (8.3)$$

In the preceding equations, k is Boltzmann's constant, T is the gas temperature, σ is the collision diameter, N is the total number of molecules passing through the tube

in a given time, and v is the average molecular speed, given by

$$v \approx \sqrt{\frac{8kT}{\pi m}} . \quad (8.4)$$

The directionality of the beam qualitatively scales with the inverse of η : if η is lower, then the beam is better directed (and the flux to the sample for a given flow rate will be higher). However, the relationship between η and beam flux profile is not linear. The effect of changes in η depends upon the magnitude of η .

For the chlorine atom source, calculation of P_{tip} and θ requires estimation of the gas temperature T , collision diameter σ , and throughput N . The ampule is water cooled, but the outer wall temperature is known to exceed the melting point of indium foil used for heat transfer. Indium melts at 156° C, so an inside wall (and gas) temperature of 200° C is assumed. The Cl-atom collision diameter is roughly estimated as 5 Å, and the throughput of Cl atoms at the nozzle is approximated as twice the molecular flow of Cl₂ into the ampule. With m in Equation (8.4) equal to 35.5 AMU, these assumptions lead to $v \approx 530$ m/s and the variations of P_{tip} , λ_{tip} , and η with flow rate (in sccm of Cl₂) and nozzle diameter shown in Figure 8.4.

The mean free paths shown in Figure 8.4 are smaller than the nozzle length, so the atom source is operating in what Gray and Sawin [1992] termed the "collisionally opaque" regime. This simply verifies that gas-phase collisions within the

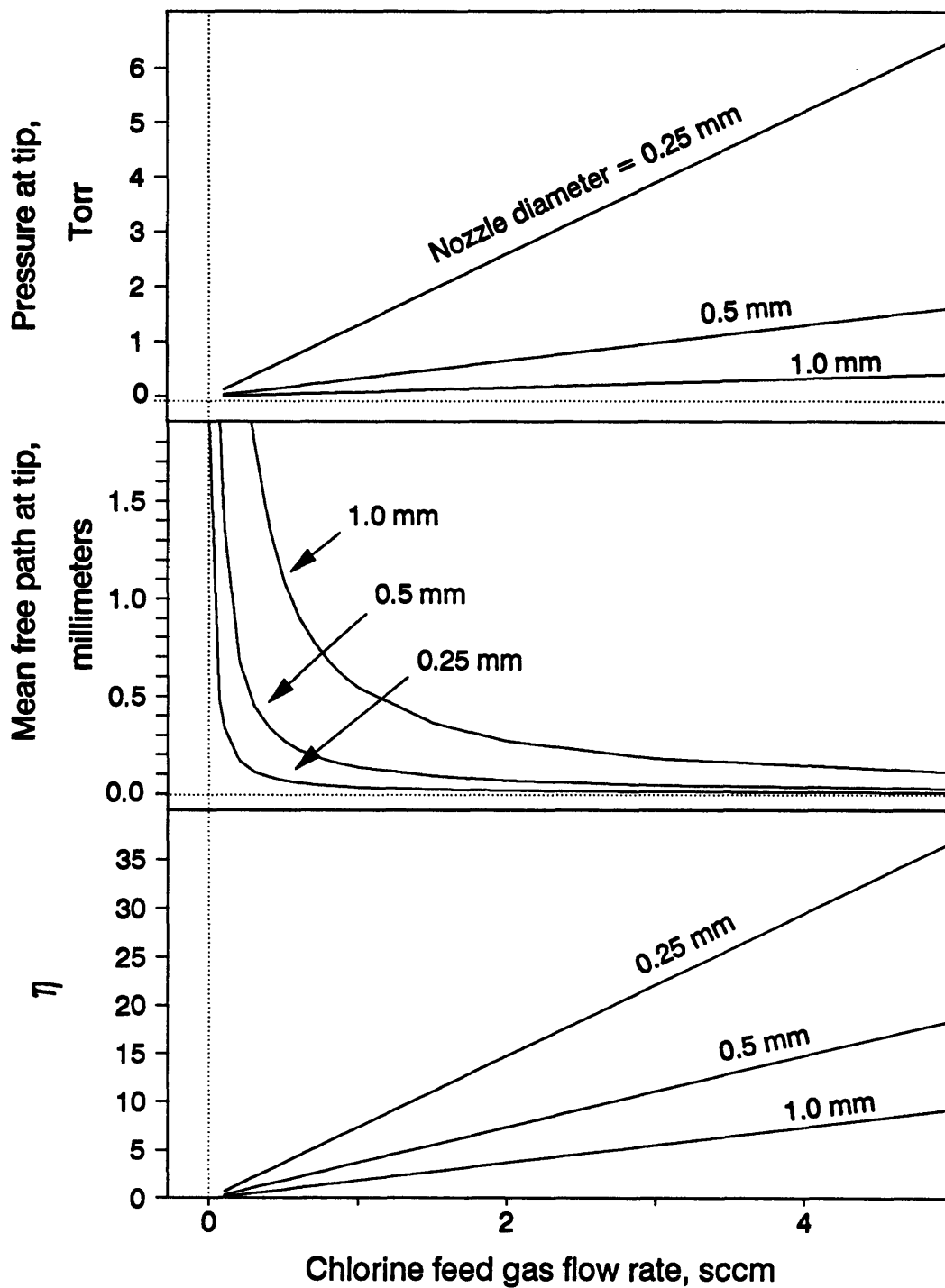


Figure 8.4: Effect of feed gas flow rate and nozzle diameter on pressure, mean free path, and dimensionless parameter η at tip of nozzle.

nozzle are significant, and that the use of η to characterize emission from the nozzle is appropriate. The computed values of η for the operating conditions of the initial kinetic study (0.25 mm nozzle diameter, up to 5 sccm) are quite high. Gray and Sawin described the behavior of sources with η in the range 0.01 to 1.0, reporting that "as $\eta > 1$ the intensity distribution looks like that of the cosine emitter." With η ranging into the 30's, the 0.25 mm nozzle is clearly incapable of producing a well-directed beam.

The high flow rate through the 0.25 mm nozzle also has a strong effect on the discharge pressure within the ampule. Because λ is smaller than the tube diameter, the gas flow through the nozzle is viscous. For viscous flow, the throughput and pressure drop are related by

$$Q = \frac{\pi}{128\eta} \frac{D^4}{L} \bar{P} \Delta P, \quad (8.5)$$

where Q is the flow rate, D and L are the tube diameter and length, \bar{P} and ΔP are the average pressure and the pressure drop across the tube, and η refers (in this Equation only) to the gas viscosity [Brunner and Batzer, 1974]. The viscosity of Cl atoms was not readily available, but approximating the viscosity by 208 μP (the value for Cl_2 at 200° C [Weast, 1983]) gave ampule pressures as shown in Figure 8.5.

Figure 8.5 shows that the ampule pressure for the 0.25 mm nozzle at 5 sccm

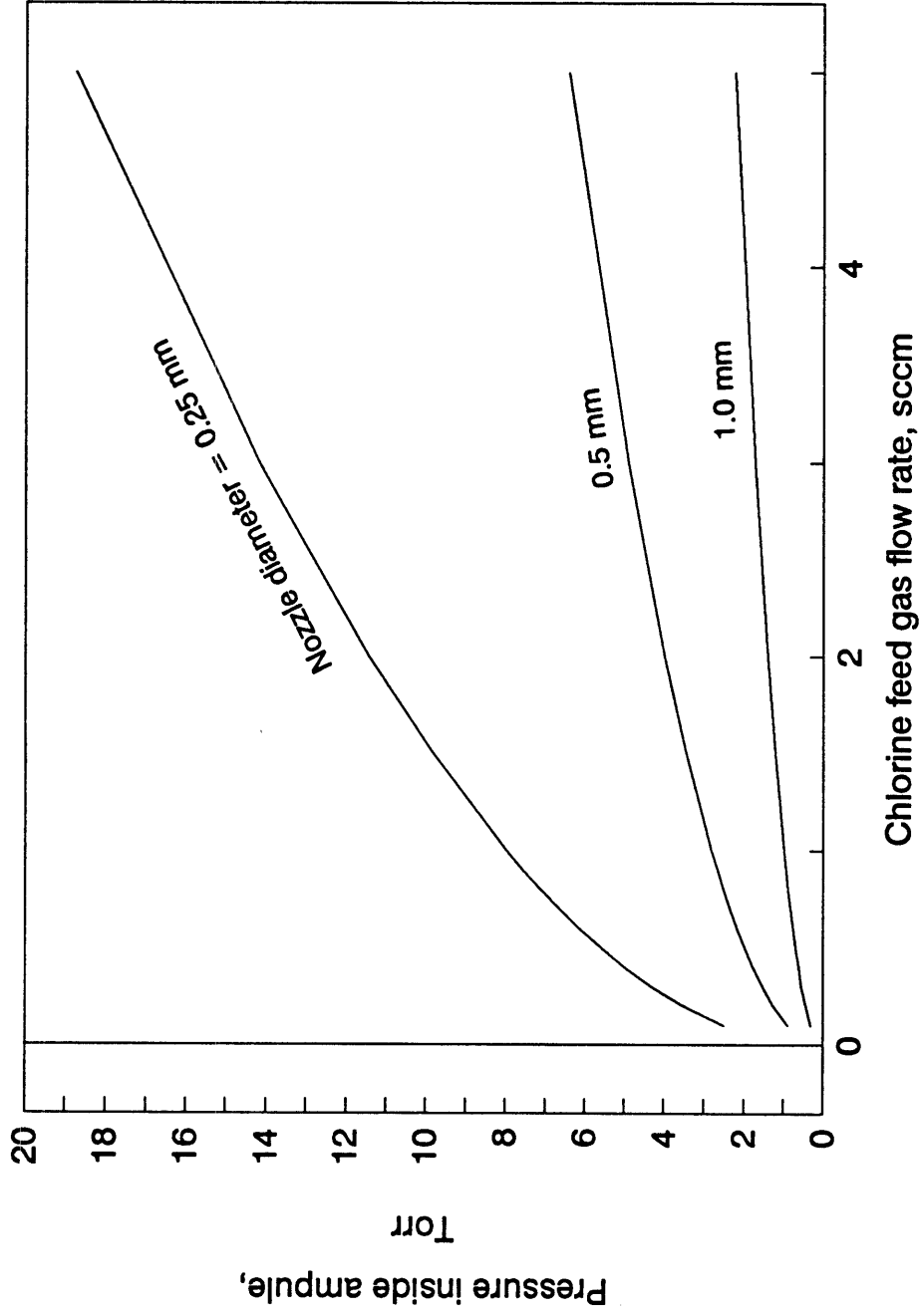


Figure 8.5: Effect of feed gas flow rate and nozzle diameter on pressure inside ampule. At 5 sccm through 0.25 mm nozzle, ampule pressure is more than 18 Torr.

was slightly above 18 Torr, more than 4 1/2 times the pressure for the 0.5 mm nozzle at 2 sccm. Such a great increase in pressure would likely account for the apparent drop in dissociation observed during the initial kinetic study. It is clear that any change to the nozzle design should consider not only the directionality of the beam, but also the pressure within the ampule.

Improving the directionality of the beam requires a reduction in η , which in turn suggests shrinking the tube diameter below the present 0.25 mm. Yet Figure 8.5 indicates that further decreases in nozzle diameter would lead to even higher ampule pressures, thus limiting the available flux (at adequate dissociation) even further.

A more promising approach is to replace the single tube with an array of similar apertures. Dividing the total gas throughput among several tubes would decrease the pressure in and the pressure drop across each. Figure 8.6 shows the effect of replacing the single 0.25 mm hole with arrays of 3, 4, and 5 such holes. The pressure within the ampule is reduced dramatically, as would be expected for a five-fold increase in the tube conductance. This improvement might allow adequate dissociation at higher flow rates (but direct measurement of the dissociation would be in order).

Increasing the number of holes would also decrease η by nearly 7 times. This would certainly seem to be an improvement, because lower η generally leads to more directed beams, but the value of η is still high. Figure 8.7 shows the beam flux profile

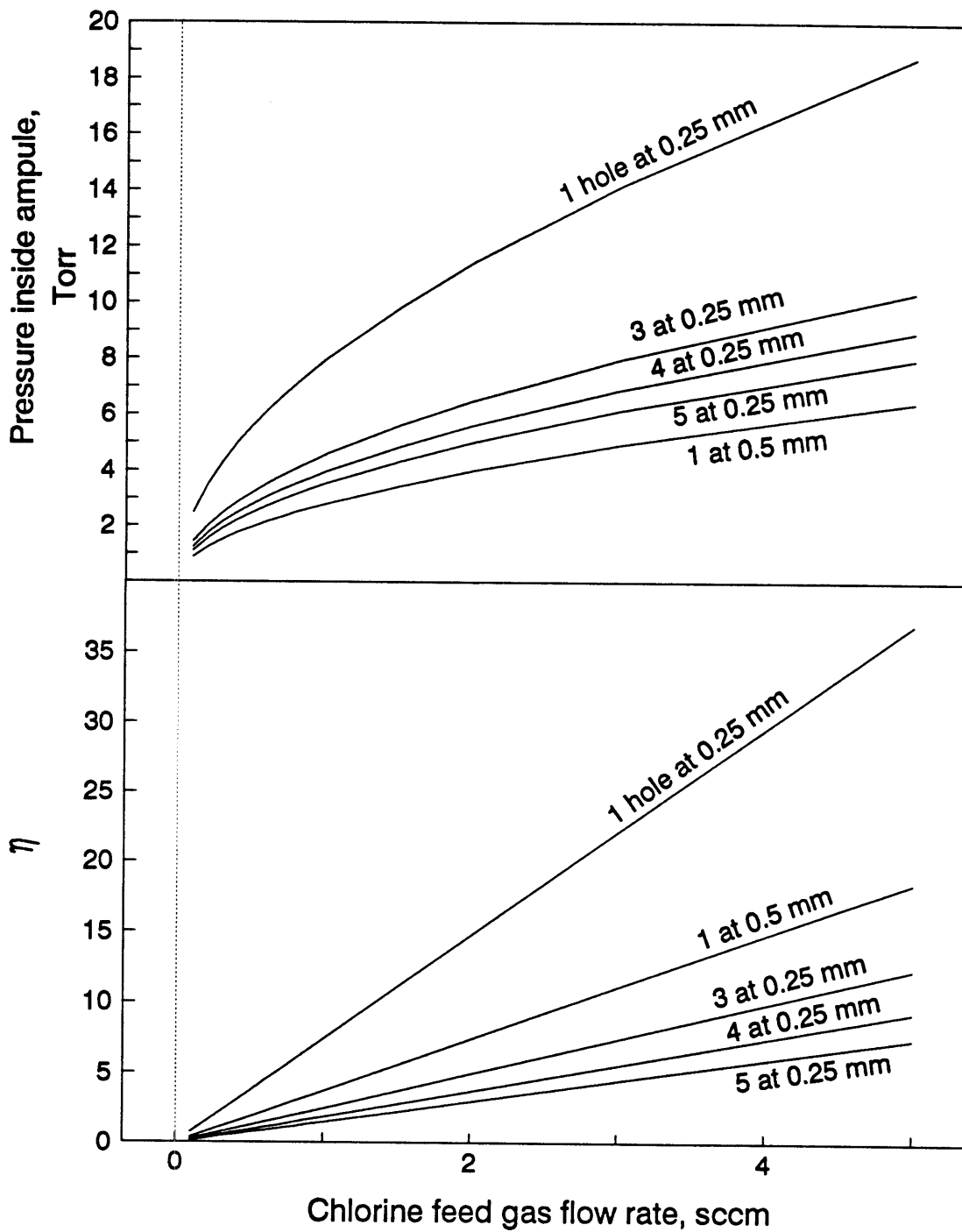


Figure 8.6: Effect of feed gas flow rate on ampule pressure and dimensionless parameter η for different nozzle arrays.

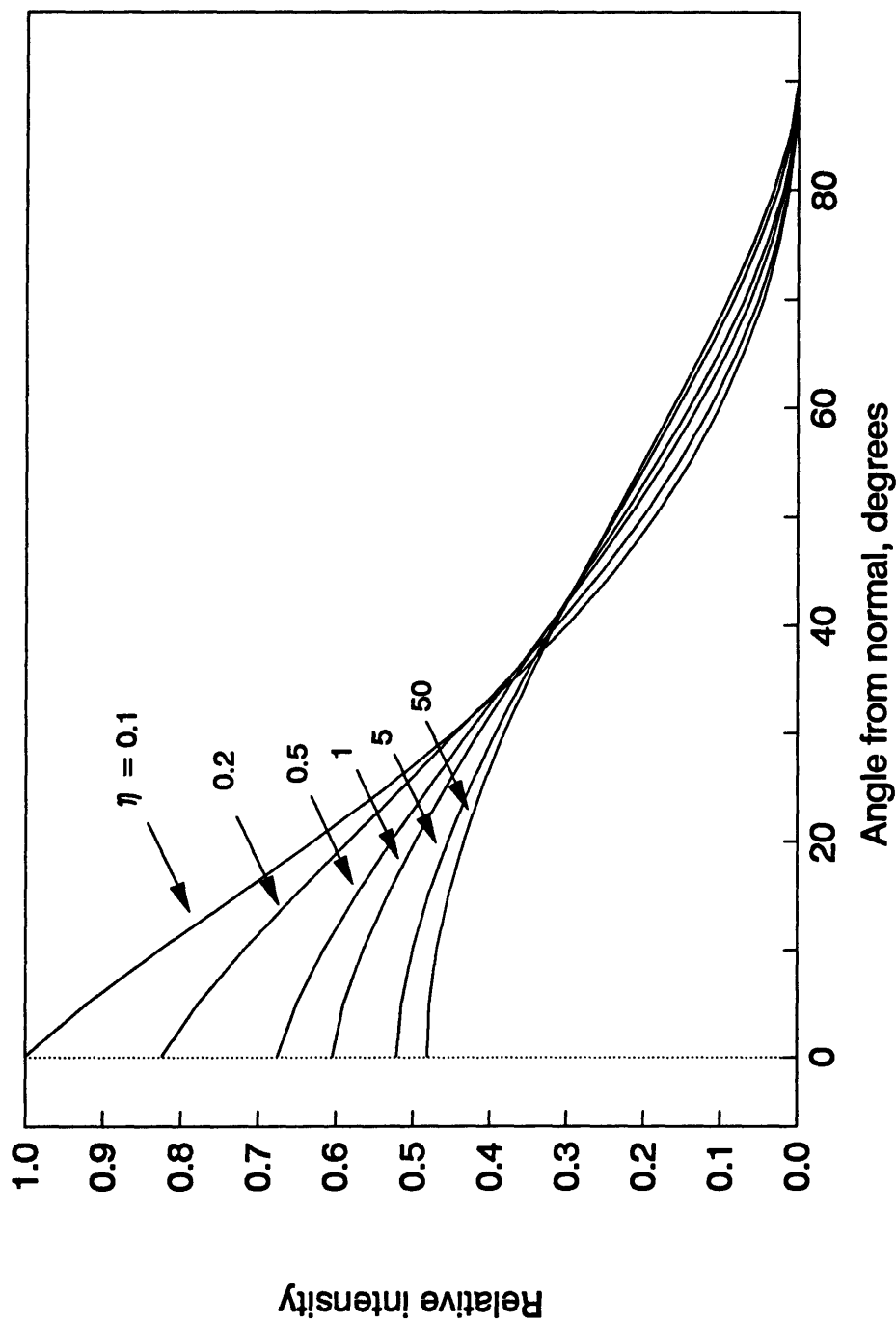


Figure 8.7: Beam intensity profiles for various values of dimensionless parameter η . Beam intensities are normalized to on-normal intensity for $\eta = 0.1$.

for various values of η , using the formulae given by Gray and Sawin [1992]. The peak beam intensity is not linear in η , so decreasing η from 35 to 5 would increase the beam intensity in the active region of the sample by only about 5%. A certain portion of that gain would be lost by the off-center placement of (some of) the nozzles.

Therefore, changing the nozzle design is not a complete solution to the current ampule's problems. While adding additional holes would greatly reduce the pressure inside the ampule, no feasible nozzle design would provide a significant improvement in beam directionality.

On the other hand, it is possible that other changes in the ampule design might improve the flux to the sample. The present beam source can not be moved much closer to the sample without interfering with the ion beam, but relocating the cooling jacket to the far side (from the ion beam) of the source, shifting the nozzles to the near side of the ampule face, or lengthening the ampule's protrusion in front of the source could all reduce the effective distance between the nozzle(s) and the sample. At $\eta = 10$, halving the nozzle-sample distance from 1 cm to 0.5 cm would increase the average flux to the active region of the sample by nearly 75%.

The final concern with the present equipment is the issue of gas backmixing from the main chamber into the CECR. The ion beam flux was depressed slightly during high atom-source flow rate operation. The ion flux measured with chlorine gas flowing into the chamber was slightly ($\approx 10\%$) lower when the Cl_2 flow rate was

above about 2 sccm. This could indicate that chlorine was mixing into the CECR and disrupting the discharge. Flowing an equivalent pressure of nitrogen did not affect the ion beam flux.

The ramifications of chlorine backmixing into the CECR are not entirely clear. If the etching yield of Cl^+ ions is significantly higher than that of Ar^+ , then backmixing might account for the inability to reach yield saturation. High flux ratios generally required high Cl_2 flow rates, so high flux ratio might lead to the introduction of some Cl^+ ions and possibly an increase in the average yield per ion. On the other hand, this hypothesis can not be tested until the yield of Cl^+ ions is known. This topic, and the related issue of differential pumping for the CECR, should be considered further if future work requires separation of the ion and atom source feed gases.

8.2 Etching of Patterned Surfaces

In addition to the kinetic study presented in the previous section, the initial work included an attempt to develop a profile evolution test structure. The proposal was as follows: if samples with known initial surface topography were etched in the 3-beam system, then the subsequent topography evolution could be used to test both the surface kinetic models and the profile evolution software. Varying the sample mounting position would allow some control of the relative ion and atom fluxes to surfaces of the initial feature, thus providing some insight into the mechanisms for

intra-feature transport.

Figure 8.8 illustrates beam etching of an initial surface containing a long rectangular trench. The 45° angle between the ion and atom beams ensures that each feature will have surfaces exposed to various flux ratios. Varying the ion incidence angle and monitoring the evolution of sharp corners could provide information on the variation of etching yield with incidence angle. The initial feature depth is chosen to ensure that some etchable material remains at the bottom, thus illuminating the evolution of concave corners as well.

This section describes an initial attempt to implement such an etching study, and presents some suggestions for future development of the method.

8.2.1 Sample Preparation

For the first effort, surface features were restricted to long rectangular trenches of the type found in the test mask previously employed by this group [Dalton, 1994]. The test mask includes trenches of various widths, down to $0.5 \mu\text{m}$. However, the capabilities of the MIT Integrated Circuits Laboratory (ICL) generally limited consideration to widths of $1.0 \mu\text{m}$ and above.

For etching of this type, the absolute feature dimensions are less important than the aspect ratio (depth divided by width). Therefore, the $1.0 \mu\text{m}$ width limit

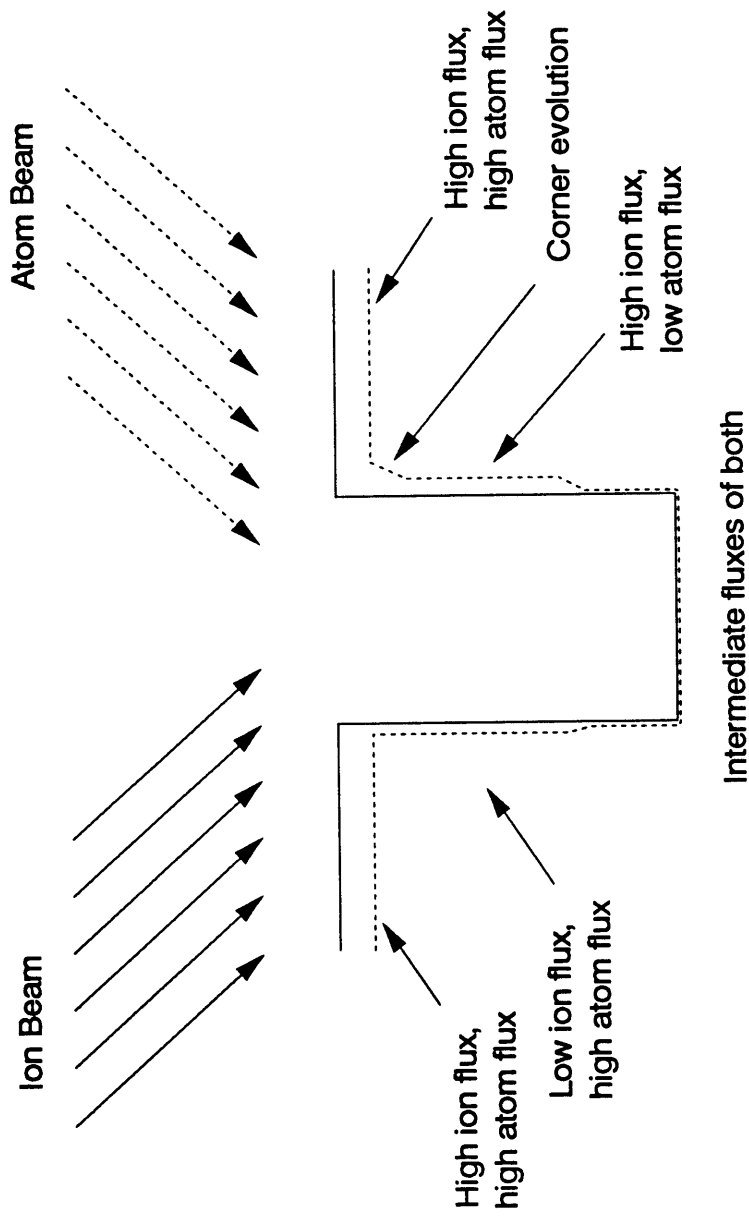


Figure 8.8: Concept for beam etching of initial surface feature. Separation of beams leads to a wide range of flux ratios in a single feature. Corner evolution displays effect of ion incidence angle.

could be accommodated by increasing the film thickness. ICL offers polysilicon films up to 2.5 μm thick, allowing initial aspect ratios up to about ≈ 1.5 .

All polysilicon films were deposited over 1000 \AA thick thermal oxide. Some of the wafers included a 500 \AA deposited oxide film on top of the polysilicon. This film was to be used as a "hard" mask which would allow stripping of the photoresist before etching of the initial trenches. Photoresist with the chosen test pattern was applied to all wafers and the wafers were returned from ICL.

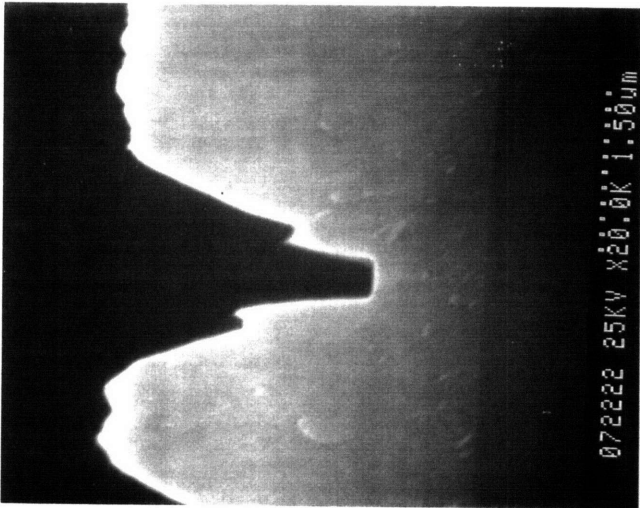
Definition of the initial trenches was performed in the AME-5000 etching system previously described by Dalton [1994]. The hard-masked samples were etched in three steps: CF_4 etching of the oxide, O_2 strip of the photoresist, and the polysilicon etching. Samples without the hard mask proceeded directly to polysilicon etching.

The polysilicon etching was accomplished by two processes. The first was the conventional Cl_2/HBr "gate" process characterized by Dalton [1994]. The second process followed a "deep trench" recipe supplied by Applied Materials, using a mixture of NF_3 , HBr , and O_2 . The etching rate was monitored using Full Wafer Interferometry [Dalton, 1994], with a target etched depth of approximately 1.5-1.7 μm . This depth would leave between 0.8 and 1.0 μm of unetched material below each trench.

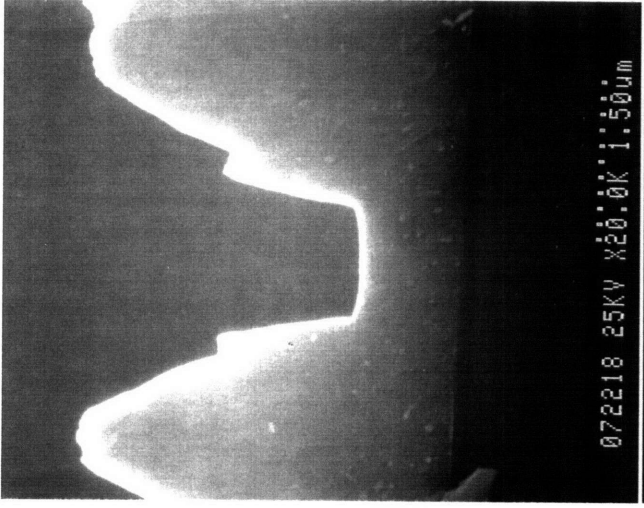
After polysilicon etching, the wafers with photoresist remaining were treated with an oxygen plasma ash. All wafers were sent back to ICL for "Piranha" cleaning (also to remove residual photoresist) and an HF dip (to remove polymeric deposits and the remaining SiO₂ mask films). Piranha cleaning utilizes a mixture of sulfuric acid and hydrogen peroxide, and is generally very effective at removing organic material. However, the very long polysilicon etching process left the photoresist so hard that even the combined stripping process (O₂ plasma followed by Piranha) was unsuccessful. As a consequence, most samples had a significant thickness of residual photoresist.

The hard masking process was also unsuccessful, because the SiO₂ mask eroded from the trench edge during the polysilicon etching process. As a result, the hard-masked trenches had strongly tapered sidewalls. The erosion was apparently caused by unexpected roughness at the top of the polysilicon film coupled with the relatively small oxide thickness (500 Å) used.

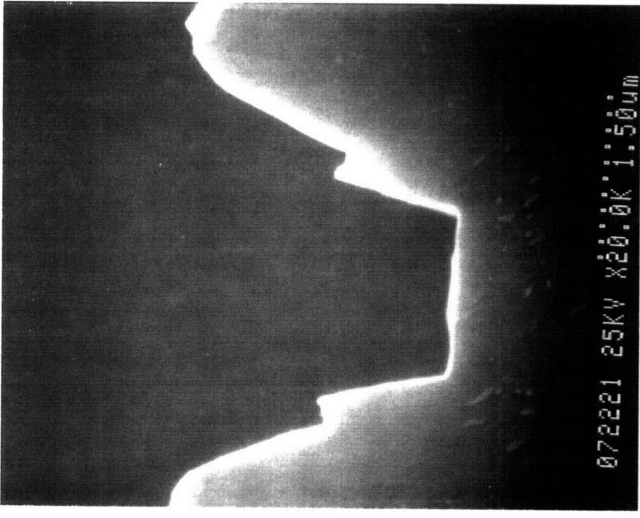
None of the wafers produced the desired initial profiles. The impending shutdown of the AME-5000 etcher made a second attempt at fabrication impossible. Analysis of the available features indicated that the best initial profiles were those formed with the trench etching (NF₃/HBr/O₂) process without the hard mask. Figure 8.9 shows typical initial profiles from this wafer.



1.0 μm nominal width



1.5 μm nominal width



2.0 μm nominal width

Figure 8.9: Typical initial profiles for long rectangular trenches of three nominal widths. Abrupt change in feature width corresponds to polysilicon/photoresist interface. Underlying oxide and substrate are visible below bottoms of features.

8.2.2 Etching and Results

Four dice from the wafer described above were selected for etching. Because the initial features all included photoresist, and the kinetics of photoresist etching were beyond the scope of this study, most of the initial goals were unattainable. On the other hand, etching a few samples at varying ion incidence angles would not be expensive or difficult and might provide some useful information.

After cleaning, the four samples were mounted for ion incidence angles of 0° , 20° , 40° , and 60° from normal. In contrast to the off-normal etching rate measurements described earlier, these samples were oriented so that the ion and atom beams would both fall in the cross-sectional plane of the trench as shown in Figure 8.8. While this was the most appropriate orientation for this study, it prevented real-time monitoring of the etching rate.

Etching conditions were chosen to give approximately the same flux ratio and etched depth for each sample. However, the variable induction time mentioned in Section 8.1.2, coupled with the lack of real-time monitoring, caused the actual etched depth to vary considerably.

Figures 8.10 to 8.13 show SEM pictures of the final profiles for samples etched at each ion incidence angle. The test mask includes several repetitions of each feature, and examination of adjacent trenches showed the etching to be relatively

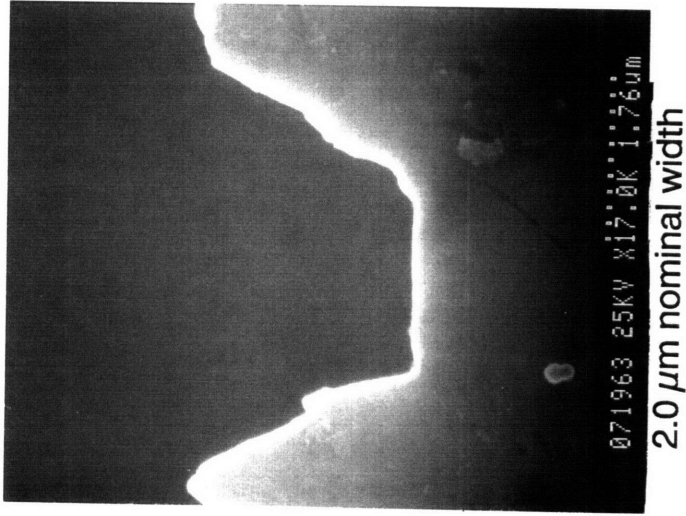
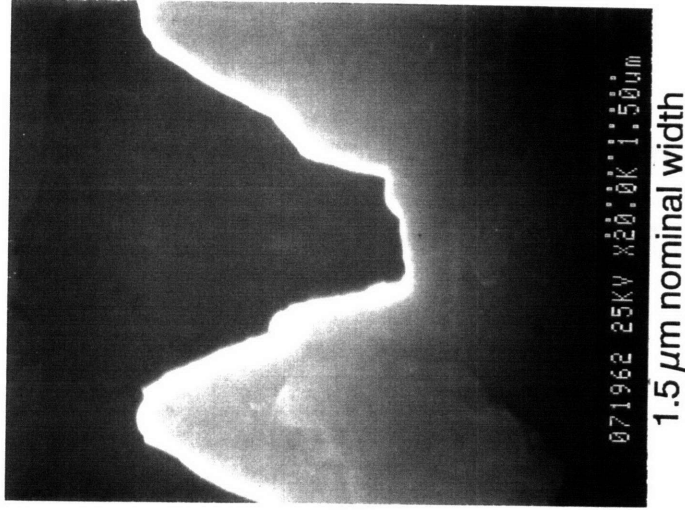
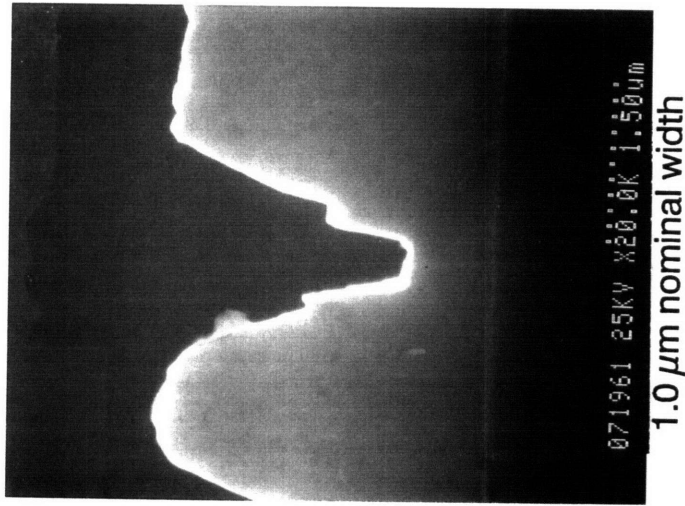
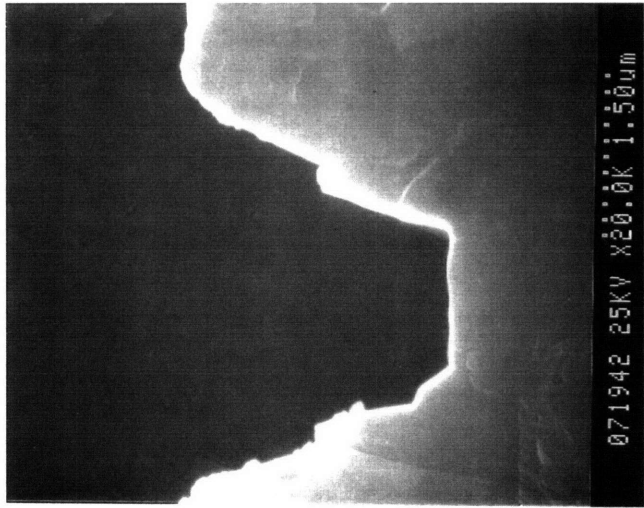
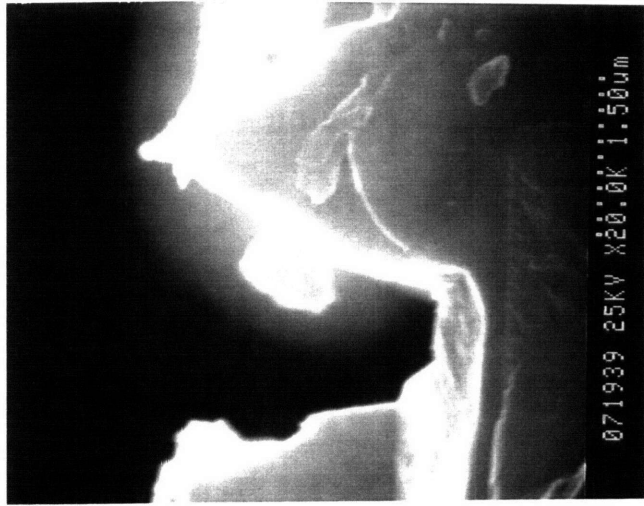


Figure 8.10: Typical surface profiles after beam etching for normal ion incidence. In these views, ion beam bombards sample along vertical line, while atom beam approaches from 45° to the right of vertical.

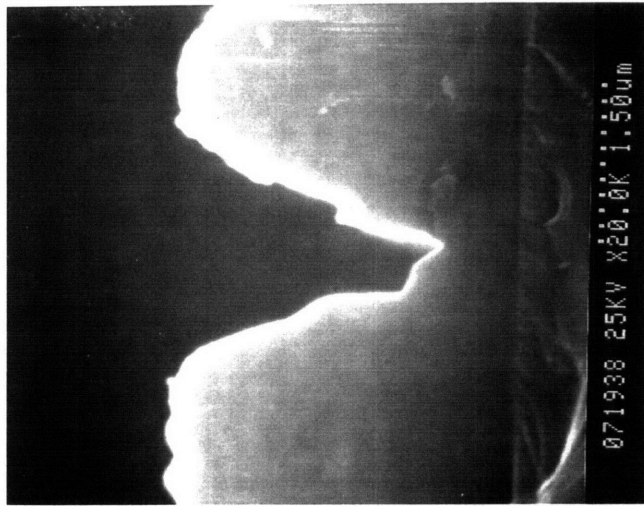
"Blank" page inserted to facilitate
reproduction of Figure 8.10.



2.0 μm nominal width



1.5 μm nominal width



1.0 μm nominal width

Figure 8.11: Typical surface profiles after beam etching for 20° off-normal ion incidence. Ion beam strikes sample along a line 20° to the left of vertical. Atoms approach from 25° to the right of vertical.

"Blank" page inserted to facilitate
reproduction of Figure 8.11.

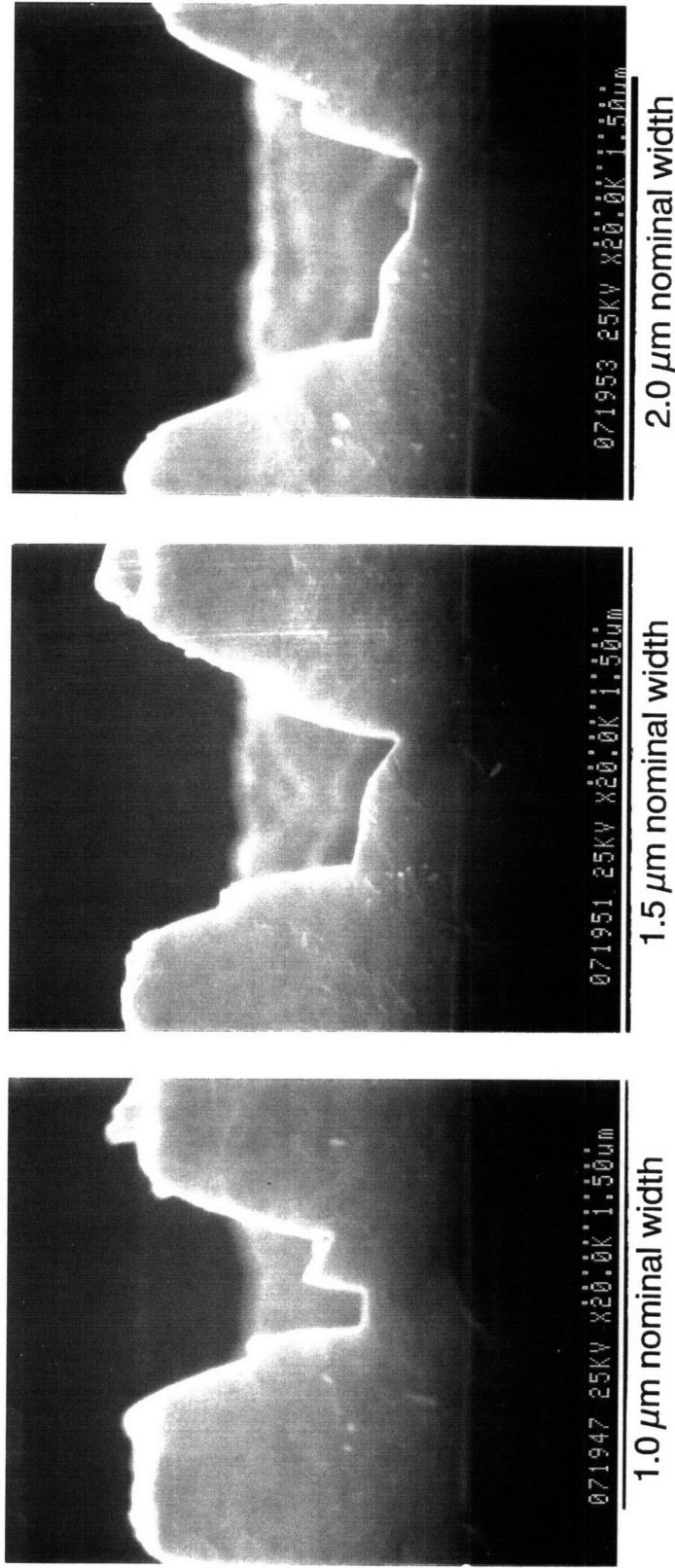
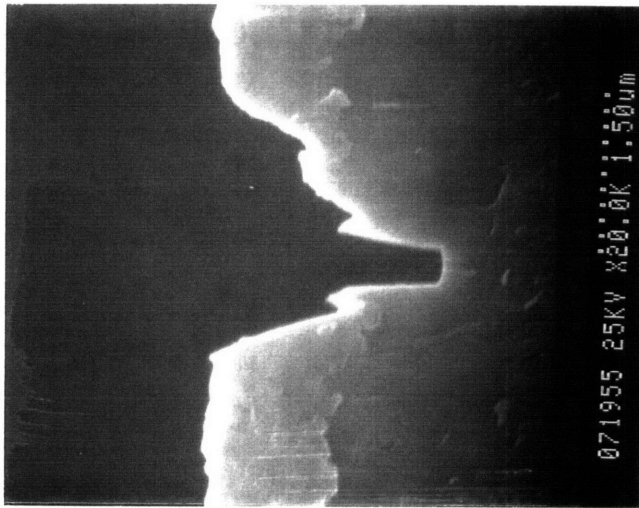
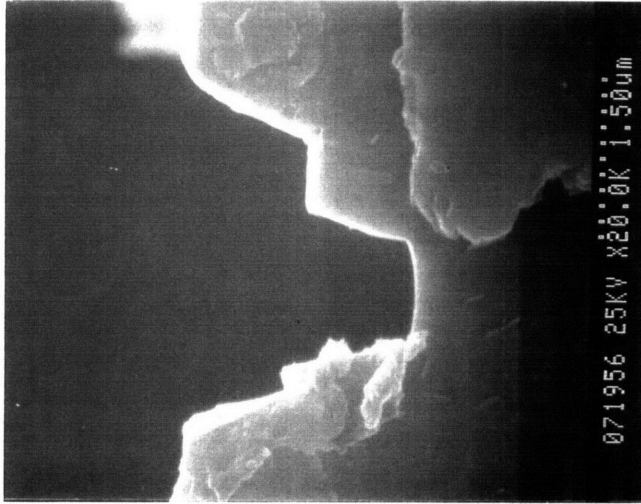


Figure 8.12: Typical surface profiles after beam etching for 40° off-normal ion incidence. Ion beam strikes sample along a line 40° to the left of vertical. Atoms approach from 5° to the right of vertical.

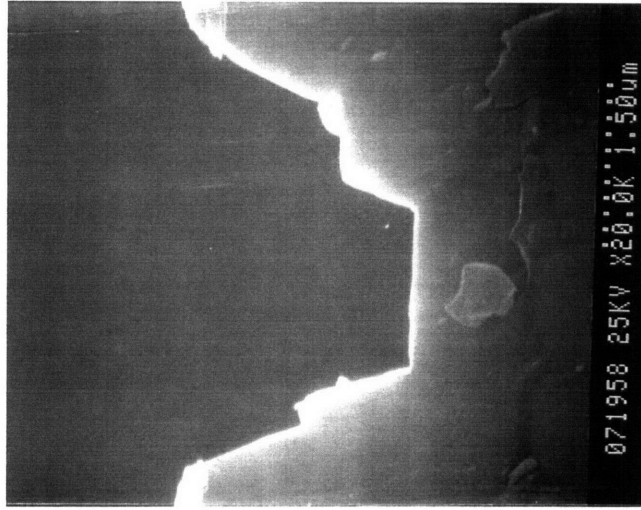
"Blank" page inserted to facilitate
reproduction of Figure 8.12.



1.0 μm nominal width



1.5 μm nominal width



2.0 μm nominal width

Figure 8.13: Typical surface profiles after beam etching for 60° off-normal ion incidence. Ion beam impinges along a line 60° to the left of vertical, striking primarily photoresist. Atoms also approach from left side of feature, along a line 15° from vertical.

"Blank" page inserted to facilitate
reproduction of Figure 8.13.

consistent. The major qualitative features shown in the Figures were consistent from feature to feature and are not due to random fluctuations.

For the most part, the etching appears to follow the ion flux. Etching proceeds primarily in those areas directly exposed to the ion beam. This is consistent with the expectation of a low spontaneous etching rate for chlorine at low temperature.

The effect of chlorine atom flux on the etching rate is unclear. The 20°, 40°, and 60° ion incidence angle samples do not show any effect at all. The 0° samples do show an effect, where the etching rate of the feature bottom is slightly lower on the side of the trench near the atom beam, but the width of the remaining step does not correspond to the expected atom incidence angle (Figure 8.14). It is possible that the actual atom incidence angle differs from the expected by 13°. If that were the case, the feature bottoms on the 0° samples would be consistent with etching synergy (between ions and atoms) and the atom beam shadowing would not be expected to affect the etching of any of the off-normal features.

Figures 8.15 to 8.17 compare the final etched profiles for the off-normal samples to simulations. The simulations, shown as a series of lighter lines on each Figure, are based on the initial profiles shown in Figure 8.9 and an etching rate which is proportional to the ion flux. The simulated profiles are all evenly spaced, starting with the initial profiles. The simulation time to best agreement with the experiment varies from sample to sample. This is thought to be a result of the

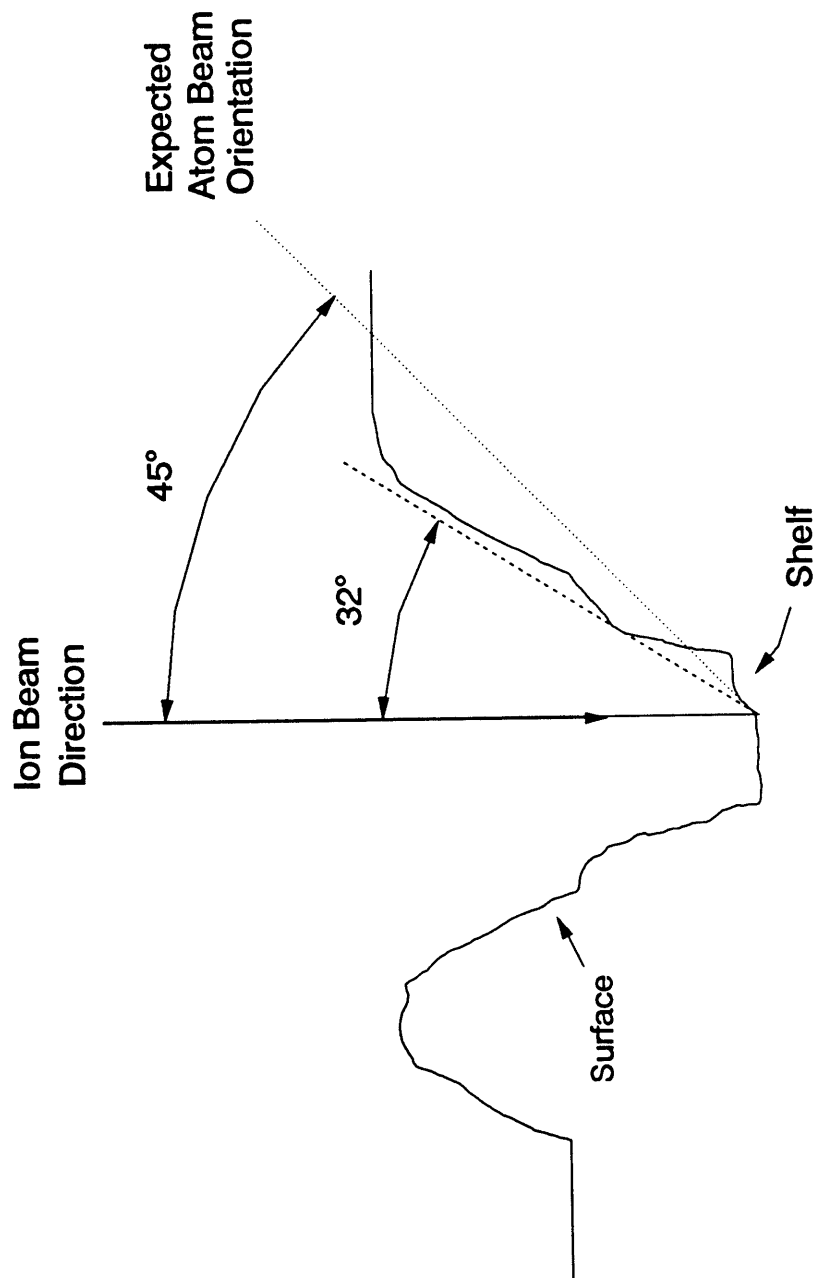


Figure 8.14: Comparison of expected atom beam direction to observed "shelf" remaining on bottom of features etched at normal ion incidence. Atom beam should be directed 45° from the ion beam, but shelf position suggests sidewall shadowing of a beam only 32° from vertical.

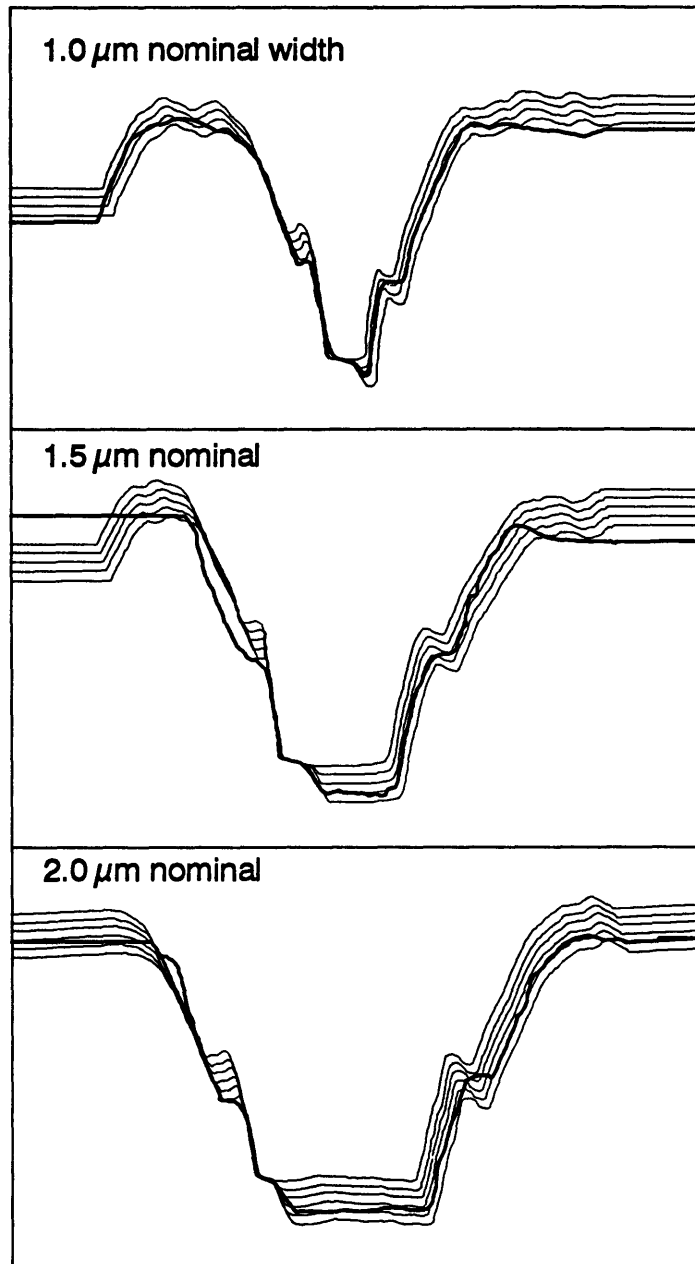


Figure 8.15: Comparison of simulated and observed profiles for samples etched at 20° off-normal ion incidence. Light lines are simulations at various etching times. Dark lines are derived from SEM photos of etched features.

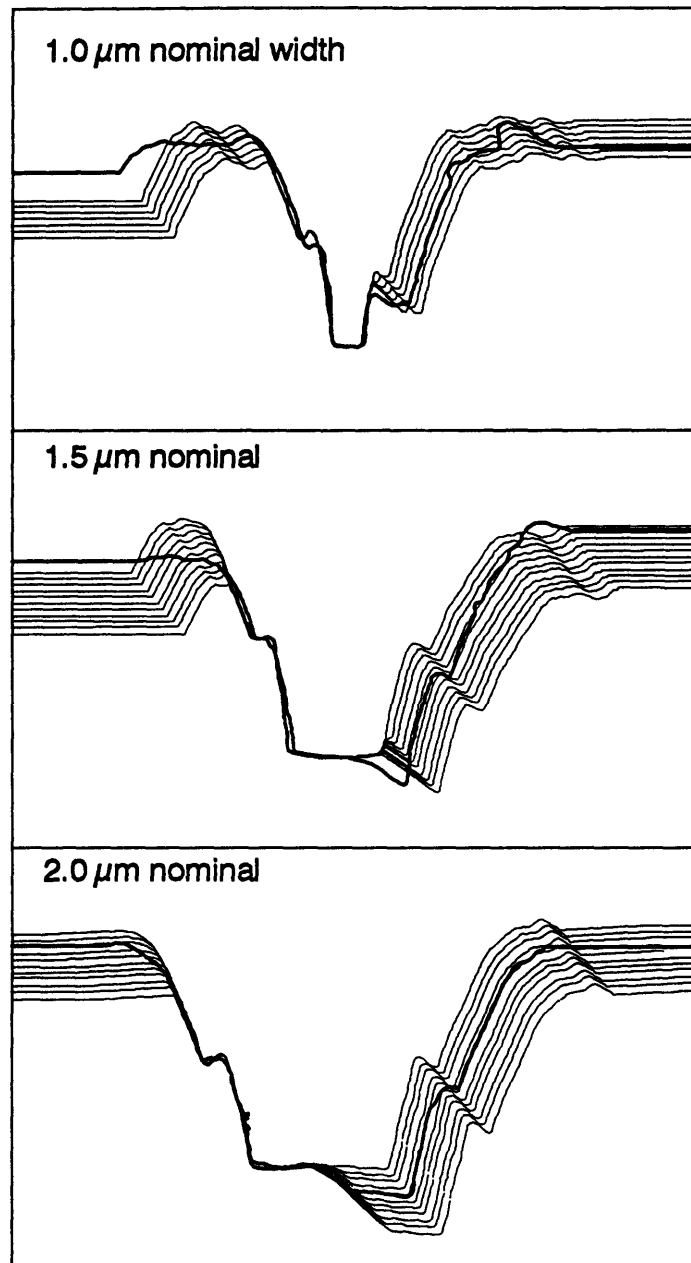


Figure 8.16: Comparison of simulated and observed profiles for samples etched at 40° off-normal ion incidence. Light lines are simulations at various etching times. Dark lines are derived from SEM photos of etched features.

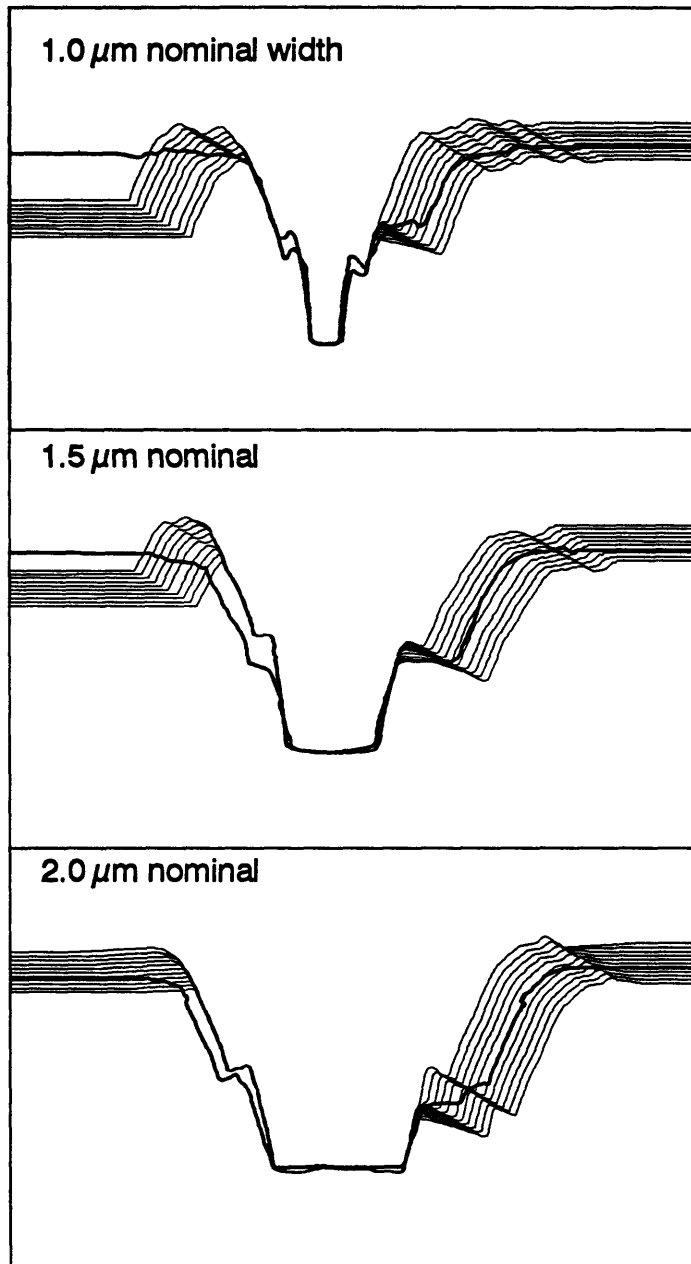


Figure 8.17: Comparison of simulated and observed profiles for samples etched at 60° off-normal ion incidence. Light lines are simulations at various etching times. Dark lines are derived from SEM photos of etched features.

variable (and unmeasured) induction period.

Given the limited understanding of photoresist kinetics and angular etching yield dependence, and the variations in initial surface profile, the agreement between simulated and experimental profiles is reasonable. The uneven topography at the feature bottoms is well-represented in most cases. It is interesting to note that the etching behavior for the photoresist appears to be similar to that of the polysilicon, even though it has not been measured and the simulations made no effort to account for differences in surface material.

8.2.3 Suggestions for Future Work

The conclusions from the trial presented here are mixed. The goals of the project were not met: the kinetic model was not tested in detail, the transport of atoms within the feature could not be modeled, and the ion angular dependence of the etching yield was not observed. On the other hand, it appears that the major barrier to successful study of pattern etching was the simple failure to remove the residual photoresist.

If the photoresist had been removed, then two things would have happened. First, the induction period could have been accounted for by measuring the thickness of polysilicon removed from flat surfaces. Second, a sharp corner of polysilicon would have been exposed to the incoming ion beam, allowing analysis of the angular

variation of etching yield. Complete removal of the photoresist, either through more aggressive stripping processes or selection of a more robust (yet removable) hard mask material, should be the major priority of any future effort in this area.

Other than the photoresist removal problems, the current process appears to be adequate. The initial trench shapes were acceptable, with straight walls and flat bottoms. The walls were not vertical, but that is not a requirement for successful interpretation. Both the initial trench etching and the beam etching processes were uniform enough to allow comparison between features and dice (all samples were selected from a single ring of dice about 1.5 cm from the wafer center). And the range of achievable aspect ratios appeared to be adequate. Higher ratios might be of some value, particularly in view of the fact that removing the photoresist would allow the ion beam to penetrate deeper into the trenches, but drastic efforts do not appear to be warranted.

Recommendations for the next attempt are simple: once a new trench etching process is chosen (given that the AME-5000 is due for removal from this lab), the bulk of the effort should go into ensuring that the mask material is fully removed. Otherwise, the polysilicon film thickness, the test mask design, and the beam etching process all appear to be adequate.

References

- Allen, K. D., H. H. Sawin, M. T. Mocella, and M. W. Jenkins, "The Plasma Etching of Polysilicon with CF_3Cl /Argon Discharges," *J. Electrochem. Soc.*, Vol. 133, No. 11, p. 2315 (1986)
- Barker, R. A., T. M. Mayer, and W. C. Pearson, "Surface Studies of and a Mass Balance for Ar^+ ion-assisted Cl_2 Etching," *J. Vac. Sci. Technol. B*, Vol. 1, No. 1, p. 37, 1983.
- Bers, A., K. Molvig, M. Porkolab, and J. L. Delcroix, "Notes for courses 6.651J, 8.613J, and 22.611J: INTRODUCTION TO PLASMA PHYSICS - I," MIT Dept. of Physics (1987)
- Blech, I. A., "Evaporated Film Profiles over Steps in Substrates," *Thin Solid Films*, Vol. 6, p. 113 (1970)
- Booth, J. P., G. Hancock, N. D. Perry, and M. J. Toogood, "Spatially and Temporally Resolved Laser-Induced Fluorescence Measurements of CF_2 and CF Radicals in a CF_4 RF Plasma," *J. Appl. Phys.*, Vol. 66, No. 11, p. 5251 (1989)
- Brunner, W. F., and T. H. Batzer, Practical Vacuum Techniques, Robert E. Krieger Publishing, Huntington, NY (1974)
- Butterbaugh, J., "Characterization and Modeling of Silicon Dioxide Etching in Tetrafluoromethane RF Glow Discharges," Ph.D. Thesis, MIT Dept. of Chemical Eng., 1990.
- Catana, C., J. S. Colligon, and G. Carter, "The Equilibrium Topography of Sputtered Amorphous Solids III. Computer Simulation," *J. Mat. Sci.*, Vol. 7, p. 467 (1972)
- Chazelle, B., and L. Guibas, "Visibility and Intersection Problems in Plane Geometry," Proceedings of ACM Symposium on Computational Geometry, p. 135 (1985)
- Chuang, T. J., "Electron Spectroscopy Study of Silicon Surfaces Exposed to XeF_2 and the Chemisorption of SiF_4 on Silicon," *J. Appl. Phys.*, Vol. 51, No. 5, p. 2614 (1980)
- Coburn, J. W., "Plasma-Assisted Etching," *Plasma Chemistry and Plasma Processing*, Vol. 2, No. 1, p. 1 (1982)
- Coburn, J. W., and H. F. Winters, "Plasma Etching - A Discussion of Mechanisms," *J. Vac. Sci. Technol.*, Vol. 16, No. 2, p. 391 (1979)

- Coburn, J. W., and H. F. Winters, "Plasma-Assisted Etching: Ion-Assisted Surface Chemistry," *Appl. Surf. Sci.*, no. 22/23, p. 63 (1985)
- Coburn, J. W., and H. F. Winters, "The Role of Energetic Ion Bombardment in Silicon-Fluorine Chemistry," *Nucl. Instr. Meth.*, Vol. B27, p. 243 (1987)
- Coburn, J. W., and H. F. Winters, "Conductance Considerations in the Reactive Ion Etching of High Aspect Ratio Features," *Appl. Phys. Lett.*, Vol. 55, No. 26, p. 2730 (1989)
- Cuthbertson, J. W., "Reflection of Plasma Ions from Metals (and Its Use as a Hyperthermal Neutral Beam Source)," Ph.D. Thesis, Princeton University Dept. of Astrophysical Sciences (1991)
- d'Agostino, R., V. Colaprico, and F. Cramarossa, "The Use of Actinometer Gases in Optical Diagnostics of Plasma Etching Mixtures: SF₆-O₂," *Plasma Chemistry and Plasma Processing*, Vol. 1, No. 4, p. 365 (1981)
- Dahl, D., and J. Delmore, The SIMION PC/PS2 User's Manual, Idaho National Engineering Laboratory (1988)
- Dalton, T. J., "Pattern Dependencies in the Plasma Etching of Polysilicon," Ph.D. Thesis, MIT Dept. of Chemical Engineering (1994)
- Dalton, T. J., J. C. Arnold, H. H. Sawin, S. Swan, and D. Corliss, "Microtrench Formation in Polysilicon Plasma Etching over Thin Gate Oxide," *J. Electrochem. Soc.*, Vol. 140, No. 8, p. 2395 (1993)
- Dalvie, M., R. T. Farouki, S. Hamaguchi, "Flux Considerations in the Coupling of Monte Carlo Plasma Sheath Simulations with Feature Evolution Models," *IEEE Trans. Electron Dev.*, ED-39, p 1090 (1992)
- Deshmukh, S. C., and D. J. Economou, "Remote Plasma Etching Reactors: Modeling and Experiment," *J. Vac. Sci. Technol. B*, Vol. 11, No. 2, p. 206 (1993)
- Donnelly, V. M., D. L. Flamm, W. C. Dautremont-Smith, and D. J. Wender, "Anisotropic Etching of SiO₂ in Low-Frequency CF₄/O₂ and NF₃/Ar Plasmas," *J. Appl. Phys.*, Vol. 55, No. 1, p. 242 (1984)
- Ducommun, J. P., M. Cantagrel, and M. Marchal, "Development of a General Surface Contour by Ion Erosion. Theory and Computer Simulation," *J. Mat. Sci.*, Vol. 9, p. 725 (1974)
- Ducommun, J. P., M. Cantagrel, and M. Moulin, "Evolution of Well-Defined Surface Contour Submitted to Ion Bombardment: Computer Simulation and Experimental Investigation," *J. Mat. Sci.*, Vol. 10, p. 52 (1975)

- Flamm, D. L., V. M. Donnelly, and J. A. Mucha, "The Reaction of Fluorine Atoms with Silicon," *J. Appl. Phys.*, Vol. 52, No. 5, p. 3633 (1981)
- Gebhart, B., Heat Transfer, Second Edition, Ch. 5, McGraw-Hill, New York, 1971
- Gerlach-Meyer, U., "Ion-Enhanced Gas-Surface Reactions: A Kinetic Model for the Etching Mechanism," *Surf. Sci.*, Vol. 103, p. 524 (1981)
- Gibson, G. W., "Miniature Retarding Grid Ion Energy Analyzer," 45th Annual Gaseous Electronics Conference, Boston, MA (1992)
- Gottscho, R. A., C. W. Jurgensen, and D. J. Vitkavage, "Microscopic Uniformity in Plasma Etching," *J. Vac. Sci. Technol. B*, Vol. 10, No. 5, p. 2133 (1992)
- Gray, D. C., "Beam Simulation Studies of Plasma-Surface Interactions in Fluorocarbon Etching of Si and SiO₂," Ph.D. Thesis, MIT Dept. of Chemical Engineering (1992)
- Gray, D. C., and H. H. Sawin, "Design Considerations for High-Flux Collisionally Opaque Molecular Beams," *J. Vac. Sci. Technol. A*, Vol. 10, No. 5, p. 3229 (1992)
- Gray, D. C., I. Tepermeister, and H. H. Sawin, "Phenomenological Modeling of Ion-Enhanced Surface Kinetics in Fluorine-Based Plasma Etching," *J. Vac. Sci. Technol. B*, Vol. 11, No. 4, p. 1243 (1993)
- Hamaguchi, S., M. Dalvie, R. Farouki, and S. Sethuraman, "A Shock-tracking Algorithm for Surface Evolution Under Reactive-Ion Etching," *J. Appl. Phys.*, Vol. 74, No. 8, p. 5172 (1993)
- Harper, J. M. E., J. J. Cuomo, P. A. Leary, G. M. Summa, H. R. Kaufman, and F. J. Bresnock, "Low Energy Ion Beam Etching," *J. Electrochem. Soc.*, Vol. 128, No. 5, p. 1077 (1981)
- Houle, F. A., "Photoeffects on the Fluorination of Silicon: I. Influence of Doping on Steady-State Phenomenon," *J. Chem. Phys.*, Vol. 79, No. 9, p. 4237, 1983.
- Houle, F. A., "Reinvestigation of the Etch Products of Silicon and XeF₂: Doping and Pressure Effects," *J. Appl. Phys.*, Vol. 60, No. 9, p. 3018, 1986.
- Jewett, R. A., "A String Model Etching Algorithm," Memorandum N. UCB/ERL M79/68, University of California, Berkeley (1979)
- Joubert, O., G. S. Oehrlein, and Y. Zhang, "Fluorocarbon High Density Plasma. V. Influence of Aspect Ratio on the Etch Rate of Silicon Dioxide in an Electron Cyclotron Resonance Plasma," *J. Vac. Sci. Technol. A*, Vol. 12, No. 3, p. 658

(1994)

Joubert, O., G. S. Oehrlein, and M. Surendra, "Fluorocarbon High Density Plasma. VI. Reactive Ion Etching Lag Model for Contact Hole Silicon Dioxide Etching in an Electron Cyclotron Resonance Plasma," *J. Vac. Sci. Technol. A*, Vol. 12, No. 3, p. 665 (1994)

Jurgensen, C. W. and E. S. G. Shaqfeh, "Kinetic Theory of Bombardment Induced Interface Evolution," *J. Vac. Sci. Technol. B*, Vol. 7, No. 6, p. 1488 (1989)

Katardjiev, I. V., G. Carter, M. J. Nobes, and R. Smith, "Precision Modeling of the Mask-Substrate Evolution During Ion Etching," *J. Vac. Sci. Technol. A*, Vol. 6, No. 4, p. 2443 (1988)

Katardjiev, I. V., "Simulation of Surface Evolution During Ion Bombardment," *J. Vac. Sci. Technol. A*, Vol. 6, No. 4, p. 2434 (1988)

Kiss, L. D. B., and H. H. Sawin, "Evaluation of CF_4 Plasma Chemistry by Power Modulation," *Plasma Chemistry and Plasma Processing*, Vol. 12, No. 4, p. 523 (1992)

Lax, P. D., "Weak Solutions of Nonlinear Hyperbolic Equations and Their Numerical Computation," *Comm. Pure Appl. Math.*, Vol. 7, p. 159 (1954)

Lax, P. D., "Hyperbolic Systems of Conservation Laws II," *Comm. Pure Appl. Math.*, Vol. 10, p. 537 (1957)

Lax, P. D. and B. Wendroff, "Systems of Conservation Laws," *Comm. Pure Appl. Math.*, Vol. 13, p. 217 (1960)

Lee, Y. H., and Z. H. Zhou, "Feature-Size Dependence of Etch Rate in Reactive Ion Etching," *J. Electrochem. Soc.*, Vol. 138, No. 8, p. 2439 (1989)

Liu, J., G. L. Huppert, and H. H. Sawin, "Ion Bombardment in RF Plasmas," *J. Appl. Phys.*, Vol. 68, No. 8, p. 3916 (1990)

Mayer, T. M., R. A. Barker, and L. J. Whitman, "Investigation of Plasma Etching Mechanisms Using Beams of Reactive Gas Ions," *J. Vac. Sci. Technol.*, Vol. 18, No. 2, p. 349 (1981)

McFeely, F. R., J. F. Morar, N. D. Shinn, G. Landgren, and F. J. Himpsel, "Synchrotron Photoemission Investigation of the Initial Stages of Fluorine Attack on Si Surfaces: Relative Abundance of Fluorosilyl Species," *Phys. Rev. B*, Vol. 30, No. 2, p. 764 (1984)

McNevin, S. C., and G. E. Becker, "Investigation of Kinetic Mechanism for the Ion-

- Assisted Etching of Si in Cl₂," *J. Vac. Sci. Technol. B*, Vol. 3, No. 2, p. 485, 1985.
- Melliar-Smith, C. M., "Ion Etching for Pattern Delineation," *J. Vac. Sci. Technol.*, Vol. 13, No. 5, p. 1008 (1976)
- Neureuther, A. R., C. Y. Liu, and C. H. Ting, "Modelling Ion Milling," *J. Vac. Sci. Technol.*, Vol. 16, No. 6, p. 1767 (1979)
- Oehrlein, G. S., Y. Zhang, D. Vender, and M. Haverlag, "Fluorocarbon High-Density Plasmas: I. Fluorocarbon Film Deposition and Etching Using CF₄ and CHF₃," *J. Vac. Sci. Technol. A*, Vol. 12, No. 2, p. 323 (1994)
- Oehrlein, G. S., Y. Zhang, D. Vender, and O. Joubert, "Fluorocarbon High-Density Plasmas: II. Silicon Dioxide and Silicon Etching Using CF₄ and CHF₃," *J. Vac. Sci. Technol. A*, Vol. 12, No. 2, p. 333 (1994)
- Ogryzlo, E. A., D. L. Flamm, D. E. Ibbotson, and J. A. Mucha, "The Etching of Doped Polycrystalline Silicon by Molecular Chlorine," *J. Appl. Phys.*, Vol. 64, No. 11, p. 6510, 1988.
- Ogryzlo, E. A., D. E. Ibbotson, D. L. Flamm, and J. A. Mucha, "Doping and Crystallographic Effects in Cl-Atom Etching of Silicon," *J. Appl. Phys.*, Vol. 67, No. 6, p. 3115, 1990.
- Oldham, W. G., S. N. Nandgaonkar, A. R. Neureuther, and M. O'Toole, "A General Simulator for VLSI Lithography and Etching Processes: Part I - Application to Projection Lithography," *IEEE Trans. Electron Devices*, Vol. ED-26, No. 4, p. 717 (1979)
- Pilz, W., H. Hübner, F. Heinrich, P. Hoffman, and M. Franosch, "Discussion in Profile Phenomena in Sub- μ m Resist Reactive Ion Etching," *Microelectronic Engineering*, Vol. 9, p. 491 (1989)
- Quinn, B. K., "Solutions with Shocks: An Example of an L₁-Contractive Semigroup," *Commun. Pure Appl. Math.*, Vol. 18, p. 125 (1971)
- Ross, D. S., "Ion Etching: An Application of the Mathematical Theory of Hyperbolic Conservation Laws," *J. Electrochem. Soc.*, Vol. 135, No. 5, p. 1235 (1988)
- Ryan, K. C., and I. C. Plumb, "A Model for the Etching of Si in CF₄ Plasmas: Comparison with Experimental Measurements," *Plasma Chemistry and Plasma Processing*, Vol. 6, No. 3, p. 231 (1986)
- Sato, M. and Y. Arita, "Etched Shape Control of Single-Crystal Silicon in Reactive Ion Etching Using Chlorine," *J. Electrochem. Soc.*, Vol. 134, No. 11, p. 2856

(1987)

- Shapiro, A. B., "FACET - A Radiation View Factor Computer Code for Axisymmetric, 2D Planar, and 3D Geometries with Shadowing," Lawrence Livermore National Laboratory Report UCID-19887 (1983)
- Shaqfeh, E. S. G., and C. W. Jurgensen, "Simulation of Reactive Ion Etching Pattern Transfer," *J. Appl. Phys.*, Vol. 66, No. 10, p. 4664 (1989)
- Shibano, T., N. Fujiwara, M. Hirayama, H. Nagata, and K. Demizu, "Etching Yields of SiO₂ by Low Energy CF_x⁺ and F⁺ Ions," *Appl. Phys. Lett.*, Vol. 63, No. 17, p. 2336 (1993)
- Siegel, R., and J. R. Howell, Thermal Radiation Heat Transfer, Second Edition, McGraw-Hill, New York (1971)
- Singh, V. K., E. S. G. Shaqfeh, and J. P. McVittie, "Simulation of Profile Evolution in Silicon Reactive Ion Etching with Re-emission and Surface Diffusion," *J. Vac. Sci. Technol. B*, Vol. 10, No. 3, p. 1091 (1992)
- Smith, R., S. J. Wilde, G. Carter, I. V. Katardjiev, and M. J. Nobes, "The Simulation of Two-Dimensional Surface Erosion and Deposition Processes," *J. Vac. Sci. Technol. B*, Vol. 5, No. 2, p. 579 (1987)
- Stewart, A. D. G., and M. W. Thompson, "Microtopography of Surfaces Eroded by Ion Bombardment," *J. Mat. Sci.*, Vol. 4, p. 56 (1969)
- Tachi, S., and S. Okudaira, "Chemical Sputtering of Silicon by F⁺, Cl⁺, and Br⁺ Ions: Reactive Spot Model for Reactive Ion Etching," *J. Vac. Sci. Technol. B*, Vol. 4, No. 2, p. 459, 1986.
- Thompson, B. E., H. H. Sawin, and D. A. Fisher, "Monte Carlo Simulation of Ion Transport Through RF Glow Discharges," *J. Appl. Phys.*, Vol. 63, No. 7, p. 2241 (1988)
- Tu, Y. Y., T. J. Chuang, and H. F. Winters, "Chemical Sputtering of Fluorinated Silicon," *Phys. Rev. B*, Vol. 23, No. 2, p. 823 (1981)
- Ulacia F., J. I., and J. P. McVittie, "A Two-Dimensional Computer Simulation for Dry Etching Using Monte Carlo Techniques," *J. Appl. Phys.*, Vol. 65, No. 4, p. 1484 (1989)
- Ulacia F., J. I., C. J. Petti, and J. P. McVittie, "Crystal-Orientation Dependent Etch Rates and A Trench Model for Dry Etching," *J. Electrochem. Soc.*, Vol. 135, No. 6, p. 1521 (1988)

Weast, R. C., Editor, CRC Handbook of Chemistry and Physics, 64th Edition, CRC Press, Boca Raton, FL (1983)

Wilson, I. H., J. Belson, and O. Auciello, in Ion Bombardment Modification of Surfaces, ed. O. Auciello and R. Kelly, Elsevier, New York, 1984

Winters, H. F., and J. W. Coburn, "Plasma-Assisted Etching Mechanisms: The Implications of Reaction Probability and Halogen Coverage," *J. Vac. Sci. Technol. B*, Vol. 3, No. 5, p. 1376 (1985)

Zauderer, E., Partial Differential Equations of Applied Mathematics, Wiley, New York (1983)

Appendix A

Ion Reflection Model for Circular Via

A.1 Description of Via

The circular contact hole or "via" is a frequently encountered structure in microelectronics. Such structures are used to make contact between layers of metal signal lines, and are usually formed by etching through a layer or insulating material. The "circular" description arises from the top-down view of the initial mask opening. As the via is etched, the opening assumes the shape of a cylinder or a frustum (because of sidewall tapering). The via retains a 2-Dimensional symmetry, because any plane passing through the central axis intersects the feature surface with the same pattern. However, sidewall curvature outside of the cross-sectional plane makes the analysis of material transport much more complicated (than for the long rectangular trench).

A.2 Geometry for Ion Reflection in Via

The natural coordinate system for flux calculations in vias is not the (α, χ) system used for trenches but the conventional spherical system (θ, ϕ) , where θ is measured from the upwardly-pointing wafer surface normal and ϕ describes rotation about that normal from some arbitrary reference direction. There are two reasons

for this: first, no other coordinate system provides the out-of-plane simplification used in trenches, and second, the curvature of the sidewalls causes the sidewall visibility in a via to change with ϕ . It is not possible to analyze visibility in a single cross-sectional plane and apply those results outside of that plane, but use of the (θ, ϕ) system limits the need for visibility calculation to once per combination of target location and ϕ .

Note that ϕ is used to denote rotation about the upward normal through the target point, not about the central axis of the feature. This Appendix uses the term γ for rotation about that axis (Figure A.1).

Not only does the sidewall visibility change with ϕ , but so does the orientation of each sidewall segment. Applying the usual linear discretization in the cross-sectional plane produces not a series of planar wall segments, but a series of frustums which are symmetric about the central axis of the feature but are not symmetric about the surface normal through any other target point. As a consequence, reflection from the sidewall changes all three spatial components of the particle velocity.

The 3-D nature of sidewall reflections led to the following procedure for flux calculations. The flux arriving at the target point is governed by three characteristic angles: the angle of arrival at the target (θ_t), the angle of incidence at the reflection point (θ_s), and the angle of departure from the sheath (θ_g). These are all given by

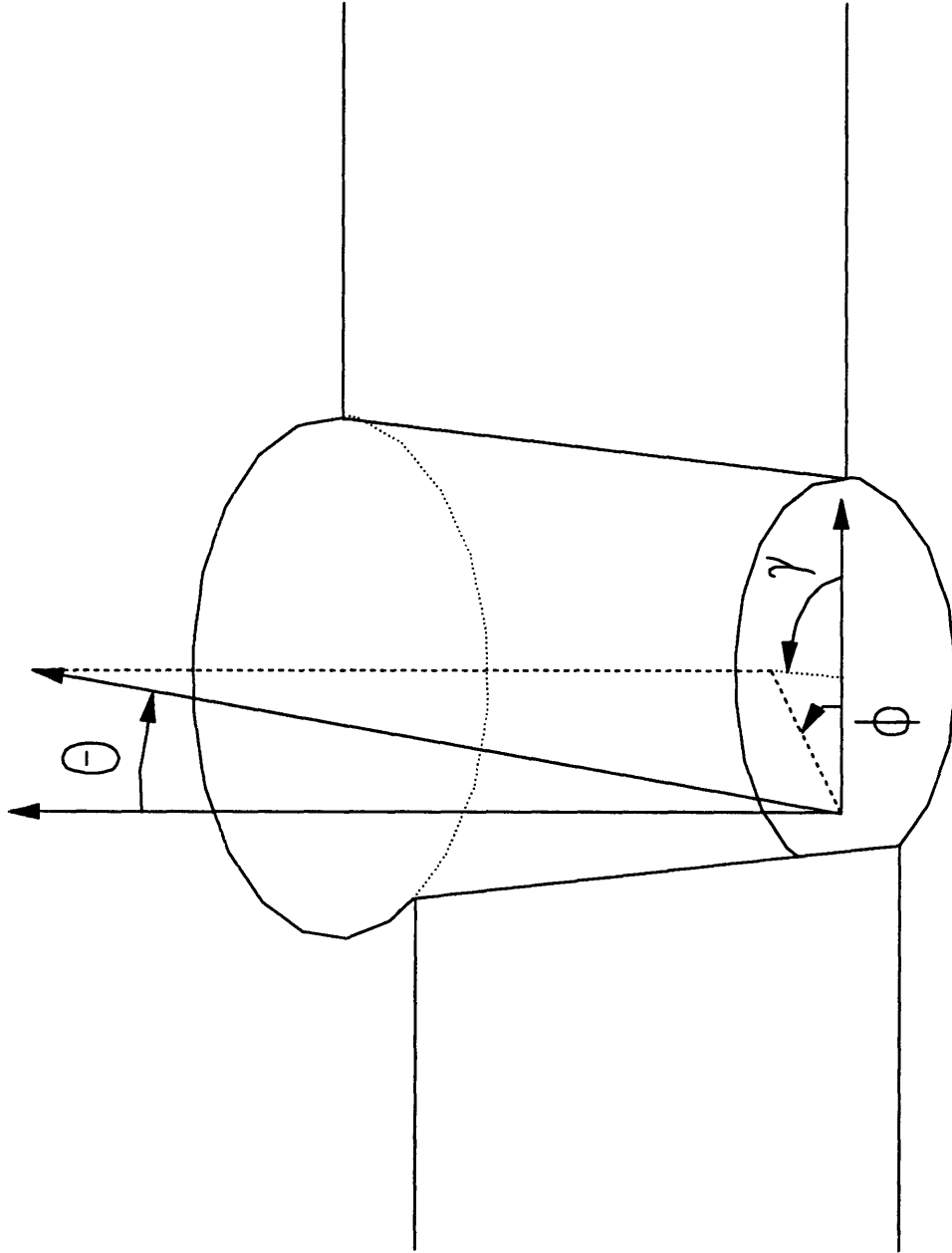


Figure A.1: Circular via and coordinate system.

the intersections of local reference lines (typically surface normals) with one or the other of two rays. The angle of arrival at the target is simply the angle between the local surface normal and a ray leading from the target to the reflection point. The angle of incidence at the reflection point is the angle between the local surface normal and that same ray, and the angle of departure from the sheath is found by comparing the reflected ray to the macroscopic wafer normal. Therefore, calculation of the characteristic angles (and the ion flux to the target) is simply a matter of determining the direction of the ray from the target to the reflection point, the orientation of the surface normal at that point, and the direction of the ray between the reflection point and the plasma. Once these directions are known, the angle between any two may be found using the general formula

$$\cos \theta_{ij} = l_i l_j + m_i m_j + n_i n_j , \quad (\text{A.1})$$

where l , m , and n are the direction cosines of each line.

The rays involved in this calculation are identified in Figure A.2 as follows: Ray 1 is the wafer normal at the plasma, 2 is the incident ray from the plasma to the reflection point, 3 is the surface normal at that point, 4 is the reflected ray from the reflection point to the target, and 5 is the local surface normal at the target. Thus,

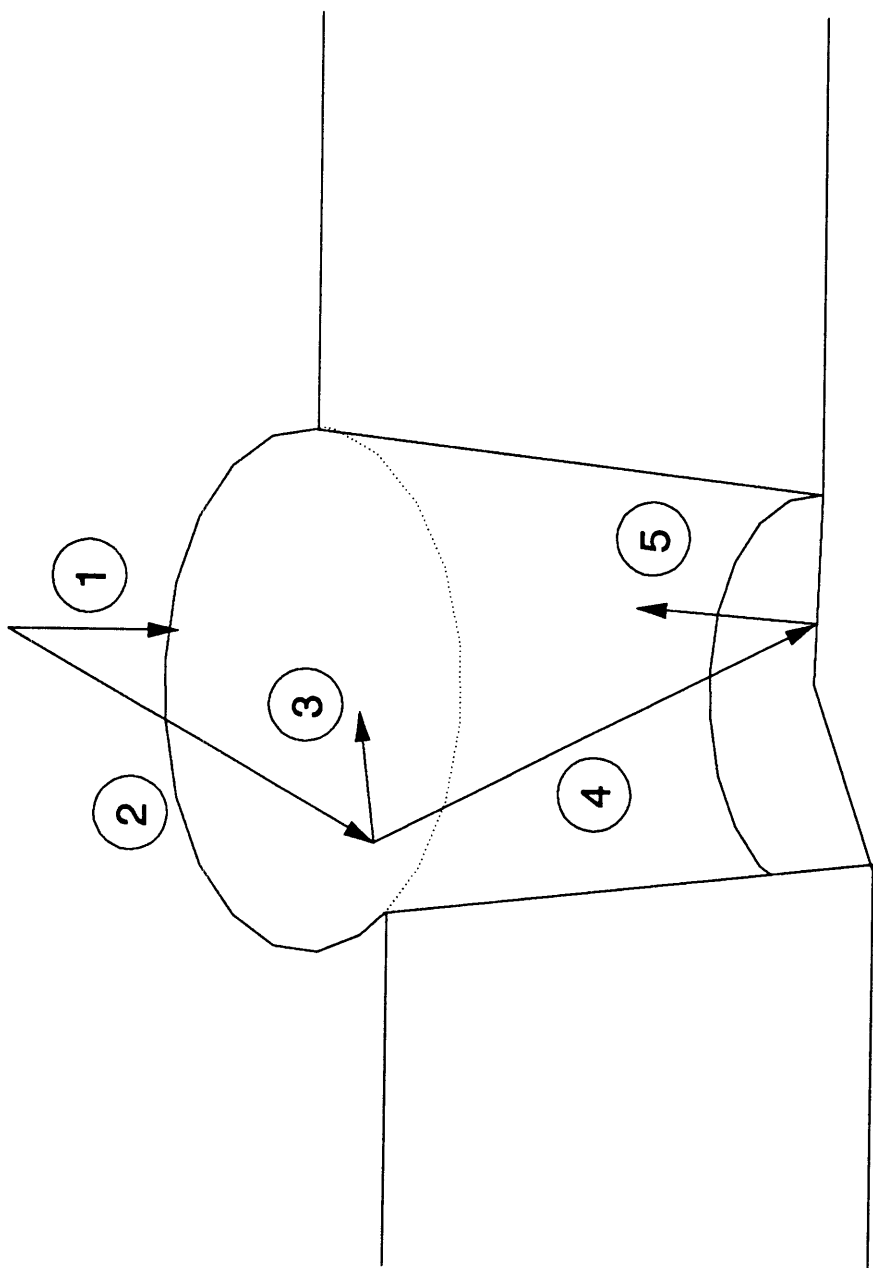


Figure A.2: Characteristic rays for ion reflection into circular via.

according to Equation (A.1),

$$\cos\theta_t = -(l_4l_5 + m_4m_5 + n_4n_5) , \quad (\text{A.2})$$

$$\cos\theta_s = -(l_2l_3 + m_2m_3 + n_2n_3) , \quad (\text{A.3})$$

and

$$\cos\theta_g = l_1l_2 + m_1m_2 + n_1n_2 . \quad (\text{A.4})$$

The negative signs in the first two Equations reflect the direction of ion travel.

Rays 1 and 5 are clearly defined by the fixed orientation of the wafer normal and the surface inclination at the target (θ_{Targ}) as

$$\begin{aligned} l_1 &= 0 \\ m_1 &= 0 \\ n_1 &= -1 . \end{aligned} \quad (\text{A.5})$$

and

$$\begin{aligned}l_5 &= \cos\left(\theta_{\text{Targ}} + \frac{\pi}{2}\right), \\m_5 &= \sin\left(\theta_{\text{Targ}} + \frac{\pi}{2}\right), \\n_5 &= 0,\end{aligned}\tag{A.6}$$

Ray 4 is found naturally from the integration angles as

$$\begin{aligned}l_4 &= -\sin\theta \cos\phi \\m_4 &= -\cos\theta \\n_4 &= -\sin\theta \sin\phi.\end{aligned}\tag{A.7}$$

Ray 3 is simply related to the reflecting segment's inclination angle (in the cross-sectional plane) and the angle of rotation about the central axis of the feature,

$$\begin{aligned}l_3 &= -\cos\gamma \cos\left(\theta_{\text{Side}} + \frac{\pi}{2}\right) \\m_3 &= \sin\left(\theta_{\text{Side}} + \frac{\pi}{2}\right) \\n_3 &= -\sin\gamma \cos\left(\theta_{\text{Side}} + \frac{\pi}{2}\right),\end{aligned}\tag{A.8}$$

but γ is not one of the integrating angles. Figure A.3 shows that γ is related to ϕ and the target position by

$$\gamma = \phi + \Delta , \quad (\text{A.9})$$

where

$$\sin \Delta = \frac{x_t \sin(\pi - \phi)}{r} . \quad (\text{A.10})$$

The final ray, 4, is found by noting that the velocity component tangential to the reflecting surface is unchanged. That direction does not correspond to any of the feature dimensions, as in the rectangular trench, but it can be found by realizing that the incident ray, the reflected ray, and the surface normal at the reflecting point all lie in a single plane. An imaginary origin for the incident ray can be located by projecting the target point onto and then past the surface normal at the reflecting point, as shown in Figure A.4. After appropriate manipulation, the incident ray is

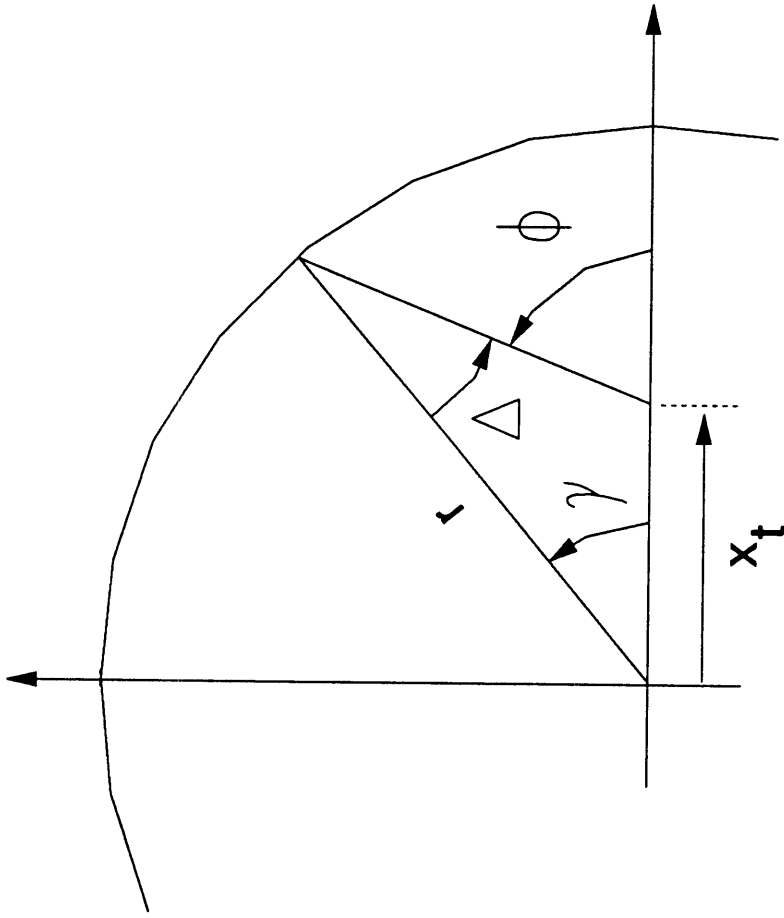


Figure A.3: Relationship between azimuthal angles about target point and central axis of feature.

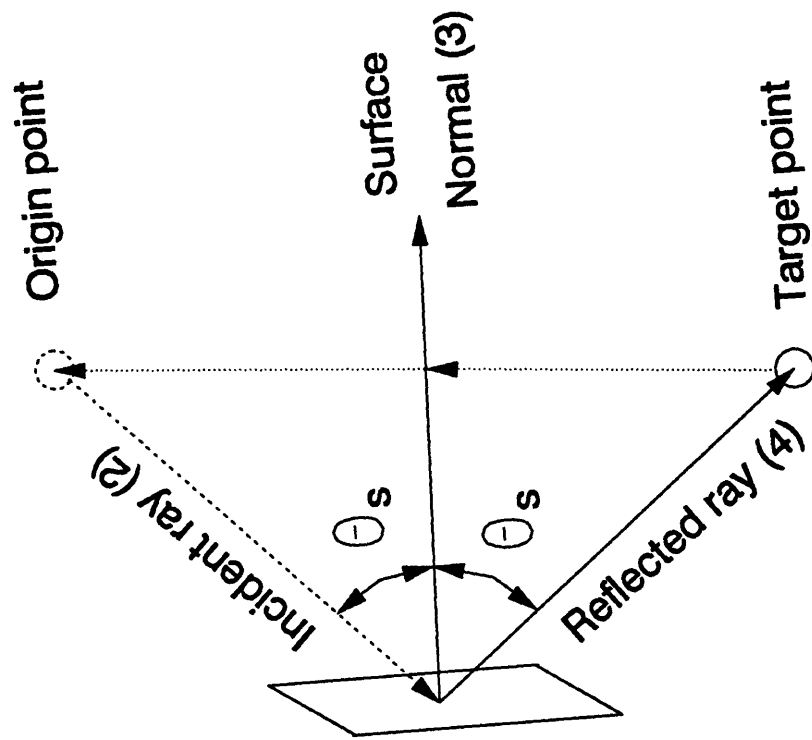


Figure A.4: Location of origin point for incident ray.

found to follow

$$\begin{aligned}l_2 &= l_4 - 2l_3 \cos \theta_s \\m_2 &= m_4 - 2m_3 \cos \theta_s \\n_2 &= n_4 - 2n_3 \cos \theta_s .\end{aligned}\tag{A.11}$$

Once the 5 rays are determined, calculation of the ion flux can proceed in a straightforward manner. Visibility between the sidewall and target remains a computational cost issue and will be discussed in Appendix B.

Appendix B

Equivalence of 2- and 3-Dimensional Visibility Calculations

B.1 Rectangular Trenches

This project utilized long rectangular trenches as a test vehicle for the physical and numerical models developed. One of the principal reasons for this choice was the ability to utilize intrafeature and feature-to-plasma visibility information from the cross-sectional plane for the transport of ions and neutrals outside of that plane. This Appendix explores the requirements for such a simplification and shows that they are met in long trenches. The second section proves that 2-Dimensional visibility data is insufficient for modeling 3-D transport in circular vias.

The proof of applicability to long trenches is fairly simple. The visibility graph is determined by the relative distances and angles from the target point to the other points on the surface. Moving out-of-plane may change the absolute angles or distances, but the 2-D relationships will still hold if the relative changes are the same.

Each point in a 2-D cross-section of a long rectangular trench is contained in an approximately infinite line. The lines are all parallel to the longitudinal axis of the trench and to each other. If the Cartesian coordinate system is used, with x and y describing the horizontal and vertical directions in the cross-sectional plane, then

moving out-of-plane along a line parallel to the longitudinal axis of the trench changes z but not x or y . The (α, ψ) coordinate system introduced in Chapter 2 is related to the Cartesian by

$$\begin{aligned} x &= d \sin \alpha \cos \psi \\ y &= d \cos \alpha \cos \psi \\ z &= d \sin \psi . \end{aligned} \tag{B.1}$$

Thus, along any longitudinal line,

$$z = \sqrt{x^2 + y^2} \tan \psi , \tag{B.2}$$

and the distance from the target point is given by

$$d = \sqrt{x^2 + y^2} \sqrt{1 + \tan^2 \psi} . \tag{B.3}$$

Rotating out-of-plane does not change the relative distances to two points. Consider two points with coordinates (x_1, y_1) and (x_2, y_2) in the cross-sectional plane. The ratio of their distances from the target is independent of ψ :

$$\frac{d_2}{d_1} = \frac{\sqrt{x_2^2 + y_2^2} \sqrt{1 + \tan^2 \psi}}{\sqrt{x_1^2 + y_1^2} \sqrt{1 + \tan^2 \psi}} = \frac{\sqrt{x_2^2 + y_2^2}}{\sqrt{x_1^2 + y_1^2}} . \tag{B.4}$$

The angle from the wafer normal (y axis in the Cartesian system described above) is related to the in-plane and out-of-plane components by

$$\cos \theta = \cos \alpha \cos \psi , \quad (\text{B.5})$$

as mentioned in Chapter 2. Moving out-of-plane changes the actual angles but not their rankings:

$$\frac{\cos \theta_2}{\cos \theta_1} = \frac{\cos \alpha_2 \cos \psi}{\cos \alpha_1 \cos \psi} = \frac{\cos \alpha_2}{\cos \alpha_1} . \quad (\text{B.6})$$

Therefore, rotating out of the cross-sectional plane has the effect of "stretching" the feature profile. The entire profile is distorted, but by a constant amount, so the relative positions of all elements are retained. Points which are visible in the 2-D plane remain visible for all ψ , and points which are blocked in 2-D remain blocked.

The distorting effect of the out-of-plane rotation can be expressed in another way. The vertical distance from the target to each point is unchanged, but the

horizontal distance d_h changes according to

$$d_h = x\sqrt{1 + \tan^2 \psi} . \tag{B.7}$$

The distortion is the same for all points because d_h is linear in x . This will be discussed further in the next Section.

B.2 Circular Via

For the circular via, rotating out of the cross-sectional plane also distorts the feature profile. In this case, however, the distortion varies between points and changes their relative positions. A sufficient condition for failure of the 2-D visibility approximation is a crossing of the angles from the target to two sidewall points. For example, consider two points A and B positioned such that $\theta_A > \theta_B$ in the 2-D plane. If rotation out of plane leads to $\theta_A < \theta_B$, then the visibility will change and the 2-D approximation is invalid. This Appendix presents a brief exploration of the conditions under which such a crossing might occur in a circular via.

The variation of θ with ϕ is conveniently expressed through the tangent of θ . The vertical separation between points remains constant as ϕ varies. The horizontal distance changes with rotation as shown in Figure B.1, where r is the via radius at a given height, x_t is the distance from the central axis of the feature to the target point, and $d(\phi)$ is the horizontal distance from the target point to the feature wall at the

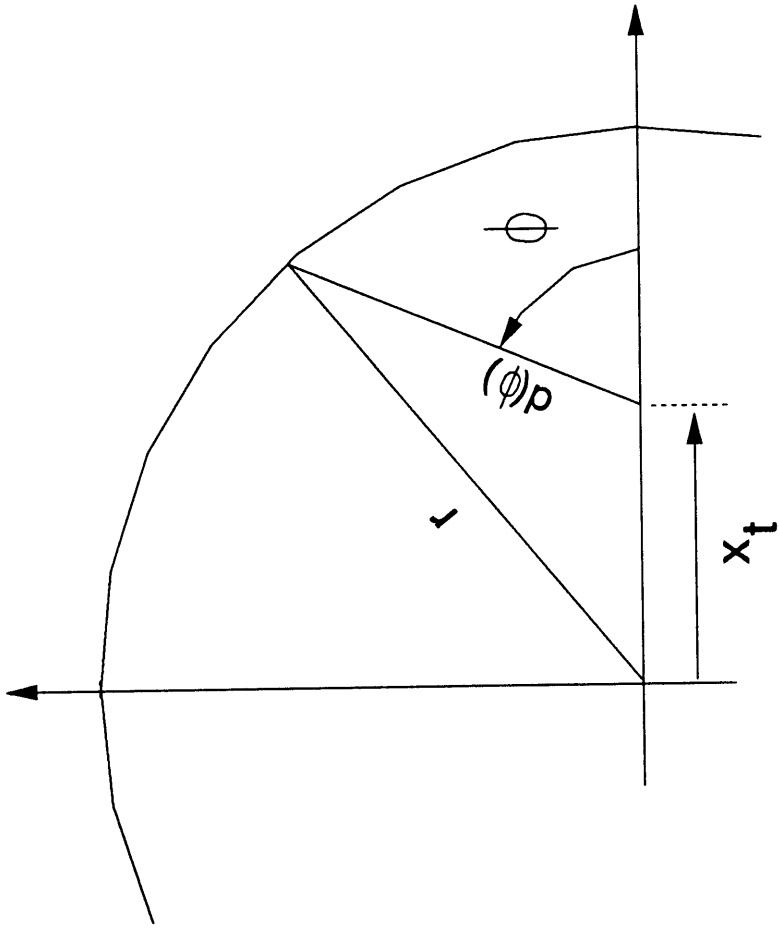


Figure B.1: Relationship between rotational angle and distance to sidewall for circular via.

angle ϕ . The tangent may be expressed as

$$\tan\theta(\phi) = \frac{y}{d(\phi)} . \quad (\text{B.8})$$

and the angles to A and B will cross if there exist two rotational angles ϕ_1 and ϕ_2 such that

$$\frac{y_A}{d_A(\phi_1)} > \frac{y_B}{d_B(\phi_1)} \quad (\text{B.9})$$

and

$$\frac{y_A}{d_A(\phi_2)} < \frac{y_B}{d_B(\phi_2)} . \quad (\text{B.10})$$

The effect of ϕ on d may be evaluated as follows. From Figure B.1 and the law of cosines,

$$r^2 = x_t^2 + d^2 - 2 x_t d \cos(\pi - \phi) , \quad (\text{B.11})$$

and

$$d = x_t \cos(\pi - \phi) \pm \sqrt{x_t^2 \cos^2(\pi - \phi) + (r^2 - x_t^2)}. \quad (\text{B.12})$$

In the typical case of outwardly tapered sidewalls, $x_t < r$, and Equation (B.12) simplifies to

$$d = -x_t \cos \phi + \sqrt{(\cos^2 \phi - 1)x_t^2 + r^2}, \quad (\text{B.13})$$

for which

$$\frac{\partial d}{\partial \phi} = x_t \sin \phi \left[1 - \frac{x_t \cos \phi}{\sqrt{(\cos^2 \phi - 1)x_t^2 + r^2}} \right]. \quad (\text{B.14})$$

For $r > x_t$ and x_t positive, d increases monotonically as ϕ increases from 0 to π , with

$$d(0) = r - x_t \quad (\text{B.15})$$

and

$$d(\pi) = r + x_t . \quad (\text{B.16})$$

The extreme values of $\tan(\theta)$ are also found at $\phi = 0$ and $\phi = \pi$. This suggests another sufficient condition for the crossing of θ_A and θ_B as

$$\frac{y_A d_B(0)}{d_A(0) y_B} > 1 > \frac{y_A d_B(\pi)}{d_A(\pi) y_B} \quad (\text{B.17})$$

or

$$\frac{y_A d_B(0)}{d_A(0) y_B} < 1 < \frac{y_A d_B(\pi)}{d_A(\pi) y_B} , \quad (\text{B.18})$$

which can be further simplified to

$$\frac{r_B - x_t}{r_A - x_t} > \frac{y_b}{y_a} > \frac{r_B + x_t}{r_A + x_t} \quad (\text{B.19})$$

or

$$\frac{r_B - x_t}{r_A - x_t} < \frac{y_B}{y_A} < \frac{r_B + x_t}{r_A + x_t} . \quad (\text{B.20})$$

These conditions are easily met. For example, if $r_A = 1$, $r_B = 3/2$, and $x_t = 1/2$, then θ_A and θ_B will cross if

$$\frac{4}{3} < \frac{y_B}{y_A} < 2 . \quad (\text{B.21})$$

There are certain combinations of feature radius and profile for which the 2-D visibility remains valid for all ϕ . However, those instances are so few and so limited that the visibility graph will generally need to be recalculated for each combination of x_t and ϕ .

Appendix C

Interchange Factors for Neutral Transport

C.1 Introduction

Chapter 4 described models for Knudsen diffusion of neutrals in features, in terms of the local sticking coefficients and the interchange factors F_{ij} . The interchange factor F_{ij} is defined as the fraction of material emitted from area j and impinging directly upon area i . Interchange factors are also commonly known as configuration factors, shape factors, or view factors.

Interchange factors could be defined for any emission profile (relationship between emission intensity and angle from the surface normal), but the most common systems involve diffuse emission. The diffuse emission intensity does not depend upon direction; consequently, the total emission from a finite area of surface varies with the cosine of the angle from normal. Thermal emission of particles from a surface is one example of diffuse emission, but a more common example is radiative heat transfer.

Siegel and Howell [1971] have considered the use of interchange factors in analysis of radiative heat transfer. They listed the following relationships for the

areas of and interchange factors between two areas of a surface:

$$A_1 F_{12} = A_2 F_{21} , \quad (\text{C.1})$$

and

$$F_{12} = \frac{1}{A_1} \int_{A_1} \int_{A_2} dF_{d1-d2} . \quad (\text{C.2})$$

For neutral transport in long rectangular trenches, elements of surface area may be replaced by line segments in the cross-sectional plane. The conditions for representation of 3-Dimensional transport by a 2-D equivalent were discussed in Chapter 2 (Section 2.4.1), and are clearly met in the case of diffuse emission. Pairs of line segments in the cross-sectional plane can be divided into two classes: segments contained within lines which intersect each other, and segments contained in lines which are parallel (or anti-parallel). The following sections describe the calculation of interchange factors for these two cases.

C.2 Segments on Intersecting Lines

Consider a pair of mutually visible line segments 1 and 2 as shown in Figure C.1. The interchange factor from segment 1 to segment 2 is given by Equation (C.2)

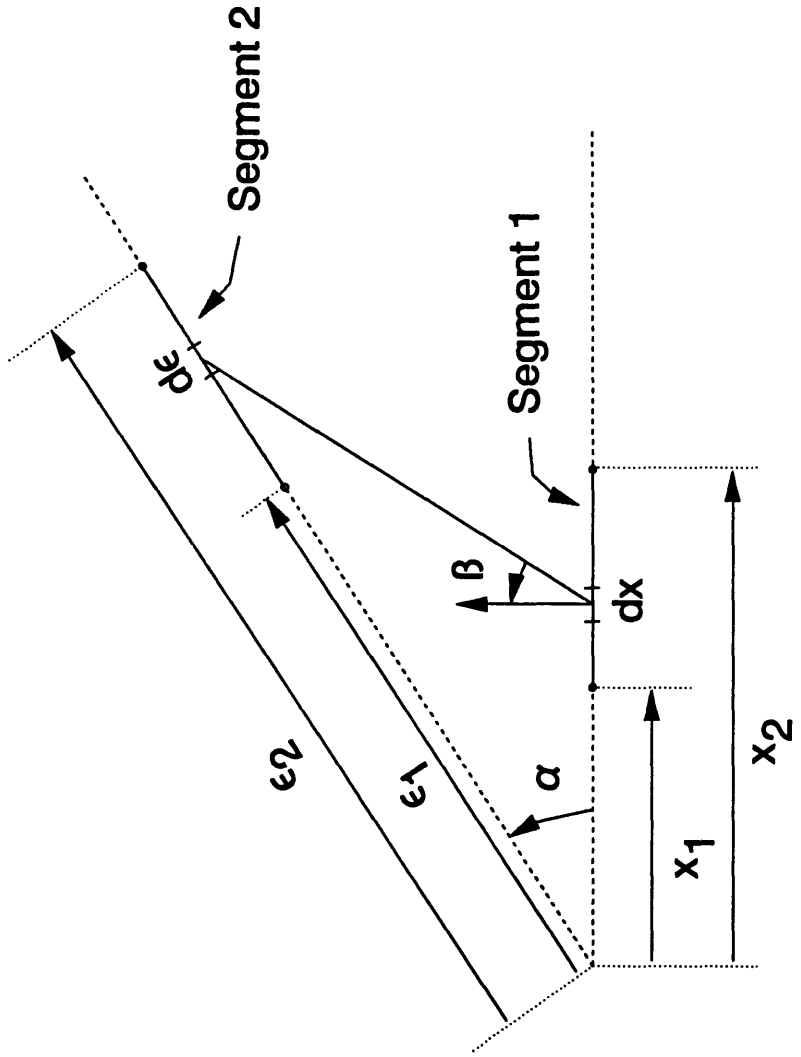


Figure C.1: Geometry and nomenclature for calculation of interchange factor for two segments on intersecting lines, following Siegel and Howell [1971].

as

$$F_{12} = \frac{1}{(x_2 - x_1)} \int_{x_1}^{x_2} \left[\int_{e_1}^{e_2} dF_{dx-de} \right] dx , \quad (C.3)$$

where Siegel and Howell [1971] have shown that

$$dF_{dx-de} = \frac{1}{2} d\sin \beta . \quad (C.4)$$

From Figure C.1,

$$\sin \beta = \frac{e \cos \alpha - x}{\sqrt{x^2 + e^2 - 2 x e \cos \alpha}} , \quad (C.5)$$

and

$$d\sin \beta = \frac{x e \sin^2 \alpha}{(x^2 + e^2 - 2 x e \cos \alpha)^{\frac{3}{2}}} de . \quad (C.6)$$

Then,

$$F_{12} = \frac{1}{2(x_2 - x_1)} \int_{x_1}^{x_2} \left[\int_{e_1}^{e_2} \frac{x e \sin^2 \alpha}{(x^2 + e^2 - 2 x e \cos \alpha)^{\frac{3}{2}}} de \right] dx, \quad (C.7)$$

where

$$\int \frac{x e \sin^2 \alpha}{(x^2 + e^2 - 2 x e \cos \alpha)^{\frac{3}{2}}} de = \frac{\cos \alpha e - x}{\sqrt{x^2 + e^2 - 2 x e \cos \alpha}}. \quad (C.8)$$

Thus,

$$F_{12} = \frac{1}{2(x_2 - x_1)} \int_{x_1}^{x_2} \left[\frac{\cos \alpha e_2 - x}{\sqrt{x^2 + e_2^2 - 2 x e_2 \cos \alpha}} - \frac{\cos \alpha e_1 - x}{\sqrt{x^2 + e_1^2 - 2 x e_1 \cos \alpha}} \right] dx, \quad (C.9)$$

where

$$\int \frac{\cos \alpha e - x}{\sqrt{x^2 + e^2 - 2 x e \cos \alpha}} dx = -\sqrt{x^2 + e^2 - 2 x e \cos \alpha}. \quad (C.10)$$

Finally,

$$F_{12} = \frac{1}{2(x_2 - x_1)} \times \left[\sqrt{x_2^2 + e_1^2 - 2x_2 e_1 \cos \alpha} - \sqrt{x_2^2 + e_2^2 - 2x_2 e_2 \cos \alpha} + \sqrt{x_1^2 + e_2^2 - 2x_1 e_2 \cos \alpha} - \sqrt{x_1^2 + e_1^2 - 2x_1 e_1 \cos \alpha} \right]. \quad (\text{C.11})$$

C.3 Segments on Parallel Lines

If two segments lie on parallel lines, as shown in Figure C.2, then

$$\sin \beta = \frac{\epsilon - x}{\sqrt{(\epsilon - x)^2 + s^2}}, \quad (\text{C.12})$$

where ϵ and x are both measured from an arbitrary reference line perpendicular to the lines containing both segments and s is the perpendicular distance between the two lines.

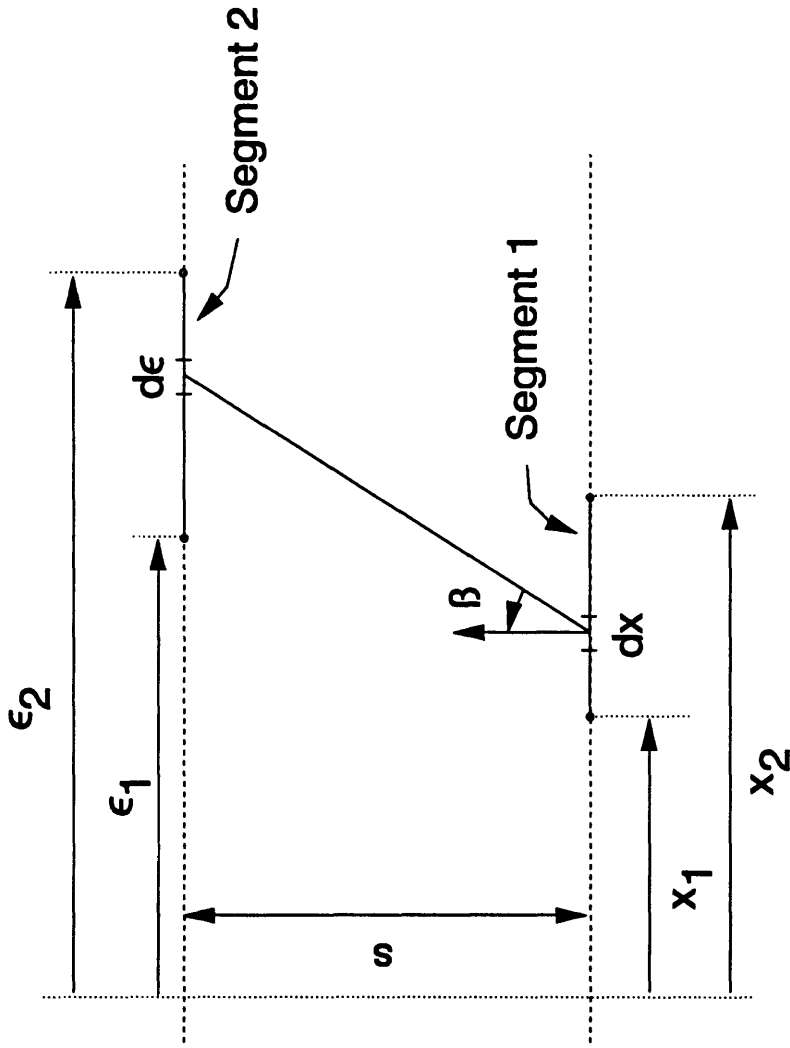


Figure C.2: Geometry and nomenclature for calculation of interchange factor for two segments on parallel lines.

In this case, it is more convenient to observe that

$$\begin{aligned}
 F_{12} &= \frac{1}{2(x_2 - x_1)} \int_{x_1}^{x_2} \left[\int_{e_1}^{e_2} d\sin \beta \right] dx \\
 &= \frac{1}{2(x_2 - x_1)} \int_{x_1}^{x_2} [\sin \beta(e_2) - \sin \beta(e_1)] dx .
 \end{aligned}
 \tag{C.13}$$

Then,

$$F_{12} = \frac{1}{2(x_2 - x_1)} \int_{x_1}^{x_2} \left[\frac{e_2 - x}{\sqrt{(e_2 - x)^2 + s^2}} - \frac{e_1 - x}{\sqrt{(e_1 - x)^2 + s^2}} \right] dx , \tag{C.14}$$

where

$$\int \frac{e - x}{\sqrt{(e - x)^2 + s^2}} dx = -\sqrt{(e - x)^2 + s^2} . \tag{C.15}$$

Therefore,

$$\begin{aligned}
 F_{12} &= \frac{1}{2(x_2 - x_1)} \left[\sqrt{(e_1 - x_2)^2 + s^2} - \sqrt{(e_2 - x_2)^2 + s^2} + \right. \\
 &\quad \left. \sqrt{(e_2 - x_1)^2 + s^2} - \sqrt{(e_1 - x_1)^2 + s^2} \right] .
 \end{aligned}
 \tag{C.16}$$

Appendix D

Development of Characteristic Equations for Surface Advancement

The derivation of these equations has been discussed previously by Hamaguchi, *et al.* [1993], but will be summarized here to avoid confusion over differences in nomenclature. The development begins with a very general representation of the surface in 2-dimensional Cartesian coordinates by

$$y = u(x,t) \tag{D.1}$$

where x is the horizontal location, y is the height of the surface above that location, and t is time since the start of etching. Thus, the height of the surface at each horizontal position varies with etching time according to $u(x,t)$. The function $u(x,t)$ is only defined over a small region, and does not necessarily represent the entire surface. The existence of retrograde features, with multiple heights for some horizontal positions, does not prevent use of this representation because $u(x,t)$ may vary along the surface.

For convenience, a parameter Ψ is defined, where

$$\Psi \equiv y - u(x,t) - 0 \tag{D.2}$$

and

$$\frac{d\Psi}{dt} - \Psi_y \dot{y} + \Psi_x \dot{x} + \Psi_t = 0 \quad (\text{D.3})$$

Throughout this Appendix, the appearance of variables as subscripts denotes partial differentiation with respect to that variable, e.g.:

$$\Psi_x = \frac{\partial \Psi}{\partial x}, \quad \Psi_y = \frac{\partial \Psi}{\partial y}, \quad \text{etc.} \quad (\text{D.4})$$

The next step, and the most important departure from common methods, is to express the motion of a surface point in time as

$$(\dot{x}, \dot{y}) \equiv \left(\frac{dx}{dt}, \frac{dy}{dt} \right) = c \bar{n} + c' \bar{\tau} \quad (\text{D.5})$$

where \bar{n} and $\bar{\tau}$ are the unit vectors normal and tangent to the surface, respectively.

This expression is completely general, and the motion of surface points is not restricted to the normal direction *a priori*. The term c is the rate of motion in the outward normal direction, and clearly corresponds to the negative of the etching rate.

The physical meaning of c' is not obvious, but it will be shown momentarily that c' does not appear in the final equations for surface evolution.

Expressing \vec{n} and $\vec{\tau}$ in terms of Ψ yields:

$$\vec{n} = \frac{\nabla\Psi}{\|\nabla\Psi\|} = \frac{\Psi_x \hat{i} + \Psi_y \hat{j}}{\|\nabla\Psi\|}, \quad (\text{D.6})$$

and, since $\vec{\tau}$ is perpendicular to \vec{n} ,

$$\vec{\tau} = \frac{-\Psi_y \hat{i} + \Psi_x \hat{j}}{\|\nabla\Psi\|}, \quad (\text{D.7})$$

where \hat{i} and \hat{j} are the unit vectors in the x and y directions, respectively. Thus,

$$\begin{aligned} \begin{pmatrix} \dot{x} \\ \dot{y} \end{pmatrix} &= \frac{1}{\|\nabla\Psi\|} \left[c \begin{pmatrix} \Psi_x \\ \Psi_y \end{pmatrix} + c' \begin{pmatrix} -\Psi_y \\ \Psi_x \end{pmatrix} \right] \\ &= \frac{1}{\|\nabla\Psi\|} \begin{bmatrix} c \Psi_x - c' \Psi_y \\ c \Psi_y + c' \Psi_x \end{bmatrix} \end{aligned} \quad (\text{D.8})$$

Substituting (D.8) into (D.3):

$$\frac{d\Psi}{dt} - \frac{c}{\|\nabla\Psi\|} \left[\Psi_x^2 + \Psi_y^2 \right] + \Psi_t = 0 . \quad (\text{D.9})$$

But

$$\|\nabla\Psi\| = \sqrt{\Psi_x^2 + \Psi_y^2} , \quad (\text{D.10})$$

so

$$\frac{d\Psi}{dt} - c \sqrt{\Psi_x^2 + \Psi_y^2} + \Psi_t = 0 . \quad (\text{D.11})$$

Notice that the terms containing c' have canceled each other, leaving an equation that depends only upon c , the negative of the local etching rate.

The definition of Ψ in Equation (D.2) gives:

$$\Psi_x = -\frac{\partial u}{\partial x} \quad (\text{D.12})$$

$$\Psi_y = 1 \quad (\text{D.13})$$

$$\Psi_t = -\frac{\partial u}{\partial t} \quad (\text{D.14})$$

Upon substitution into (D.11),

$$\frac{d\Psi}{dt} = c \sqrt{\left(\frac{\partial u}{\partial x}\right)^2 + 1} - \frac{\partial u}{\partial t} = 0, \quad (\text{D.15})$$

and, finally,

$$u_t = c \sqrt{u_x^2 + 1} = -ER \sqrt{u_x^2 + 1}. \quad (\text{D.16})$$

This first order, nonlinear partial differential equation (PDE) is decomposed into a set of ordinary differential equations (ODE's) by the Method of Characteristics (see, for example, Zauderer [1983]).

For clarity, make the following substitutions:

$$p \equiv u_x \tag{D.17}$$

$$q \equiv u_t, \tag{D.18}$$

so that Equation (D.16) becomes

$$q = -ER \sqrt{p^2+1}. \tag{D.19}$$

Define a function F by

$$F \equiv q + ER \sqrt{p^2+1} = 0, \tag{D.20}$$

where

$$F = F(q,p,c) \tag{D.21}$$

and

$$ER = ER(u,x,t) , \tag{D.22}$$

so that

$$F = F(u,x,t,p,q) = 0 . \tag{D.23}$$

Next, introduce a parameter s such that:

$$x = x(s) , \tag{D.24}$$

$$u = u(s) , \tag{D.25}$$

$$p = p(s) , \tag{D.26}$$

$$q = q(s) , \tag{D.27}$$

$$t = t(s) , \tag{D.28}$$

and

$$F = q(s) + ER \sqrt{p(s)^2 + 1} . \quad (\text{D.29})$$

After manipulation, obtain

$$\frac{dx}{ds} = F_p , \quad (\text{D.30})$$

$$\frac{dt}{ds} = F_q , \quad (\text{D.31})$$

$$\frac{du}{ds} = pF_p + qF_q , \quad (\text{D.32})$$

$$\frac{dp}{ds} = -F_x - pF_u , \quad (\text{D.33})$$

and

$$\frac{dq}{ds} = -F_t - qF_u . \quad (\text{D.34})$$

From the definition of F in Equation (D.29),

$$F_q = 1 \quad (\text{D.35})$$

and

$$\frac{dt}{ds} = 1 , \quad (\text{D.36})$$

so

$$s = t . \quad (\text{D.37})$$

This leads to a set of 3 coupled differential equations:

$$\frac{dx}{ds} = \frac{dx}{dt} = F_p = \frac{ER_p}{\sqrt{p^2 + 1}} + ER_p \sqrt{p^2 + 1} , \quad (\text{D.38})$$

$$\frac{du}{ds} - \frac{dy}{dt} = \frac{ER p^2}{\sqrt{p^2 + 1}} + (pER_p - ER) \sqrt{p^2 + 1} , \quad (\text{D.39})$$

and

$$\frac{dp}{ds} - \frac{dp}{dt} = - (ER_x + pER_y) \sqrt{p^2 + 1} . \quad (\text{D.40})$$

The final equations for surface advancement are found by modifying Equations (D.38) - (D.40) in two ways. First, it is evident that p would be difficult to work with in a numerical simulation, because p approaches infinity as the surface become vertical. Therefore, p is replaced by θ , through

$$p \equiv u_x = \frac{dy}{dx} , \quad (\text{D.41})$$

$$\theta = \arctan(p) , \quad (\text{D.42})$$

and

$$\frac{d\theta}{dp} = \frac{1}{p^2 + 1} . \quad (\text{D.43})$$

Then,

$$\dot{x} \equiv \frac{dx}{dt} = ER \sin(\theta) + ER_{\theta} \cos(\theta) , \quad (\text{D.44})$$

$$\dot{y} \equiv \frac{dy}{dt} = - ER \cos(\theta) + ER_{\theta} \sin(\theta), \quad (\text{D.45})$$

and

$$\frac{d\theta}{dt} = \frac{d\theta}{dp} \frac{dp}{dt} = - \frac{ER_x + p ER_y}{\sqrt{p^2 + 1}} . \quad (\text{D.46})$$

Second, Equation (D.46) as written above contains the terms ER_x and ER_y , but it is not obvious how these values would be calculated when the ion and reactant fluxes (and etching rate) are defined only upon the surface. However, Equation

(D.46) may be manipulated by observing

$$ER_x + p ER_y - \left(\frac{\partial ER}{\partial x} + \frac{dy}{dx} \frac{\partial ER}{\partial y} \right) \quad (\text{D.47})$$

and

$$\sqrt{p^2 + 1} = \sqrt{\left(\frac{dy}{dx} \right)^2 + 1} = \frac{dl}{dx}, \quad (\text{D.48})$$

where l is the arc length, or the distance along the surface from some reference location.

Equations (D.46) - (D.48) may be combined to yield

$$\frac{d\theta}{dt} = - \left(\frac{\partial ER}{\partial x} + \frac{dy}{dx} \frac{\partial ER}{\partial y} \right) \frac{dx}{dl} = - \frac{dER}{dl} \Big|_0. \quad (\text{D.49})$$

Appendix E

Comparison of Delooping to Entropy and Jump Conditions

Ross [1988] described two conditions which a properly computed surface profile must meet. These are the Entropy Condition, defining the stability of shocks in the initial surface and the formation of new shocks during evolution, and a Jump Condition governing the motion of those shocks. This Appendix demonstrates that the delooping method meets both of these conditions.

Note that the nomenclature used in this Appendix differs somewhat from that used in Chapter 5, in that single and double differentiation are denoted by use of the "prime" (') and "double prime" (") symbols, while subscripts are used only as identifiers for specific values of the given variable. These changes are made to maintain consistency with Ross's paper and to facilitate comparisons with that work.

E.1 Entropy Condition

Consider a shock where the slope changes from p_- to p_+ . Ross has stated that the entropy condition is satisfied if

$$\frac{f(p_+) - f(p)}{p_+ - p} \leq \frac{f(p_+) - f(p_-)}{p_+ - p_-} \leq \frac{f(p_-) - f(p)}{p_- - p} \quad (\text{E.1})$$

for all p between p_- and p_+ . Now consider a region of surface with slopes ranging from p_1 to p_2 , containing the shock so that $\min(p_1, p_2) < \min(p_-, p_+)$ and $\max(p_1, p_2) > \max(p_-, p_+)$. If the shock from p_- to p_+ satisfies the entropy condition, then p_- and p_+ are points of tangency between $f(p)$ and the envelope over $f(p)$, and

$$f'(p_-) \equiv \left. \frac{df}{dp} \right|_{p_-} = \frac{f(p_+) - f(p_-)}{p_+ - p_-} = f'(p_+) \equiv \left. \frac{df}{dp} \right|_{p_+}. \quad (\text{E.2})$$

In this case, the entropy condition can be restated as

$$f(p) > f(p_+) + (p - p_+)f'(p_+) \quad (\text{E.3})$$

and

$$f(p) > f(p_-) + (p - p_-)f'(p_-) \quad (\text{E.4})$$

if the shock is concave (so $p_- \leq p \leq p_+$), or

$$f(p) < f(p_+) + (p - p_+)f'(p_+) \quad (\text{E.5})$$

and

$$f(p) < f(p_-) + (p - p_-)f'(p_-) \quad (\text{E.6})$$

if the shock is convex ($p_- \geq p \geq p_+$). Points meeting the criteria specified by Equations (E.3) and (E.4) or (E.5) and (E.6) are excluded from the final solution; they disappear into the shock.

This condition can be expanded and restated as follows: the stable profile joining the slopes p_1 and p_2 will include the set of slopes p_s such that, for all p between p_1 and p_2 ,

$$f(p_s) + (p - p_s)f'(p_s) \leq f(p) \quad (\text{E.7})$$

if the region from p_1 to p_2 is concave ($p_1 < p_2$), or

$$f(p_s) + (p - p_s)f'(p_s) \geq f(p) \quad (\text{E.8})$$

if the surface is convex ($p_1 > p_2$). Equations (E.7) and (E.8) simply define the concave and convex envelopes over $f(p)$ between p_1 and p_2 (see Figure E.1). All points not satisfying Equation (E.7) or (E.8) disappear into shocks in the new surface.

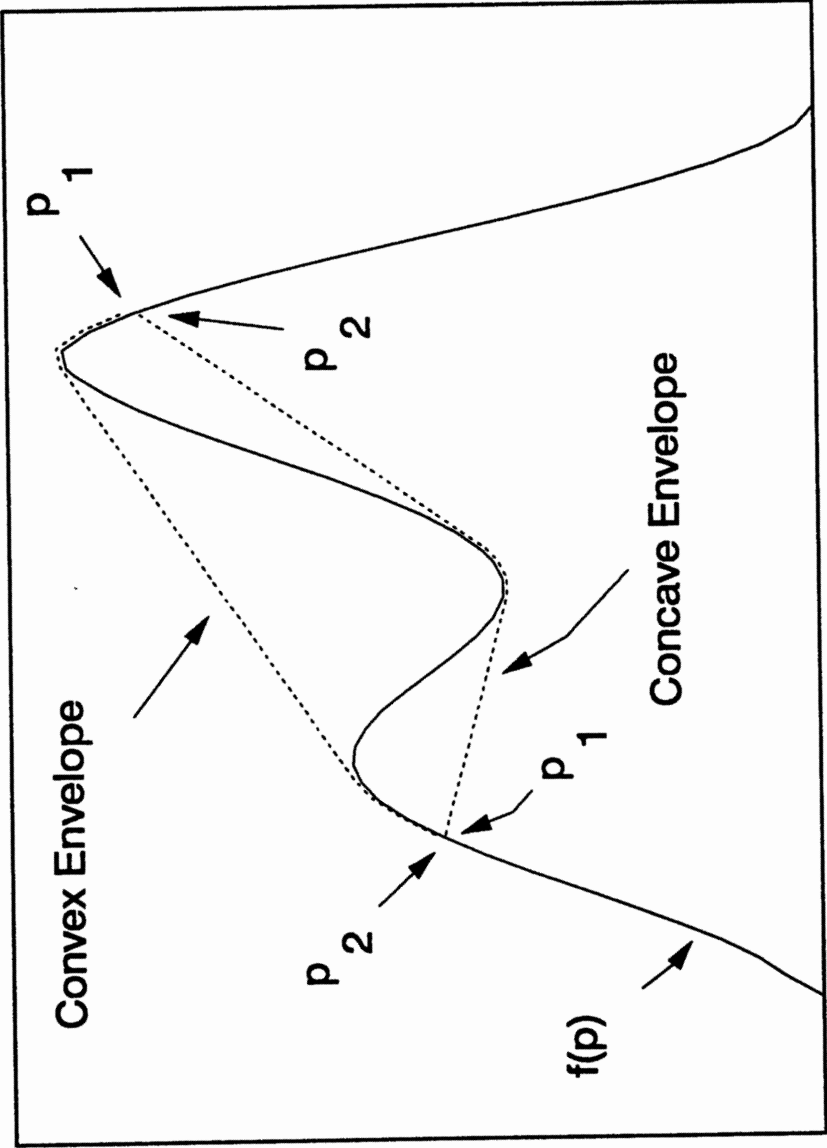


Figure E.1: Convex and concave envelopes over an arbitrary $f(p)$.

For reasons of clarity, we will restrict the following discussion to a convex surface. Figure E.2a shows the example of $p_1 = 60^\circ$, $p_2 = -60^\circ$, evolving under ion milling conditions with the sputtering yield introduced in Equation (5.5). The initial shock splits into two curved regions joined by a single shock spanning 45° to -45° , with the slopes between 45° and -45° forming a closed loop. Figure E.2b shows $f(p)$ and the convex envelope over $f(p)$ for this yield curve and angular range.

The convex envelope shown in Figure E.2b is tangential to $f(p)$ at slopes $\pm 45^\circ$ (p_- and p_+). Therefore, the points at p_- and p_+ share the same \dot{x} and \dot{y} (in fact, $\dot{x} = 0$ in Figure E.2a). If $f(p)$ and its first derivative are varying but continuous between p_- and p_+ , then \dot{x} and \dot{y} are also continuous and a closed loop must be formed.

This may also be visualized by considering the direction vector from the original shock location to a point on the characteristic locus, with the direction characterized by

$$\frac{\dot{y}}{\dot{x}} = \frac{pf'(p) - f(p)}{f'(p)} . \quad (\text{E.9})$$

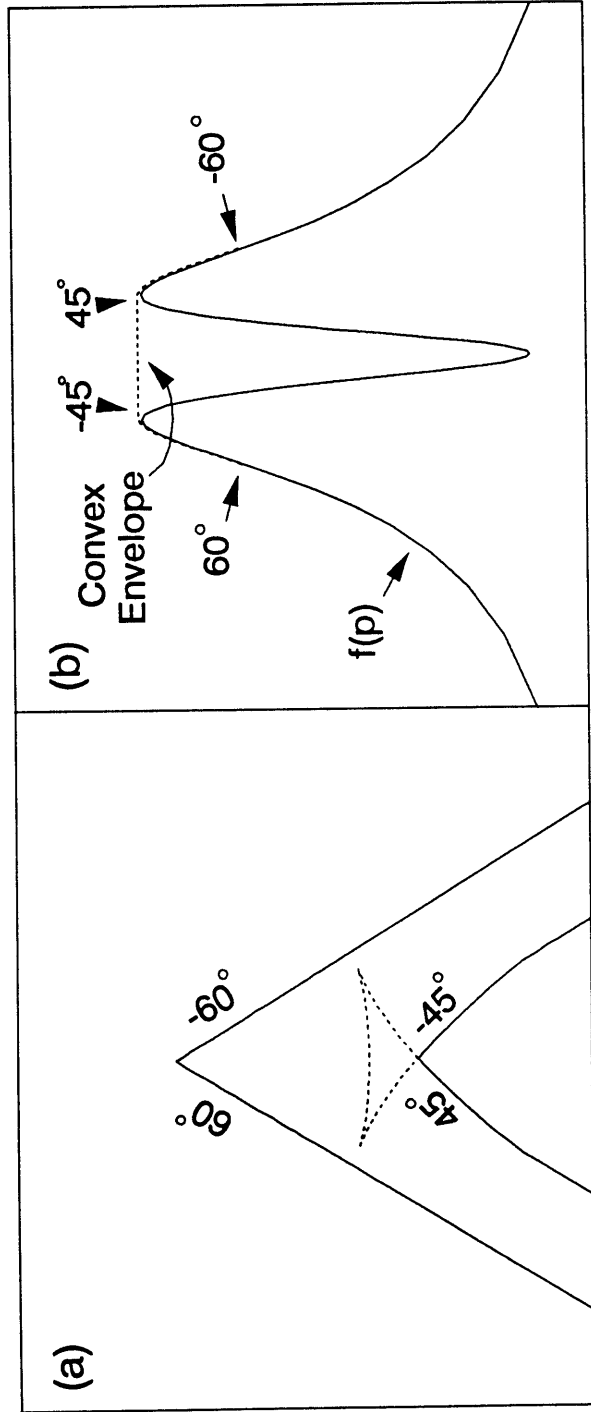


Figure E.2: Evolution of example convex shock. a) Expansion of shock in initial profile to form two smooth curves and a new shock after removal of closed loop. b) Flux function $f(p)$ and convex envelope.

The variation of direction with slope is found by differentiation as

$$\frac{d}{dp} \left(\frac{\dot{y}}{\dot{x}} \right) = \frac{f(p) f''(p)}{f'(p)^2}, \quad (\text{E.10})$$

where

$$f''(p) \equiv \frac{d^2 f}{dp^2}. \quad (\text{E.11})$$

The direction vector rotates according to the sign of $f''(p)$. If p_- and p_+ are two points of tangency between $f(p)$ and a straight line, then the sign of $f''(p)$ is the same at p_- and p_+ . Therefore, the direction vector is rotating the same way (clockwise, in this example) as p passes through both p_- and p_+ , and it must change direction at least twice in order for \dot{x} and \dot{y} to be the same at both points.

The direction vector can also be used to compare the final locations of two points with different slopes. In particular, if two points with slopes p_s and p share the same direction vector, then

$$\dot{x}(p_s) = f'(p_s) = a \dot{x}(p) = a f'(p) \quad (\text{E.12})$$

and

$$\dot{y}(p_s) - p_s f'(p_s) - f(p_s) - a \dot{y}(p) - a(p f'(p) - f(p)) , \quad (\text{E.13})$$

where a is some positive constant. If p_s meets the entropy condition, and p does not, then (from Equation (E.8))

$$f(p_s) - p_s f'(p_s) > f(p) - p f'(p) . \quad (\text{E.14})$$

Substituting Equations (E.11) and (E.12) leads to

$$a(f(p) - p f'(p)) > f(p) - p(a f'(p)) , \quad (\text{E.15})$$

$$a f(p) > f(p) , \quad (\text{E.16})$$

and

$$a > 1 . \quad (\text{E.17})$$

In other words, if two points share a direction vector, and only one of those points meets the entropy condition, then that point will move farther from the original shock location than will the other. This means that the closed loop formed by the points between p_- and p_+ lies entirely upon the near (nearer to the original shock location) side of the curves connecting p_1 , p_- (or p_+), and p_2 in the final profile. This was clearly visible in Figure E.2a.

A similar analysis for the concave case shows that the closed loop composed of points not meeting the entropy condition lies entirely upon the far (from the original shock location) side of the stable profile (Figure 5.12). Therefore, eliminating the closed loops in either case leaves the correct curve.

E.2 Jump Condition

In the example presented above, the total angular range p_1 to p_2 was chosen so that both p_- and p_+ were tangent points to $f(p)$. In such a case, the shock jump condition described by Ross [1988] reduces to the equations of motion for the individual points p_- and p_+ .

For certain values of p_1 and p_2 , however, the envelope over $f(p)$ may not approach $f(p)$ tangentially at the end points. Figure E.3 illustrates such a case. In this example, a single convex shock spans $p_1 = 25^\circ$ to $p_2 = -35^\circ$. Figure E.3a shows that

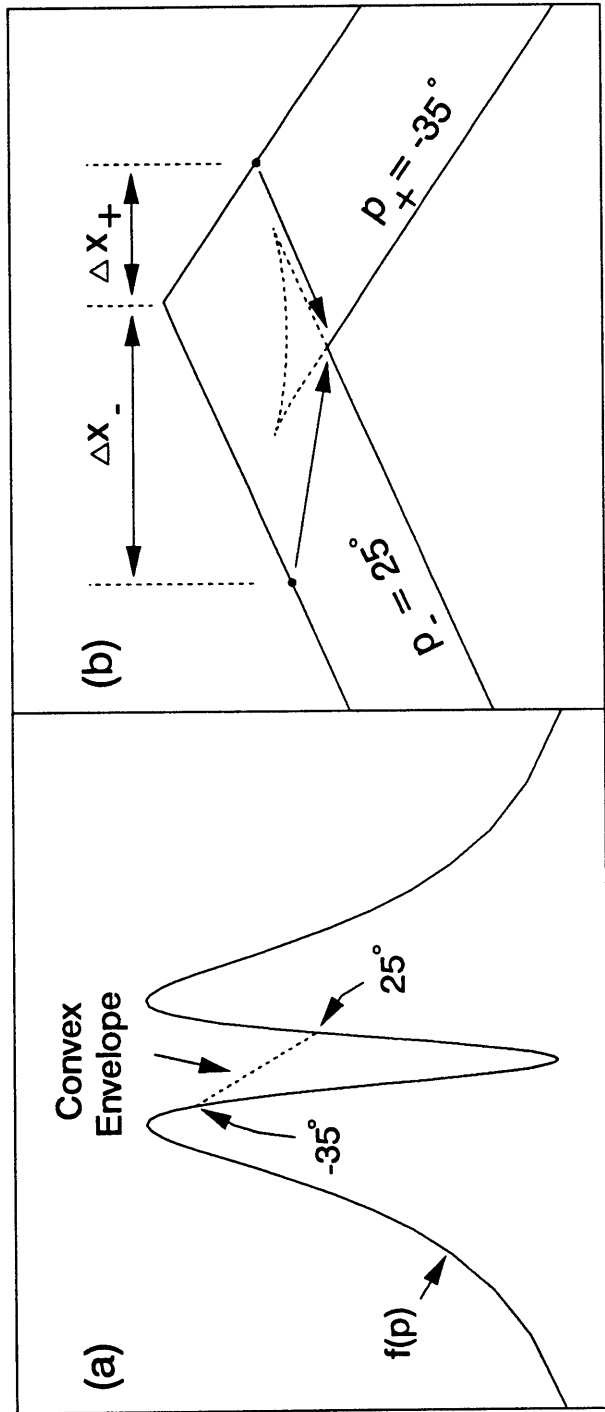


Figure E.3: Evolution of convex shock with non-tangential approach of envelope to $f(p)$. a) Flux function $f(p)$ and convex envelope. b) Evolution of surface, showing new shock location as the intersection of characteristic trajectories from two sidewall points.

the envelope over $f(p)$ for this example approaches $f(p)$ abruptly at both p_1 and p_2 . None of the slopes between p_1 and p_2 satisfy the entropy condition, so the angular range of the shock does not change upon advancement. However, examination of Equations (5.6), (5.7), (5.9) and (5.10) shows that a non-tangential intersection between $f(p)$ and its envelope causes the shock and surface to move relative to each other. The position of the shock along the surface changes in time. This is visible in Figure E.3b, where the two flat surfaces move toward each other and the shock progresses "downward" along each surface.

To maintain consistency with the previously introduced terminology, let $p_- = p_1$, and $p_+ = p_2$. The initial shock is located at (x_i, y_i) and joins lines of slope p_- and p_+ . The shock location after advancement, (x_f, y_f) , is determined by the intersection of two characteristic trajectories. The first originates at an unknown point along the line of slope p_- . This point is removed from the shock location by an unknown displacement of Δx_- , as shown in Figure E.3b, and advances to (x_f, y_f) by

$$x_f = x_i + \Delta x_- + f'(p_-) \Delta t \quad (\text{E.18})$$

and

$$y_f = y_i + p_- \Delta x_- + (p_- f'(p_-) - f(p_-)) \Delta t . \quad (\text{E.19})$$

The second trajectory originates at a similar point along the line of slope p_+ , and advances to (x_f, y_f) by

$$x_f - x_i = \Delta x_+ + f'(p_+) \Delta t \quad (\text{E.20})$$

and

$$y_f - y_i = p_+ \Delta x_+ + (p_+ f'(p_+) - f(p_+)) \Delta t . \quad (\text{E.21})$$

Combining (E.18) - (E.21) yields

$$\dot{x}_s = \frac{x_f - x_i}{\Delta t} = \frac{\Delta x_+}{\Delta t} + f'(p_+) , \quad (\text{E.22})$$

$$\dot{y}_s = \frac{y_f - y_i}{\Delta t} = p_+ \frac{\Delta x_+}{\Delta t} + p_+ f'(p_+) - f(p_+) , \quad (\text{E.23})$$

and

$$\frac{\Delta x_+}{\Delta t} = \frac{p_+ f'(p_+) - f(p_+) - p_- f'(p_+) + f(p_-)}{p_- - p_+} . \quad (\text{E.24})$$

Therefore,

$$\dot{x}_s = \frac{f(p_-) - f(p_+)}{p_- - p_+} , \quad (\text{E.25})$$

and

$$\dot{y}_s = \frac{p_+ f(p_-) - p_- f(p_+)}{p_- - p_+} , \quad (\text{E.26})$$

in agreement with the jump condition described previously by Ross [1988].

The behavior of concave shocks is analogous and will not be shown.

Appendix F

Shock Trajectories for Segment Advancement

One of the more popular surface evolution algorithms operates by advancing the straight segments between surface points parallel to themselves. The intersections of adjacent segments after advancement determine the new surface point locations [Neureuther, *et al.*, 1979]. This simple method was apparently developed from geometric considerations, but this Appendix shows that the segment intersection points move along the characteristic trajectories described by Hamaguchi, *et al.* [1993].

This Appendix follows the nomenclature used by Ross [1988]: subscripts are used to identify specific values, and the prime symbol (') refers to single differentiation.

Consider a shock at (x_i, y_i) , joining two segments at slopes p_- and p_+ . The segments each advance according to

$$\frac{dx}{dt} = ER \sin(\theta) = \frac{ER p}{\sqrt{p^2 + 1}} \quad (\text{F.1})$$

and

$$\frac{dy}{dt} = -ER \cos(\theta) = -\frac{ER}{\sqrt{p^2 + 1}} . \quad (\text{F.2})$$

These equations apply to any point on the segment. Because the segments do not change slope, advancing a segment parallel to itself (along its normal) changes only the intercept b of the line containing the segment. Each line initially includes the shock location, so

$$b = y_i - px_i \quad (\text{F.3})$$

for either segment. Advancing the segment for a short time Δt changes the intercept

to

$$\begin{aligned}
 b &= (y_i + \frac{dy}{dt} \Delta t) - p(x_i + \frac{dx}{dt} \Delta t) \\
 &= y_i - \frac{ER}{\sqrt{p^2 + 1}} \Delta t - p \left(x_i + \frac{ER p}{\sqrt{p^2 + 1}} \Delta t \right) \\
 &= y_i - p x_i - \left(ER \frac{p^2 + 1}{\sqrt{p^2 + 1}} \Delta t \right) \\
 &= y_i - p x_i - f(p) \Delta t
 \end{aligned} \tag{F.4}$$

where

$$f(p) \equiv ER \sqrt{p^2 + 1} \tag{F.5}$$

following Ross [1988].

The new location of the shock, (x_f, y_f) , is at the intersection of the new lines containing each segment

$$y_f = p_- x_f + b_- = p_+ x_f + b_+ . \tag{F.6}$$

Therefore,

$$x_f = \frac{b_+ - b_-}{p_- - p_+} - x_i + \frac{f(p_-) - f(p_+)}{p_- - p_+} \Delta t \quad (\text{F.7})$$

and

$$y_f = p_+ x_f + b_+ = y_i + \frac{p_+ f(p_-) - p_- f(p_+)}{p_- - p_+} \Delta t . \quad (\text{F.8})$$

Thus, the motion of the shock is described by

$$\frac{dx}{dt} = \frac{f(p_-) - f(p_+)}{p_- - p_+} \quad (\text{F.9})$$

and

$$\frac{dy}{dt} = \frac{p_+ f(p_-) - p_- f(p_+)}{p_- - p_+} . \quad (\text{F.10})$$

The trajectory described by Equations (F.9) and (F.10) is exactly the jump condition described by Ross [1988]. Furthermore, as the difference between p_+ and p_- decreases (as the surface becomes smooth), Equations (F.9) and (F.10) approach the characteristic equations for individual points.

We first introduce a small parameter δ such that

$$p_+ = p + \delta \tag{F.11}$$

and

$$p_- = p - \delta . \tag{F.12}$$

Then, Equations (F.9) and (F.10) become

$$\begin{aligned} \frac{dx}{dt} &= \frac{f(p - \delta) - f(p + \delta)}{(p - \delta) - (p + \delta)} \\ &= - \frac{f(p + \delta) - f(p - \delta)}{2\delta} \end{aligned} \tag{F.13}$$

and

$$\begin{aligned} \frac{dy}{dt} &= \frac{(p + \delta)f(p - \delta) - (p - \delta)f(p + \delta)}{(p - \delta) - (p + \delta)} \\ &= p \frac{f(p + \delta) - f(p - \delta)}{2\delta} - \frac{f(p - \delta) + f(p + \delta)}{2} . \end{aligned} \tag{F.14}$$

Finally, in the limit of small δ ,

$$\lim_{\delta \rightarrow 0} \frac{dx}{dt} = \frac{df(p)}{dp} \equiv f'(p) \tag{F.15}$$

and

$$\lim_{\delta \rightarrow 0} \frac{dy}{dt} = p \frac{df(p)}{dp} - f(p) = pf'(p) - f(p) , \tag{F.16}$$

in agreement with the previously discussed equations for point motion.